frontiers | Research Topics

# Tumor microenvironment and therapeutic resistance in gynecologic malignancies

**Edited by**
Xia Bai Rong, Gang Chen and Dong Hoon Suh

**Published in**
Frontiers in Oncology

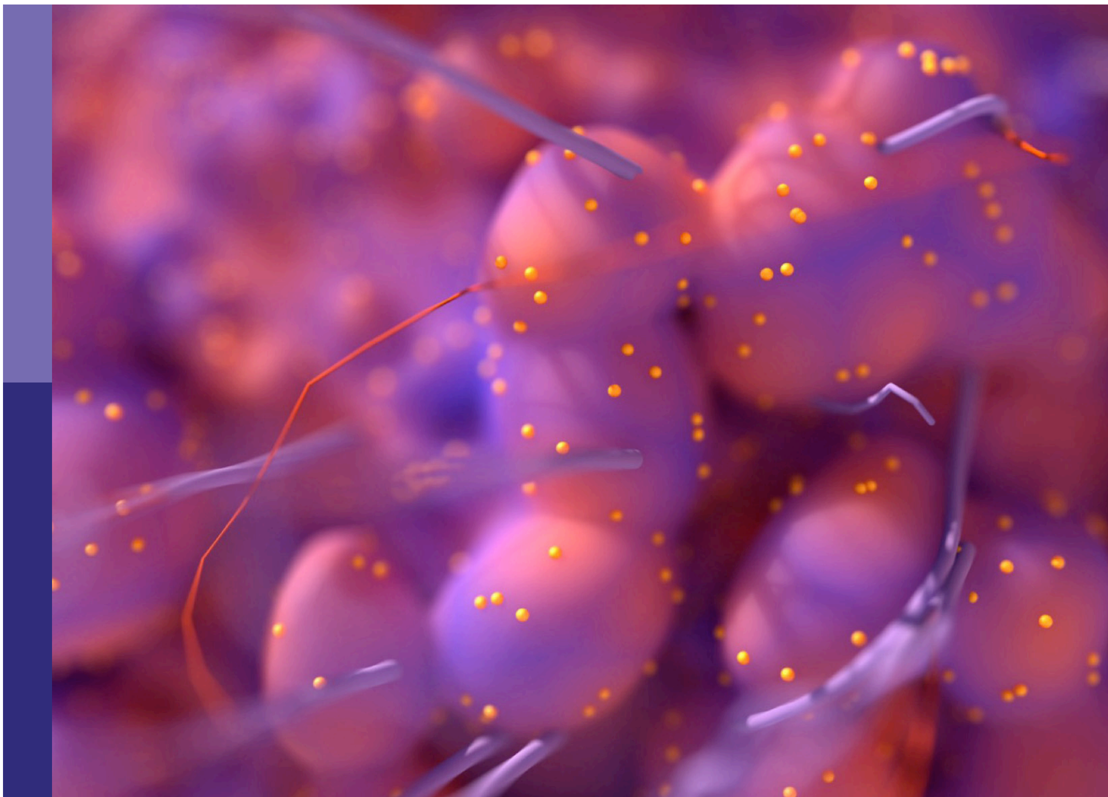

January 2023

ISSN 1664-8714
ISBN 978-2-83251-306-4
DOI 10.3389/978-2-83251-306-4

## About Frontiers

Frontiers is more than just an open access publisher of scholarly articles: it is a pioneering approach to the world of academia, radically improving the way scholarly research is managed. The grand vision of Frontiers is a world where all people have an equal opportunity to seek, share and generate knowledge. Frontiers provides immediate and permanent online open access to all its publications, but this alone is not enough to realize our grand goals.

## Frontiers journal series

The Frontiers journal series is a multi-tier and interdisciplinary set of open-access, online journals, promising a paradigm shift from the current review, selection and dissemination processes in academic publishing. All Frontiers journals are driven by researchers for researchers; therefore, they constitute a service to the scholarly community. At the same time, the *Frontiers journal series* operates on a revolutionary invention, the tiered publishing system, initially addressing specific communities of scholars, and gradually climbing up to broader public understanding, thus serving the interests of the lay society, too.

## Dedication to quality

Each Frontiers article is a landmark of the highest quality, thanks to genuinely collaborative interactions between authors and review editors, who include some of the world's best academicians. Research must be certified by peers before entering a stream of knowledge that may eventually reach the public - and shape society; therefore, Frontiers only applies the most rigorous and unbiased reviews. Frontiers revolutionizes research publishing by freely delivering the most outstanding research, evaluated with no bias from both the academic and social point of view. By applying the most advanced information technologies, Frontiers is catapulting scholarly publishing into a new generation.

## What are Frontiers Research Topics?

Frontiers Research Topics are very popular trademarks of the *Frontiers journals series*: they are collections of at least ten articles, all centered on a particular subject. With their unique mix of varied contributions from Original Research to Review Articles, Frontiers Research Topics unify the most influential researchers, the latest key findings and historical advances in a hot research area.

Find out more on how to host your own Frontiers Research Topic or contribute to one as an author by contacting the Frontiers editorial office: frontiersin.org/about/contact

# Tumor microenvironment and therapeutic resistance in gynecologic malignancies

**Topic editors**
Xia Bai Rong — The First Affiliated Hospital of University of Science and Technology of China Anhui Provincial Hospital, China
Gang Chen — Huazhong University of Science and Technology, China
Dong Hoon Suh — Seoul National University, Republic of Korea

**Citation**
Rong, X. B., Chen, G., Suh, D. H., eds. (2023). *Tumor microenvironment and therapeutic resistance in gynecologic malignancies*. Lausanne: Frontiers Media SA. doi: 10.3389/978-2-83251-306-4

# Table of contents

frontiers in Oncology

ORIGINAL RESEARCH
published: 21 October 2021
doi: 10.3389/fonc.2021.752127

# Generation of Two Paclitaxel-Resistant High-Grade Serous Carcinoma Cell Lines With Increased Expression of P-Glycoprotein

*Mariana Nunes*[1,2], *Patrícia M. A. Silva*[3,4], *Ricardo Coelho*[5], *Carla Pinto*[3,6], *Albina Resende*[3,6], *Hassan Bousbaa*[3], *Gabriela M. Almeida*[7,8] *and Sara Ricardo*[1,4,8]*

*[1] Differentiation and Cancer Group, Institute for Research and Innovation in Health (i3S) of the University of Porto/Institute of Molecular Pathology and Immunology of the University of Porto (Ipatimup), Porto, Portugal, [2] Institute of Biomedical Sciences Abel Salazar (ICBAS), University of Porto, Porto, Portugal, [3] CESPU, Institute of Research and Advanced Training in Health Sciences and Technologies (IINFACTS), Gandra, Portugal, [4] TOXRUN, Toxicology Research Unit, University Institute of Health Sciences, Polytechnic and University Cooperative (CESPU), Gandra, Portugal, [5] Ovarian Cancer Research, Department of Biomedicine, University Hospital Basel and University of Basel, Basel, Switzerland, [6] Interdisciplinary Centre of Marine and Environmental Research (CIIMAR), University of Porto, Porto, Portugal, [7] Expression Regulation in Cancer Group, Institute for Research and Innovation in Health (i3S) of the University of Porto/Institute of Molecular Pathology and Immunology of the University of Porto (Ipatimup), Porto, Portugal, [8] Faculty of Medicine from University of Porto (FMUP), Porto, Portugal*

**Edited by:**
*Xia Bai Rong,*
*Anhui Provincial Hospital, China*

**Reviewed by:**
*Mark Borris D. Aldonza,*
*Korea Advanced Institute of Science and Technology, South Korea*
*Ewa Grzybowska,*
*Maria Skoldowska-Curie National Research Institute of Oncology, Poland*

***Correspondence:**
*Sara Ricardo*
*sricardo@ipatimup.pt*

**Specialty section:**
*This article was submitted to Gynecological Oncology, a section of the journal Frontiers in Oncology*

**Received:** *02 August 2021*
**Accepted:** *30 September 2021*
**Published:** *21 October 2021*

**Citation:**
*Nunes M, Silva PMA, Coelho R, Pinto C, Resende A, Bousbaa H, Almeida GM and Ricardo S (2021) Generation of Two Paclitaxel-Resistant High-Grade Serous Carcinoma Cell Lines With Increased Expression of P-Glycoprotein. Front. Oncol. 11:752127. doi: 10.3389/fonc.2021.752127*

Debulking surgery followed by chemotherapy are the standard of care for high-grade serous carcinoma. After an initial good response to treatment, the majority of patients relapse with a chemoresistant profile, leading to a poor overall survival. Chemotherapy regimens used in high-grade serous carcinomas are based in a combination of classical chemotherapeutic drugs, namely, Carboplatin and Paclitaxel. The mechanisms underlying drug resistance and new drug discovery are crucial to improve patients' survival. To uncover the molecular mechanisms of chemoresistance and test drugs capable of overcoming this resistant profile, it is fundamental to use good cellular models capable of mimicking the chemoresistant disease. Herein, we established two high-grade serous carcinoma cell lines with intrinsic resistance to Carboplatin and induced Paclitaxel resistance (OVCAR8 PTX R C and OVCAR8 PTX R P) derived from the OVCAR8 cell line. These two chemoresistant cell line variants acquired an enhanced resistance to Paclitaxel-induced cell death by increasing the drug efflux capacity, and this resistance was stable in long-term culture and following freeze/thaw cycles. The mechanism underlying Paclitaxel resistance resides in a significant increase in P-glycoprotein expression and, when this drug efflux pump was blocked with Verapamil, cells re-acquired Paclitaxel sensitivity. We generated two high-grade serous carcinoma cell lines, with a double-chemoresistant (Carboplatin and Paclitaxel) phenotype that mimics the majority of tumor recurrences in ovarian cancer context. This robust tool is suitable for preliminary drug testing towards the development of therapeutic strategies to overcome chemoresistance.

**Keywords: high-grade serous carcinoma, ovarian cancer, chemoresistance, Paclitaxel, P-glycoprotein**

## 1 INTRODUCTION

Late diagnosis and resistance to treatment are the main reasons for the high mortality rate of high-grade serous carcinoma (HGSC) patients (1, 2). There is still a lot to improve on these two issues to extend patients' survival. On the treatment side, a successful debulking surgery (R0, defined as microscopic or no residual disease) is still the best prognostic factor for HGSC patients (3). After surgery, treatment with a combination of classical chemotherapy drugs, such as Carboplatin and Paclitaxel (PTX), is the standard of care (2, 4–6), although improvements in survival have been described in patients treated with Bevacizumab and PARP inhibitors (7–12).

Platinum-taxane-based chemotherapy is often used in cancer therapy in order to disrupt different cellular mechanisms involved in the regulation of the cell cycle to induce tumor cell death (13, 14). Unfortunately, in many HGSC patients, disease relapses within 6 months after first-line therapy and, in this setting, the median overall survival is approximately 12 months (15). The resistance mechanisms to platinum-based drugs are associated with a decrease in drug uptake (mediated by CTR1, CTR2, and OCT), an increase in drug efflux (mediated by ATP7A/ATP7B and MRP2), drug inactivation (mediated by GSH and Metallothionein), and alterations in DNA damage repair system (ERCC1, XPF, and BRCA1/BRCA2) (16). PTX resistance mechanisms are different and involve alterations in α- and β-tubulin, increased expression and activity of multidrug resistance (MDR) efflux transporters, overexpression of anti-apoptotic proteins, inhibition of apoptotic and tumor-suppressor proteins, and modulation of several cytokines, chemokines, and transcription factor pathways (17–25).

In the majority of established chemoresistant cell lines, Cisplatin is the drug mostly used for the induction of resistance (26). PTX-resistance induction is less commonly accessible, being established in gastric adenocarcinoma (OCUM-2M/PTX), breast cancer (MCF7/TAX), and prostate cancer (DU145-TxR, PC-3-TxR) models (27–29). In the ovarian cancer (OC) context, the majority of established chemoresistant cell lines are patient derived and have intrinsic resistance (30, 31). Also, A2780 and IGROV1 PTX-induced variants are available, but these cell lines correspond to endometrioid OC subtype (32–36).

Since HGSC is the most frequent epithelial OC histotype and double-resistant tumors are the major contributors to high mortality rate, we herein present a HGSC cell line model that combines intrinsic resistance to Carboplatin and acquired PTX chemoresistance. We generated two PTX-resistant cell lines derived from OVCAR8, with a stable acquired PTX resistance induced by P-glycoprotein (P-gp) overexpression. The development of these HGSC cell lines, capable of recapitulating the characteristics of double-resistant epithelial ovarian carcinoma, constitutes a key tool for the discovery of therapeutic alternatives to improve patients' outcome.

## 2 MATERIALS AND METHODS

### 2.1 Cell Line and Drugs

OVCAR8 was selected as a HGSC model, particularly since it is described as a Carboplatin-resistant OC cell line retrieved from a HGSC patient after a high-dose Carboplatin treatment (37). Parental OVCAR8 cell line was kindly provided by Doctor Francis Jacob, Gynecological Cancer Center and Ovarian Cancer Research, Department of Biomedicine, University Hospital Basel and University of Basel, Basel, Switzerland. Cells were grown in complete media, specifically, RPMI-1640 medium (ThermoFisher Scientific, Massachusetts, USA), supplemented with 10% (v/v) inactivated and filtered fetal bovine serum (FBS; Biowest, Nuaillé, France) and 1% (v/v) penicillin/streptomycin (ThermoFisher Scientific) and maintained at 37°C and 5% $CO_2$. OVCAR8 was authenticated using short tandem repeat profiling and regularly tested for the absence of mycoplasma.

PTX was purchased from Selleckchem (Houston, Texas, USA), dissolved in dimethyl sulfoxide (DMSO; AppliChem, Barcelona, Spain) and stored at −80°C, according to the manufacturer's instructions. Immediately prior to use, an aliquot was diluted at required concentrations.

### 2.2 Generation of OVCAR8 PTX R Cell Lines

Two OVCAR8 PTX R variants were established in our laboratory from parental OVCAR8 by continuous (C) and pulse (P) exposure to a stepwise increasing PTX concentration (2 to 74.9 nM), for 3 months (details are shown in **Figure 1A**). The starting concentration used for PTX R induction corresponded to the IC10 value obtained from dose–response curves after exposing parental OVCAR8 to PTX (1.56 to 200 nM) for 48 h (**Supplementary Figure 1A**).

Initially, each OVCAR8 PTX R variant was maintained uninterruptedly in the presence of PTX for a continuous-selection strategy. After 1 month, two different approaches were adopted: (i) cells were exposed to PTX constantly (continuous-selection strategy) and (ii) cells were exposed to PTX, for 4 days followed by recovery in drug-free media for 4 days (pulse-selection strategy) for 2 months. Next, we tested if PTX R phenotype was stable in culture without drug. Hence, after 2 months of freezing cycles, cells were cultured in the absence of PTX medium supplementation (**Figure 1B**). Preston Blue (PB) assay was used to evaluate cell viability to PTX at different time points in order to confirm the maintenance of IC50 values after freezing cycles and persistent cultures.

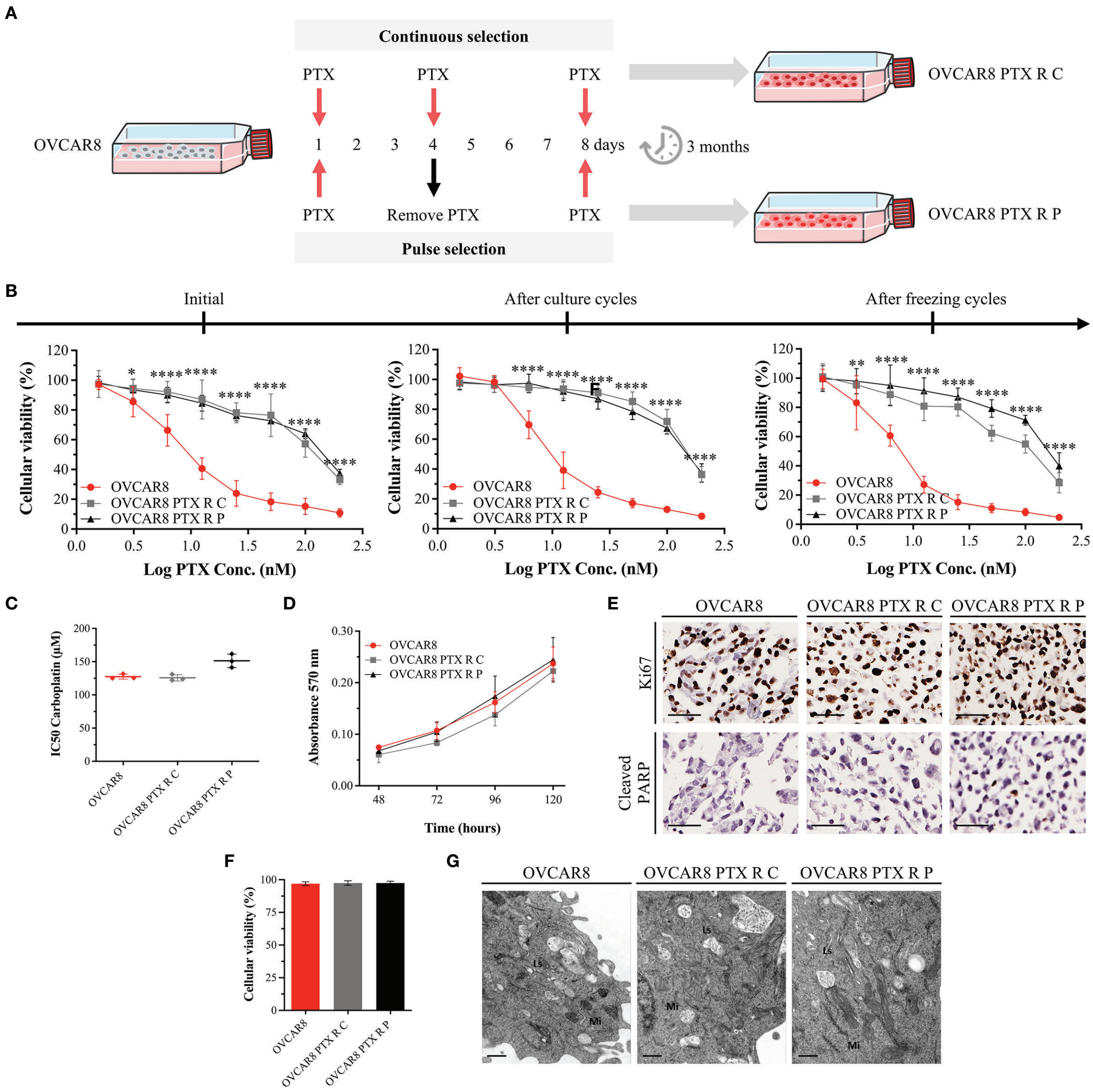

**FIGURE 1** | OVCAR8 PTX R Variants Demonstrate High Resistance to PTX. **(A)** Experimental design used to generate two OVCAR8 PTX R variants using two different treatment approaches: continuous (C) and pulse (P) selection. **(B)** Line chart showing cell viability for PTX in OVCAR8 and OVCAR8 PTX R cell lines obtained by PB assay after exposure to PTX (1.56 to 200 nM) for 48 h. **(C)** Dot plot showing IC50 for Carboplatin in OVCAR8 and OVCAR8 PTX R cell lines obtained by PB assay after exposure to Carboplatin (3.12 to 400 μM) for 48 h. **(D)** Line chart showing cell proliferation of OVCAR8 and OVCAR8 PTX R cell lines obtained by MTT assay for 120 h. **(E)** Representative immunocytochemistry images for Ki67 and cleaved-PARP of OVCAR8 and OVCAR8 PTX R cell lines after 96 h in culture. **(F)** Bar chart showing cell viability of OVCAR8 and OVCAR8 PTX R cell lines determined by trypan blue exclusion assay after 48 h in culture. **(G)** Ultrathin sections of OVCAR8 and OVCAR8 PTX R cell lines showing the ultrastructure of mitochondria (Mi), lysosomes (Ls), Golgi complex (asterisk), and rough endoplasmic reticulum (RER, arrows). All assays were done in triplicate in at least three independent experiments. Data are expressed as mean ± standard deviation and plotted using GraphPad Prism Software Inc. v6. Statistical analysis was performed using ordinary two-way ANOVA followed by Tukey's multiple comparison test **(B, D)** and ordinary one-way ANOVA followed by Tukey's multiple comparison test **(C, F)**, and values of *< 0.05; **< 0.001; ****< 0.0001 were considered statistically significant. Scale bar, 50 μm **(E)** and 0.5 μm **(G)** for immunocytochemistry images.

## 2.3 Cell Viability Assay

To determine cell viability to PTX, a resazurin-based assay—Presto Blue (PB)—was performed, according to the manufacturer's instructions. Briefly, 2 × $10^3$ cells/well were seeded into a 96-well plate in complete media and incubated at 37°C and 5% $CO_2$. After 48 h, cells were treated with increasing concentrations of PTX (1.56 to 200 nM) and incubated under the same conditions. After 48 h, 50 μl of PrestoBlue$^{TM}$ Cell Viability Reagent 1× (ThermoFisher Scientific) was added and incubated for 45 min at 37°C and 5% $CO_2$, protected from light.

Fluorescence was measured (560 nm excitation/590 nm emission) using a Bio Tek SynergyTM 2 multi-mode microplate reader (BioTek, Vermont, USA). Treated cells were compared with control cells (considered 100% viable) containing 1% (v/v) of the vehicle (DMSO). The IC50 for parental OVCAR8 and PTX R variants was used to determine fold resistance, according to the following formula (38, 39):

$$\text{Fold Resistance} = \frac{\text{Resistant Cell Line IC50}}{\text{Parental Cell Line IC50}}$$

## 2.4 Proliferation Assay

To evaluate cell proliferation, MTT [3-(4.5-Dimethylthiazol-2-yl)-2,5-diphenyltetrazolium] assay was performed as previously described (40). Briefly, $1 \times 10^3$ cells/well were seeded into a 96-well plate in complete media and incubated at 37°C and 5% $CO_2$ up to 6 days. At each time point, 500 µg/ml of MTT dye reagent (Sigma-Aldrich, Missouri, USA) was added and incubated at 37°C and 5% $CO_2$ for 3 h. Formazan crystals were dissolved in 100 µl of DMSO. Absorbance was measured (570 nm wavelength) using a Bio Tek SynergyTM 2 multi-mode microplate reader.

## 2.5 Viability Test

To differentiate viable and non-viable cells, trypan blue assay was performed. Cells at 80% confluence were diluted and mixed with a 0.4% trypan blue solution (ThermoFisher Scientific), placed in a Neubauer chamber, and counted in five counting grid squares, under a Leica DMi1 inverted phase contrast microscope (Leica Microsystems, Wetzlar, Germany), at 50× magnification.

## 2.6 Cell MicroArray Construction and Immunocytochemistry Expression Analysis

All conditions were arrayed in a Cell MicroArray (CMA) block designed and constructed as previously described (41, 42). Briefly, $2 \times 10^5$ cells/well were seeded into six-well plates and incubated at 37°C and 5% $CO_2$. After 48 h, cells were treated with 10 nM PTX and incubated under the same conditions. After 48 h, cells were scraped from culture dishes and fixed with 10% (v/v) neutral-buffered formalin (AppliChem). Cells were re-suspended in liquefied HistoGel™ (ThermoFisher Scientific), according to the manufacturer's instructions, followed by standard histological processing and paraffin embedding. Finally, CMA block was constructed and sectioned with a microtome (43). To perform immunocytochemistry, slides were deparaffinized and hydrated. Next, heat-induced (98°C) antigen retrieval was performed with citrate buffer solution (1:100 at pH 6.0; ThermoFisher Scientific) or ethylenediamine tetraacetic acid (EDTA; 1:100; ThermoFisher Scientific) for 40 min. Endogenous peroxidase activity was blocked with hydrogen peroxide solution 3% (v/v) (ThermoFisher Scientific) for 10 min. Slides were incubated with a specific primary antibody (conditions described in **Supplementary Table 1**) and detected using a secondary antibody with horseradish peroxidase (HRP)-labeled polymer (Dako REAL™ EnVision™ Detection System Peroxidase/DAB+, Rabbit/Mouse) for 30 min. Visualization of the reaction was performed using diaminobenzidine according to the manufacturer's instructions. Finally, nuclear staining with hematoxylin was performed and slides were dehydrated, clarified, and coverslipped using a permanent mounting medium for optical microscope analysis.

Immunocytochemistry results were evaluated by two independent observers (MN and SR) that register the staining pattern (nuclear, cytoplasm, or membrane) and the percentage of cells stained (0%, 1%–10%, 11%–25%, 26%–50%, 51%–75%, and 76%–100%).

## 2.7 Electronic Microscopy Analysis

To perform a qualitative assessment of cell ultrastructure, an electron microscopy analysis was performed. Briefly, for transmission electron microscopy and semithin section analysis, cultured cells were grown until 80% confluence, washed three times with phosphate buffer saline (PBS, ThermoFisher Scientific), gently scraped from culture dishes and fixed overnight in a glutaraldehyde (2.5%), paraformaldehyde (2%), and 0.1 M sodium cacodylate buffer (1:1) solution, at 4°C. After fixation, cells were pelleted by centrifugation and washed three times in 0.1 M sodium cacodylate buffer for 5 min. A post-fixation in 0.1 M sodium cacodylate buffered 2% osmium tetroxide was performed for 2 h at room temperature (RT). Then, cells were washed three times in distilled water for 5 min. The samples were incubated with 1% uranyl acetate for 30 min at RT, followed by three washes in distilled water for 5 min. Finally, cell pellet was imbedded in Histogel™, dehydrated in ethanol, and embedded in an epoxy resin. Ultrathin sections were stained and observed in a JEOL 100CXII transmission electron microscope (JEOL, Tokyo, Japan) operated at 80 kV, and images were digitally recorded using a CCD digital camera Orius 1100W (JEOL).

## 2.8 Apoptosis and Cell Cycle Analysis

To evaluate cell apoptosis and cell cycle distributions, Annexin V-FITC apoptosis detection kit™ (ThermoFisher Scientific) and propidium iodide (PI) staining were used, according to the manufacturer's instructions. Briefly, $2 \times 10^5$ cells/well were seeded into six-well plates and incubated at 37°C and 5% $CO_2$. After 48 h, cells were treated with 10 nM PTX and incubated under the same conditions.

For apoptosis analysis, after 48 h, floating and adherent cells were collected using a cell dissociation buffer enzyme-free in PBS, pelleted by centrifugation (800 g, 5 min), filtrated through a 70-µm filter to obtain single-cell suspensions, and suspended in 195 µl of binding buffer. Next, 5 µl of Annexin V-FITC was added and incubated for 10 min, protected from light. Cells were washed, resuspended in 190 µl of binding buffer, and 10 µl of PI (20 µg/ml) was added and cells were incubated for 1 min, protected from light.

For cell cycle, following 24 h, floating and adherent cells were collected, pelleted by centrifugation, and resuspended in PBS. Cells were fixed with 70% (v/v) cold ethanol and incubated at 4°C for 30 min. Next, cells were pelleted by centrifugation, resuspended in PBS containing PI (250 µg/ml), and RNase A (100 µg/ml) and incubated at 4°C for 15 min, protected from light.

Fluorescence from both assays was assessed by BD FACS Canto™ II flow cytometer and data were analyzed by FlowJo software v10.0.7 (Ashland, Oregon, USA).

## 2.9 Time-Lapse Microscopy, Image Acquisition, and Processing

Live-cell imaging experiments were performed as previously described (44). Briefly, $1.2 \times 10^5$ cells were seeded into LabTek II chambered cover glass (Nunc, New York, USA) containing 1 ml of culture medium and incubated at 37°C with 5% $CO_2$. After 24 h, cells were treated with 20 nM PTX in RPMI without phenol red and supplemented with 5% FBS. Images were captured at 5-min intervals up to 72 h under differential interference contrast (DIC) optics, with a 63× objective under an Axio Observer Z.1 SD inverted microscope, equipped with an incubation chamber at 37°C and 5% $CO_2$. Movies were generated from time-lapse images using ImageJ 1.4v software (Rasband, W.S., ImageJ, U.S. National Institutes of Health, Bethesda, Maryland, USA). The mitosis duration and the number of cells arrested at mitosis, dead by apoptosis, or bypassing cytokinesis were scored.

## 2.10 Anoikis Resistance Assay

To evaluate anoikis resistance, an aggregate formation assay was performed as previously described (40). Briefly, $1 \times 10^6$ cells/well were seeded into polyHEMA (Poly2-hydroxyethyl methacrylate; Sigma-Aldrich)-coated plates and incubated at 37°C and 5% $CO_2$ up to 15 days. At each time point (5, 10, and 15 days), floating cells were collected and dissociated using trypsin, pelleted by centrifugation, and resuspended in PBS. Cell suspensions were incubated with DAPI (1 μg/ml) for 2 min. Fluorescence was assessed by BD FACS Canto™ II flow cytometer, and data were analyzed by FlowJo software v10.0.7.

## 2.11 Colony Formation Assay

To evaluate clonogenic capacity, $1 \times 10^3$ cells/well were seeded into six-well plates and incubated at 37°C and 5% $CO_2$. Following 24 h, cells were treated with 10 nM PTX and incubated under the same conditions. After 48 h, media was replaced, and cells were allowed to recover for 8 days. Surviving colonies were fixed and stained as previously described (45). The percentage of cell survival was determined according to the following formula:

$$\text{Cell Survival } (\%) = \frac{\text{Colonies Number in Control} \times 100\,\%}{\text{Colonies Number in Treatment}}$$

## 2.12 Wound Healing Assay

To analyze migration capacity, cell monolayers at confluence cultured in six-well plates were serum starved overnight and incubated at 37°C and 5% $CO_2$. Then, monolayers were washed twice with PBS and scratched in half with a sterile 200-μl pipette tip. To monitor cell migration, a phase contrast microscopy image was taken at 0, 24, and 48 h. The quantification of wound closure was performed by measuring the unmigrated remaining area using ImageJ 1.4v software.

## 2.13 RNA Isolation and Quantitative Real-Time PCR

Total RNA was extracted from cells with PureZOL™ RNA Isolation Reagent (Bio-Rad Laboratories, California, USA), according to the manufacturer's instructions. cDNA synthesis was performed with iScript™ cDNA Synthesis Kit (Bio-Rad), using total cell RNA as template, following supplier's instructions. For real-time PCR, cDNA was amplified using iQ™ SYBR Green Supermix Kit (Bio-Rad). Primers for P-gp were as follows: forward: 5'-GCCAAAGCCAAAATATCAGC-3' and reverse: 5'-TTCCAATGTGTTCGGCATTA-3'; GAPDH: forward: 5'-ACAGTCCAGCCGCATCTTC-3' and reverse: 5'-GCCCAATACGACCAAATCC-3'; and β-Actin, used as housekeeping gene: forward: 5'-AAT CTG GCA CCA CAC CTT CTA-3' and reverse 5'-ATA GCA CAG CCT GGA TAG CAA-3'. Data were acquired with CFX Manager™ Software v1.0 (Bio-Rad) and results were analyzed according to ΔCT.

## 2.14 Cell Extracts and Western Blotting

Total cell protein extracts and Western blotting were performed as previously described (46). Membrane was incubated with primary (**Supplementary Table 1**) and secondary antibodies [anti-rabbit horseradish peroxidase (Vector Laboratories, Burlingame, USA) and anti-mouse horseradish peroxidase (Sigma-Aldrich), diluted at 1:1,000 or 1:4,000, respectively]. The protein signal intensity was quantified using ImageJ 1.4v software and normalized against α-tubulin expression levels.

## 2.15 Rhodamine 123 Accumulation Assay

To evaluate P-gp functional activity, a total of $1 \times 10^5$ cells of OVCAR8 and OVCAR8 PTX R were seeded into six-well plates and incubated at 37°C and 5% $CO_2$. After 24 h, 1 μM of the fluorescent P-gp substrate Rhodamine 123 (RH-123; Sigma-Aldrich) was added, in the presence or absence of 20 μM Verapamil (Sigma-Aldrich)—P-gp inhibitor—and incubated under the same conditions. After 1 h, cells were harvested and washed twice with ice-cold PBS, and cell pellet was gently re-suspended in ice-cold PBS for analysis. The mean fluorescence intensity (MFI) was assessed by BD Accuri C6™ II flow cytometer (BD Biosciences, California, USA), and data were analyzed by BD Accuri C6 Plus Software, version 1.0.27.1 (BD Biosciences).

## 2.16 SRB Assay

To determine cell viability to PTX after Verapamil incubation, a Sulforhodamine B (SRB) assay was performed. Briefly, $5 \times 10^6$ cells/well were seeded in 96-well plates and incubated at 37°C and 5% $CO_2$. After 24 h, cells were treated with 10-fold serial dilutions of PTX, in the presence or absence of 10 μM Verapamil and incubated under the same conditions. In parallel, cells were treated with equivalent amount of vehicle (DMSO) up to 0.25% concentration. Then, cells were fixed with 50% (m/v) trichloroacetic acid (Merck Millipore, Darmstadt, Germany) for 1 h, washed with distilled water, and stained with 0.1% (m/v) SRB in acetic acid (Sigma-Aldrich) for 30 min at RT. After washing with 1% (v/v) acetic acid aquae solution (Merck Millipore), plates were left to dry at RT followed by SRB complex solubilization with 10 mM Tris-Base buffer (Sigma-Aldrich) for 30 min. Absorbance was measured (515 nm wavelength) using a Bio Tek SynergyTM 2 multi-mode microplate reader. The IC50 of PTX, in the presence or absence of Verapamil, was determined as described above in *Section 2.3*.

## 2.17 Statistical Analysis

All assays were done in triplicate with at least three independent experiments. Data were expressed as mean ± standard deviation (SD), statistical analysis was carried out in GraphPad Prism Software Inc. v6 using ordinary one-way or two-way ANOVA followed by Tukey's or Šidák's multiple comparison test, and values of *<0.05; **<0.001; ***<0.0005; ****<0.0001 were considered statistically significant.

# 3 RESULTS

## 3.1 OVCAR8 PTX R Variants Demonstrate High Resistance to PTX

OVCAR8 and OVCAR8 PTX R cell lines were treated with increasing concentrations of PTX, and cell viability was evaluated by PB assay. Cell viability of OVCAR8 cell line exposure to 10 nM PTX was 51.52% ± 7.69%, whereas for OVCAR8 PTX R C and OVCAR8 PTX R P variants, it was 89.16% ± 6.62% and 86.79% ± 4.25%, respectively (**Figure 1B**). A significant increase in IC50 PTX was observed for OVCAR8 PTX R C (128.97 ± 6.48 nM, $p < 0.001$) and OVCAR8 PTX R P (152.80 ± 6.51 nM, $p < 0.001$) variants when compared to OVCAR8 cell line (10.51 ± 1.99 nM), demonstrating a 12.27-fold and 14.54-fold increase in resistance, respectively (**Supplementary Figure 1B**).

In order to assess the stability of acquired resistance in both OVCAR8 PTX R variants, sensitivity to PTX was assessed after two continuous months in culture and after cryopreservation cycles, without PTX medium supplementation. Our results show that OVCAR8 PTX R variants have a long-term stability without drug supplementation and retain their resistant phenotype following freeze/thawing cycles (**Figure 1B** and **Supplementary Figure 1B**).

Additionally, we evaluated if OVCAR8 PTX R variants increased resistance to Carboplatin, since parental OVCAR8 cell line was described as a Carboplatin chemoresistant model. Our results show no significant differences in IC50 for Carboplatin concentrations in OVCAR8 PTX R C (125.74 ± 3.60 nM) and OVCAR8 PTX R P (151.26 ± 10.17 nM, $p < 0.05$) when compared to OVCAR8 cell line (127.49 ± 4.76 nM) (**Figure 1C**).

To further evaluate the PTX R phenotype, we performed cell proliferation, apoptosis, and viability assays. By MTT assay, no significant increase in proliferation was observed in OVCAR8 PTX R variants compared to OVCAR8 cell line, at 120 h in culture (**Figure 1D**). Accordingly, by immunocytochemistry, no significant differences were observed in proliferation (75%–100% of Ki67 staining) and apoptosis (1%–10% of cleaved-PARP staining) for OVCAR8 PTX R variants when compared to OVCAR8 cell line after 48 h in culture (**Figure 1E**). Trypan blue exclusion assay for assessing viability indicated no significant differences between OVCAR8 PTX R variants (both 97.50% viable) when compared to OVCAR8 cell line (97.50% viable) (**Figure 1F**).

To assess ultrastructural alterations in OVCAR8 PTX R variants, we performed qualitative analysis of several transmission electron microscopy micrographs. No significant ultrastructural differences were observed between OVCAR8 and OVCAR8 PTX R cell lines, which revealed similar ultrastructure aspects such as numerous dense mitochondria, developed Golgi apparatus and rough endoplasmic reticulum, and multiple lysosomes (**Figure 1G**).

## 3.2 OVCAR8 PTX R Variants Overcome PTX-Induced G2/M Arrest and Apoptosis

Levels of PTX-induced apoptosis were determined by the Annexin V-FITC apoptosis detection kit™ using flow cytometry. Upon 48 h incubation with 10 nM PTX, a significant ($p < 0.0001$) increase in PTX-induced apoptosis was observed on OVCAR8 cell line (37.01% ± 1.63%) when compared with the nontreated control (7.40 ± 2.48%) (**Figure 2A**). In contrast, after 10 nM PTX exposure, our results show a significant decrease ($p < 0.0001$) in PTX-induced apoptosis in OVCAR8 PTX R C and P variants (11.74% ± 4.58% and 13.38% ± 2.33%, respectively) when compared to OVCAR8 cell line (37.01% ± 1.63%) (**Figure 2A**).

Cell cycle distribution was assessed through PI staining by flow cytometry. After 10 nM PTX exposure, a significant decrease ($p < 0.0001$) in the percentage of cells in G1 phase (54.61 ± 3.32% *vs*. 27.84 ± 2.89%) and accumulation of cells in G2/M phase (18.77 ± 0.56% *vs*. 44.18 ± 4.75%) was observed in the OVCAR8 cell line when compared to control (**Figure 2B**). On the other hand, after 10 nM PTX exposure, OVCAR8 PTX R variants showed no significant changes in G1, S, and G2/M subpopulations when compared to control (**Figure 2B**). After 10 nM PTX exposure, a significant difference ($p < 0.0001$) in the percentage of cells in G1 phase was found in OVCAR8 PTX R C and P variants (48.92% ± 0.84% and 46.41% ± 2.62%, respectively) when compared to parental cell line (27.84% ± 2.89%) (**Figure 2B**). Likewise, a significant difference ($p < 0.0001$) in the G2/M population was found in OVCAR8 PTX R C and P variants (19.57% ± 1.94% and 20.82% ± 2.45%, respectively) when compared to the parental cell line (44.18% ± 4.75%) (**Figure 2B**). A significant increase ($p < 0.001$) was also observed in sub-G1 fraction (debris and apoptotic cells) for the OVCAR8 cell line (3.11% ± 0.91% *vs*. 7.60% ± 1.16%) and the OVCAR8 PTX R P variant (2.41% ± 0.79% and 7.15% ± 0.76%) when compared to controls (**Supplementary Figure 2A**) after exposure to 10 nM of PTX. OVCAR8 and OVCAR8 PTX R cell lines presented a similar proportion of polyploid (>4C) population (**Supplementary Figures 2A, B**).

To further characterize the behavior of OVCAR8 and OVCAR8 PTX R C cell lines, we analyzed mitosis duration and cell fate by live-cell imaging using time-lapse DIC microscopy. We found that the OVCAR8 PTX R C variant

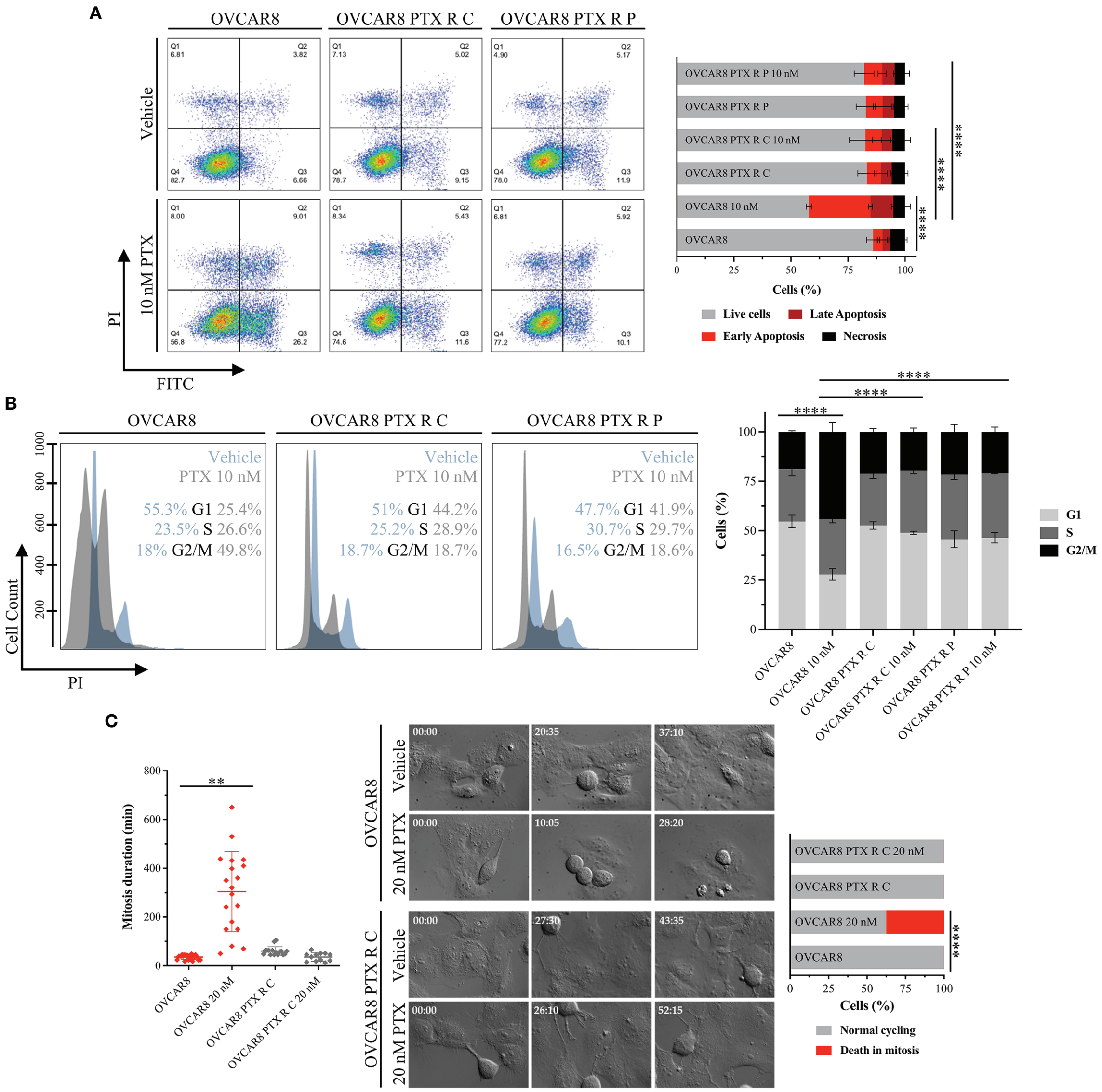

**FIGURE 2** | OVCAR8 PTX R Variants Overcome PTX-Induced G2/M Arrest and Apoptosis. **(A)** Representative flow cytometry dot plots and bar chart showing the percentage of cell populations—necrosis (Q1), late apoptosis (Q2), early apoptosis (Q3), and live cells (Q4)—of OVCAR8 and OVCAR8 PTX R cell lines using Annexin V/PI staining, after exposure to 10 nM PTX for 48 h. **(B)** Representative flow cytometry histogram and bar chart for cell cycle distribution (G1, S, and G2/M) of OVCAR8 and OVCAR8 PTX R cell lines using propidium iodide (PI) staining, after exposure to 10 nM PTX for 24 h. **(C)** Representative time-lapse images and corresponding dot plot for mitosis duration and bar chart for quantification of cell fate (normal cycling or death in mitosis) in OVCAR8 and OVCAR8 PTX R cell lines, after exposure to 20 nM PTX for 72 h. All assays were done in triplicate in at least three independent experiments. Flow cytometry was performed using BD FACS Canto$^{TM}$ II (BD Biosciences) flow cytometer and data were analyzed by FlowJo software v10.0.7. Data are expressed as mean ± standard deviation and plotted using GraphPad Prism Software Inc. v6. Statistical analysis was performed using ordinary one-way ANOVA followed by Tukey's multiple comparison test **(A–C)** and two-way ANOVA followed by Tukey's multiple comparison test **(C)**, and values of **< 0.001; ****< 0.0001 were considered statistically significant. Scale bar, 100 µm for microscopic images.

spent 55.33 ± 7.66 min in mitosis, from nuclear envelope breakdown to anaphase onset, similarly to what was observed in the OVCAR8 cell line that spent 39.35 ± 16.70 min (**Figure 2C**). Under 20 nM PTX exposure, the mitosis duration in OVCAR8 PTX R C variant is similar to that in untreated cells (33.00 ± 15.18 min) (**Figure 2C**) contrasting with the significant increase ($p < 0.001$) exhibited by the OVCAR8 cell line (331.29 ± 106.82 min). After 20 nM PTX exposure, the survival fate (outcome of cells delayed in mitosis under PTX exposure) analysis showed that 37.5% of parental OVCAR8 cells died in mitosis after mitotic arrest, and 62.5% of cells underwent normal cycling (**Figure 2C**). In contrast, OVCAR8 PTX R C variant undertook normal and multiple mitosis (**Figure 2C**).

## 3.3 OVCAR8 PTX R Variants Retain Parental OVCAR8 Features: High Anoikis Resistance, Colony Formation, and Migration Capacity

To assess anoikis (cell detachment-induced apoptosis) resistance, an aggregate formation assay was performed and evaluated by flow cytometry. Our results for anoikis resistance demonstrate no significant differences in cell viability (DAPI negative cells) for OVCAR8 PTX R C (87.88% ± 3.29% and 78.20% ± 3.73%) and OVCAR8 PTX R P variants (89.96% ± 1.74% and 84.03% ± 4.97%) when compared to parental OVCAR8 cell line (94.32% ± 1.15% and 86.47% ± 1.66%), upon 5 and 10 days of culture, respectively (**Figure 3A**). Moreover, no significant differences were observed in the percentage of positive cells for Ki67 (76%–99%), BrdU (11%–25%), cleaved caspase 3 (1%–10%), and cleaved PARP (1%–10%) for OVCAR8 PTX R variants when compared to the parental OVCAR8 cell line (**Figure 3B**). Additionally, we demonstrate that aggregation capacity was partially affected, since different and irregular aggregates were formed in OVCAR8 PTX R cells when compared to OVCAR8 (**Figure 3C**).

To evaluate clonogenic capacity, we performed a colony-forming assay. Our results show that after 10 nM PTX exposure, a significant decrease ($p < 0.0005$) occurs in the number of colonies in the OVCAR8 cell line (274.78 ± 49.27 *vs*. 10.56 ± 8.59) when compared to the untreated control (**Figure 3D**). One the other hand, after 10 nM PTX exposure, no significant differences in colony formation capacity were observed in OVCAR8 PTX R C (294.22 ± 57.45 *vs*. 254.00 ± 58.68) and OVCAR8 PTX R P variants (241.44 ± 24.44 *vs*. 182.11 ± 44.29) when compared to untreated control (**Figure 3D**). In fact, the percentage of cell survival was significantly higher ($p < 0.0005$) in OVCAR8 PTX R C (85.80% ± 4.80%) and OVCAR8 PTX R P variants (74.92% ± 7.72%) when compared to the parental OVCAR8 cell line (3.98% ± 2.08%) (**Figure 3D**).

To evaluate migration capacity, we performed a wound healing assay. Our results display no significant differences on migration behavior for OVCAR8 PTX R C (32.48% ± 4.79%) and OVCAR8 PTX R P variants (25.27% ± 3.55%) when compared to the OVCAR8 cell line (27.63% ± 0.81%) at 48 h (**Figure 3E**).

## 3.4 OVCAR8 PTX R Variants Acquire a New Phenotype With P-gp Overexpression

P-gp encoded by *MDR1* is abundantly expressed in cellular membrane, where it functions as a multidrug efflux pump that transports a wide range of structurally different substrates, including PTX (47). P-gp overexpression is the main mechanism of resistance to chemotherapeutics, being responsible for pumping the drug out of the cells, resulting in low intracellular concentration of the drugs and survival of cancer cells (48, 49). P-gp expression was evaluated at mRNA and protein levels, by qRT-PCR, Western blot, and immunocytochemistry. From qRT-PCR analysis, we found an increase in P-gp expression on OVCAR8 PTX R C (12.60 ± 2.90-fold increase) and OVCAR8 PTX R P variants (8.08 ± 4.00-fold increase) when compared to OVCAR8 cell lines (**Figure 4A**). This result was confirmed at the protein level by Western blot and immunocytochemistry that revealed a high percentage of cells positive for P-gp in OVCAR8 PTX R variants (76%–100% positive cells) when compared to the OVCAR8 cell line (negative/residual expression) (**Figure 4A**).

To confirm if P-gp upregulation is the chemoresistance mechanism in OVCAR8 PTX R variants, we determined the IC50 PTX in the presence and absence of Verapamil, a well-known P-gp inhibitor. We found that the IC50 of PTX decreased in OVCAR8 PTX R C (40-fold) and OVCAR8 PTX R P variants (33-fold) when Verapamil was added (**Figure 4B**). We also analyzed by flow cytometry the activity of P-gp through the evaluation of the mean fluorescence intensity (MIF) of cells exposed to RH-123, a known P-gp fluorescent substrate. The percentage of MIF is proportional to intracellular uptake and extracellular efflux of RH-123. We found that intracellular accumulation of RH-123 was very low for OVCAR8 PTX R C and OVCAR8 PTX R P variants (16.57% ± 8.46% and 6.99% ± 3.91%, respectively) when compared to the parental OVCAR8 cell line (considered 100%). Moreover, in the presence of Verapamil, the relative MIF significantly increased ($p < 0.0005$) for OVCAR8 PTX R C (89.73% ± 3.22%) and OVCAR8 PTX R P variants (83.14% ± 3.30%) when compared to control, demonstrating an accumulation of RH-123 due to P-gp pump inhibition (**Figure 4C**).

# 4 DISCUSSION

Surgery and chemotherapy remain the two major pillars in oncology treatments. Unfortunately, tumor recurrences and multidrug-resistant phenotype are common phenomena in HGSC context. Since second surgery is not a valid option for the majority of patients, alternatives to first-line chemotherapy are the ultimate source of hope in OC treatment. In this research work, our aim was to establish a double-resistant HGSC cell line. We used a cell line with intrinsic resistance to Carboplatin and OVCAR8, and induced PTX resistance by pulse and continuous drug exposure (39). Both methods resulted in the generation of two PTX-resistant cell lines presenting over 12-fold resistance when compared to parental OVCAR8 cells (12.3- and 14.5-fold resistance for OVCAR8 PTX R C and OVCAR8 PTX R P, respectively). Interestingly, when looking at long-term survival (using the clonogenic assay), we saw that these values were even higher, with the PTX-resistant cells being over 18-fold more resistant to PTX than their parental cells, which is particularly relevant in the biological tumor context. In addition, in our models, PTX-resistance phenotype was stable in long-term cultures without PTX medium supplementation and following freeze/thaw cycles. This stability of acquired resistance is a guarantee of reliability in this type of *in vitro* tools commonly used to study drug resistance mechanisms and drug discovery (39, 50).

The combination of therapies with independent mechanism of action, such as platinum and taxane drugs, is widely used in oncology in order to minimize the evolution of drug resistance. Some reports suggest that Cisplatin-resistant cells are also cross-

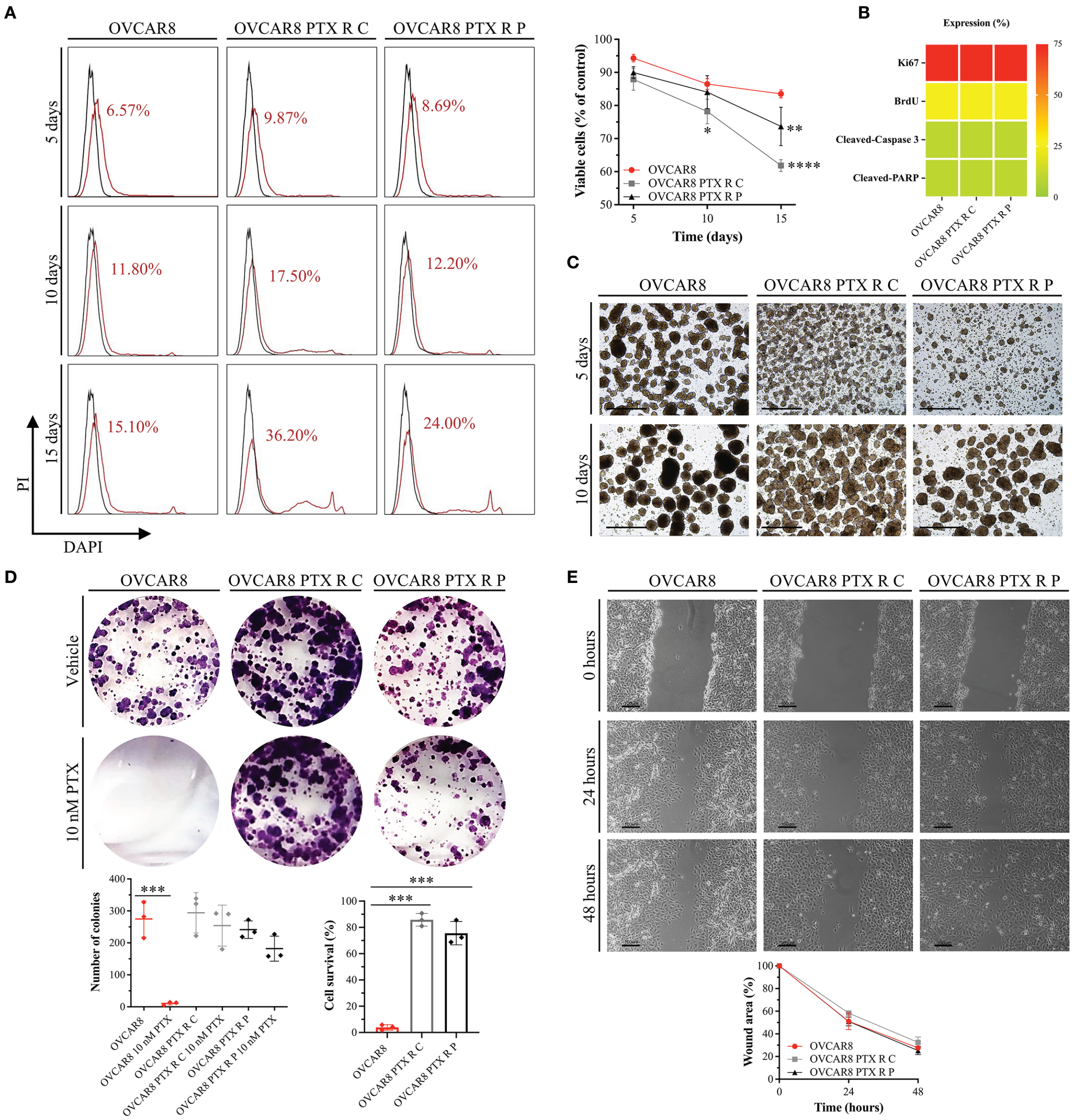

**FIGURE 3** | OVCAR8 PTX R Variants Reveal a High Anoikis Resistance, Colony Formation, and Migration Capacity. **(A)** Representative flow cytometry histograms for cell-detachment-induced apoptosis (anoikis) and line chart showing percentage of viable cells (DAPI negative cells) for OVCAR8 and OVCAR8 PTX R cell lines, for 5, 10, and 15 days. Unstained (black) and percentage of DAPI-stained cells (dead cells, red). DAPI positivity percentage is mentioned in each histogram. **(B)** Proliferation (Ki67 and BrdU) and apoptosis (cleaved-PARP and cleaved-caspase 3) expression for OVCAR8 and OVCAR8 PTX R cell lines were evaluated by immunocyto chemistry and cultured after 15 days in low adhesion culture conditions. **(C)** Representative images of OVCAR8 and OVCAR8 PTX R cell lines, cultured after 5 and 10 days in low adhesion culture conditions. **(D)** Representative wells from colony-forming assay and dot plot showing quantification of number of cell colonies (*n* = 9 wells) and percentage of cell survival for OVCAR8 and OVCAR8 PTX R cell lines after 8 days in culture. **(E)** Representative phase-contrast microscopy images for wound healing assay and line chart showing wound area quantification for OVCAR8 and OVCAR8 PTX R cell lines at 0, 24, and 48 h. All assays were done in triplicate in at least three independent experiments. Data are expressed as mean ± standard deviation and plotted using GraphPad Prism Software Inc. v6. Statistical analysis was performed using two-way ANOVA followed by Tukey's multiple comparison test **(A, E)** and ordinary one-way ANOVA followed by Tukey's multiple comparison test **(D)**, and values of *< 0.05; **< 0.001; ***< 0.0005; ****< 0.0001 were considered statistically significant. Scale bar, 20 μm **(C)** and 100 μm **(E)** for microscopic images.

resistant to anti-microtubules drugs, such as PTX (51–53). Recently, Patel et al. generated two Cisplatin-resistant cell lines and found that the less Cisplatin-resistant cell line (OVCAR8-CP1) maintained the level of resistance to PTX while the more Cisplatin-resistant cell line (OVCAR8-CP5) presented a significantly higher resistance to anti-microtubule drugs (54). In this report, the authors associate high levels of Cisplatin-resistance with cross-resistance to PTX and demonstrate that this

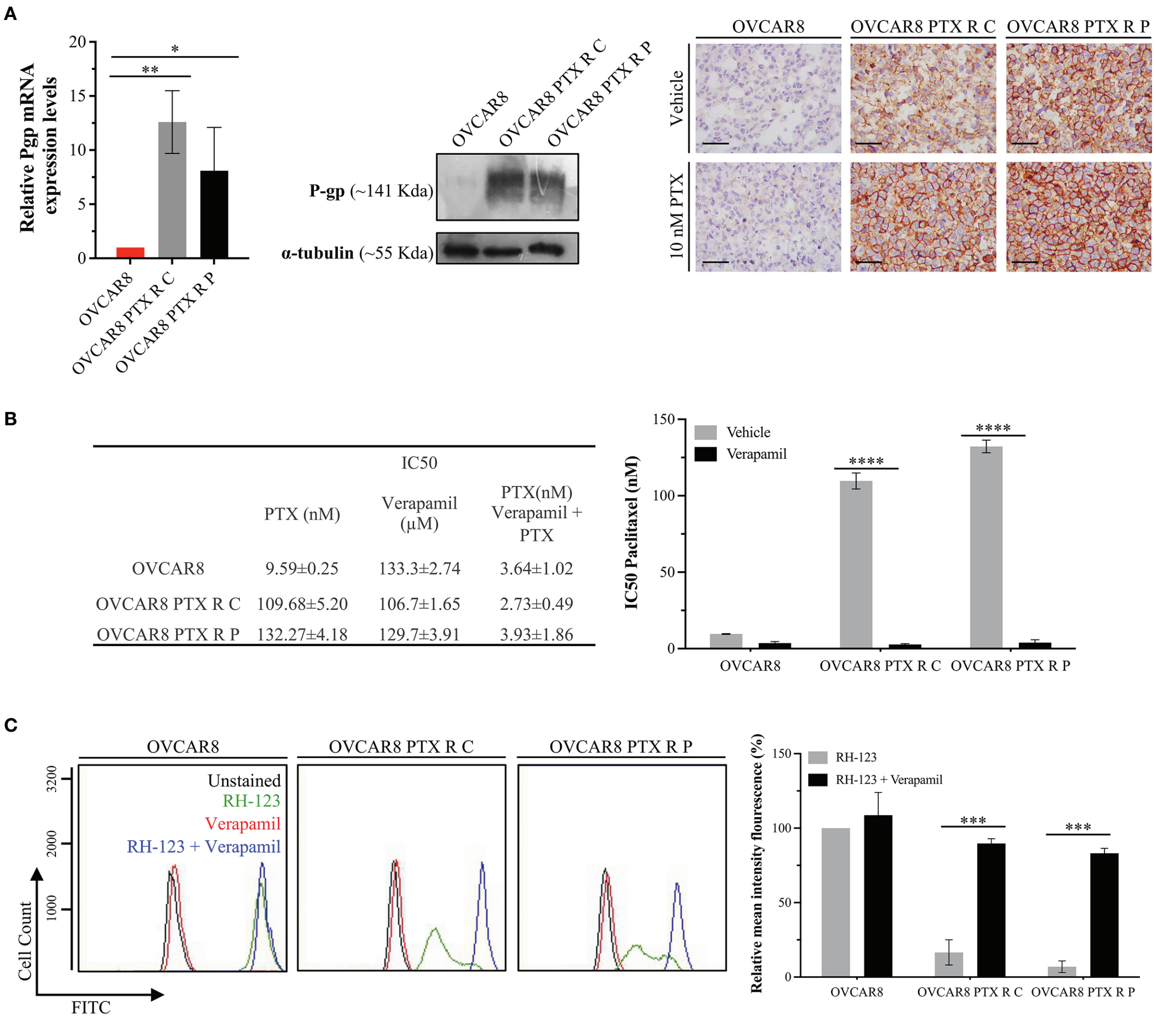

| | IC50 | | |
|---|---|---|---|
| | PTX (nM) | Verapamil (µM) | PTX(nM) Verapamil + PTX |
| OVCAR8 | 9.59±0.25 | 133.3±2.74 | 3.64±1.02 |
| OVCAR8 PTX R C | 109.68±5.20 | 106.7±1.65 | 2.73±0.49 |
| OVCAR8 PTX R P | 132.27±4.18 | 129.7±3.91 | 3.93±1.86 |

**FIGURE 4** | OVCAR8 PTX R Variants P-gp Overexpression. **(A)** Bar chart showing relative P-gp mRNA expression levels in OVCAR8 and OVCAR8 PTX R cell lines determined by qRT-PCR with β-Actin used as housekeeping gene. Representative Western blot showing P-gp expression in OVCAR8 and OVCAR8 PTX R cell lines using α-tubulin as loading control. Representative immunocytochemistry images for P-gp expression in OVCAR8 and OVCAR8 PTX R cell lines, after exposure to 10 nM PTX for 48 h. **(B)** Table showing IC50 PTX (in the presence and absence of 10 µM Verapamil) and IC50 Verapamil for OVCAR8 and OVCAR8 PTX R cell lines obtained by SRB assay for 48 h. Bar chart showing IC50 PTX for OVCAR8 and OVCAR8 PTX R cell lines, obtained by SRB assay after exposure to 10-fold serial dilutions of PTX, in the presence or absence of 10 µM of Verapamil for 48 h. **(C)** Representative flow cytometry histogram and respective bar chart showing RH-123 accumulation using FITC-A intensity in untreated (unstained, black) and RH-123-treated (stained, green) cells in the presence (blue) or absence (red) of P-gp inhibitor (Verapamil) for OVCAR8 and OVCAR8 PTX R cell lines. All assays were done in triplicate in at least three independent experiments. Data are expressed as mean ± standard deviation and plotted using GraphPad Prism Software Inc. v6. Statistical analysis was performed using ordinary two-way ANOVA followed by Tukey's multiple comparison test **(A)** or Šídák's multiple comparison test **(B, C)**, and values of *< 0.05; **< 0.001; ***< 0.0005; ****< 0.0001 were considered statistically significant. Scale bar, 500 µm for immunocytochemistry images.

phenomenon is mediated by increased levels of pro-survival TNF/NFkB signaling I (54). However, other authors did not observe cross-resistance between oncology drugs with different mechanisms of action (55). These contradicting findings demonstrate that there is a lot to improve in order to clarify the mechanism behind cross-resistance. As far as we know, the OVCAR8 cell line was obtained from a patient subjected to high-dose Carboplatin. Our results show that OVCAR8 PTX R variants maintained a high resistance level to Carboplatin, not presenting cross-resistance. Similar results were reported by Vaidyanathan et al., which established a PTX-resistant OC cell line model (A2780pacR) without interfering with Carboplatin resistance (56). Analyzing pre-clinical and clinical literature investigating the relationship between platinum and taxane resistance, Stordal et al. observed that there is a positive interaction between taxanes and platinum with residual cross-resistance (14). They also concluded that the inverse relationship between platinum and taxanes resistance seen in cell lines is mirrored in the clinical response to these agents in OC (14), emphasizing that resistant cellular models are valuable in predicting response to chemotherapy and useful to identify new therapeutic targets.

To better characterize the phenotype of these new PTX-resistant variants, we performed a series of functional assays. Our results show that OVCAR8 PTX R variants have similar levels of proliferation and cell viability in culture, maintaining the apoptotic level, anoikis resistance, and migratory capacity when compared to the parental OVCAR8 cell line. OVCAR8 is a Carboplatin-resistant cell line, with an intrinsic high proliferation index, resistance to anoikis and clonogenic survival, and migration capacity (37, 40). These results demonstrate that the main features of the parental OVCAR8 cell line were maintained and the induced PTX resistance did not intensify these original cellular characteristics. These results contrast with some studies, observing an increased migratory capacity induced on chemoresistant variants (57). It has been reported that, at the ultrastructural level, PTX-resistant cells frequently present morphological alterations in mitochondria due to the accumulation of reactive oxygen species (58). The careful inspection of cellular organelles revealed that OVCAR8 PTX R variants and the OVCAR8 cell line display similar mitochondrial morphology. Therefore, the induced PTX resistance did not alter the biological behavior or parental cell line morphology.

Since PTX is an antimitotic agent that binds to β-tubulin and affects microtubule dynamics, PTX-treated cells undergo G2/M arrest, which ultimately leads to apoptosis (59–61). We showed that the mechanism of cell survival in OVCAR8 PTX R variants relied on the acquisition of a new cancer hallmark, an enhanced drug efflux capacity, avoiding drug retention and G2/M arrest. This cell death escape capacity is well reported in several PTX-resistant cell lines (62). The most common mechanism of PTX resistance is the overexpression of drug transporters of the ATP-binding cassette family, promoting cellular drug efflux (49, 63). P-gp is one of these drug efflux pumps being expressed in a variety of normal tissues, such as brain, liver, kidney, placenta, and intestine (64), and having a protective action against xenobiotic substances and toxic compounds (63). In the cancer setting, P-gp is highly expressed in ovary, colon, kidney, adrenocortical, and hepatocellular tumors (65–68) and is correlated with multidrug resistance phenotype (67). In breast and ovarian carcinomas, high P-gp expression levels are associated with the lack of chemotherapy response and poor prognosis (63, 69, 70). Our results show that the expression levels of P-gp in parental OVCAR8 are residual and OVCAR8 PTX R variants present a significant increase in P-gp expression, i.e., more that 75% of cells have a strong membrane staining observed by immunocytochemistry. This switch in P-gp expression profile was observed in other OC cell lines following PTX induction (56) and it is reported that this increase in protein levels is mediated by gene overexpression (14).

Verapamil is a P-gp inhibitor that increases the efficacy of PTX *in vitro* in several cancer cell lines (71, 72). It is well known that P-gp inhibition and/or decreased expression can reverse PTX resistance (19). Our results show a significantly increased accumulation of RH-123 in OVCAR8 PTX R variants in the presence of Verapamil. These results suggest that following P-gp inhibition, cells retain PTX, leading to a decreased cell viability and apoptosis induction. Despite some contradictory data (56), it was previously shown that following P-gp inhibition, PTX-resistant cell lines maintained the high levels of P-gp expression, suggesting that the inhibitory effects were the result of a direct inhibition of the efflux pump and not related to changes in protein expression levels (63). In line with these results, we observed that OVCAR8 PTX R variants maintained the P-gp high expression levels following an inhibition molecule treatment (data not shown).

The inhibition of P-gp is a therapeutic strategy to re-sensitize tumor cells to chemotherapeutic drugs, such as PTX. The importance of this strategy is implicit in the development of a great number of P-gp inhibitors (73) and some of them reached clinical trials (NCT00001302, NCT00001383, and NCT00001944) but with some efficacy limitations. We generated two HGSC cell lines with induced PTX resistance and P-gp overexpression suitable to test new and more effective P-gp inhibitors. Moreover, since OVCAR 8 has intrinsic Carboplatin resistance, our two OVCAR8 PTX R models are also apt to test the efficacy of drugs to revert platinum-taxane resistance. The generation of powerful tools to study chemoresistance in HGSC setting is crucial to discover effective drugs for the treatment of double-resistant tumors. Our goal for future studies is to use these double-chemoresistant cell models to test the capacity of non-oncology drugs to re-sensitize cells to first-line chemotherapy drugs.

## DATA AVAILABILITY STATEMENT

The original contributions presented in the study are included in the article/**Supplementary Material**. Further inquiries can be directed to the corresponding author.

## AUTHOR CONTRIBUTIONS

MN and SR contributed to conceptualization and design of the study. MN and SR organized the database. MN, PS, CP, and AR performed the experiments and statistical analysis. MN wrote the first draft of the manuscript. MN, PS, RC, CP, AR, HB, GA, and SR wrote sections of the manuscript. All authors contributed to manuscript revision, read, and approved the submitted version.

## FUNDING

This work was developed at i3S/IPATIMUP, an Associate Laboratory of the Portuguese Ministry of Science, Technology and Higher Education, and partially supported by Fundação para a Ciência e a Tecnologia (FCT). This research was supported by European Regional Development Funds (ERDF) funds through the COMPETE 2020–Operational Program for Competitiveness and Internationalization (POCI), Portugal 2020, Fundação para a Ciência e a Tecnologia (FCT)/Ministério da Ciência, Tecnologia e Inovação (MCTES), under the project POCI 01-0145-FEDER-029503 (PTDC/MEC-ONC/29503/2017) and CESPU (Cooperativa de Ensino Superior Politécnico e

Universitário) under the project ComeTarget_CESPU_2017 (to HB). MN acknowledges FCT/MCTES and UE for financial support through a PhD fellowship (2020.04720.BD) co-sponsored by Fundo Social Europeu (FSE) through Programa Operacional Regional Norte (Norte 2020).

## ACKNOWLEDGMENTS

The authors acknowledge the support of the i3S Scientific Platform HEMS, member of the national infrastructure PPBI—Portuguese Platform of Bioimaging (PPBI-POCI-01-0145-FEDER-022122). The authors also acknowledge the support of the Translational Cytometry Unit (TraCy) i3S Scientific Platform.

## SUPPLEMENTARY MATERIAL

The Supplementary Material for this article can be found online at: https://www.frontiersin.org/articles/10.3389/fonc.2021.752127/full#supplementary-material

## REFERENCES

1. Cheng WF, Huang CY, Chang MC, Hu YH, Chiang YC, Chen YL, et al. High Mesothelin Correlates With Chemoresistance and Poor Survival in Epithelial Ovarian Carcinoma. *Br J Cancer* (2009) 100(7):1144–53. doi: 10.1038/sj.bjc.6604964
2. Weidle UH, Birzele F, Kollmorgen G, Rueger R. Mechanisms and Targets Involved in Dissemination of Ovarian Cancer. *Cancer Genomics Proteomics* (2016) 13(6):407–23. doi: 10.21873/cgp.20004
3. Lyons YA, Reyes HD, McDonald ME, Newtson A, Devor E, Bender DP, et al. Interval Debulking Surgery Is Not Worth the Wait: A National Cancer Database Study Comparing Primary Cytoreductive Surgery Versus Neoadjuvant Chemotherapy. *Int J Gynecol Cancer* (2020) 30(6):845–52. doi: 10.1136/ijgc-2019-001124
4. Gonzalez-Martin A, Sanchez-Lorenzo L, Bratos R, Marquez R, Chiva L. First-Line and Maintenance Therapy for Ovarian Cancer: Current Status and Future Directions. *Drugs* (2014) 74(8):879–89. doi: 10.1007/s40265-014-0221-9
5. Kim A, Ueda Y, Naka T, Enomoto T. Therapeutic Strategies in Epithelial Ovarian Cancer. *J Exp Clin Cancer Res* (2012) 31:14. doi: 10.1186/1756-9966-31-14
6. Testa U, Petrucci E, Pasquini L, Castelli G, Pelosi E. Ovarian Cancers: Genetic Abnormalities, Tumor Heterogeneity and Progression, Clonal Evolution and Cancer Stem Cells. *Medicines (Basel)* (2018) 5(1):16. doi: 10.3390/medicines5010016
7. Burger RA, Brady MF, Bookman MA, Fleming GF, Monk BJ, Huang H, et al. Incorporation of Bevacizumab in the Primary Treatment of Ovarian Cancer. *N Engl J Med* (2011) 365(26):2473–83. doi: 10.1056/NEJMoa1104390
8. Perren TJ, Swart AM, Pfisterer J, Ledermann JA, Pujade-Lauraine E, Kristensen G, et al. A Phase 3 Trial of Bevacizumab in Ovarian Cancer. *N Engl J Med* (2011) 365(26):2484–96. doi: 10.1056/NEJMoa1103799
9. Mirza MR, Monk BJ, Herrstedt J, Oza AM, Mahner S, Redondo A, et al. Niraparib Maintenance Therapy in Platinum-Sensitive, Recurrent Ovarian Cancer. *N Engl J Med* (2016) 375(22):2154–64. doi: 10.1056/NEJMoa1611310
10. Fong PC, Yap TA, Boss DS, Carden CP, Mergui-Roelvink M, Gourley C, et al. Poly(ADP)-Ribose Polymerase Inhibition: Frequent Durable Responses in BRCA Carrier Ovarian Cancer Correlating With Platinum-Free Interval. *J Clin Oncol* (2010) 28(15):2512–9. doi: 10.1200/JCO.2009.26.9589
11. Ledermann J, Harter P, Gourley C, Friedlander M, Vergote I, Rustin G, et al. Olaparib Maintenance Therapy in Patients With Platinum-Sensitive Relapsed Serous Ovarian Cancer: A Preplanned Retrospective Analysis of Outcomes by BRCA Status in a Randomised Phase 2 Trial. *Lancet Oncol* (2014) 15(8):852–61. doi: 10.1016/S1470-2045(14)70228-1
12. Cortez AJ, Tudrej P, Kujawa KA, Lisowska KM. Advances in Ovarian Cancer Therapy. *Cancer Chemother Pharmacol* (2018) 81(1):17–38. doi: 10.1007/s00280-017-3501-8
13. Brasseur K, Gevry N, Asselin E. Chemoresistance and Targeted Therapies in Ovarian and Endometrial Cancers. *Oncotarget* (2017) 8(3):4008–42. doi: 10.18632/oncotarget.14021
14. Stordal B, Pavlakis N, Davey R. A Systematic Review of Platinum and Taxane Resistance From Bench to Clinic: An Inverse Relationship. *Cancer Treat Rev* (2007) 33(8):688–703. doi: 10.1016/j.ctrv.2007.07.013
15. Naumann RW, Coleman RL. Management Strategies for Recurrent Platinum-Resistant Ovarian Cancer. *Drugs* (2011) 71(11):1397–412. doi: 10.2165/11591720-000000000-00000
16. Mikula-Pietrasik J, Witucka A, Pakula M, Uruski P, Begier-Krasinska B, Niklas A, et al. Comprehensive Review on How Platinum- and Taxane-Based Chemotherapy of Ovarian Cancer Affects Biology of Normal Cells. *Cell Mol Life Sci* (2019) 76(4):681–97. doi: 10.1007/s00018-018-2954-1
17. Bae T, Weon KY, Lee JW, Eum KH, Kim S, Choi JW. Restoration of Paclitaxel Resistance by CDK1 Intervention in Drug-Resistant Ovarian Cancer. *Carcinogenesis* (2015) 36(12):1561–71. doi: 10.1093/carcin/bgv140
18. Chang MC, Chen CA, Hsieh CY, Lee CN, Su YN, Hu YH, et al. Mesothelin Inhibits Paclitaxel-Induced Apoptosis Through the PI3K Pathway. *Biochem J* (2009) 424(3):449–58. doi: 10.1042/BJ20082196
19. Das T, Anand U, Pandey SK, Ashby CR Jr, Assaraf YG, Chen ZS, et al. Therapeutic Strategies to Overcome Taxane Resistance in Cancer. *Drug Resist Update* (2021) 55:100754. doi: 10.1016/j.drup.2021.100754
20. Huang KC, Yang J, Ng MC, Ng SK, Welch WR, Muto MG, et al. Cyclin A1 Expression and Paclitaxel Resistance in Human Ovarian Cancer Cells. *Eur J Cancer* (2016) 67:152–63. doi: 10.1016/j.ejca.2016.08.007
21. Kelland L. The Resurgence of Platinum-Based Cancer Chemotherapy. *Nat Rev Cancer* (2007) 7(8):573–84. doi: 10.1038/nrc2167
22. Mosca L, Ilari A, Fazi F, Assaraf YG, Colotti G. Taxanes in Cancer Treatment: Activity, Chemoresistance and Its Overcoming. *Drug Resist Update* (2021) 54:100742. doi: 10.1016/j.drup.2020.100742
23. Sobue S, Mizutani N, Aoyama Y, Kawamoto Y, Suzuki M, Nozawa Y, et al. Mechanism of Paclitaxel Resistance in a Human Prostate Cancer Cell Line, PC3-PR, and Its Sensitization by Cabazitaxel. *Biochem Biophys Res Commun* (2016) 479(4):808–13. doi: 10.1016/j.bbrc.2016.09.128
24. Song Y, Brady ST. Post-Translational Modifications of Tubulin: Pathways to Functional Diversity of Microtubules. *Trends Cell Biol* (2015) 25(3):125–36. doi: 10.1016/j.tcb.2014.10.004
25. Wloga D, Joachimiak E, Fabczak H. Tubulin Post-Translational Modifications and Microtubule Dynamics. *Int J Mol Sci* (2017) 18(10):2207. doi: 10.3390/ijms18102207
26. Amaral MVS, Desp AJ, Das EL, Deos L, Dasm JH, Dem MEA, et al. Establishment of Drug-Resistant Cell Lines as a Model in Experimental Oncology: A Review. *Anticancer Res* (2019) 39(12):6443–55. doi: 10.21873/anticanres.13858
27. Zhang X, Yashiro M, Qiu H, Nishii T, Matsuzaki T, Hirakawa K. Establishment and Characterization of Multidrug-Resistant Gastric Cancer Cell Lines. *Anticancer Res* (2010) 30(3):915–21.
28. Chen SY, Hu SS, Dong Q, Cai JX, Zhang WP, Sun JY, et al. Establishment of Paclitaxel-Resistant Breast Cancer Cell Line and Nude Mice Models, and Underlying Multidrug Resistance Mechanisms *In Vitro* and *In Vivo*. *Asian Pac J Cancer Prev* (2013) 14(10):6135–40. doi: 10.7314/APJCP.2013.14.10.6135
29. Takeda M, Mizokami A, Mamiya K, Li YQ, Zhang J, Keller ET, et al. The Establishment of Two Paclitaxel-Resistant Prostate Cancer Cell Lines and the Mechanisms of Paclitaxel Resistance With Two Cell Lines. *Prostate* (2007) 67(9):955–67. doi: 10.1002/pros.20581
30. Tudrej P, Olbryt M, Zembala-Nozynska E, Kujawa KA, Cortez AJ, Fiszer-Kierzkowska A, et al. Establishment and Characterization of the Novel High-Grade Serous Ovarian Cancer Cell Line Ovpa8. *Int J Mol Sci* (2018) 19(7):2080. doi: 10.3390/ijms19072080

31. Teng PN, Bateman NW, Wang G, Litzi T, Blanton BE, Hood BL, et al. Establishment and Characterization of a Platinum- and Paclitaxel-Resistant High Grade Serous Ovarian Carcinoma Cell Line. *Hum Cell* (2017) 30(3):226–36. doi: 10.1007/s13577-017-0162-1
32. Chen FQ, Zhang JM, Fang XF, Yu H, Liu YL, Li H, et al. Reversal of Paclitaxel Resistance in Human Ovarian Cancer Cells With Redox-Responsive Micelles Consisting of Alpha-Tocopheryl Succinate-Based Polyphosphoester Copolymers. *Acta Pharmacol Sin* (2017) 38(6):859–73. doi: 10.1038/aps.2016.150
33. Chu SW, Badar S, Morris DL, Pourgholami MH. Potent Inhibition of Tubulin Polymerisation and Proliferation of Paclitaxel-Resistant 1A9PTX22 Human Ovarian Cancer Cells by Albendazole. *Anticancer Res* (2009) 29(10):3791–6.
34. Feng J, Peng Z, Gao L, Yang X, Sun Z, Hou X, et al. ClC-3 Promotes Paclitaxel Resistance *via* Modulating Tubulins Polymerization in Ovarian Cancer Cells. *BioMed Pharmacother* (2021) 138:111407. doi: 10.1016/j.biopha.2021.111407
35. Szenajch J, Szabelska-Beresewicz A, Swiercz A, Zyprych-Walczak J, Siatkowski I, Goralski M, et al. Transcriptome Remodeling in Gradual Development of Inverse Resistance Between Paclitaxel and Cisplatin in Ovarian Cancer Cells. *Int J Mol Sci* (2020) 21(23):9218. doi: 10.3390/ijms21239218
36. Wang L, Jia E. Ovarian Cancer Targeted Hyaluronic Acid-Based Nanoparticle System for Paclitaxel Delivery to Overcome Drug Resistance. *Drug Deliv* (2016) 23(5):1810–7. doi: 10.3109/10717544.2015.1101792
37. Schilder RJ, Hall L, Monks A, Handel LM, Fornace AJ Jr, Ozols RF, et al. Metallothionein Gene Expression and Resistance to Cisplatin in Human Ovarian Cancer. *Int J Cancer* (1990) 45(3):416–22. doi: 10.1002/ijc.2910450306
38. Jensen NF, Stenvang J, Beck MK, Hanakova B, Belling KC, Do KN, et al. Establishment and Characterization of Models of Chemotherapy Resistance in Colorectal Cancer: Towards a Predictive Signature of Chemoresistance. *Mol Oncol* (2015) 9(6):1169–85. doi: 10.1016/j.molonc.2015.02.008
39. McDermott M, Eustace AJ, Busschots S, Breen L, Crown J, Clynes M, et al. *In Vitro* Development of Chemotherapy and Targeted Therapy Drug-Resistant Cancer Cell Lines: A Practical Guide With Case Studies. *Front Oncol* (2014) 4:40. doi: 10.3389/fonc.2014.00040
40. Coelho R, Ricardo S, Amaral AL, Huang YL, Nunes M, Neves JP, et al. Regulation of Invasion and Peritoneal Dissemination of Ovarian Cancer by Mesothelin Manipulation. *Oncogenesis* (2020) 9(6):61. doi: 10.1038/s41389-020-00246-2
41. Avninder S, Ylaya K, Hewitt SM. Tissue Microarray: A Simple Technology That has Revolutionized Research in Pathology. *J Postgrad Med* (2008) 54 (2):158–62. doi: 10.4103/0022-3859.40790
42. Simon R, Mirlacher M, Sauter G. Tissue Microarrays. *Methods Mol Med* (2004) 97:377–89. doi: 10.1385/1-59259-760-2:377
43. Coelho R, Marcos-Silva L, Mendes N, Pereira D, Brito C, Jacob F, et al. Mucins and Truncated O-Glycans Unveil Phenotypic Discrepancies Between Serous Ovarian Cancer Cell Lines and Primary Tumours. *Int J Mol Sci* (2018) 19 (7):2045. doi: 10.3390/ijms19072045
44. Henriques AC, Silva PMA, Sarmento B, Bousbaa H. Antagonizing the Spindle Assembly Checkpoint Silencing Enhances Paclitaxel and Navitoclax-Mediated Apoptosis With Distinct Mechanistic. *Sci Rep* (2021) 11(1):4139. doi: 10.1038/s41598-021-83743-7
45. Silva PM, Ribeiro N, Lima RT, Andrade C, Diogo V, Teixeira J, et al. Suppression of Spindly Delays Mitotic Exit and Exacerbates Cell Death Response of Cancer Cells Treated With Low Doses of Paclitaxel. *Cancer Lett* (2017) 394:33–42. doi: 10.1016/j.canlet.2017.02.024
46. Silva PM, Tavares AA, Bousbaa H. Co-Silencing of Human Bub3 and Dynein Highlights an Antagonistic Relationship in Regulating Kinetochore-Microtubule Attachments. *FEBS Lett* (2015) 589(23):3588–94. doi: 10.1016/j.febslet.2015.10.017
47. Robey RW, Pluchino KM, Hall MD, Fojo AT, Bates SE, Gottesman MM. Revisiting the Role of ABC Transporters in Multidrug-Resistant Cancer. *Nat Rev Cancer* (2018) 18(7):452–64. doi: 10.1038/s41568-018-0005-8
48. Choi CH. ABC Transporters as Multidrug Resistance Mechanisms and the Development of Chemosensitizers for Their Reversal. *Cancer Cell Int* (2005) 5:30. doi: 10.1186/1475-2867-5-30
49. Choi YH, Yu AM. ABC Transporters in Multidrug Resistance and Pharmacokinetics, and Strategies for Drug Development. *Curr Pharm Des* (2014) 20(5):793–807. doi: 10.2174/138161282005140214165212
50. Cunnea P, Stronach EA. Modeling Platinum Sensitive and Resistant High-Grade Serous Ovarian Cancer: Development and Applications of Experimental Systems. *Front Oncol* (2014) 4:81. doi: 10.3389/fonc.2014.00081
51. Hubaux R, Thu KL, Vucic EA, Pikor LA, Kung SH, Martinez VD, et al. Microtubule Affinity-Regulating Kinase 2 Is Associated With DNA Damage Response and Cisplatin Resistance in Non-Small Cell Lung Cancer. *Int J Cancer* (2015) 137(9):2072–82. doi: 10.1002/ijc.29577
52. Li L, Huang X, Huang R, Gou S, Wang Z, Wang H. Pt(IV) Prodrugs Containing Microtubule Inhibitors Displayed Potent Antitumor Activity and Ability to Overcome Cisplatin Resistance. *Eur J Med Chem* (2018) 156:666–79. doi: 10.1016/j.ejmech.2018.07.016
53. Stordal B, Hamon M, McEneaney V, Roche S, Gillet JP, O'Leary JJ, et al. Resistance to Paclitaxel in a Cisplatin-Resistant Ovarian Cancer Cell Line Is Mediated by P-Glycoprotein. *PloS One* (2012) 7(7):e40717. doi: 10.1371/journal.pone.0040717
54. Patel RP, Kuhn S, Yin D, Hotz JM, Maher FA, Robey RW, et al. Cross-Resistance of Cisplatin Selected Cells to Anti-Microtubule Agents: Role of General Survival Mechanisms. *Transl Oncol* (2021) 14(1):100917. doi: 10.1016/j.tranon.2020.100917
55. Januchowski R, Wojtowicz K, Sujka-Kordowska P, Andrzejewska M, Zabel M. MDR Gene Expression Analysis of Six Drug-Resistant Ovarian Cancer Cell Lines. *BioMed Res Int* (2013) 2013:241763. doi: 10.1155/2013/241763
56. Vaidyanathan A, Sawers L, Gannon AL, Chakravarty P, Scott AL, Bray SE, et al. ABCB1 (MDR1) Induction Defines a Common Resistance Mechanism in Paclitaxel- and Olaparib-Resistant Ovarian Cancer Cells. *Br J Cancer* (2016) 115(4):431–41. doi: 10.1038/bjc.2016.203
57. Huang HK, Lin YH, Chang HA, Lai YS, Chen YC, Huang SC, et al. Chemoresistant Ovarian Cancer Enhances Its Migration Abilities by Increasing Store-Operated Ca(2+) Entry-Mediated Turnover of Focal Adhesions. *J BioMed Sci* (2020) 27(1):36. doi: 10.1186/s12929-020-00630-5
58. Kim HS, Oh JM, Jin DH, Yang KH, Moon EY. Paclitaxel Induces Vascular Endothelial Growth Factor Expression Through Reactive Oxygen Species Production. *Pharmacology* (2008) 81(4):317–24. doi: 10.1159/000119756
59. Ganesh T, Yang C, Norris A, Glass T, Bane S, Ravindra R, et al. Evaluation of the Tubulin-Bound Paclitaxel Conformation: Synthesis, Biology, and SAR Studies of C-4 to C-3' Bridged Paclitaxel Analogues. *J Med Chem* (2007) 50 (4):713–25. doi: 10.1021/jm061071x
60. White D, Honore S, Hubert F. Exploring the Effect of End-Binding Proteins and Microtubule Targeting Chemotherapy Drugs on Microtubule Dynamic Instability. *J Theor Biol* (2017) 429:18–34. doi: 10.1016/j.jtbi.2017.06.014
61. Woods CM, Zhu J, McQueney PA, Bollag D, Lazarides E. Taxol-Induced Mitotic Block Triggers Rapid Onset of a P53-Independent Apoptotic Pathway. *Mol Med* (1995) 1(5):506–26. doi: 10.1007/BF03401588
62. Wang TH, Wang HS, Soong YK. Paclitaxel-Induced Cell Death: Where the Cell Cycle and Apoptosis Come Together. *Cancer* (2000) 88(11):2619–28. doi: 10.1002/1097-0142(20000601)88:11<2619::AID-CNCR26>3.0.CO;2-J
63. Nanayakkara AK, Follit CA, Chen G, Williams NS, Vogel PD, Wise JG. Targeted Inhibitors of P-Glycoprotein Increase Chemotherapeutic-Induced Mortality of Multidrug Resistant Tumor Cells. *Sci Rep* (2018) 8(1):967. doi: 10.1038/s41598-018-19325-x
64. Cascorbi I. P-Glycoprotein: Tissue Distribution, Substrates, and Functional Consequences of Genetic Variations. *Handb Exp Pharmacol* (2011) 201):261–83. doi: 10.1007/978-3-642-14541-4_6
65. Bourhis J, Goldstein LJ, Riou G, Pastan I, Gottesman MM, Benard J. Expression of a Human Multidrug Resistance Gene in Ovarian Carcinomas. *Cancer Res* (1989) 49(18):5062–5.
66. Fojo AT, Shen DW, Mickley LA, Pastan I, Gottesman MM. Intrinsic Drug Resistance in Human Kidney Cancer Is Associated With Expression of a Human Multidrug-Resistance Gene. *J Clin Oncol* (1987) 5(12):1922–7. doi: 10.1200/JCO.1987.5.12.1922
67. Goldstein LJ, Galski H, Fojo A, Willingham M, Lai SL, Gazdar A, et al. Expression of a Multidrug Resistance Gene in Human Cancers. *J Natl Cancer Inst* (1989) 81(2):116–24. doi: 10.1093/jnci/81.2.116
68. Pirker R, Goldstein LJ, Ludwig H, Linkesch W, Lechner C, Gottesman MM, et al. Expression of a Multidrug Resistance Gene in Blast Crisis of Chronic

Myelogenous Leukemia. *Cancer Commun* (1989) 1(2):141–4. doi: 10.3727/095535489820875354

69. Mechetner E, Kyshtoobayeva A, Zonis S, Kim H, Stroup R, Garcia R, et al. Levels of Multidrug Resistance (MDR1) P-Glycoprotein Expression by Human Breast Cancer Correlate With *In Vitro* Resistance to Taxol and Doxorubicin. *Clin Cancer Res* (1998) 4(2):389–98.
70. Penson RT, Oliva E, Skates SJ, Glyptis T, Fuller AF Jr, Goodman A, et al. Expression of Multidrug Resistance-1 Protein Inversely Correlates With Paclitaxel Response and Survival in Ovarian Cancer Patients: A Study in Serial Samples. *Gynecol Oncol* (2004) 93(1):98–106. doi: 10.1016/j.ygyno.2003.11.053
71. Burns BS, Edin ML, Lester GE, Tuttle HG, Wall ME, Wani MC, et al. Selective Drug Resistant Human Osteosarcoma Cell Lines. *Clin Orthop Relat Res* (2001) 383):259–67. doi: 10.1097/00003086-200102000-00030
72. Reinecke P, Schmitz M, Schneider EM, Gabbert HE, Gerharz CD. Multidrug Resistance Phenotype and Paclitaxel (Taxol) Sensitivity in Human Renal Carcinoma Cell Lines of Different Histologic Types. *Cancer Invest* (2000) 18 (7):614–25. doi: 10.3109/07357900009032828
73. Zhang H, Xu H, Ashby CR Jr, Assaraf YG, Chen ZS, Liu HM. Chemical Molecular-Based Approach to Overcome Multidrug Resistance in Cancer by Targeting P-Glycoprotein (P-Gp). *Med Res Rev* (2021) 41(1):525–55. doi: 10.1002/med.21739

**Conflict of Interest:** The authors declare that the research was conducted in the absence of any commercial or financial relationships that could be construed as a potential conflict of interest.

frontiers in Oncology

CORRECTION
published: 04 February 2022
doi: 10.3389/fonc.2022.853608

# Corrigendum: Generation of Two Paclitaxel-Resistant High-Grade Serous Carcinoma Cell Lines With Increased Expression of P-Glycoprotein

*Mariana Nunes*[1,2], *Patrícia M. A. Silva*[3,4], *Ricardo Coelho*[5], *Carla Pinto*[3,6], *Albina Resende*[3,6], *Hassan Bousbaa*[3], *Gabriela M. Almeida*[7,8] *and Sara Ricardo*[1,4,8]*

*[1] Differentiation and Cancer Group, Institute for Research and Innovation in Health (i3S) of the University of Porto/Institute of Molecular Pathology and Immunology of the University of Porto (Ipatimup), Porto, Portugal, [2] Institute of Biomedical Sciences Abel Salazar (ICBAS), University of Porto, Porto, Portugal, [3] CESPU, Institute of Research and Advanced Training in Health Sciences and Technologies (IINFACTS), Gandra, Portugal, [4] TOXRUN, Toxicology Research Unit, University Institute of Health Sciences, Polytechnic and University Cooperative (CESPU), Gandra, Portugal, [5] Ovarian Cancer Research, Department of Biomedicine, University Hospital Basel and University of Basel, Basel, Switzerland, [6] Interdisciplinary Centre of Marine and Environmental Research (CIIMAR), University of Porto, Porto, Portugal, [7] Expression Regulation in Cancer Group, Institute for Research and Innovation in Health (i3S) of the University of Porto/Institute of Molecular Pathology and Immunology of the University of Porto (Ipatimup), Porto, Portugal, [8] Faculty of Medicine from University of Porto (FMUP), Porto, Portugal*

OPEN ACCESS

**Approved by:**
*Frontiers Editorial Office,*
*Frontiers Media SA, Switzerland*

***Correspondence:**
*Sara Ricardo*
*sricardo@ipatimup.pt*

**Specialty section:**
*This article was submitted to Gynecological Oncology, a section of the journal Frontiers in Oncology*

**Received:** *12 January 2022*
**Accepted:** *13 January 2022*
**Published:** *04 February 2022*

**Citation:**
*Nunes M, Silva PMA, Coelho R, Pinto C, Resende A, Bousbaa H, Almeida GM and Ricardo S (2022) Corrigendum: Generation of Two Paclitaxel-Resistant High-Grade Serous Carcinoma Cell Lines With Increased Expression of P-Glycoprotein. Front. Oncol. 12:853608. doi: 10.3389/fonc.2022.853608*

**Keywords: high-grade serous carcinoma, ovarian cancer, chemoresistance, Paclitaxel, P-glycoprotein**

**A Corrigendum on**

**Generation of Two Paclitaxel-Resistant High-Grade Serous Carcinoma Cell Lines With Increased Expression of P-Glycoprotein**
*By Nunes M, Silva PMA, Coelho R, Pinto C, Resende A, Bousbaa H, Almeida GM and Ricardo S (2021). Front. Oncol. 11:752127. doi:10.3389/fonc.2021.752127*

In the original article, we neglected to include the funder. The correct Funding statement appears below. "This work was developed at i3S/IPATIMUP, an Associate Laboratory of the Portuguese Ministry of Science, Technology and Higher Education, and partially supported by Fundação para a Ciência e a Tecnologia (FCT). This research was supported by European Regional Development Funds (ERDF) funds through the COMPETE 2020–Operational Program for Competitiveness and Internationalization (POCI), Portugal 2020, Fundação para a Ciência e a Tecnologia (FCT)/Ministério da Ciência, Tecnologia e Inovação (MCTES), under the project POCI 01-0145-FEDER-029503 (PTDC/MEC-ONC/29503/2017) and CESPU (Cooperativa de Ensino Superior Politécnico e Universitário) under the project ComeTarget_CESPU_2017 (to HB). MN acknowledges FCT/MCTES and UE for financial support through a PhD fellowship (2020.04720.BD) co-sponsored by Fundo Social Europeu (FSE) through Programa Operacional Regional Norte (Norte 2020)."

In the published article, there was an error in affiliation 4. Instead of "TOXRUN, Toxicology Research Unit, University Institute of Health Sciences, Advanced Polytechnic and University Cooperative (CESPU), Gandra, Portugal" it should be "TOXRUN, Toxicology Research Unit, University Institute of Health Sciences, Polytechnic and University Cooperative (CESPU), Gandra, Portugal".

The authors apologize for these errors and state that this does not change the scientific conclusions of the article in any way. The original article has been updated.

frontiers
in Oncology

SYSTEMATIC REVIEW
published: 28 October 2021
doi: 10.3389/fonc.2021.737155

# Prognostic Role of the C-Reactive Protein/Albumin Ratio in Patients With Gynecological Cancers: A Meta-Analysis

*Yingji Fang**, *Tingting Zheng* and *Chengling Zhang*

*Department of Gynecology, Jinan Maternal and Child Care Hospital, Jinan, China*

**Background:** Many studies have investigated the prognostic role of the C-reactive protein/albumin ratio (CRP/Alb ratio) in patients with gynecological cancers; however, there is lack of consensus owing to conflicting results across studies. We performed a meta-analysis to determine the prognostic role of the CRP/Alb ratio in gynecological cancers.

**Methods:** We searched the PubMed, Embase, the Web of Science, Cochrane Library, China National Knowledge Infrastructure, and Wanfang electronic databases since inception to April 2021. Combined hazard ratios (HRs) and 95% confidence intervals (CIs) were used to estimate the prognostic effect of the CRP/Alb ratio in gynecological cancers. Pooled odds ratios (ORs) and 95% CIs were used to investigate the association between the CRP/Alb ratio and clinicopathological features.

**Results:** The meta-analysis included seven studies with 1,847 patients. The pooled results showed that a high pretreatment CRP/Alb ratio was associated with poor overall survival (HR, 1.84; 95% CI, 1.41–2.40; $p < 0.001$) and progression-/disease-free survival (HR, 2.58; 95% CI, 1.42–4.68; $p = 0.002$). Additionally, a high CRP/Alb ratio was significantly associated with stages III–IV disease (the International Federation of Gynecology and Obstetrics classification) (OR, 2.98; 95% CI, 1.45–6.14; $p = 0.003$). However, we observed a non-significant correlation between the CRP/Alb ratio and lymph node metastasis, tumor size, and histopathological grade.

**Conclusions:** The CRP/Alb ratio is a convenient and accurate predictor of survival outcomes in gynecological cancers. A high CRP/Alb ratio also predicts tumor progression.

**Keywords: gynecological cancers, meta-analysis, prognostic, CRP/Alb ratio, risk factors**

***Edited by:***
*Dong Hoon Suh*
*Seoul National University College of Medicine, South Korea*

***Reviewed by:***
*Bala Audu,*
*University of Maiduguri, Nigeria*
*Marco D'Indinosante,*
*Catholic University of the Sacred Heart, Italy*

***Correspondence:**
*Yingji Fang*
*jnlh1971@sina.com*

***Specialty section:***
*This article was submitted to Gynecological Oncology, a section of the journal Frontiers in Oncology*

***Received:*** *13 July 2021*
***Accepted:*** *16 September 2021*
***Published:*** *28 October 2021*

***Citation:***
*Fang Y, Zheng T and Zhang C (2021) Prognostic Role of the C-Reactive Protein/Albumin Ratio in Patients With Gynecological Cancers: A Meta-Analysis. Front. Oncol. 11:737155. doi: 10.3389/fonc.2021.737155*

## INTRODUCTION

Gynecological cancers (GCs) represent the second most common cancer in women worldwide (1). Cervical cancer (CC), ovarian cancer (OC), and endometrial cancer (EC) are the predominant types of GC, which constitute a major public health concern globally (2). The 5-year survival rates in patients with GC are poor despite the availability of well-established surgical and chemoradiotherapeutic approaches (3). For example, the 5-year survival rate in patients with stages III–IV EC was only 17% (4). Therefore, it is important to identify effective novel biomarkers that predict survival outcomes and also establish individualized therapeutic regimens.

Accumulating evidence has shown an association between tumor-induced inflammatory responses and tumor development and progression (5). Reportedly, various inflammatory and immune response biomarkers serve as prognostic factors for solid tumors (6). For example, in a recent study, Marchetti et al. (7) observed that the neutrophil–lymphocyte ratio (NLR) was an independent prognostic marker for progression-free survival (PFS) in patients with high-grade advanced serous ovarian cancer. Another study (8), which recruited 1,266 patients with CC, showed that the platelet–lymphocyte ratio (PLR), NLR, derived NLR, and the PLR + NLR in combination showed equivalent efficacy as prognostic factors for overall survival (OS) in patients with locally advanced CC and are therefore considered promising prognostic biomarkers. The aforementioned studies (7, 8) highlight the role of systemic inflammatory biomarkers in the prognosis of GC. The C-reactive protein (CRP)/albumin ratio (CRP/Alb) is an index based on measurement of serum CRP and Alb levels (9) and is calculated as the serum CRP level divided by the serum Alb level. This ratio was initially proposed to predict outcomes in patients with acute medical admissions (9). In recent years, studies have investigated the utility of the CRP/Alb ratio as a prognostic factor in various cancers (10, 11). Previous studies have reported the independent prognostic value of the CRP/Alb ratio in colorectal cancer (CRC) (12), oral squamous cell carcinoma (13), gastric cancer (14), non-small-cell lung cancer (15), and gallbladder cancer (16). Many studies have also investigated the prognostic utility of the CRP/Alb ratio in patients with GC; however, the results remain inconclusive (17–23). We performed a meta-analysis to systemically investigate the prognostic and clinical significance of the CRP/Alb ratio in GC.

# MATERIALS AND METHODS

## Study Guidelines and Ethics

This meta-analysis was performed in accordance with the Preferred Reporting Items for Systematic Reviews and Meta-Analyses statement (24). All analyses were based on previously published studies; therefore, ethical approval and informed consent were waived for this study.

## Literature Search

We performed a comprehensive search of the PubMed, Embase, the Web of Science, Cochrane Library, China National Knowledge Infrastructure, and Wanfang electronic databases from inception to April 2021. Based on relevant studies (25, 26), we used the following search terms: gynecological cancer OR gynecological carcinoma OR gynecological neoplasm OR endometrial neoplasm OR endometrial carcinoma OR endometrial cancer OR endometrium cancer OR endometrium carcinoma OR cervical cancer OR cervical carcinoma OR ovarian carcinoma OR ovarian cancer OR uterine neoplasm and C-reactive protein OR albumin OT CAR OR CRP/Alb OR C-reactive protein to albumin ratio, C-reactive protein/albumin ratio and prognosis OR prognostic OR survival OR outcome OR mortality. Both free text and medical subject heading terms were used for the literature search. We selected articles in English and Chinese. References from the identified publications were also retrieved for potential inclusion.

## Inclusion and Exclusion Criteria

Following were the inclusion criteria: (1) histopathologically diagnosed GC; (2) studies that investigated the prognostic role of CRP/Alb ratio for survival outcomes including but not limited to OS, cancer-specific survival (CSS), disease-free survival (DFS), PFS, and recurrence-free survival; (3) availability of hazard ratios (HRs) and 95% confidence intervals (CIs) or sufficient data to calculate these values; and (4) availability of cutoff values of the CRP/Alb ratio. Following were the exclusion criteria: (1) reviews, meeting abstracts, case reports, and letters; (2) unavailability of data to calculate HRs and corresponding 95% CIs; (3) studies in languages other than English or Chinese; and (4) overlapping or duplication of studies.

## Data Extraction and Quality Assessment

Two investigators (YF and TZ) independently screened all retrieved articles and extracted information using a predetermined form. All disagreements were resolved through discussion with a third investigator (CZ). The following data were recorded: first author's name, year of publication, country, age, cancer type, the International Federation of Gynecology and Obstetrics (FIGO) stage, treatment, study period, cutoff value of the CRP/Alb ratio, method used to determine the cutoff value, duration of follow-up or the last date of follow-up, survival endpoints, and HRs and 95% CIs for OS, PFS, and DFS. HRs and 95% CIs were extracted from multivariable analyses depending on availability; HRs and 95% CIs were extracted from univariate analyses in the remaining cases. Two independent reviewers assessed the methodological quality of the included studies based on the Newcastle–Ottawa Quality Assessment Scale (NOS) (http://www.ohri.ca/programs/clinical_epidemiology/oxford.asp). The NOS consists of the following three dimensions: selection (four stars), comparability (two stars), and outcome assessment (three points). NOS scores range from 0 to 9, and scores ≥6 indicate high-quality studies.

## Statistical Analysis

Combined HRs and 95% CIs were used to estimate the prognostic effect of the CRP/Alb ratio in GC. HR >1 without a 95% CI overlapping 1 indicates that a high CRP/Alb ratio predicts poor prognosis. Heterogeneity among studies was assessed using the Cochrane Q test and the $I^2$ statistic. $p < 0.10$ and/or $I^2 > 50\%$ was interpreted as indicative of significant heterogeneity, and a random-effects model was used in such cases; a fixed-effects model was used in the remaining cases. Subgroup analysis stratified by various factors was performed to determine the source of heterogeneity. Pooled odds ratios (ORs) and 95% CIs were used to determine the association between the CRP/Alb ratio and clinicopathological features. Publication bias was evaluated using Begg's funnel plots. All statistical analyses were performed using the Stata software, version 12.0 (Stata Corporation, College Station, TX, USA). A $p < 0.05$ was considered statistically significant.

# RESULTS

## Literature Search

The initial literature search identified 292 studies from the aforementioned databases; 126 studies remained after exclusion of duplicate studies (**Figure 1**). After screening titles and abstracts, 112 studies were eliminated, and we reviewed the full text in 14 articles, of which 7 studies with insufficient data were excluded. Finally, seven studies with 1,847 patients (17–23) were included in this meta-analysis.

## Characteristics of Included Studies

**Table 1** summarizes the characteristics of studies included in this meta-analysis. The studies were published between 2017 and 2021. Five studies were performed in China (17, 19, 20, 22, 23) and two in Japan (18, 21). Six studies were published in English (17–19, 21–23) and one in Chinese (20). Four studies enrolled patients with CC (17, 20–22) and three recruited patients with OC (18, 19, 23). The sample size ranged from 200 to 407 (median, 235). The cutoff values of the CRP/Alb ratio ranged from 0.022 to 0.68 (median, 0.15). Therefore, we used 0.15 as the cutoff value of the CRP/Alb ratio for subgroup analysis. Five studies used receiver operating characteristic curve analysis to determine the cutoff value (17–20, 22), one study used the median value (21), and one study used cutoff finder software (23). Six studies (17, 19–23) reported the prognostic value of the CRP/Alb ratio for OS, two studies (22, 23) reported its prognostic value for PFS, and one study (18) for DFS. Five studies (17–19,

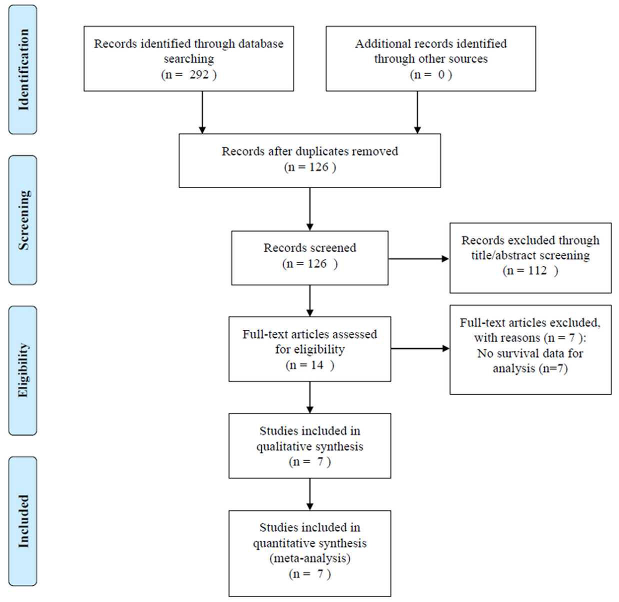

**FIGURE 1** | Flowchart describing the literature search and study selection.

**TABLE 1** | Summary of clinical studies included in meta-analysis.

| Study | Year | Country | Sample size | Age | Cancer type | FIGO stage | Treatment | Study period | Cutoff value | Follow-up (months) or the date of last follow-up | Determination of cutoff value | Survival endpoints | CRP/Alb value (high/low) | NOS score |
|---|---|---|---|---|---|---|---|---|---|---|---|---|---|---|
| He et al. (17) | 2018 | China | 229 | 44 (28–79) | Cervical cancer | I–IV | Surgery + chemotherapy | 2007–2009 | 0.022 | To Jan, 2016 | ROC analysis | OS | 138/91 | 7 |
| Komura et al. (18) | 2020 | Japan | 308 | NA | Ovarian cancer | I–IV | Surgery + chemotherapy | 2007–2016 | 0.048 | NA | ROC analysis | DFS | 156/152 | 6 |
| Liu et al. (19) | 2017 | China | 200 | 53 (18–83) | Ovarian cancer | I–IV | Surgery + chemotherapy | 2006–2012 | 0.68 | To Dec, 2014 | ROC analysis | OS | 69/131 | 9 |
| Su et al. (20) | 2020 | China | 407 | NA | Cervical cancer | I–II | Surgery | 2009–2013 | 0.15 | To Apr, 2018 | ROC analysis | OS | 61/346 | 7 |
| Taguchi et al. (21) | 2021 | Japan | 231 | 67 | Cervical cancer | I–IV | Radiotherapy | 2004-2015 | 0.18 | 16.4 | Median value | OS | 116/115 | 8 |
| Zhang et al. (22) | 2018 | China | 235 | 46 (29–78) | Cervical cancer | I–II | Surgery | 2005–2009 | 0.15 | 77(32–96) | ROC analysis | OS, PFS | 113/122 | 7 |
| Zhang et al. (23) | 2017 | China | 237 | NA | Ovarian cancer | I–IV | Surgery + chemotherapy | 2007–2015 | 0.5 | To Dec, 2016 | Cutout finder | OS, PFS | 95/142 | 7 |

*FIGO, International Federation of Gynecology and Obstetrics; NA, not available; OS, overall survival; PFS, progression-free survival; DFS, disease-free survival; ROC, receiver operating characteristics; NOS, Newcastle-Ottawa Scale; CRP/Alb, C-reactive protein/albumin ratio.*

21, 23) enrolled patients with FIGO stages I–IV, and two studies (20, 22) included patients with FIGO stages I–II. NOS scores of the included studies ranged from 6 to 9 (median, 7), which indicates that all included studies were of high quality. **Table 2** shows NOS score details.

## Prognostic Role of the C-Reactive Protein/Albumin Ratio in Overall Survival and Progression- and Disease-Free Survival

A total of six studies that included 1,539 patients (17, 19–23) investigated the association between the CRP/Alb ratio and OS in GC. Pooled data showed HR of 1.84, 95% CI of 1.41–2.40, and $p < 0.001$ (**Figure 2**; **Table 3**). Owing to significant heterogeneity ($I^2 = 71.2\%$, $p = 0.004$), we used a random-effects model. Subgroup analyses based on various factors showed that a high CRP/Alb ratio remained a prognostic tool to determine poor survival in subgroups across different countries, cancer types, FIGO stage, cutoff values, cutoff value determination methods, and treatment modalities (**Table 3**). Three studies that included 780 patients (18, 22, 23) reported the role of the CRP/Alb ratio for prognosis of PFS/DFS (HR, 2.58; 95% CI, 1.42–4.68; $p = 0.002$) based on a random-effects model (**Figure 3**; **Table 3**). Similar to the findings associated with OS, subgroup analysis revealed that an elevated CRP/Alb ratio was an indicator of poor PFS/DFS in various subgroups of patients with GC.

## Correlation Between the C-Reactive Protein/Albumin Ratio and Clinical Features

Using data from five studies, we investigated the association between the CRP/Alb ratio and clinicopathological characteristics (17–20, 22). A high CRP/Alb ratio was significantly associated with FIGO stages III–IV (OR, 2.98; 95% CI, 1.45–6.14; $p = 0.003$) (**Figure 4**; **Table 4**). However, we observed a non-significant correlation between the CRP/Alb ratio and lymph node metastasis (yes vs. no) (OR, 2.54; 95% CI, 0.59–10.90; $p = 0.209$), tumor size (≥4 vs. <4 cm) (OR, 2.54; 95% CI, 0.84–7.72; $p = 0.100$), and histopathological grade (G3 vs. G1/G2) (OR, 1.07; 95% CI, 0.75–1.53; $p = 0.176$) (**Figure 4**; **Table 4**).

## Publication Bias

Begg's funnel plots were used to assess the potential publication bias for OS and PFS/DFS. We observed no significant publication bias for OS ($p = 0.135$) or PFS/DFS ($p = 0.296$) in this meta-analysis (**Figure 5**). Therefore, the results of our meta-analysis are reliable.

# DISCUSSION

The CRP/Alb ratio has been investigated as a prognostic factor for patients with GC; however, there is lack of consensus owing to inconsistent results across studies. In the present meta-analysis, we used pooled data from seven studies that included 1,847 patients; our results showed that a high CRP/Alb ratio was an independent prognostic factor for poor OS, PFS, and DFS. Results of subgroup analyses performed after stratification based on country, cancer type, FIGO stage, cutoff values, cutoff value determination methods, and treatment modalities were in agreement with the results of the overall analysis. An elevated CRP/Alb ratio was also associated with advanced FIGO stages in GC. These results indicate that the CRP/Alb ratio may serve as an efficient and cost-effective prognostic biomarker in clinical

**TABLE 2** | The details of NOS scale for studies in the meta-analysis.

| First author | Year | Selection | | | | Comparability | Outcome | | | Total score |
|---|---|---|---|---|---|---|---|---|---|---|
| | | Representativeness of the exposed cohort | Selection of the non-exposed cohort | Ascertainment of exposure | Demonstration that outcome of interest was not present at start of study | Comparability of cohorts on the basis of the design or analysis | Assessment of outcome | Was follow-up long enough for outcomes to occur | Adequacy of follow up of cohorts | |
| He et al. (17) | 2018 | ★ | ★ | ★ | ★ | ★ | ★ | – | ★ | 7 |
| Komura et al. (18) | 2020 | ★ | ★ | – | ★ | ★ | ★ | ★ | – | 6 |
| Liu et al. (19) | 2017 | ★ | ★ | ★ | ★ | ★★ | ★ | ★ | ★ | 9 |
| Su et al. (20) | 2020 | ★ | ★ | ★ | ★ | ★ | ★ | – | ★ | 7 |
| Taguchi et al. (21) | 2021 | ★ | ★ | ★ | ★ | ★★ | ★ | – | ★ | 8 |
| Zhang et al. (22) | 2018 | ★ | ★ | ★ | ★ | ★ | ★ | ★ | – | 7 |
| Zhang et al. (23) | 2017 | ★ | ★ | – | ★ | ★★ | ★ | – | ★ | 7 |

*NOS, Newcastle–Ottawa Scale A star is one point.*

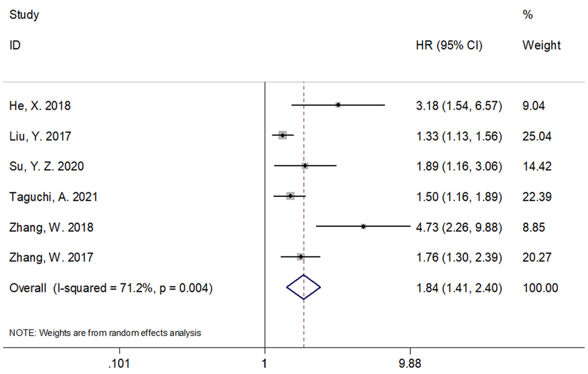

**FIGURE 2** | Forest plots of studies evaluating the hazard ratio for overall survival (OS) of patients with gynecological cancers of a high CRP/Alb ratio.

**TABLE 3** | Subgroup analysis of the prognostic value of CRP/Alb for OS and PFS/DFS in patients with gynecological cancers.

| Subgroups | No. of studies | No. of patients | Effects model | HR (95% CI) | p | Heterogeneity | |
|---|---|---|---|---|---|---|---|
| | | | | | | $I^2$ (%) | Ph |
| OS | | | | | | | |
| Total | 6 | 1539 | Random | 1.84 (1.41–2.40) | <0.001 | 71.2 | 0.004 |
| Country | | | | | | | |
| China | 5 | 1308 | Random | 2.05 (1.42–2.97) | <0.001 | 76.9 | 0.002 |
| Japan | 1 | 231 | – | 1.50 (1.18–1.91) | 0.001 | – | – |
| Cancer type | | | | | | | |
| Cervical cancer | 4 | 1102 | Random | 2.33 (1.43–3.79) | 0.001 | 73.1 | 0.011 |
| Ovarian cancer | 2 | 437 | Random | 1.49 (1.13–1.94) | 0.004 | 61.0 | 0.109 |
| Tumor stage | | | | | | | |
| I–II | 2 | 642 | Random | 2.86 (1.17–7.01) | 0.022 | 76.1 | 0.041 |
| I–IV | 4 | 897 | Random | 1.58 (1.27–1.98) | <0.001 | 58.4 | 0.066 |
| Cut–off value | | | | | | | |
| ≤0.15 | 3 | 871 | Random | 2.88 (1.65–5.02) | <0.001 | 55.7 | 0.105 |
| >0.15 | 3 | 668 | Fixed | 1.44 (1.27–1.63) | <0.001 | 26.7 | 0.256 |
| Cutoff value determination | | | | | | | |
| ROC analysis | 4 | 1071 | Random | 2.28 (1.31–3.99) | 0.004 | 81.7 | 0.001 |
| Median value/cutoff finder | 2 | 468 | Fixed | 1.60 (1.32–1.93) | <0.001 | 0 | 0.417 |
| Treatment | | | | | | | |
| Surgery + chemotherapy | 3 | 666 | Random | 1.46 (1.27–1.68) | <0.001 | 72.1 | 0.028 |
| Surgery | 2 | 642 | Random | 2.49 (1.66–3.73) | <0.001 | 76.1 | 0.041 |
| Radiotherapy | 1 | 231 | – | 1.50 (1.18–1.91) | 0.001 | – | – |
| PFS/DFS | | | | | | | |
| Total | 3 | 780 | Random | 2.58 (1.42–4.68) | 0.002 | 73.8 | 0.022 |
| Country | | | | | | | |
| China | 2 | 472 | Random | 2.85 (0.99–8.17) | 0.052 | 86.5 | 0.006 |
| Japan | 1 | 308 | – | 2.35 (1.27–4.36) | 0.007 | – | – |
| Cancer type | | | | | | | |
| Cervical cancer | 1 | 235 | – | 5.16 (2.50–10.69) | <0.001 | – | – |
| Ovarian cancer | 2 | 545 | Fixed | 1.84 (1.43–2.37) | <0.001 | 0 | 0.395 |
| Tumor stage | | | | | | | |
| I–II | 1 | 235 | – | 5.16 (2.50–10.69) | <0.001 | – | – |
| I–IV | 2 | 545 | Fixed | 1.84 (1.43–2.37) | <0.001 | 0 | 0.395 |
| Cutoff value | | | | | | | |
| ≤0.15 | 2 | 543 | Random | 3.40 (1.57–7.34) | 0.002 | 61.7 | 0.106 |
| >0.15 | 1 | 237 | – | 1.75 (1.33–2.31) | <0.001 | – | – |
| Cutoff value determination | | | | | | | |
| ROC analysis | 2 | 543 | Random | 3.40 (1.57–7.34) | 0.002 | 61.7 | 0.106 |
| Median value/cutoff finder | 1 | 237 | – | 1.75 (1.33–2.31) | <0.001 | – | – |
| Treatment | | | | | | | |
| Surgery + chemotherapy | 2 | 545 | Fixed | 1.84 (1.43–2.37) | <0.001 | 0 | 0.395 |
| Surgery | 1 | 235 | – | 5.16 (2.50–10.69) | <0.001 | – | – |

*OS, overall survival; PFS, progression-free survival; DFS, disease-free survival; ROC, receiver operating characteristics.*

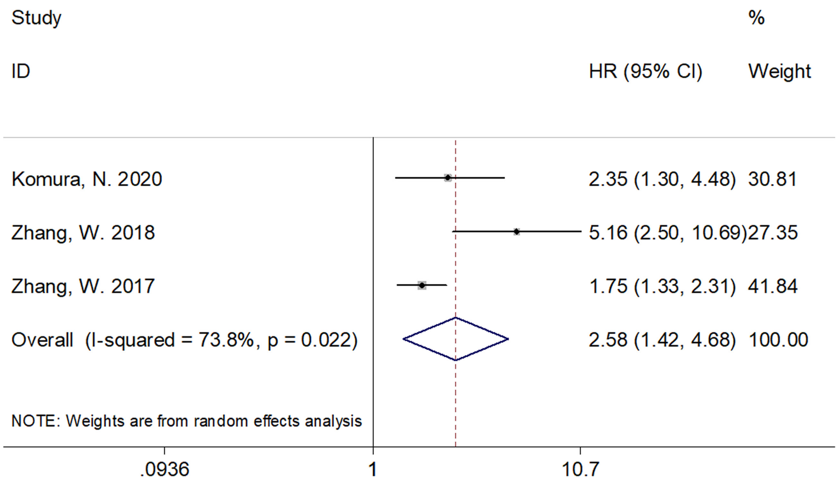

**FIGURE 3** | Forest plots of studies evaluating the hazard ratio for progression-free survival (PFS)/disease-free survival (DFS) of patients with gynecological cancers of a high CRP/Alb ratio.

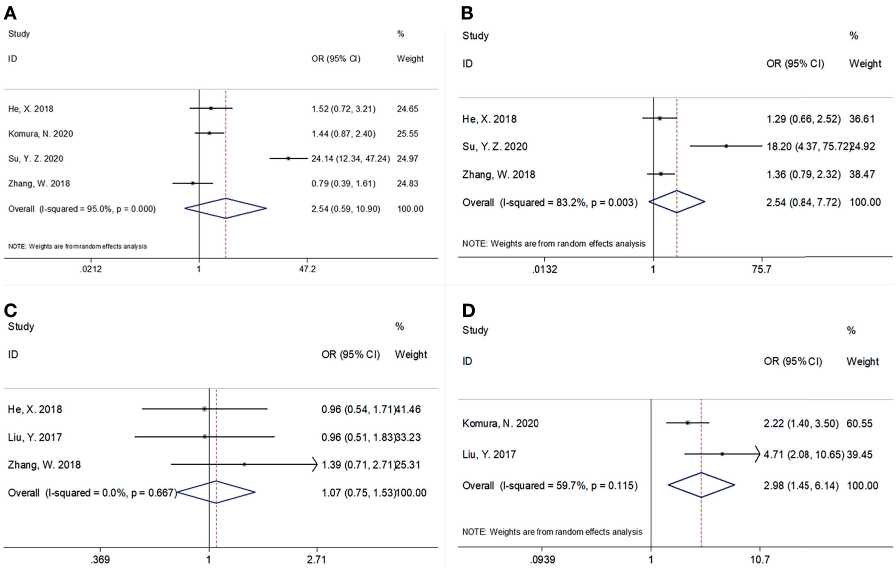

**FIGURE 4** | The association between CRP/Alb ratio and clinicopathological features in patients with gynecological cancers. **(A)** Lymph node metastasis (yes vs. no), **(B)** tumor size (≥4 vs. <4 cm), **(C)** histological grade (G3 vs. G1/G2), and **(D)** FIGO stage (III–IV vs. I–II).

settings for patients with GC. To our knowledge, this is the first meta-analysis that discusses the prognostic role of the CRP/Alb ratio in GC.

Inflammatory responses are known to promote tumorigenesis through their effects on the tumor microenvironment in GC (27). Tumor growth, invasion, necrosis, and hypoxia initiate immune responses in the tumor microenvironment, which consequently triggers the production of a variety of inflammatory cytokines (28). CRP is an acute-phase protein that is mediated by several proinflammatory cytokines, including interleukin-1 (IL-1), IL-6, and tumor necrosis factor-α (29). IL-6 can lead to inflammation and angiogenesis, which contribute to tumor progression (30). Serum Alb levels reflect patients' nutritional status; a low serum Alb level indicates a state of malnutrition (31). Hypoalbuminemia is implicated in the nutritional decline observed in patients with cancer (17). Therefore, the CRP/Alb ratio (as a combination of CRP and Alb) provides a biological rationale to be considered a promising prognostic tool in GC.

Many studies have investigated the prognostic value of the CRP/Alb ratio in a variety of cancer types (26, 29, 32–35). Yu et al. showed that an elevated pretreatment CRP/Alb ratio was a prognostic marker of poor OS and CSS in patients with gastric

**TABLE 4** | The correlation between CRP/Alb ratio and clinicopathological features in patients with gynecological cancers.

| Variables | No. of studies | No. of patients | Effects model | HR (95%CI) | p | Heterogeneity | |
|---|---|---|---|---|---|---|---|
| | | | | | | $I^2$ (%) | Ph |
| Lymph node metastasis (yes vs. no) | 4 | 1,179 | Random | 2.54 (0.59–10.90) | 0.209 | 95.0 | <0.001 |
| Tumor size (≥4 vs. <4 cm) | 3 | 871 | Random | 2.54 (0.84–7.72) | 0.100 | 83.2 | 0.003 |
| Histological grade (G3 vs. G1/G2) | 3 | 664 | Fixed | 1.07 (0.75–1.53) | 0.716 | 0 | 0.667 |
| FIGO stage (III–IV vs. I–II) | 2 | 508 | Random | 2.98 (1.45–6.14) | 0.003 | 59.7 | 0.115 |

*FIGO, International Federation of Gynecology and Obstetrics.*

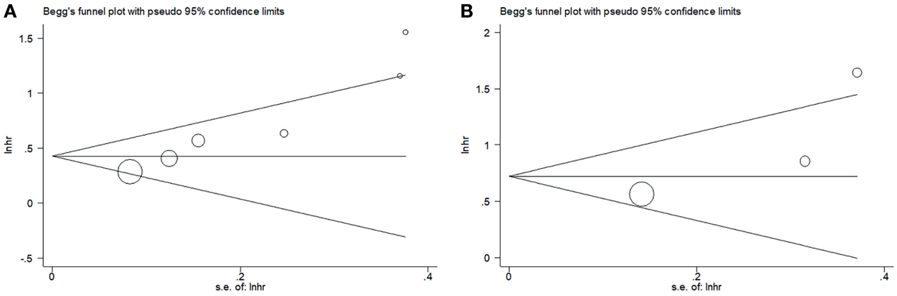

**FIGURE 5** | Publication bias tested by funnel plots in this meta-analysis. **(A)** OS; **(B)** PFS/DFS.

cancer (26). A high CRP/Alb ratio was shown to be associated with clinicopathological features that reflect tumor progression in patients with gastric cancer (26). A meta-analysis of 15 studies that included 6,329 patients reported that a high CRP/Alb ratio was associated with various survival outcomes in patients with CRC (29). Another recent meta-analysis suggested that an elevated pretreatment CRP/Alb ratio could independently predict poor OS in patients with pancreatic cancer (33). Zhou et al. observed that a high pretreatment CRP/Alb ratio predicted poor survival in patients with renal cell carcinoma (36). In our meta-analysis, the CRP/Alb ratio was correlated with poor OS, PFS, and DFS and also predicted advanced FIGO stages. Therefore, the CRP/Alb ratio also serves as a promising tool for risk stratification of patients.

Following are the limitations of this meta-analysis: (a) we investigated studies that described only a few types of GC; only CC and OC were considered in this study. Other GCs, such as EC, were not included in our meta-analysis. Although the search items included all GCs; however, no eligible study on EC was identified. (b) All eligible studies were retrospectively designed, which may introduce selection bias in the meta-analysis. (c) All patients were from China and Japan; therefore, our findings may not be generalizable and are perhaps more applicable to Asian patients. The prognostic value of the CRP/Alb ratio in non-Asian patients warrants investigation.

## CONCLUSIONS

Our meta-analysis showed that the CRP/Alb ratio is a convenient and accurate predictor of survival outcomes in GC. A high CRP/Alb ratio also predicts tumor progression. However, owing to several limitations of this study, large-scale trials that include patients of diverse ethnicities are warranted to validate our findings.

## DATA AVAILABILITY STATEMENT

The original contributions presented in the study are included in the article/supplementary material. Further inquiries can be directed to the corresponding author.

## AUTHOR CONTRIBUTIONS

YF and TZ came up with the study. All authors collaborated on the design of the project. YF, TZ, and CZ collated, screened, and analyzed the data together and drafted the manuscript. YF and TZ reviewed the content, revised the manuscript, and approved the final manuscript. All authors contributed to the article and approved the submitted version.

## REFERENCES

1. Bray F, Ferlay J, Soerjomataram I, Siegel RL, Torre LA, Jemal A. Global Cancer Statistics 2018: GLOBOCAN Estimates of Incidence and Mortality Worldwide for 36 Cancers in 185 Countries. *CA: Cancer J Clin* (2018) 68 (6):394–424. doi: 10.3322/caac.21492
2. Gultekin M, Kucukyildiz I, Karaca MZ, Dundar S, Boztas G, Turan SH, et al. Trends of Gynecological Cancers in Turkey: Toward Europe or Asia? *Int J*

*Gynecol Cancer* (2017) 27(8S Suppl 1):S1–s9. doi: 10.1097/igc.0000000000001026

3. Lu JJ, Gu Y, Li Q, Zhong HX, Wang XX, Zheng ZX, et al. Wilms' Tumor 1 (WT1) as a Prognosis Factor in Gynecological Cancers A Meta-Analysis. *Medicine* (2018) 97(28):e11485. doi: 10.1097/md.0000000000011485
4. McDonald ME, Bender DP. Endometrial Cancer: Obesity, Genetics, and Targeted Agents. *Obstet Gynecol Clinics North Am* (2019) 46(1):89–105. doi: 10.1016/j.ogc.2018.09.006
5. Diakos CI, Charles KA, McMillan DC, Clarke SJ. Cancer-Related Inflammation and Treatment Effectiveness. *Lancet Oncol* (2014) 15(11): e493–503. doi: 10.1016/s1470-2045(14)70263-3
6. Zou PJ, Yang E, Li ZY. Neutrophil-To-Lymphocyte Ratio Is an Independent Predictor for Survival Outcomes in Cervical Cancer: A Systematic Review and Meta-Analysis. *Sci Rep* (2020) 10(1):21917. doi: 10.1038/s41598-020-79071-x
7. Marchetti C, D'Indinosante M, Bottoni C, Di Ilio C, Di Berardino S, Costantini B, et al. NLR and BRCA Mutational Status in Patients With High Grade Serous Advanced Ovarian Cancer. *Sci Rep* (2021) 11(1):11125. doi: 10.1038/s41598-021-90361-w
8. Santos Thuler LC, Reis Wariss B, Nogueira-Rodrigues A, de Melo AC, Bergmann A. The Utility of Pretreatment Systemic Inflammatory Response Biomarkers on Overall Survival of Cervical Cancer Patients Stratified by Clinical Staging. *Eur J Obstet Gynecol Reprod Biol* (2021) 264:281–8. doi: 10.1016/j.ejogrb.2021.07.034
9. Fairclough E, Cairns E, Hamilton J, Kelly C. Evaluation of a Modified Early Warning System for Acute Medical Admissions and Comparison With C-Reactive Protein/Albumin Ratio as a Predictor of Patient Outcome. *Clin Med (London England)* (2009) 9(1):30–3. doi: 10.7861/clinmedicine.9-1-30
10. Li N, Tian GW, Wang Y, Zhang H, Wang ZH, Li G. Prognostic Role of the Pretreatment C-Reactive Protein/Albumin Ratio in Solid Cancers: A Meta-Analysis. *Sci Rep* (2017) 7:41298. doi: 10.1038/srep41298
11. Xu HJ, Ma Y, Deng F, Ju WB, Sun XY, Wang H. The Prognostic Value of C-Reactive Protein/Albumin Ratio in Human Malignancies: An Updated Meta-Analysis. *Onco Targets Ther* (2017) 10:3059–70. doi: 10.2147/ott.S137002
12. Tamai K, Okamura S, Makino S, Yamamura N, Fukuchi N, Ebisui C, et al. C-Reactive Protein/Albumin Ratio Predicts Survival After Curative Surgery in Elderly Patients With Colorectal Cancer. *Updates Surg* (2021). doi: 10.1007/s13304-021-01011-9
13. Keinänen A, Uittamo J, Marinescu-Gava M, Kainulainen S, Snäll J. Preoperative C-Reactive Protein to Albumin Ratio and Oral Health in Oral Squamous Cell Carcinoma Patients. *BMC Oral Health* (2021) 21(1):132. doi: 10.1186/s12903-021-01516-0
14. Yu Q, Li KZ, Fu YJ, Tang Y, Liang XQ, Liang ZQ, et al. Clinical Significance and Prognostic Value of C-Reactive Protein/Albumin Ratio in Gastric Cancer. *Ann Surg Treat Res* (2021) 100(6):338–46. doi: 10.4174/astr.2021.100.6.338
15. Araki T, Tateishi K, Sonehara K, Hirota S, Komatsu M, Yamamoto M, et al. Clinical Utility of the C-Reactive Protein:Albumin Ratio in Non-Small Cell Lung Cancer Patients Treated With Nivolumab. *Thorac Cancer* (2021) 12 (5):603–12. doi: 10.1111/1759-7714.13788
16. Bao Y, Yang J, Duan Y, Chen Y, Chen W, Sun D. The C-Reactive Protein to Albumin Ratio Is an Excellent Prognostic Predictor for Gallbladder Cancer. *Biosci Trends* (2021) 14(6):428–35. doi: 10.5582/bst.2020.03326
17. He X, Li JP, Liu XH, Zhang JP, Zeng QY, Chen H, et al. Prognostic Value of C-Reactive Protein/Albumin Ratio in Predicting Overall Survival of Chinese Cervical Cancer Patients Overall Survival: Comparison Among Various Inflammation Based Factors. *J Cancer* (2018) 9(10):1877–84. doi: 10.7150/jca.23320
18. Komura N, Mabuchi S, Shimura K, Kawano M, Matsumoto Y, Kimura T. Significance of Pretreatment C-Reactive Protein, Albumin, and C-Reactive Protein to Albumin Ratio in Predicting Poor Prognosis in Epithelial Ovarian Cancer Patients. *Nutr Cancer* (2021) 73(8):1357–64. doi: 10.1080/01635581.2020.1798479
19. Liu Y, Chen S, Zheng C, Ding M, Zhang L, Wang L, et al. The Prognostic Value of the Preoperative C-Reactive Protein/Albumin Ratio in Ovarian Cancer. *BMC Cancer* (2017) 17(1):285. doi: 10.1186/s12885-017-3220-x
20. Su YZ, Xu ZY, Xiang HF, Wei ZL, Cao YX. Relationship Between CAR and Prognosis of Cervical Cancer Patients. *Med Inf* (2020) 33(08):80–3.
21. Taguchi A, Nakajima Y, Furusawa A, Yoshino Y, Takao M, Kashiyama T, et al. High Neutrophil-to-Lymphocyte Ratio Is a Predictor of Short-Term Survival for Patients With Recurrent Cervical Cancer After Radiation-Based Therapy. *J Obstet Gynaecol Res* (2021) 47(5):1862–70. doi: 10.1111/jog.14712
22. Zhang W, Liu K, Ye B, Liang W, Ren Y. Pretreatment C-Reactive Protein/Albumin Ratio Is Associated With Poor Survival in Patients With Stage IB-IIA Cervical Cancer. *Cancer Med* (2018) 7(1):105–13. doi: 10.1002/cam4.1270
23. Zhang W, Ye B, Liang W, Ren Y. Preoperative Prognostic Nutritional Index Is a Powerful Predictor of Prognosis in Patients With Stage III Ovarian Cancer. *Sci Rep* (2017) 7(1):9548. doi: 10.1038/s41598-017-10328-8
24. Moher D, Liberati A, Tetzlaff J, Altman DG, Grp P. Preferred Reporting Items for Systematic Reviews and Meta-Analyses: The PRISMA Statement. *PLoS Med* (2009) 6(7):e1000097. doi: 10.1371/journal.pmed.1000097
25. Hu JL, Wu XR, Huang PZ, Teng F, Wang YM, Xue FX. The Proportion and Prognostic Significance of T-Regulatory Cells in Patients With Gynecological Cancers: A Systematic Review and Meta-Analysis. *J Cancer* (2020) 11 (11):3340–8. doi: 10.7150/jca.42472
26. Yu J, Liu H, Zeng X, Zhao Y, Jiang D, Lu H, et al. Prognostic and Clinicopathological Significance of C-Reactive Protein/Albumin Ratio (CAR) in Patients With Gastric Cancer: A Meta-Analysis. *PLoS One* (2021) 16(4):e0250295. doi: 10.1371/journal.pone.0250295
27. Polastro L, Closset C, Kerger J. Immunotherapy in Gynecological Cancers: Where Are We? *Curr Opin Oncol* (2020) 32(5):459–70. doi: 10.1097/cco.0000000000000661
28. Kinoshita A, Onoda H, Imai N, Iwaku A, Oishi M, Tanaka K, et al. The C-Reactive Protein/Albumin Ratio, a Novel Inflammation-Based Prognostic Score, Predicts Outcomes in Patients With Hepatocellular Carcinoma. *Ann Surg Oncol* (2015) 22(3):803–10. doi: 10.1245/s10434-014-4048-0
29. Liao CK, Yu YL, Lin YC, Hsu YJ, Chern YJ, Chiang JM, et al. Prognostic Value of the C-Reactive Protein to Albumin Ratio in Colorectal Cancer: An Updated Systematic Review and Meta-Analysis. *World J Surg Oncol* (2021) 19(1):139. doi: 10.1186/s12957-021-02253-y
30. Wakasaki T, Yasumatsu R, Masuda M, Takeuchi T, Manako T, Matsuo M, et al. Prognostic Biomarkers of Salvage Chemotherapy Following Nivolumab Treatment for Recurrent and/or Metastatic Head and Neck Squamous Cell Carcinoma. *Cancers (Basel)* (2020) 12(8):2299. doi: 10.3390/cancers12082299
31. Saito H, Kono Y, Murakami Y, Shishido Y, Kuroda H, Matsunaga T, et al. Postoperative Serum Albumin Is a Potential Prognostic Factor for Older Patients With Gastric Cancer. *Yonago Acta Med* (2018) 61(1):72–8. doi: 10.33160/yam.2018.03.010
32. Luan CW, Yang HY, Tsai YT, Hsieh MC, Chou HH, Chen KS. Prognostic Value of C-Reactive Protein-To-Albumin Ratio in Head and Neck Cancer: A Meta-Analysis. *Diagnostics (Basel Switzerland)* (2021) 11(3):403. doi: 10.3390/diagnostics11030403
33. Zang Y, Fan Y, Gao Z. Pretreatment C-Reactive Protein/Albumin Ratio for Predicting Overall Survival in Pancreatic Cancer: A Meta-Analysis. *Med (Baltimore)* (2020) 99(23):e20595. doi: 10.1097/md.0000000000020595
34. Xie Q, Wang L, Zheng S. Prognostic and Clinicopathological Significance of C-Reactive Protein to Albumin Ratio in Patients With Pancreatic Cancer: A Meta-Analysis. *Dose Response Publ Int Hormesis Soc* (2020) 18 (2):1559325820931290. doi: 10.1177/1559325820931290
35. Fang E, Wang X, Feng J, Zhao X. The Prognostic Role of Glasgow Prognostic Score and C-Reactive Protein to Albumin Ratio for Sarcoma: A System Review and Meta-Analysis. *Dis Markers* (2020) 2020:8736509. doi: 10.1155/2020/8736509
36. Zhou W, Zhang GL. C-Reactive Protein to Albumin Ratio Predicts the Outcome in Renal Cell Carcinoma: A Meta-Analysis. *PLoS One* (2019) 14 (10):e0224266. doi: 10.1371/journal.pone.0224266

**Conflict of Interest:** The authors declare that the research was conducted in the absence of any commercial or financial relationships that could be construed as a potential conflict of interest.

frontiers in Oncology

ORIGINAL RESEARCH
published: 13 December 2021
doi: 10.3389/fonc.2021.749144

# Splicing Factor DDX23, Transcriptionally Activated by E2F1, Promotes Ovarian Cancer Progression by Regulating FOXM1

*Chen Zhao*[1,2], *Yingwei Li*[1,2], *Chunping Qiu*[1,2], *Jingying Chen*[1,2], *Huan Wu*[1,2], *Qiuman Wang*[1,2], *Xinyue Ma*[1,2], *Kun Song*[1,2]* *and Beihua Kong*[1,2]*

[1] *Department of Obstetrics and Gynecology, Qilu Hospital, Cheeloo College of Medicine, Shandong University, Jinan, China,*
[2] *Gynecology Oncology Key Laboratory, Qilu Hospital, Shandong University, Jinan, China*

**Edited by:**
*Xia Bai Rong,*
*Anhui Provincial Hospital, China*

**Reviewed by:**
*Yuliang Wu,*
*University of Saskatchewan, Canada*
*Hui Xing,*
*Xiangyang Central Hospital, China*

***Correspondence:**
*Beihua Kong*
*kongbeihua@sdu.edu.cn*
*Kun Song*
*songkun2001226@sdu.edu.cn*

**Specialty section:**
*This article was submitted to*
*Gynecological Oncology,*
*a section of the journal*
*Frontiers in Oncology*

**Received:** 29 July 2021
**Accepted:** 23 November 2021
**Published:** 13 December 2021

**Citation:**
*Zhao C, Li Y, Qiu C, Chen J, Wu H, Wang Q, Ma X, Song K and Kong B (2021) Splicing Factor DDX23, Transcriptionally Activated by E2F1, Promotes Ovarian Cancer Progression by Regulating FOXM1. Front. Oncol. 11:749144. doi: 10.3389/fonc.2021.749144*

Ovarian carcinoma remains the most lethal gynecological carcinoma. Abnormal expression of splicing factors is closely related to the occurrence and development of tumors. The DEAD-box RNA helicases are important members of the splicing factor family. However, their role in the occurrence and progression of ovarian cancer is still unclear. In this study, we identified DEAD-box helicase 23 (DDX23) as a key DEAD-box RNA helicase in ovarian cancer using bioinformatics methods. We determined that DDX23 was upregulated in ovarian cancer and its high expression predicted poor prognosis. Functional assays indicated that DDX23 silencing significantly impeded cell proliferation/invasion *in vitro* and tumor growth *in vivo*. Mechanistically, transcriptomic analysis showed that DDX23 was involved in mRNA processing in ovarian cancer cells. Specifically, DDX23 regulated the mRNA processing of FOXM1. DDX23 silencing reduced the production of FOXM1C, the major oncogenic transcript of FOXM1 in ovarian cancer, thereby decreasing the FOXM1 protein expression and attenuating the malignant progression of ovarian cancer. Rescue assays indicated that FOXM1 was a key executor in DDX23-induced malignant phenotype of ovarian cancer. Furthermore, we confirmed that DDX23 was transcriptionally activated by the transcription factor (TF) E2F1 in ovarian cancer using luciferase reporter assays and chromatin immunoprecipitation (ChIP) assays. In conclusion, our study demonstrates that high DDX23 expression is involved in malignant behavior of ovarian cancer and DDX23 may become a potential target for precision therapy of ovarian cancer.

**Keywords: ovarian cancer, DDX23, proliferation, invasion, FOXM1, mRNA processing**

## INTRODUCTION

According to statistics from the American Cancer Society (ACS), ovarian cancer is the most lethal gynecological malignancy, ranking fifth among the mortality rates of female cancers (1). Globally, the five-year relative survival rate is generally between 30% and 40% (2). High-grade serous ovarian carcinoma (HGSOC) has the highest incidence and aggressiveness of all subtypes, and accounts for 70-80% of ovarian cancer deaths (3, 4). Current first-line treatments for ovarian cancer include both surgery and systemic treatment. The application of antiangiogenic agents and poly ADP-ribose polymerase (PARP) inhibitors has produced beneficial therapeutic effects for ovarian cancer patients (5, 6). Despite the continued progress in diagnosis and treatment technologies, some patients still relapse in a short time. Therefore, further research is needed to gain new insights into the pathogenesis of ovarian cancer.

mRNA splicing is ubiquitous in human genes. Specifically, the spliceosome removes introns to produce different mature mRNAs, which contribute to the expansion of genomic coding capacity and proteomic diversity (7, 8). Emerging data suggest that aberrant splicing or abnormal expression of splicing factors is associated with cancer progression and cancer immune disorders (9, 10). Many studies have shown that aberrant mRNA splicing is involved in key processes of ovarian cancer development. For example, splicing factor SFPQ participates in *caspase-9* alternative splicing and its overexpression is correlated with platinum resistance (11). Splicing factor SRp20 knockdown impairs growth and malignancy of ovarian cancer cells (12). We have previously shown that splicing factor USP39 and CTNNBL1 were overexpressed in HGSOC and predicted poor clinical outcomes (13, 14).

The RNA helicase family is an important part of splicing factors (15). Members of the DEAD-box RNA helicase family, with conserved sequence Asp-Glu-Ala-Asp (D-E-A-D), play important roles in various aspects of RNA processing, from transcription to RNA decay (16). Therefore, they are given crucial function in tumorigenesis and tumor development. A study has shown that DDX5 is amplified and associated with breast cancer proliferation (17). In addition, DDX39B is overexpressed in colorectal cancer (CRC) and enhances the migration and invasion of CRC cells (18). DDX23 belongs to DEAD-box family of RNA helicases and plays a crucial role in spliceosome formation and pre-mRNA splicing (15). Missense alterations in DDX23 have been reported to be associated with a syndrome characterized by atypical neurodevelopment (19). Abnormal DDX23 expression has been implicated in glioma progression and poor survival (20). However, the specific role of DDX23 in ovarian cancer is less studied.

In this study, DDX23 was first identified as a key DEAD-box RNA helicase in ovarian cancer, and its overexpression was associated with poor clinical outcomes. Functional assays indicated that DDX23 silencing significantly impeded cell proliferation/invasion *in vitro* and tumor growth *in vivo*. Mechanistically, DDX23 regulated the mRNA processing of FOXM1 and DDX23 silencing reduced the production of FOXM1C. FOXM1 was a key executor in DDX23-induced malignant phenotype of ovarian cancer. Moreover, DDX23 was transcriptionally activated by the E2F1 in ovarian cancer. Taken together, this study demonstrates the clinical and biological significance of DDX23 in ovarian cancer and provides a new target for tumor precision therapy.

## MATERIALS AND METHODS

### Bioinformatics Analysis

The genes involved in mRNA splicing (major pathway) were obtained from GeneCards (https://pathcards.genecards.org/card/mrna_splicing_-_major_pathway) (21). The protein expression data were obtained from the clinical proteomic tumor analysis consortium (CPTAC) (https://cptac-data-portal.georgetown.edu/studies) (22). The Cancer Genome Atlas (TCGA) ovarian cancer data (AffyU133a, n = 593) were obtained from UCSC Xena (http://xena.ucsc.edu/) (23). Survival curves were plotted by Kaplan-Meier plotter (https://kmplot.com/analysis/) (24). Co-expression analysis was performed on cbioportal (https://www.cbioportal.org/) (25). JASPAR (http://jaspar.genereg.net/) (26) and Cistrome Cancer (http://cistrome.org/CistromeCancer/) (27) were used to predict potential TFs. Visualization and analysis of TFs binding peaks were performed with the use of Cistrome Data Browser (http://cistrome.org/db/#/) (28) based on the online chromatin immunoprecipitation sequencing (ChIP-seq) data. Gene Ontology (GO) analysis was conducted on WebGestalt (http://www.webgestalt.org/) (29). The TCGA differential expression gene (DEG) list of ovarian cancer was obtained from Gene Expression Profiling Interactive Analysis (GEPIA) (http://gepia.cancer-pku.cn/) (30).

### Tissue Samples and Clinical Information

Ovarian cancer specimens were obtained from primary patients without neoadjuvant chemotherapy. Fallopian tube (FT) specimens from patients with benign diseases were used as controls. The 46 fresh-frozen ovarian cancer tissues and 29 FT tissues were obtained for quantitative real-time PCR (qRT-PCR) analysis. A total of 124 ovarian cancer and 69 FT specimens from our center were used for clinical information analysis. Patients' informed consent were provided. The study had been approved by the Ethics Committee of Shandong University.

### Immunohistochemistry Staining

The fresh tissues were formalin fixed and paraffin embedded. An immunohistochemistry (IHC) staining kit (ZSGB-BIO, China) was used for staining of tissue microarray (TMA) sections or xenografts tissue sections following the manufacturer's instructions. Paraffin sections were deparaffined with xylene and rehydrated with ethanol. After antigen retrieval, 3% hydrogen peroxide and goat serum were used to block the endogenous peroxidase and nonspecific binding respectively. Tissue sections were incubated with primary antibodies anti-DDX23 (ab70459, Abcam) and anti-Ki-67 (#9449, CST) at 4°C overnight. The next day, tissue was labeled with secondary antibody and detected using the diaminobenzidine (DAB) staining system.

Two pathologists completed the IHC staining score independently. The intensity of staining was scored as 0 (negative), 1 (weak), 2 (moderate), or 3 (strong). The final H-score (0-300) was determined by the extent and intensity of staining (H-score = percentage of weak intensity area×1+ percentage of moderate intensity area×2+ percentage of strong intensity area×3). The specimens were divided into high expression group (final score $< 170$) and low expression group (final score $\geq 170$).

### RNA Isolation and qRT-PCR

TRIzol reagent (Invitrogen, USA) was used for total RNA extraction. PrimeScript RT Reagent Kit (Takara, Japan) and

SYBR-Green qPCR master mix (Takara, Japan) were used for RNA reverse transcription and qRT-PCR respectively. ACTB served as an internal control. The primers used are listed in **Supplementary Table 1**.

## Cell Lines and Cell Culture

A2780 and SKOV3 were cultured in RPMI 1640 medium plus 10% fetal bovine serum (FBS) (BioInd, Israel). HEY and HEK293T were cultured in DMEM medium plus 10% FBS. Cells were cultured in standard conditions (37°C, 5% CO2) in a humidified incubator.

## Plasmid Constructs and Cell Transfection

The shDDX23 sequence was cloned into pLKO.1 vector (Addgene, United States). The open reading frames (ORFs) of E2F1 and FOXM1 were cloned into pLenti-C-Myc-DDK-IRES-Puro (PCMV) vector (Origene, USA) separately. The psPAX2, pMD2.G and constructed lentivirus vectors were co-transfected into HEK293T cells for lentivirus production. To gain stable-expression, ovarian cancer cells were infected with lentivirus for 24 hours and selected for 7 days in a medium including puromycin (2 μg/mL, Merck Millipore, USA).

The small interfering RNAs (siRNAs) targeting DDX23, E2F1, FOXM1 were obtained from GenePharma (Shanghai, China). Transient transfection was carried out by Lipofectamine 2000 reagent (Invitrogen, USA) following the manufacturer's instructions. Details of shRNA or siRNA sequences are shown in **Supplementary Table 1**.

## Cell Proliferation Assay

The 3-(4, 5)-dimethylthiahiazo(-z-y1)-3,5-di-phenytetrazoliumromide (MTT) assay was conducted to measure cell proliferation ability. Cells (800–1000 cells/well) were seeded in 96-well plates, then incubated and monitored continuously. At a fixed time point of each day, 20 μL 5 mg/mL of MTT (Sigma-Aldrich, USA) solution was added to each well. After 4 hours of incubation, the supernatant was replaced by 100 μL DMSO (Sangon Biotech, China). The absorbance value at 490nm was quantified by a microplate reader (Bio-Rad, USA).

## Clonogenic Assay

Cells (800–1000 cells/well) were cultured in 6-well plates under standard condition for 2 weeks. Methanol was applied for colony fixation and 0.1% crystal violet was applied for staining. Colonies containing more than 50 cells were included in statistical analysis.

## Cell Cycle Assay

Flow cytometry was used to analyze cell cycle progression. Each group of ovarian cancer cells was harvested and stained with propidium iodide (PI) according to the manufacturer's protocol (MultiSciences, China). The cell cycle distribution was analyzed by A Modifit LT software (BD Biosciences, USA).

## Western Blotting

RIPA Lysis Buffer (Beyotime, China), supplemented with 1% PMSF, was used for cell lysis. A BCA Assay Kit (Millipore, USA) was used to quantify the protein concentration. Protein samples were separated by SDS-PAGE and transferred to PVDF membranes (Millipore, USA), and then blocked in 5% skimmed milk for 1 hour. The membranes were incubated in diluted primary antibodies at 4°C overnight. The target proteins were labeled with HRP-conjugated secondary antibodies and detected with an ECL system (PerkinElmer, USA). β-actin was used as an endogenous control. All antibodies are listed in **Supplementary Table 2**.

## Cell Migration and Invasion Assays

Cells ($1\times10^5$) suspended in 200 μL serum-free medium were seeded into the upper Transwell chambers (8μm pores, BD Biosciences, USA). The lower compartments contained 700 μL medium with 20% FBS. Methanol was applied for cell fixation and 0.1% crystal violet was applied for staining. Cells that penetrated through the chambers were counted under a light microscope.

Cell motility ability was also evaluated by wound healing assays. Ovarian cancer cells were cultured in 24-well plates for appropriate time. Then straight scratches were produced on the confluent cell monolayer with 20 μL pipette tips. The scratch width was measured at appropriate time points (0 h, 12 h) after scratching.

## Nude Mouse Xenograft Models

Female BALB/c nude mice (aged 4–5 weeks, NBRI of Nanjing University, China) were randomly divided into two groups and injected subcutaneously with DDX23 knockdown or control cells (HEY, $5\times10^6$). Mice were kept in the SFP environment before they were euthanized. Then tumors were harvested and weighed. Animal experiments were approved by Shandong University Animal Care and Use Committee.

## Luciferase Reporter Assay

HEK293T cells were co-transfected with DDX23 wild-type (WT) or mutant-type (MT) (Deletion mutation) promoter reporter vectors, PCMV-NC or PCMV-E2F1 and pRL-TK plasmids using Lipofectamine 2000. After 48 hours of transfection, the luciferase activity was tested by Dual-Glo Luciferase Assay System (Promega, USA). The relative luciferase activity was determined by the ratio of firefly luminescence to Renilla luminescence.

## Chromatin Immunoprecipitation Assay

A Chromatin immunoprecipitation kit (Beyotime, China) was used for ChIP assay as previously described (13). E2F1 antibody and IgG rabbit antibody were obtained from Cell Signaling Technology (CST, USA) (**Supplementary Table 2**). Reverse transcription PCR was performed to analyze the purified DNA. The primer sequences for DDX23 promoter are listed in **Supplementary Table 1**.

## RNA Sequencing and Differential Gene Expression Analysis

Total RNA was extracted from A2780 cells of DDX23 knockdown and control group with Trizol reagent. Then high-throughput RNA sequencing (RNA-seq) assay was performed by the Biomaker Technologies (Beijing, China). The threshold for different expression was set to 1.5-fold change (FC) and $P < 0.05$ was the significance threshold.

## Statistical Analysis

SPSS statistics 24.0 and GraphPad Prism 8.0 were used in data analysis. The chi-square test and student's t test were used to analyze statistically significant differences between groups. Univariate and multivariate Cox proportional hazard regression analysis was used to analyze high-risk factors related to overall survival (OS). The survival curves of independent high-risk factors were plotted using Kaplan-Meier analysis. The data of three independent experiments were presented as the means ± SEMs. $P < 0.05$ was considered statistically significant.

# RESULTS

## DDX23 Was Upregulated in Ovarian Cancer and Associated With Poor Clinical Outcomes

To clarify the importance of DEAD-box RNA helicases involved in mRNA processing, we screened 8 candidates of 322 genes related to mRNA splicing (Major Pathway) from the GeneCards online database. Based on CPTAC proteomic data, we found that all 8 genes were upregulated in ovarian cancer (**Figure 1A**). Meanwhile, according to previous transcriptome analysis results, 33 upregulated core splicing factors, including DDX23, were found in HGSOCs (n=6) compared with FT tissues (n=6) (GSE135886) (13). Combined data mining with previous transcriptome analysis results, DDX23 was selected for further investigation. We first investigated its protein expression patterns in various cancer types using CPTAC database. Specifically, DDX23 expression was found to be elevated in multiple tumor types including ovarian cancer ($P < 0.0001$) (**Figures 1B, C**). We further analyzed data of TCGA cohort and found a significantly higher mRNA level of DDX23 in ovarian cancer samples (n = 585) compared with normal ovary samples (n = 8) ($P < 0.01$) (**Figure 1D**). Similarly, we detected the DDX23 mRNA expression in our cohort by qRT-PCR and found that DDX23 had higher expression in ovarian cancer samples (n = 46) than in FT specimens (n = 29) ($P < 0.001$) (**Figure 1E**).

To further explore the relationship between the expression of DDX23 and the clinicopathological characteristics of ovarian cancer patients, IHC analysis was performed using TMAs containing 124 ovarian cancer and 69 FT specimens. Results showed that 14.5% (10/69) FT samples had high DDX23 expression, whereas 33.9% (42/124) ovarian cancer samples belonged to high DDX23 group. Compared with FT specimens, IHC staining revealed significantly higher DDX23 expression in ovarian cancer specimens ($P < 0.01$) (**Figures 1F, G**). Clinicopathological feature analysis indicated that high DDX23 expression was positively correlated with poor OS (P = 0.037) (**Table 1**). In addition, univariate and multivariate Cox proportional hazard regression analysis indicated that DDX23 expression was an independent high-risk factor for OS (hazard ratio [HR] 1.58, 95% confidence interval [CI] 1.05–2.37, P = 0.029), besides FIGO stage (HR 2.00, 95% CI 1.19–3.37, P = 0.009) (**Table 2**). We further performed Kaplan-Meier survival analysis in our cohort, and confirmed that patients in the high DDX23 expression group had a shorter OS than those in the low expression group (HR 1.56, 95% CI 1.04–2.34, P = 0.031) (**Figure 1H**). Meanwhile, based on the online data of the Kaplan-Meier plotter, we also verified that patients with high DDX23 expression had significantly worse progression-free survival (PFS) (HR 1.32, 95% CI 1.15–1.52, P = 5.7e-0.5) and OS (HR 1.16, 95% CI 1.01–1.33, P = 0.038) rates than patients with low expression (**Figures 1I, J**). Taken together, these results strongly indicated that DDX23 was highly expressed in ovarian cancer tissues and was significantly associated with poor prognosis in ovarian cancer patients.

## DDX23 Was Required for the Proliferation and Cell Cycle Progression of Ovarian Cancer Cells

Given that DDX23 was upregulated in ovarian cancer, we then explored the role of DDX23 in the proliferation of ovarian cancer cells. First, DDX23 knockdown ovarian cell lines were established by lentiviral infection. In MTT assays, compared to the negative control (NC) groups, DDX23 silencing inhibited the growth of A2780, SKOV3, and HEY cells and the inhibition was most evident in the last two days (**Figure 2A**). Similarly, in clonogenic assays, DDX23 knockdown reduced the colony formation ability of A2780, SKOV3, and HEY cells by 60% ($P < 0.001$), 55% ($P < 0.001$), and 40% ($P < 0.01$) respectively (**Figure 2B**). To further investigate the effect of DDX23 on cell cycle progression, flow cytometry was conducted. Cell cycle analysis revealed that compared to NC group, DDX23 silencing could increase the percentage of cells in the G1 phase while decreasing the percentage of cells in S phase in three ovarian cancer cell lines (**Figure 2C**). Furthermore, we measured G1 phase arrest related markers by western blotting and the results showed that DDX23 knockdown decreased the expression of CCND1 and CDK4, but increased p21 expression (**Figure 2D**).

Overall, these data suggested that DDX23 was required for ovarian cancer cell proliferation, and DDX23 knockdown inhibited cell proliferation through G1 phase arrest.

## DDX23 Silencing Suppressed the Migration and Invasion of Ovarian Cancer Cells

Transwell assays were carried out to detect the effect of DDX23 on the migration and invasion of ovarian cancer cells. Compared to the NC group, DDX23 knockdown could weaken the migration (all $P < 0.01$) and invasion (all $P < 0.0001$) capacity in A2780, SKOV3, and HEY cells (**Figures 3A, B**). In wound healing assays, at 12h post-scratch, ovarian cancer cells with DDX23 knockdown migrated less than NC group in A2780, SKOV3, and HEY cells (all $P < 0.0001$) (**Figure 3C**). These experimental results collectively suggested that DDX23 could promote the migration and invasion ability of ovarian cancer cells.

## DDX23 Knockdown Inhibited the Growth of Xenograft Tumors *in Vivo*

Since the effect of DDX23 on the progression of ovarian cancer was determined *in vitro*, we further constructed nude mouse

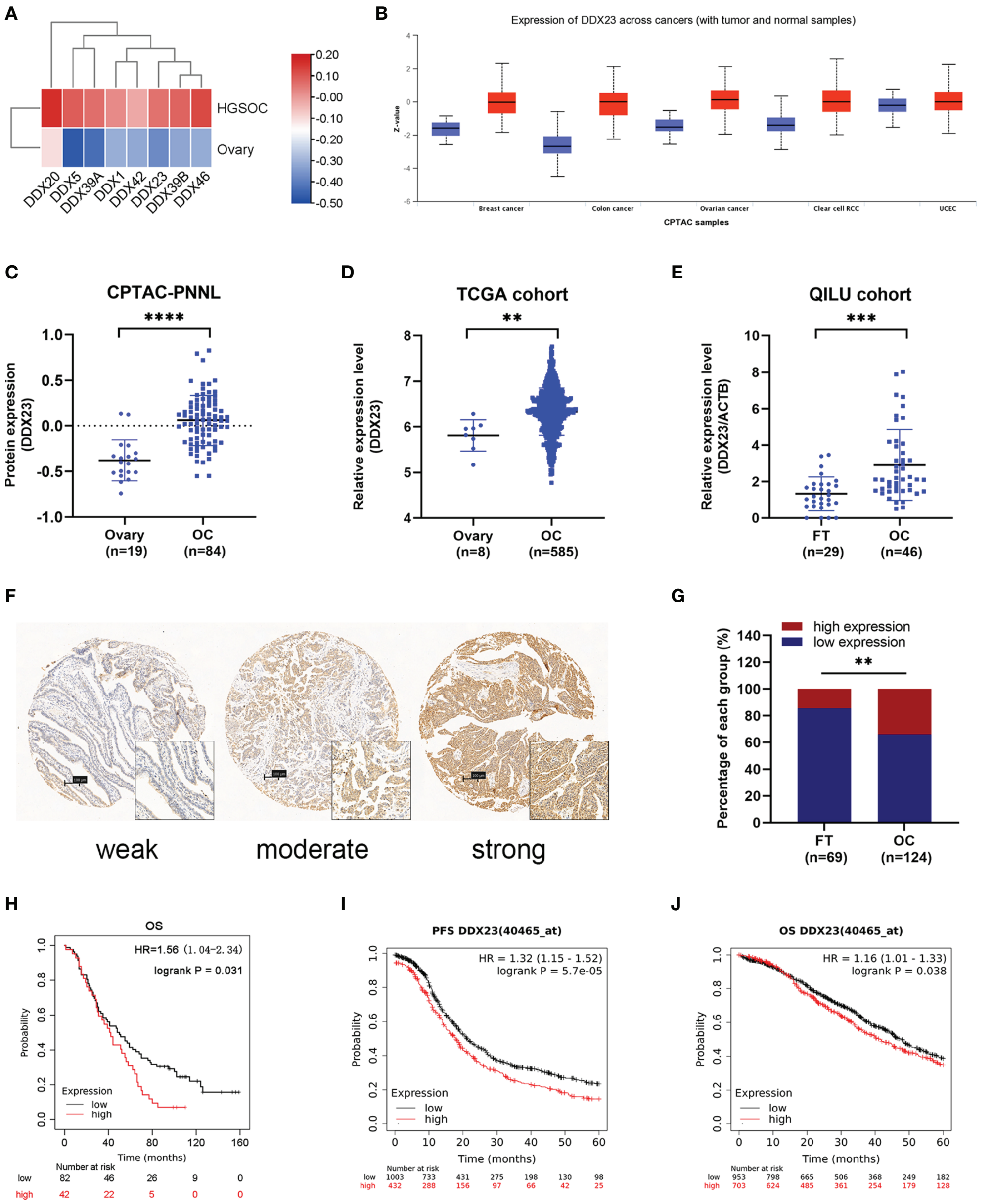

**FIGURE 1** | DDX23 was upregulated in ovarian cancer and associated with poor clinical outcomes. **(A)** Heatmap map reflecting the expression of 8 DEAD-box RNA helicases involved in the mRNA splicing in HGSOC and normal ovary samples based on CPTAC proteomic data. **(B)** DDX23 protein expression profile in various cancers based on CPTAC proteomic data. **(C)** DDX23 protein expression in ovarian cancer and normal ovary samples in CPTAC-PNNL cohort. **(D)** DDX23 mRNA expression in ovarian cancer and normal ovary samples in a TCGA cohort (AffyU133a, n = 593). **(E)** qRT-PCR analysis of DDX23 mRNA expression in 46 HGSOC and 29 FT tissue samples in Qilu cohort. **(F)** Representative IHC staining images of DDX23 in FT and ovarian cancer tissues based on TMAs. **(G)** Statistical analysis of the DDX23 expression profile in 69 FT and 124 ovarian cancer tissues based on IHC staining score of TMAs. **(H)** Kaplan-Meier analysis of the correlation between DDX23 expression and OS based on the follow-up information from our TMAs. **(I, J)** Kaplan-Meier analysis of PFS **(I)** and OS **(J)** in ovarian cancer patients with high- or low- DDX23 expression based on data from Kaplan-Meier Plotter. HGSOC, high-grade serous ovarian carcinoma; CPTAC, clinical proteomic tumor analysis consortium; PNNL, Pacific Northwest National Laboratory; TCGA, The Cancer Genome Atlas; FT, fallopian tube; IHC, immunohistochemistry; TMAs, tissue microarrays; OS, overall survival; PFS, progression-free survival. $^{**}P < 0.01$, $^{***}P < 0.001$, $^{****}P < 0.0001$.

xenograft models to explore the role of DDX23 in ovarian cancer tumorigenesis *in vivo*. HEY cells with DDX23 knockdown and the control cells were subcutaneously injected into two groups of nude mice (n=5). As expected, DDX23 silencing could apparently inhibit the growth of xenograft tumors (**Figure 4A**). The tumor weights of NC group were significantly higher than those of DDX23 knockdown group ($P < 0.05$) (**Figure 4B**). The protein expression level in xenograft tumors was also measured

**TABLE 1 |** Correlation of clinical characteristics with DDX23 expression.

| Clinical characteristics | | DDX23 expression | | | *P* value |
|---|---|---|---|---|---|
| | | Total (n = 124) | Low expression (n = 82) | High expression (n = 42) | |
| **Age (years)** | <56 | 55 (44.4) | 37 (45.1) | 18 (42.9) | 0.810 |
| | ≥56 | 69 (55.6) | 45 (54.9) | 24 (57.1) | |
| **FIGO stage (2014)** | I and II | 26 (21.0) | 17 (20.7) | 9 (21.4) | 0.928 |
| | II and III | 98 (79.0) | 65 (79.3) | 33 (78.6) | |
| **Histology** | HGSOC | 103 (83.1) | 68 (82.9) | 35 (83.3) | 0.404 |
| | Non-HGSOC | 8 (6.5) | 6 (7.3) | 2 (4.8) | |
| | Unknown | 13 (10.5) | 8 (9.8) | 5 (11.9) | |
| **Grade** | II (moderately) | 8 (6.5) | 6 (7.3) | 2 (4.8) | 0.859 |
| | III (poorly) | 110 (88.7) | 72 (87.8) | 38 (90.5) | |
| | Unknown | 6 (4.8) | 4 (4.9) | 2 (4.8) | |
| **Ascites** | Yes | 23 (18.5) | 14 (17.1) | 9 (21.4) | 0.706 |
| | No | 7 (5.6) | 4 (4.9) | 3 (7.1) | |
| | Unknown | 94 (75.8) | 64 (78.0) | 30 (71.4) | |
| **CA-125 (U/mL)** | <785 | 58 (46.8) | 36 (43.9) | 22 (52.4) | 0.371 |
| | ≥785 | 66 (53.2) | 46 (56.1) | 20 (47.6) | |
| **Tumor diameter (cm)** | <8 | 37 (29.8) | 27 (32.9) | 10 (23.8) | 0.294 |
| | ≥8 | 87 (70.2) | 55 (67.1) | 32 (76.2) | |
| **Residual disease (cm)** | <1 | 51 (41.1) | 38 (46.3) | 13 (31.0) | 0.099 |
| | ≥1 | 73 (58.9) | 44 (53.7) | 29 (69.0) | |
| **Adjuvant chemotherapy** | Yes | 122 (98.4) | 81 (98.8) | 41 (97.6) | 1.000 |
| | No | 2 (1.6) | 1 (1.2) | 1 (2.4) | |
| **Death** | Yes | 103 (83.1) | 64 (78.0) | 39 (92.9) | **0.037** |
| | No | 21 (16.9) | 18 (22.0) | 3 (7.1) | |
| **Follow-up time (month)** | | 45.5 (1-159) | 49 (1-159) | 41.5 (1-110) | 0.166 |

*Values are present as n (%) or median (range). DDX23, DEAD-Box Helicase 23; FIGO, International Federation of Gynecology and Obstetrics; HGSOC, high-grade serous ovarian carcinoma; CA-125, Cancer Antigen 125.*

**TABLE 2 |** Univariate and multivariate Cox proportional hazards regression analysis of OS.

| Clinical characteristics | | Univariate | | Multivariate | |
|---|---|---|---|---|---|
| | | HR (95%CI) | *P* value | HR (95%CI) | *P* value |
| **DDX23 expression** | Low | 1 | 0.034 | 1 | 0.029 |
| | High | 1.56 (1.04-2.34) | | 1.58 (1.05-2.37) | |
| **Age (years)** | <56 | 1 | 0.616 | | |
| | ≥56 | 1.01 (0.99-1.03) | | | |
| **FIGO stage (2014)** | I and II | 1 | 0.010 | 1 | 0.009 |
| | II and III | 1.98 (1.17-3.34) | | 2.00 (1.19-3.37) | |
| **Histology** | HGSOC | 1 | | | |
| | Non-HGSOC | 1.14 (0.53-2.47) | 0.736 | | |
| | Unknown | 1.49 (0.81-2.74) | 0.196 | | |
| **Grade** | II (moderately) | 0.75 (0.25-2.25) | 0.609 | | |
| | III (poorly) | 0.67 (0.29-1.55) | 0.349 | | |
| | Unknown | 1 | | | |
| **Ascites** | Yes | 0.90 (0.56-1.46) | 0.681 | | |
| | No | 0.46 (0.16-1.34) | 0.153 | | |
| | Unknown | 1 | | | |
| **CA-125 (U/mL)** | <785 | 1 | 0.242 | | |
| | ≥785 | 1.26 (0.86-1.86) | | | |
| **Tumor diameter (cm)** | <8 | 1 | 0.924 | | |
| | ≥8 | 0.98 (0.65-1.49) | | | |
| **Residual disease (cm)** | <1 | 1 | 0.008 | | |
| | ≥1 | 1.73 (1.15-2.59) | | | |
| **Adjuvant chemotherapy** | Yes | 0.92 (0.23-3.73) | 0.903 | | |
| | No | 1 | | | |

*OS, overall survival; DDX23, DEAD-Box Helicase 23; FIGO, International Federation of Gynecology and Obstetrics; CA-125, Cancer Antigen 125.*

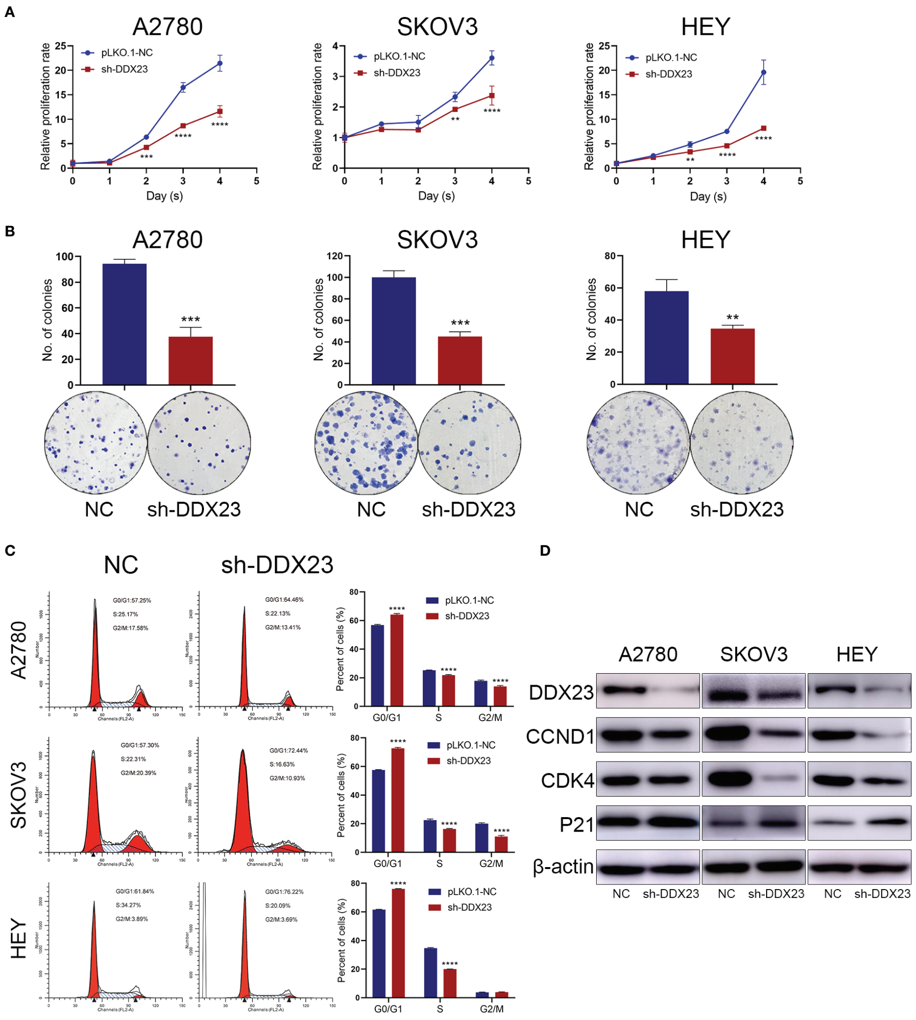

**FIGURE 2** | DDX23 was required for the proliferation and cell cycle progression of ovarian cancer cells. **(A, B)** Representative MTT proliferation **(A)** and clonogenic **(B)** assays in A2780, SKOV3 and HEY cells with or without DDX23 knockdown. **(C)** Cell cycle analysis of A2780, SKOV3, and HEY cells with or without DDX23 knockdown was performed by flow cytometry (left). Graphs depict the distribution of cells in indicated phases of the cell cycle (right). **(D)** Western blotting analysis of cell cycle regulatory proteins in A2780, SKOV3, and HEY cells transfected with sh-NC or sh-DDX23. Data are presented as mean ± SEM. $^{**}P < 0.01$, $^{***}P < 0.001$, $^{****}P < 0.0001$.

to confirm that DDX23 was effectively depleted in the shDDX23 group ($P < 0.01$) (**Figure 4C**). IHC staining showed that Ki-67 expression was decreased in xenograft tumors of shDDX23-treated mice group, indicating that DDX23 knockdown reduced the proliferation activity of tumor cells *in vivo* (**Figure 4D**).

## E2F1 Activated DDX23 Transcription in Ovarian Cancer Cells

Dysregulation of TFs is associated with tumor progression. To explore the transcriptional regulatory mechanism of DDX23 expression, we performed co-expression analysis using cBioPortal database to obtain the genes positively related to DDX23 expression (TCGA U133 microarray, Spearman's Correlation ≥ 0.35) (**Supplementary Table 3**). We also analyzed the TFs predicted to bind to the promoter of DDX23 from Cistrome Data Browser (**Supplementary Table 4**). Subsequently, 5 candidate TFs were screened by determining the intersection of the above two gene sets (**Figure 5A**). The differential expression analysis of the 5 TFs were performed using TCGA-GTEx data, and the results showed that the expression of E2F1 in ovarian cancer increased most significantly compared to the other 4 TFs (**Supplementary Figure S1**). Co-expression analysis revealed that the mRNA expression of E2F1 and DDX23 were positively correlated in ovarian cancer (Spearman's correlation = 0.38, $P$ = 1.34e-7) (**Figure 5B**). To determine whether E2F1 was involved in the regulation of DDX23 transcription, we first detected the expression of DDX23 in E2F1 knockdown and control ovarian cancer cells. We noted that the inhibition of E2F1 by siRNA decreased the expression of DDX23 at both mRNA and protein

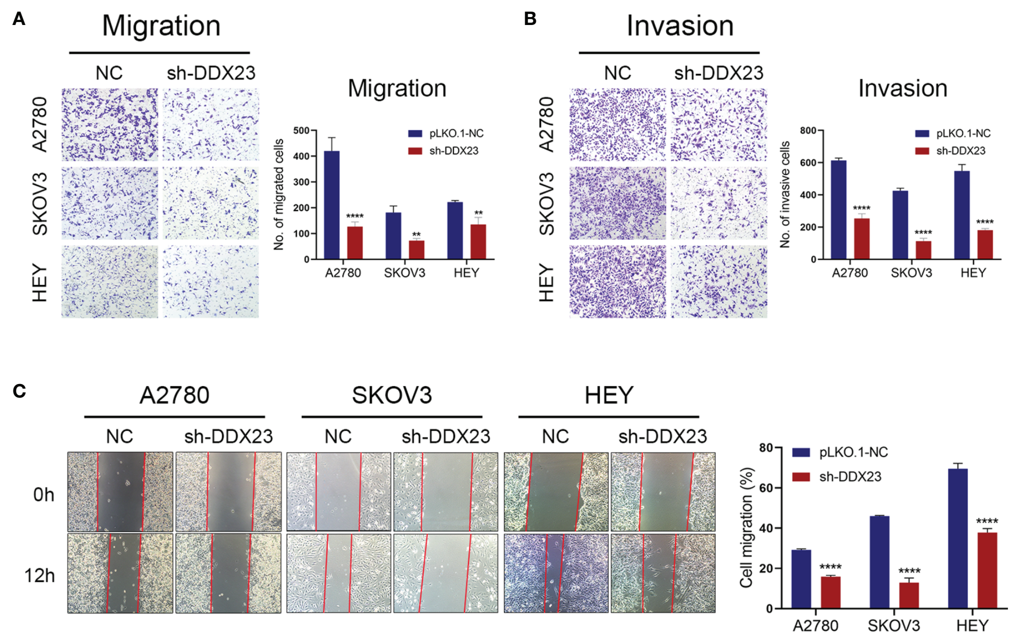

**FIGURE 3** | DDX23 silencing suppressed the migration and invasion of ovarian cancer cells. **(A, B)** Representative microscopic images (×10) of A2780, SKOV3, and HEY cells that penetrated through the Transwell chambers in migration **(A)** and invasion **(B)** assays. **(C)** Representative wound healing assays in A2780, SKOV3, and HEY cells with or without DDX23 knockdown. Data are presented as mean ± SEM. $^{**}P < 0.01$, $^{****}P < 0.0001$.

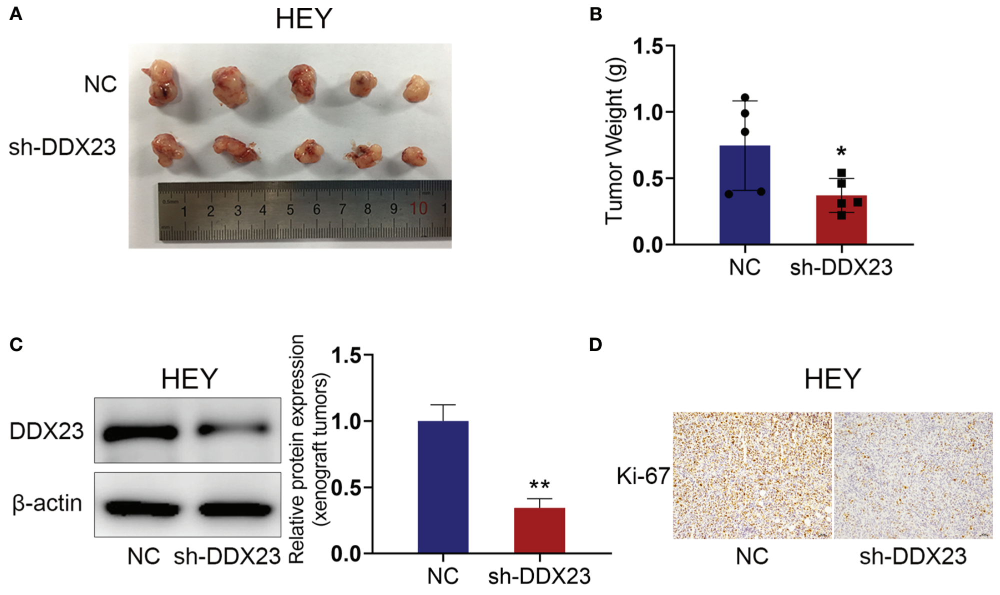

**FIGURE 4** | DDX23 knockdown inhibited the growth of xenograft tumors *in vivo*. **(A)** Images of xenograft tumors from mice subcutaneously injected with DDX23 knockdown or control HEY cells (n = 5 mice per group). **(B)** The xenografts tumors were weighed and compared. ***(C)*** Western blotting analysis of protein samples extracted from xenografts tumors in DDX23 knockdown or corresponding control group. **(D)** Representative IHC staining patterns of Ki-67 in xenografts tumors in DDX23 knockdown or corresponding control group. IHC, immunohistochemistry. Data are presented as mean ± SEM. $^{*}P < 0.05$, $^{**}P < 0.01$.

levels (**Figures 5C, D**). Meanwhile, we found that DDX23 knockdown had no effect on E2F1 expression at both mRNA and protein levels in three ovarian cancer cell lines (**Supplementary Figures S2A, B**).

According to the ChIP-seq data from the Cistrome Data Browser database, we found that the binding peaks of E2F1 were enriched in the promoter region of DDX23 in HELA, MCF-7, U2OS, and K652 cell lines (**Figure 5E**). We next searched the

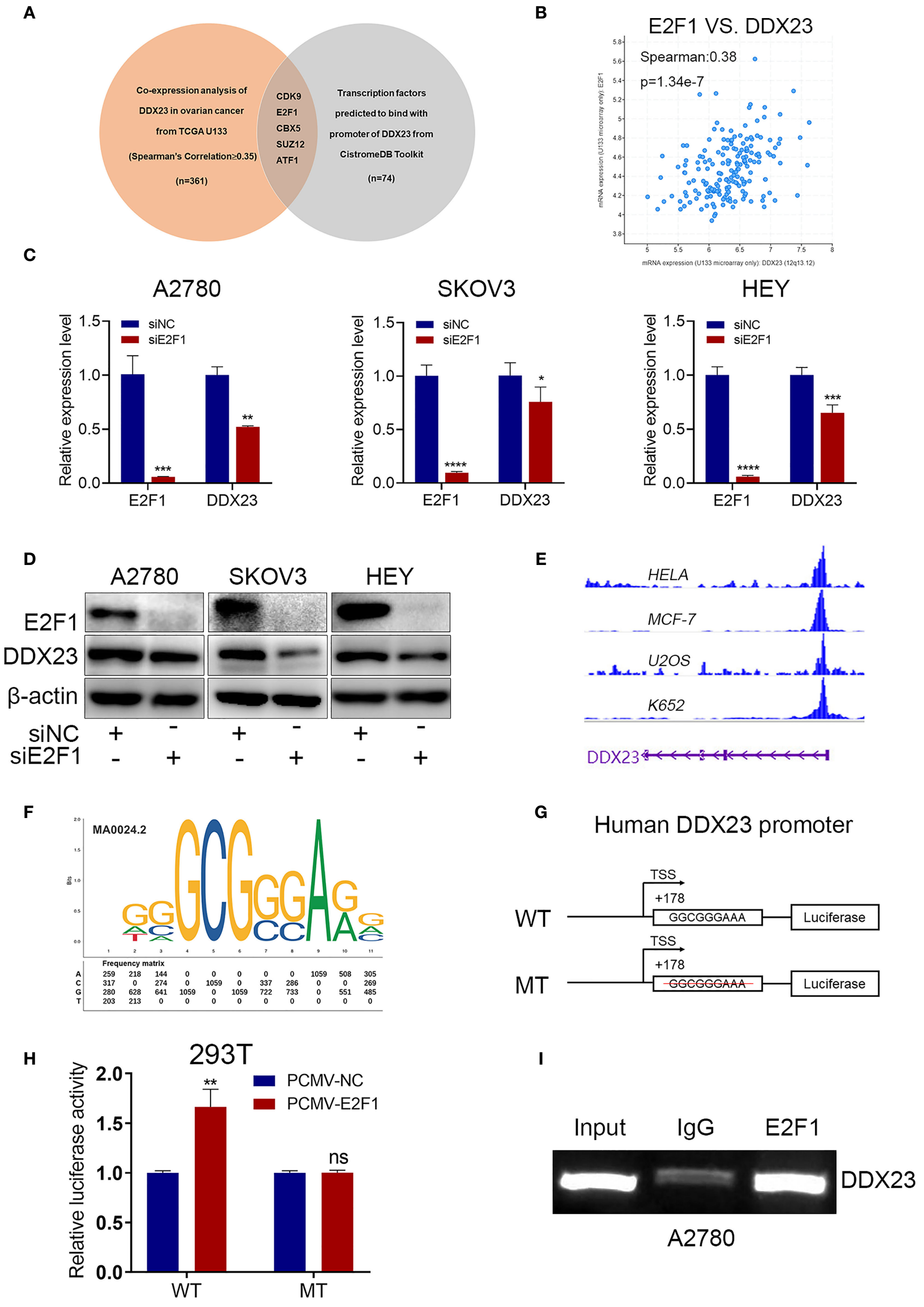

**FIGURE 5** | E2F1 activated DDX23 transcription in ovarian cancer cells. **(A)** Venn diagram of 5 hub TFs positively related to DDX23 expression (TCGA U133 microarray, Spearman's Correlation ≥ 0.35) and predicted to bind with the promoter of DDX23. **(B)** Co-expression analysis between DDX23 and E2F1 expression in ovarian cancer based on the cBioPortal database. **(C, D)** The mRNA and protein levels of E2F1 and DDX23 in ovarian cancer cells with or without E2F1 knockdown were measured by qRT-PCR **(C)** and Western blotting **(D)**. **(E)** Visualization of E2F1 binding peaks. The binding peaks of E2F1 were enriched in the promoter region of DDX23 in HELA, MCF-7, U2OS, and K652 cell lines based on ChIP-seq data from the Cistrome Data Brower. **(F)** The sequence logo of a potential E2F1 binding site on DDX23 promoter predicted by JASPAR**. (G)** Schematic diagram of the DDX23 WT and MT promoter sequences. **(H)** Dual-luciferase reporter assays showing that E2F1 overexpression increased the luciferase activity in HEK293T cells transfected with the DDX23 promoter WT plasmid, but not in cells with MT plasmid. **(I)** ChIP assay and semi-quantitative PCR analysis showed that E2F1 could bind to the DDX23 promoter region directly. TFs, transcription factors; ChIP, Chromatin immunoprecipitation; WT, wild type; MT, mutant type. Data are presented as mean ± SEM. ns, no significant, *$P < 0.05$, **$P < 0.01$, ***$P < 0.001$, ****$P < 0.0001$.

JASPAR online database and a potential E2F1 binding site with the highest score was found on the DDX23 promoter region (**Figure 5F**) (**Supplementary Table 5**). We constructed WT and MT plasmids of DDX23 promoter using pGL4.26 vector (**Figure 5G**). Luciferase assays showed that E2F1 overexpression increased the luciferase activity in HEK293T cells transfected with the DDX23 promoter WT plasmid, but not in cells with MT plasmid. (**Figure 5H**). Subsequently, ChIP assays were performed in A2780 cells to further verify the binding of E2F1 to DDX23 promotor. Results confirmed that E2F1 could bind to the DDX23 promoter region directly (**Figure 5I**). In summary, these data indicated that DDX23 was a direct transcriptional target of E2F1 in ovarian cancer cells.

## Identification of Differentially Expressed Genes Involved in DDX23 Function by RNA-seq

To explore the regulatory mechanisms of DDX23 on tumor progression, RNA-seq was performed in DDX23 knockdown and control A2780 cells. The changes in the transcriptome with DDX23 knockdown were analyzed and a total of 4115 differentially expressed genes (DEGs) were identified (1.5-FC, $P < 0.05$). There were 1921 upregulated genes and 2194 downregulated genes (**Figure 6A**). Biological process analysis showed that DDX23 was involved in mRNA processing, which confirmed the splicing-related functions of DDX23 in ovarian cancer (**Figure 6B**). Then, GO enrichment analysis was performed with the 2194 downregulated DEGs. Multiple downregulated genes (Gene set 1) were found to be associated with mitotic cell cycle process, which is an important underlying mechanism of tumor progression and consistent with the results of functional assays *in vivo* and *in vitro* (**Figure 6C**). Next, we searched the GEPIA database to obtain the upregulated genes in TCGA ovarian cancer cohort ($\text{Log}_2\text{FC} \geq 1$, $q < 0.01$) (Gene set 2). The cBioPortal database was also used to obtain genes that were positively associated with DDX23 expression (TCGA U133 microarray, Spearman's Correlation ≥ 0.3) (Gene set 3). Finally, 17 genes were screened by overlapping the three gene sets (**Figure 6D**). The expression details of the 17 candidates in TCGA cohort were showed in **Figures 6E, F**. Meanwhile, we demonstrated the low mRNA expression of these 17 genes in DDX23 knockdown A2780 cell line (**Figure 6G**). Co-expression analysis revealed the expression correlation between DDX23 and 17 candidates, and the details are shown in **Figure 6H**. Based on data from Cistrome Cancer, we found that among the five genes (ESPL1, KIF14, TUBG1, KIF11, FOXM1) with the highest correlation with DDX23 expression, four genes (ESPL1, KIF14, TUBG1, KIF11) were potential target genes of FOXM1 (Regular potential score, 0.943365, 0.96575, 0.644621, 0.988351, respectively) (**Supplementary Table 6**). DDX23 was shown to be positively associated with the expression of a well-known oncogene FOXM1 (Spearman's correlation = 0.41, $P = 6.59\text{e-}9$) (**Figure 6I**). Based on data from TCGA and CPTAC, we found that FOXM1 was upregulated in ovarian cancer at both mRNA and protein levels (**Figures 6J, K**). Numerous studies had proven that FOXM1 promoted the progression of various cancer types (31–33). Integrated genomic analyses of ovarian carcinoma from TCGA Research Network reported that the FOXM1 transcription factor network changed significantly in 87% of ovarian cancer cases (34). FOXM1, as a transcription factor, regulated many important proliferation-related target genes (AURB, CCNB1, BIRC5, CDC25, and PLK1, etc.) and was important oncogenic driver in ovarian cancer progression (34–36). Therefore, our subsequent studies focused on FOXM1 as a downstream target of DDX23.

## DDX23 Regulated the Production of the Main Oncogenic Transcript of FOXM1

First, we measured FOXM1 expression after DDX23 knockdown and results showed that FOXM1 expression decreased at both mRNA and protein levels (**Figures 7A, B**). Moreover, we validated that FOXM1 silencing inhibited the proliferation and migration capacity of A2780 and HEY cells, while ectopic expression of FOXM1 enhanced their proliferation and migration potential (**Figures 7C, D**). It has been reported in glioma that DDX23 was an essential tool for miR-21 mature, revealing the powerful RNA processing function of DDX23 (20). However, whether FOXM1 mRNA processing was regulated by DDX23 remained unknown. The human FOXM1 gene consists of 10 exons, and the differential splicing of exons Va and VIIa produces three transcripts, FOXM1A, FOXM1B, and FOXM1C. Both FOXM1B and C have transcriptional activity, while FOXM1A does not due to the addition of exon VIIa in C-terminal transactivation domain (31, 37, 38). Subsequently, we measured the mRNA expression of FOXM1A, FOXM1B, and FOXM1C after DDX23 knockdown in A2780 and HEY cells by qRT-PCR. We found that FOXM1C expression was tens of times higher than the other two transcripts in ovarian cancer cells. FOXM1C expression was dramatically decreased after DDX23 knockdown, whereas FOXM1A and FOXM1B expression did not change significantly (**Figure 7E**). Therefore, these findings suggested that FOXM1 was a downstream target of DDX23. DDX23 was required for the mRNA processing of FOXM1. DDX23 silencing reduced the production of FOXM1C, the major oncogenic transcript of FOXM1 in ovarian cancer, thereby decreasing the FOXM1 protein expression and attenuating the malignant progression of ovarian cancer.

## FOXM1 Mediated DDX23-Driven Malignant Progression of Ovarian Cancer Cells

In the foregoing sections, we demonstrated that FOXM1 mRNA and protein levels were decreased by DDX23 knockdown (**Figures 7A, B**). To determine whether DDX23 contribute to overall FOXM1 function, we performed rescue experiments by co-transfecting the ovarian cancer cells with DDX23 siRNA and FOXM1 plasmid, and examined the cell proliferation and migration. As expected, transfection of FOXM1 plasmid into HEY cells rescued the decreased FOXM1 protein levels caused by DDX23 knockdown (**Figure 8A**). In addition, FOXM1 overexpression enhanced the proliferation and migration capacity of SKOV3 and HEY cells. DDX23 knockdown significantly

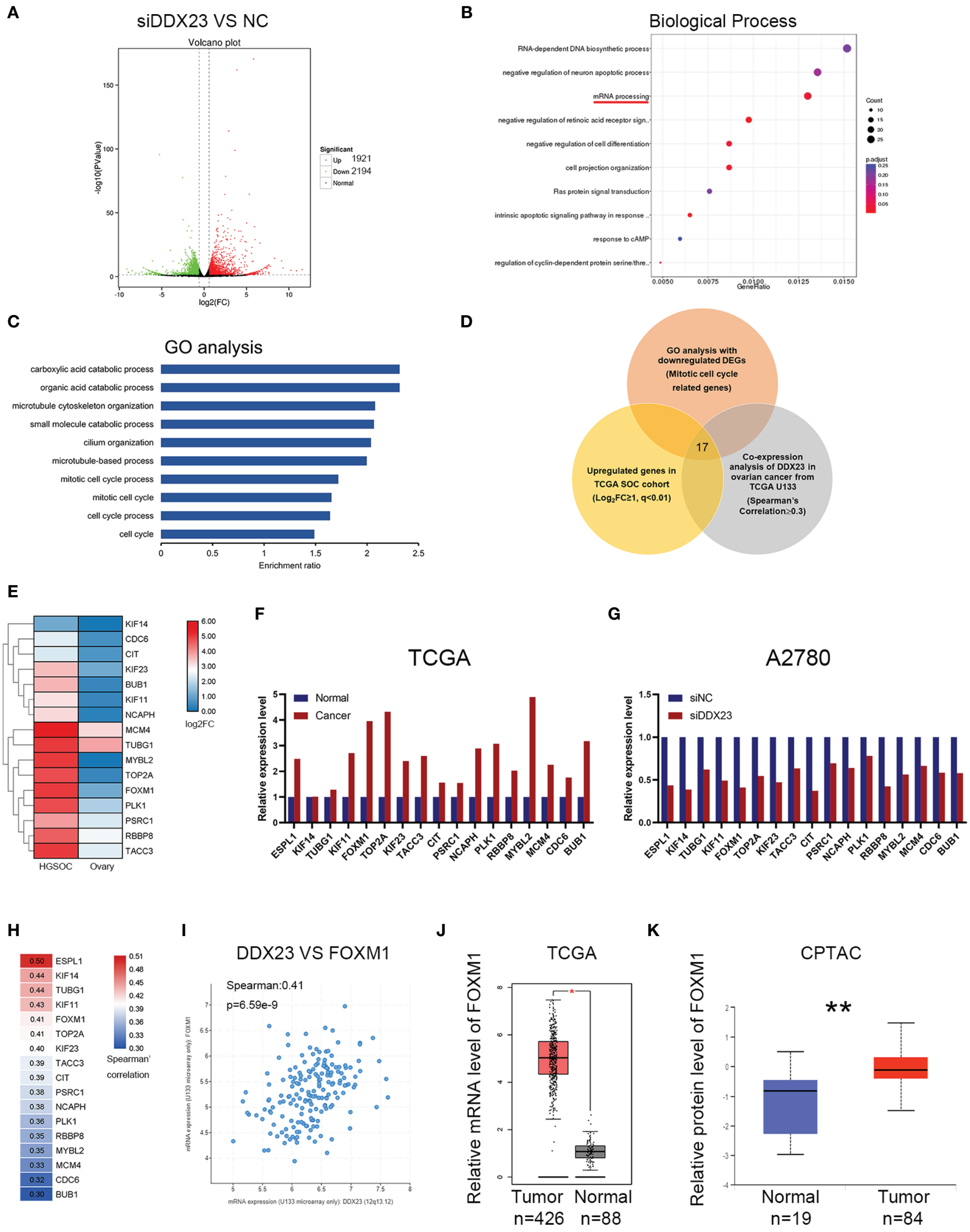

**FIGURE 6** | Identification of differentially expressed genes involved in DDX23 function by RNA-seq. **(A)** Volcano plot for the DEGs between siDDX23 and NC groups (1.5-FC, $P < 0.05$). **(B)** Biological process analysis showed that DDX23 was involved in mRNA processing. **(C)** GO enrichment analysis of the downregulated DEGs between siDDX23 and NC groups. **(D)** Venn diagram of 17 hub genes obtained by overlapping three gene sets. Gene set 1, 123 downregulated genes related to mitotic cell cycle processes identified by RNA-seq; Gene set 2, upregulated genes in ovarian cancer from GEPIA ($Log_2FC \geq 1$, $q < 0.01$); Gene set 3, genes that positively related to DDX23 expression (TCGA U133 microarray, Spearman's Correlation ≥ 0.3). **(E, F)** Relative mRNA expression of 17 candidate downstream genes in TCGA database. **(G)** qRT-PCR analysis of mRNA expression of 17 candidates in A2780 cells. **(H)** Co-expression analysis between DDX23 and 17candidates expression in ovarian cancer based on the cBioPortal database. **(I)** Co-expression analysis between DDX23 and FOXM1 expression in ovarian cancer based on the cBioPortal database. **(J)** FOXM1 mRNA expression in ovarian cancer and normal ovary samples in TCGA cohort from GEPIA. **(K)** FOXM1 protein expression in ovarian cancer and normal ovary samples in CPTAC cohort. DEG, differential expression gene; NC, negative control; FC, fold change; GO, Gene Ontology; GEPIA, Gene Expression Profiling Interactive Analysis; TCGA, The Cancer Genome Atlas. $^*P < 0.05$, $^{**}P < 0.01$.

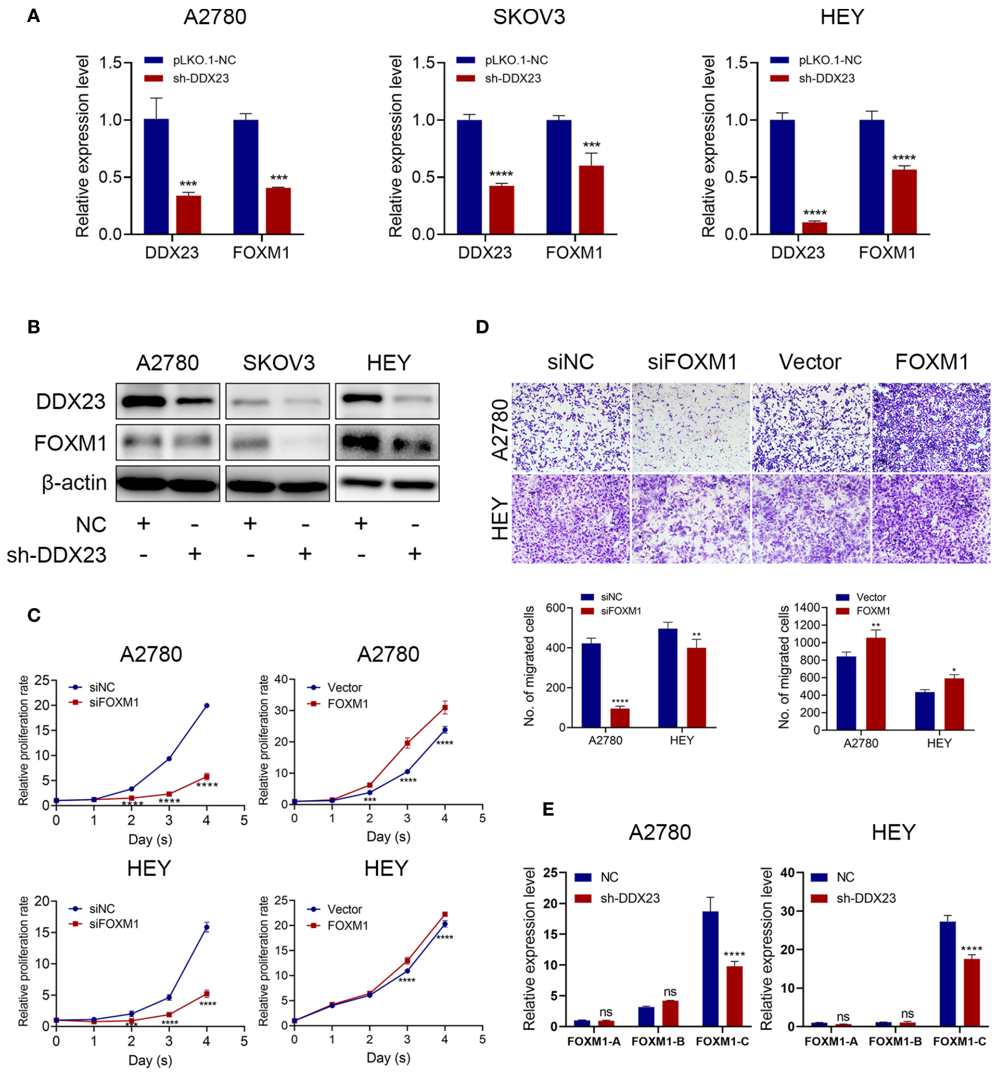

**FIGURE 7** | DDX23 regulated the production of the main oncogenic transcript of FOXM1. **(A, B)** The mRNA and protein levels of DDX23 and FOXM1 in ovarian cancer cells with or without DDX23 knockdown were measured by qRT-PCR **(A)** and western blotting **(B)**. **(C)** Representative MTT proliferation assays in A2780 and HEY cells with FOXM1 knockdown or overexpression. **(D)** Representative microscopic images (×10) of A2780 and HEY cells that penetrated through the Transwell chambers in migration assays. **(E)** Relative expression changes of different FOXM1 transcripts after DDX23 knockdown were analyzed in A2780 and HEY cells by qRT-PCR. Data are presented as mean ± SEM. ns, no significant, *$P < 0.05$, **$P < 0.01$, ***$P < 0.001$, ****$P < 0.0001$.

decreased cell proliferation and migration, whereas overexpression of FOXM1 partially restored the reduced cell proliferation and migration induced by DDX23 silencing (**Figures 8B, C**). Altogether, these results indicated that FOXM1 was a key executor in DDX23-induced malignant phenotype of ovarian cancer (**Figure 8D**).

## DISCUSSION

The extreme malignancy of ovarian cancer is related to a variety of carcinogenic mechanisms, including mRNA processing dysregulation. Aberrant expression of splicing factors is implicated in tumor initiation and progression (39). Splicing factor SFPQ regulated alternative splicing of caspase-9 mRNA and was involved in ovarian cancer sensitivity to platinum (11). Our previous study showed that USP39 functioned as an oncogenic splicing factor in ovarian cancer through maintaining efficient splicing of HMGA2 (13). The DEAD-box RNA helicases are important members of the splicing factor family and they usually function as components of large multi-protein complexes and play essential roles in RNA processing including spliceosome biogenesis, miRNA biogenesis and splicing, which are crucial for cellular proliferation and transformation of tumorigenicity (40, 41). DDX23 expression was elevated in glioma patients and it had been strongly linked to the poor prognosis of glioma (20). DDX23 was also upregulated in hepatocellular carcinoma and correlated

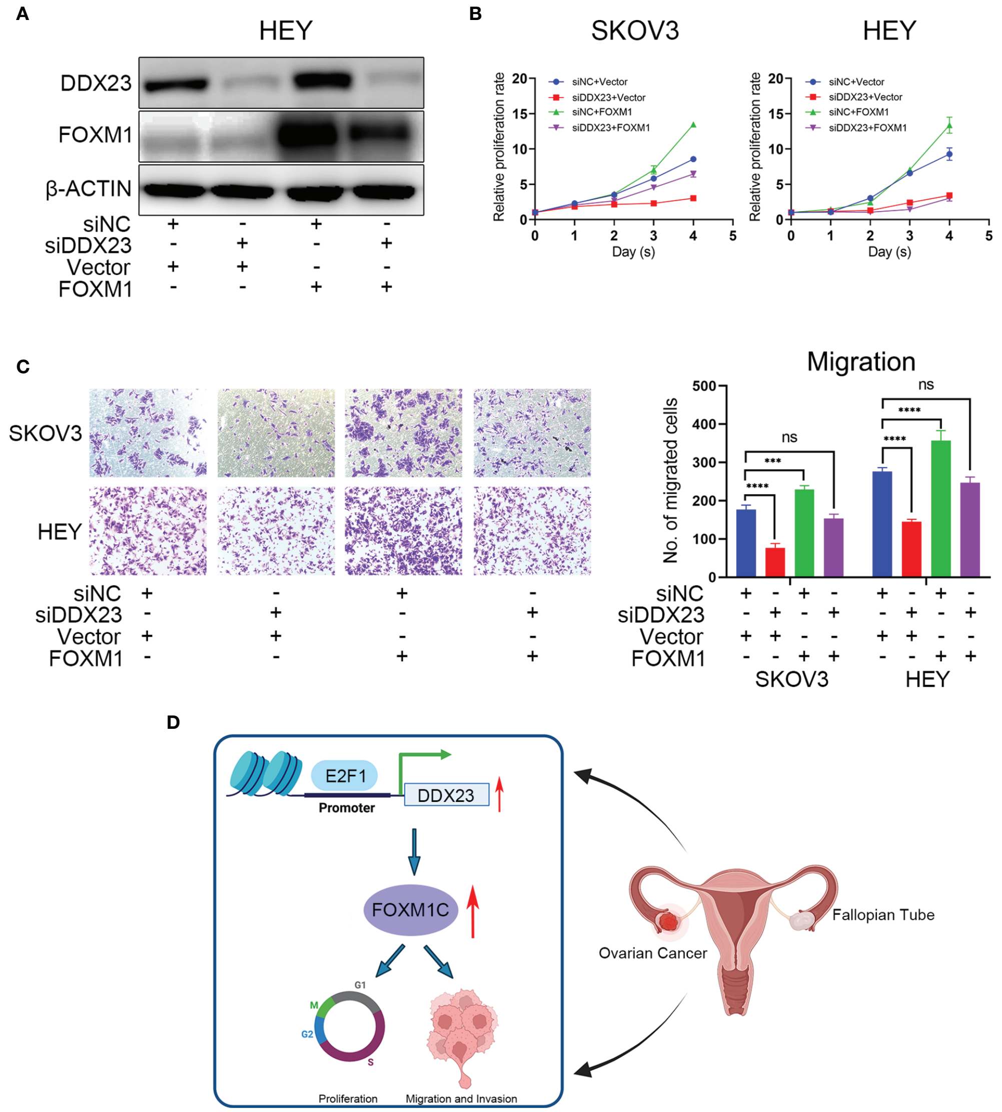

**FIGURE 8** | FOXM1 mediated DDX23-driven malignant progression of ovarian cancer cells. Control siRNAs or DDX23 siRNAs were co-transfected into ovarian cancer cells with PCMV-NC or PCMV-FOXM1 plasmids. **(A)** Western blotting analysis of DDX23 and FOXM1 expression in four rescue groups of HEY cells. **(B, C)** overexpression of FOXM1 partially restored the reduced cell proliferation **(B)** and migration **(C)** induced by DDX23 silencing. **(D)** Schematic diagram showing that DDX23 is transcriptionally activated by E2F1. DDX23 promotes ovarian cancer progression by regulating FOXM1C production. Data are presented as mean ± SEM. ns, no significant, ***$P < 0.001$, ****$P < 0.0001$.

with advanced clinicopathological stages (42). However, its clinical significance and biological function in ovarian cancer have not been characterized to date. In our study, we first determined that DDX23 was overexpressed and significantly correlated with poor clinical outcomes in ovarian cancer. DDX23 expression was an independent high-risk factor closely associated with the OS of ovarian cancer patients. These results indicate that DDX23 can serve as an indicator of prognostic prediction in ovarian cancer patients.

To further explore the role of DDX23 in ovarian cancer, we performed relevant functional experiments *in vitro* and *in vivo*. DDX23 was previously reported to promote the invasion and proliferation of glioma cells (20). In hepatocellular carcinoma, SDC4/DDX23 axis played a crucial role in driving cell proliferation and migration (42). In our study, DDX23 silencing significantly impeded the proliferation of ovarian cancer cells through G1 phase arrest. The expression of associated cell cycle regulators also changed in DDX23-depleted ovarian cancer cells. In addition, loss of DDX23 also inhibited cell migration and invasion. These results highlight the pathogenic role of DDX23 in ovarian cancer.

However, the function mechanism of splicing factor DDX23 in ovarian cancer has not been elucidated. DEAD-box RNA helicase family proteins, including DDX23 (also known as Prp28), participate in the assembly of spliceosomes (43). For example, DDX23 is a mediator for switching the U1 snRNA/pre-mRNA 5'splice site (5'SS) base-pairing interaction (44). Prp28 mediates the transfer of the 5'SS from U1 snRNP to the U6 snRNA ACAGAGA sequence, which is an important prerequisite for the formation of the catalytic center of the spliceosome (45). DDX23 phosphorylation influences the formation of tri-snRNP and B complex (15, 46). Prp28's ATPase is activated by the phosphorylated Npl3 to trigger specific conformational changes, which is essential for spliceosome remodeling (47). Therefore, DDX23 mainly perform their functions by processing the mRNA of downstream genes. Maintaining efficient splicing and promoting pre-mRNA maturation are important functions of splicing factors. For example, SF3B1 regulated KSR2 RNA maturation to promote endometrial cancer progression (48). hnRNPA2B1 improved the stability of Lin28B mRNA and enhanced malignant potential of ovarian cancer (49). We speculated that DDX23 might perform a similar function on FOXM1 mRNA.

Among the FOXM1 isoforms, FOXM1C is generally elevated and exerts oncogenic function. Kong et al. reported that FOXM1C was mainly expressed in pancreatic tumors and promoted the growth and motility of pancreatic cancer, whereas FOXM1A was commonly undetectable (31). The FOXM1C was predominantly overexpressed in esophageal cancer compared to the other FOXM1 isoforms and promoted its metastasis (50). Consistently, we overexpressed FOXM1C in ovarian cancer cells and observed that FOXM1C facilitated their proliferation and migration potential (**Figures 7C, D**). We also noted that the expression of FOXM1C in ovarian cancer cells was much higher than that of FOXM1A and FOXM1B. Moreover, FOXM1C expression was dramatically decreased after DDX23 knockdown, whereas FOXM1A and FOXM1B expression did not change significantly (**Figure 7E**). Because of the relative low expression of FOXM1A and FOXM1B in ovarian cancer cells, the FOXM1C expression presented the most significantly decrease after DDX23 knockdown. These findings suggest that DDX23 mainly regulates the generation of FOXM1C, the main oncogenic transcript of FOXM1, thereby regulating the malignant behavior of ovarian cancer. Further experiments are needed to study the specific mRNA processing mechanism of DDX23 on FOXM1.

Meanwhile, our study also investigated the DDX23 promoter region to predict potential TFs that might regulate the DDX23 upregulation observed in ovarian cancer. We found that the binding peak of E2F1 were enriched in the promoter region of DDX23 in HELA, MCF-7, U2OS and K652 cell lines. The E2F-family members have emerged as crucial transcriptional regulators of proliferation-promoting genes (51). The upregulation of E2Fs and their target genes has been linked with poor prognosis of various cancers, including breast and liver cancers (52, 53). E2F1, a member of the E2F-family activator subcategory, plays a crucial role in cancer cell proliferation, invasion, and apoptosis (54, 55). In ovarian cancer, low expression of E2F1 was reported to be correlated with favorable disease-free survival (DFS) and OS (56). In our study, we found that E2F1 knockdown decreased DDX23 expression at both the mRNA and protein levels. We subsequently confirmed that E2F1 could bind to the DDX23 promoter region directly and regulate DDX23 transcription in ovarian cancer cells. These results indicated that DDX23 was a direct transcriptional target of E2F1. Transcriptional activation of DDX23 by E2F1 in turn upregulates DDX23 in ovarian cancer.

In summary, our study was the first to demonstrate that DDX23 was upregulated in ovarian cancer and was associated with poor clinical outcomes. High expression of DDX23 was involved in the malignant proliferation and aggressiveness of ovarian cancer cells by regulating FOXM1 mRNA processing. FOXM1 was a key executor in DDX23-induced malignant phenotype of ovarian cancer. Our study also revealed that DDX23 was transcriptionally activated by E2F1, contributing to the elevated expression of DDX23 in ovarian cancer.

Although we have confirmed that DDX23 is involved in the FOXM1 mRNA processing, the underlying mechanism of DDX23 regulating FOXM1 is still unclear. Whether DDX23 regulates FOXM1 mRNA processing directly or indirectly remains to be further studied. At present, small-molecule inhibitor targeting DDX23 is still unavailable. Therefore, tumor suppression experiments with the specific inhibitor cannot be completed *in vivo*, which might restrict its clinical transformation. However, our research provides a promising therapeutic target for precision treatment of ovarian cancer and also provides new insights into the important biological functions of splicing-related factors. With the development of molecular biology and the molecular structure analysis techniques, corresponding targeted drugs are expected to be developed and applied.

## DATA AVAILABILITY STATEMENT

The raw data supporting the conclusions of this article will be made available by the authors, without undue reservation, to any qualified researcher. The RNA-seq data has been uploaded to GEO, and the accession number is GSE181078.

## ETHICS STATEMENT

The studies involving human participants were reviewed and approved by Ethics Committee of Shandong University. The patients/participants provided their written informed consent to participate in this study. The animal study was reviewed and approved by Shandong University Animal Care and Use Committee.

## AUTHOR CONTRIBUTIONS

This study was conceived, designed, and interpreted by BK and KS. YL and KS were responsible for the comprehensive technical support. CZ and YL contributed to the data acquisition, analysis and interpretation. CZ, HW and CQ analyzed the clinical prognosis. CZ, JC, QW, HW, and XM collected the clinical samples. CZ was the major contributor in writing the manuscript. CZ and CQ contributed to the inspection of data and final manuscript. All authors contributed to the article and approved the submitted version.

## FUNDING

This work was financially supported by the National Natural Science Foundation of China (Nos. 81874107, 82072871, and 81902650), the Tai-Shan Scholar Program of Shandong Province (No. ts20070743), and the Key Research and Development Program of Shandong Province (No. 2019GSF108048).

## ACKNOWLEDGMENTS

We sincerely thank all participants in the study. We thank BioRender (https://app.biorender.com/) because the schematic diagram (**Figure 8D**) was created with BioRender.com.

## SUPPLEMENTARY MATERIAL

The Supplementary Material for this article can be found online at: https://www.frontiersin.org/articles/10.3389/fonc.2021.749144/full#supplementary-material

**Supplementary Figure S1 |** Relative mRNA expression of CDK9, E2F1, CBX5, SUZ12, and ATF1 in HGSOC and normal ovarian tissues using data from TCGA-GTEx. ns, no significant, ***P* < 0.01, *****P* < 0.0001.

**Supplementary Figure S2 | (A, B)** The mRNA and protein levels of E2F1 in ovarian cancer cells with or without DDX23 knockdown were measured by qRT-PCR **(A)** and Western blotting **(B)**. ns, no significant, *****P* < 0.0001.

**Supplementary Table 1 |** Sequences of siRNA, shRNA and primers used in this study.

**Supplementary Table 2 |** Primary antibodies used in this study.

**Supplementary Table 3 |** Genes positively related to DDX23 expression (TCGA U133 microarray) from cBioPortal database.

**Supplementary Table 4 |** Transcription factors predicted to bind to the promoter of DDX23 from Cistrome Data Browser.

**Supplementary Table 5 |** The potential E2F1 binding sites on the DDX23 promoter region from JASPAR online database.

**Supplementary Table 6 |** Regular potential score of FOXM1 target genes from Cistrome Cancer.

## REFERENCES

1. Siegel RL, Miller KD, Fuchs HE, Jemal A. Cancer Statistics, 2021. *CA Cancer J Clin* (2021) 71:7–33. doi: 10.3322/caac.21654
2. Reid BM, Permuth JB, Sellers TA. Epidemiology of Ovarian Cancer: A Review. *Cancer Biol Med* (2017) 14:9–32. doi: 10.20892/j.issn.2095-3941.2016.0084
3. Lheureux S, Gourley C, Vergote I, Oza AM. Epithelial Ovarian Cancer. *Lancet* (2019) 393:1240–53. doi: 10.1016/S0140-6736(18)32552-2
4. Bowtell DD, Böhm S, Ahmed AA, Aspuria P, Bast RC, Beral V, et al. Rethinking Ovarian Cancer II: Reducing Mortality From High-Grade Serous Ovarian Cancer. *Nat Rev Cancer* (2015) 15:668–79. doi: 10.1038/nrc4019
5. Ray-Coquard I, Pautier P, Pignata S, Perol D, Gonzalez-Martin A, Berger R, et al. Olaparib Plus Bevacizumab as First-Line Maintenance in Ovarian Cancer. *N Engl J Med* (2019) 381:2416–28. doi: 10.1056/NEJMoa1911361
6. Franzese E, Centonze S, Diana A, Carlino F, Guerrera LP, Di Napoli M, et al. PARP Inhibitors in Ovarian Cancer. *Cancer Treat Rev* (2019) 73:1–9. doi: 10.1016/j.ctrv.2018.12.002
7. Bonnal SC, Lopez-Oreja I, Valcarcel J. Roles and Mechanisms of Alternative Splicing in Cancer - Implications for Care. *Nat Rev Clin Oncol* (2020) 17:457–74. doi: 10.1038/s41571-020-0350-x
8. Chen J, Weiss WA. Alternative Splicing in Cancer: Implications for Biology and Therapy. *Oncogene* (2015) 34:1–14. doi: 10.1038/onc.2013.570
9. Wang B, Lee N. Aberrant RNA Splicing in Cancer and Drug Resistance. *Cancers* (2018) 10:458. doi: 10.3390/cancers10110458
10. Frankiw L, Baltimore D, Li G. Alternative mRNA Splicing in Cancer Immunotherapy. *Nat Rev Immunol* (2019) 19:675–87. doi: 10.1038/s41577-019-0195-7
11. Pellarin I, Dall Acqua A, Gambelli A, Pellizzari I, D Andrea S, Sonego M, et al. Splicing Factor Proline- and Glutamine-Rich (SFPQ) Protein Regulates Platinum Response in Ovarian Cancer-Modulating SRSF2 Activity. *Oncogene* (2020) 39:4390–403. doi: 10.1038/s41388-020-1292-6
12. He X, Arslan AD, Pool MD, Ho TT, Darcy KM, Coon JS, et al. Knockdown of Splicing Factor SRp20 Causes Apoptosis in Ovarian Cancer Cells and Its Expression Is Associated With Malignancy of Epithelial Ovarian Cancer. *Oncogene* (2011) 30:356–65. doi: 10.1038/onc.2010.426
13. Wang S, Wang Z, Li J, Qin J, Song J, Li Y, et al. Splicing Factor USP39 Promotes Ovarian Cancer Malignancy Through Maintaining Efficient Splicing of Oncogenic HMGA2. *Cell Death Dis* (2021) 12:294. doi: 10.1038/s41419-021-03581-3
14. Li Y, Guo H, Jin C, Qiu C, Gao M, Zhang L, et al. Spliceosome-Associated Factor CTNNBL1 Promotes Proliferation and Invasion in Ovarian Cancer. *Exp Cell Res* (2017) 357:124–34. doi: 10.1016/j.yexcr.2017.05.008
15. Cordin O, Beggs JD. RNA Helicases in Splicing. *RNA Biol* (2013) 10:83–95. doi: 10.4161/rna.22547
16. Linder P, Jankowsky E. From Unwinding to Clamping — the DEAD Box RNA Helicase Family. *Nat Rev Mol Cell Bio* (2011) 12:505–16. doi: 10.1038/nrm3154
17. Mazurek A, Luo W, Krasnitz A, Hicks J, Powers RS, Stillman B. DDX5 Regulates DNA Replication and Is Required for Cell Proliferation in a Subset of Breast Cancer Cells. *Cancer Discov* (2012) 2:812–25. doi: 10.1158/2159-8290.CD-12-0116
18. He C, Li A, Lai Q, Ding J, Yan Q, Liu S, et al. The DDX39B/FUT3/TGFbetaR-I Axis Promotes Tumor Metastasis and EMT in Colorectal Cancer. *Cell Death Dis* (2021) 12:74. doi: 10.1038/s41419-020-03360-6
19. Burns W, Bird LM, Heron D, Keren B, Ramachandra D, Thiffault I, et al. Syndromic Neurodevelopmental Disorder Associated With *De Novo* Variants in DDX23. *Am J Med Genet A* (2021) 185:2863–72. doi: 10.1002/ajmg.a.62359
20. Yin J, Park G, Lee JE, Choi EY, Park JY, Kim T, et al. DEAD-Box RNA Helicase DDX23 Modulates Glioma Malignancy *via* Elevating miR-21 Biogenesis. *Brain* (2015) 138:2553–70. doi: 10.1093/brain/awv167
21. Belinky F, Nativ N, Stelzer G, Zimmerman S, Iny ST, Safran M, et al. PathCards: Multi-Source Consolidation of Human Biological Pathways. *Database (Oxford)* (2015) 2015:1–13. doi: 10.1093/database/bav006
22. Wang L, Karpova A, Gritsenko MA, Kyle JE, Cao S, Li Y, et al. Proteogenomic and Metabolomic Characterization of Human Glioblastoma. *Cancer Cell* (2021) 39:509–28.e20. doi: 10.1016/j.ccell.2021.01.006
23. Goldman MJ, Craft B, Hastie M, Repečka K, McDade F, Kamath A, et al. Visualizing and Interpreting Cancer Genomics Data *via* the Xena Platform. *Nat Biotechnol* (2020) 38:675–8. doi: 10.1038/s41587-020-0546-8

24. Győrffy B, Lánczky A, Szállási Z. Implementing an Online Tool for Genome-Wide Validation of Survival-Associated Biomarkers in Ovarian-Cancer Using Microarray Data From 1287 Patients. *Endocr-Relat Cancer* (2012) 19:197–208. doi: 10.1530/ERC-11-0329
25. Cerami E, Gao J, Dogrusoz U, Gross BE, Sumer SO, Aksoy BA, et al. The Cbio Cancer Genomics Portal: An Open Platform for Exploring Multidimensional Cancer Genomics Data: Figure 1. *Cancer Discov* (2012) 2:401–4. doi: 10.1158/2159-8290.CD-12-0095
26. Fornes O, Castro-Mondragon JA, Khan A, van der Lee R, Zhang X, Richmond PA, et al. JASPAR 2020: Update of the Open-Access Database of Transcription Factor Binding Profiles. *Nucleic Acids Res* (2019) 48:D87–92. doi: 10.1093/nar/gkz1001
27. Mei S, Meyer CA, Zheng R, Qin Q, Wu Q, Jiang P, et al. Cistrome Cancer: A Web Resource for Integrative Gene Regulation Modeling in Cancer. *Cancer Res* (2017) 77:e19–22. doi: 10.1158/0008-5472.CAN-17-0327
28. Mei S, Qin Q, Wu Q, Sun H, Zheng R, Zang C, et al. Cistrome Data Browser: A Data Portal for ChIP-Seq and Chromatin Accessibility Data in Human and Mouse. *Nucleic Acids Res* (2017) 45:D658–62. doi: 10.1093/nar/gkw983
29. Liao Y, Wang J, Jaehnig EJ, Shi Z, Zhang B. WebGestalt 2019: Gene Set Analysis Toolkit With Revamped UIs and APIs. *Nucleic Acids Res* (2019) 47: W199–205. doi: 10.1093/nar/gkz401
30. Tang Z, Li C, Kang B, Gao G, Li C, Zhang Z. GEPIA: A Web Server for Cancer and Normal Gene Expression Profiling and Interactive Analyses. *Nucleic Acids Res* (2017) 45:W98–W102. doi: 10.1093/nar/gkx247
31. Kong X, Li L, Li Z, Le X, Huang C, Jia Z, et al. Dysregulated Expression of FOXM1 Isoforms Drives Progression of Pancreatic Cancer. *Cancer Res* (2013) 73:3987–96. doi: 10.1158/0008-5472.CAN-12-3859
32. Chan DW, Hui WW, Wang JJ, Yung MM, Hui LM, Qin Y, et al. DLX1 Acts as a Crucial Target of FOXM1 to Promote Ovarian Cancer Aggressiveness by Enhancing TGF-Beta/SMAD4 Signaling. *Oncogene* (2017) 36:1404–16. doi: 10.1038/onc.2016.307
33. Arceci A, Bonacci T, Wang X, Stewart K, Damrauer JS, Hoadley KA, et al. FOXM1 Deubiquitination by USP21 Regulates Cell Cycle Progression and Paclitaxel Sensitivity in Basal-Like Breast Cancer. *Cell Rep* (2019) 26:3076–3086.e6. doi: 10.1016/j.celrep.2019.02.054
34. The Cancer Genome Atlas Research Network. Integrated Genomic Analyses of Ovarian Carcinoma. *Nature* (2011) 474:609–15. doi: 10.1038/nature10166
35. Li Y, Guo H, Wang Z, Bu H, Wang S, Wang H, et al. Cyclin F and KIF20A, FOXM1 Target Genes, Increase Proliferation and Invasion of Ovarian Cancer Cells. *Exp Cell Res* (2020) 395:112212. doi: 10.1016/j.yexcr.2020.112212
36. Bu H, Li Y, Jin C, Yu H, Wang X, Chen J, et al. Overexpression of PRC1 Indicates a Poor Prognosis in Ovarian Cancer. *Int J Oncol* (2020) 56:685–96. doi: 10.3892/ijo.2020.4959
37. Laoukili J, Stahl M, Medema RH. FoxM1: At the Crossroads of Ageing and Cancer. *Biochim Biophys Acta (BBA) - Rev Cancer* (2007) 1775:92–102. doi: 10.1016/j.bbcan.2006.08.006
38. Ye H, Kelly TF, Samadani U, Lim L, Rubio S, Overdier DG, et al. Hepatocyte Nuclear Factor 3/Fork Head Homolog 11 Is Expressed in Proliferating Epithelial and Mesenchymal Cells of Embryonic and Adult Tissues. *Mol Cell Biol* (1997) 17:1626–41. doi: 10.1128/MCB.17.3.1626
39. Anczuków O, Krainer AR. Splicing-Factor Alterations in Cancers. *Rna* (2016) 22:1285–301. doi: 10.1261/rna.057919.116
40. Fuller-Pace FV. DEAD Box RNA Helicase Functions in Cancer. *RNA Biol* (2013) 10:121–32. doi: 10.4161/rna.23312
41. Treiber T, Treiber N, Plessmann U, Harlander S, Daiß J, Eichner N, et al. A Compendium of RNA-Binding Proteins That Regulate MicroRNA Biogenesis. *Mol Cell* (2017) 66:270–84.e13. doi: 10.1016/j.molcel.2017.03.014
42. Yang H, Liu Y, Zhao MM, Guo Q, Zheng XK, Liu D, et al. Therapeutic Potential of Targeting Membrane-Spanning Proteoglycan SDC4 in Hepatocellular Carcinoma. *Cell Death Dis* (2021) 12:492. doi: 10.1038/s41419-021-03780-y
43. Wilkinson ME, Charenton C, Nagai K. RNA Splicing by the Spliceosome. *Annu Rev Biochem* (2020) 89:359–88. doi: 10.1146/annurev-biochem-091719-064225
44. Staley JP, Guthrie C. An RNA Switch at the 5' Splice Site Requires ATP and the DEAD Box Protein Prp28p. *Mol Cell* (1999) 3:55–64. doi: 10.1016/s1097-2765(00)80174-4
45. Charenton C, Wilkinson ME, Nagai K. Mechanism of 5' Splice Site Transfer for Human Spliceosome Activation. *Science* (2019) 364:362–7. doi: 10.1126/science.aax3289
46. Mathew R, Hartmuth K, Mohlmann S, Urlaub H, Ficner R, Luhrmann R. Phosphorylation of Human PRP28 by SRPK2 Is Required for Integration of the U4/U6-U5 tri-snRNP Into the Spliceosome. *Nat Struct Mol Biol* (2008) 15:435–43. doi: 10.1038/nsmb.1415
47. Yeh FL, Chang SL, Ahmed GR, Liu HI, Tung L, Yeh CS, et al. Activation of Prp28 ATPase by Phosphorylated Npl3 at a Critical Step of Spliceosome Remodeling. *Nat Commun* (2021) 12:3082. doi: 10.1038/s41467-021-23459-4
48. Popli P, Richters MM, Chadchan SB, Kim TH, Tycksen E, Griffith O, et al. Splicing Factor SF3B1 Promotes Endometrial Cancer Progression *via* Regulating KSR2 RNA Maturation. *Cell Death Dis* (2020) 11:842. doi: 10.1038/s41419-020-03055-y
49. Yang Y, Wei Q, Tang Y, Yuanyuan W, Luo Q, Zhao H, et al. Loss of Hnrnpa2b1 Inhibits Malignant Capability and Promotes Apoptosis *via* Down-Regulating Lin28B Expression in Ovarian Cancer. *Cancer Lett* (2020) 475:43–52. doi: 10.1016/j.canlet.2020.01.029
50. Zhou Y, Wang Q, Chu L, Dai W, Zhang X, Chen J, et al. FOXM1c Promotes Oesophageal Cancer Metastasis by Transcriptionally Regulating IRF1 Expression. *Cell Prolif* (2019) 52:e12553. doi: 10.1111/cpr.12553
51. Kent LN, Leone G. The Broken Cycle: E2F Dysfunction in Cancer. *Nat Rev Cancer* (2019) 19:326–38. doi: 10.1038/s41568-019-0143-7
52. Sun CC, Li SJ, Hu W, Zhang J, Zhou Q, Liu C, et al. Comprehensive Analysis of the Expression and Prognosis for E2Fs in Human Breast Cancer. *Mol Ther* (2019) 27:1153–65. doi: 10.1016/j.ymthe.2019.03.019
53. Kent LN, Bae S, Tsai SY, Tang X, Srivastava A, Koivisto C, et al. Dosage-Dependent Copy Number Gains in E2f1 and E2f3 Drive Hepatocellular Carcinoma. *J Clin Invest* (2017) 127:830–42. doi: 10.1172/JCI87583
54. Xiang S, Wang Z, Ye Y, Zhang F, Li H, Yang Y, et al. E2F1 and E2F7 Differentially Regulate KPNA2 to Promote the Development of Gallbladder Cancer. *Oncogene* (2019) 38:1269–81. doi: 10.1038/s41388-018-0494-7
55. Putzer BM, Engelmann D. E2F1 Apoptosis Counterattacked: Evil Strikes Back. *Trends Mol Med* (2013) 19:89–98. doi: 10.1016/j.molmed.2012.10.009
56. Reimer D, Sadr S, Wiedemair A, Stadlmann S, Concin N, Hofstetter G, et al. Clinical Relevance of E2F Family Members in Ovarian Cancer–An Evaluation in a Training Set of 77 Patients. *Clin Cancer Res* (2007) 13:144–51. doi: 10.1158/1078-0432.CCR-06-0780

**Conflict of Interest:** The authors declare that the research was conducted in the absence of any commercial or financial relationships that could be construed as a potential conflict of interest.

frontiers
in Oncology

ORIGINAL RESEARCH
published: 03 March 2022
doi: 10.3389/fonc.2022.798680

# CAF-Associated Paracrine Signaling Worsens Outcome and Potentially Contributes to Chemoresistance in Epithelial Ovarian Cancer

**Michael Wessolly[1]*, Elena Mairinger[1], Sabrina Borchert[1], Agnes Bankfalvi[1], Pawel Mach[2], Kurt Werner Schmid[1], Rainer Kimmig[2], Paul Buderath[2†] and Fabian Dominik Mairinger[1†]**

[1] Institute of Pathology, University Hospital Essen, Essen, Germany, [2] Department of Gynecology and Obstetrics, University Hospital Essen, Essen, Germany

**Edited by:**
Xia Bai Rong,
Anhui Provincial Hospital, China

**Reviewed by:**
Paula Cunnea,
Imperial College London,
United Kingdom
Susan Percy Ivy,
National Cancer Institute (NIH),
United States

***Correspondence:**
Michael Wessolly
michael.wessolly@uk-essen.de

†These authors have contributed equally to this work and share last authorship

**Specialty section:**
This article was submitted to Gynecological Oncology, a section of the journal Frontiers in Oncology

**Received:** 20 October 2021
**Accepted:** 07 February 2022
**Published:** 03 March 2022

**Citation:**
Wessolly M, Mairinger E, Borchert S, Bankfalvi A, Mach P, Schmid KW, Kimmig R, Buderath P and Mairinger FD (2022) CAF-Associated Paracrine Signaling Worsens Outcome and Potentially Contributes to Chemoresistance in Epithelial Ovarian Cancer. Front. Oncol. 12:798680. doi: 10.3389/fonc.2022.798680

**Background:** High-grade serous ovarian cancer (HGSOC) is the predominant and deadliest form of ovarian cancer. Some of its histological subtypes can be distinguished by frequent occurrence of cancer-associated myofibroblasts (CAFs) and desmoplastic stroma reaction (DSR). In this study, we want to explore the relationship between therapy outcome and the activity of CAF-associated signaling pathways in a homogeneous HGSOC patient collective. Furthermore, we want to validate these findings in a general Epithelial ovarian cancer (EOC) cohort.

**Methods:** The investigation cohort consists of 24 HGSOC patients. All of them were treated with platinum-based components and clinical follow-up was available. The validation cohort was comprised of 303 patients. Sequencing data (whole transcriptome) and clinical data were extracted from The Cancer Genome Atlas (TCGA). RNA of HGSOC patients was isolated using a Maxwell RSC instrument and the appropriate RNA isolation kit. For digital expression analysis a custom-designed gene panel was employed. All genes were linked to various DSR- and CAF- associated pathways. Expression analysis was performed on the NanoString nCounter platform. Finally, data were explored using the R programming environment (v. 4.0.3).

**Result:** In total, 15 CAF-associated genes were associated with patients' survival. More specifically, 6 genes (MMP13, CGA, EPHA3, PSMD9, PITX2, PHLPP1) were linked to poor therapy outcome. Though a variety of different pathways appeared to be associated with therapy failure, many were related to CAF paracrine signaling, including MAPK, Ras and TGF-β pathways. Similar results were obtained from the validation cohort.

**Discussion:** In this study, we could successfully link CAF-associated pathways, as shown by increased Ras, MAPK and PI3K-Akt signaling to therapy failure (chemotherapy) in HGSOC and EOCs in general. As platinum-based chemotherapy has been the state-of-the-art therapy to treat HGSOC for decades, it is necessary to unveil the reasons behind resistance developments and poor outcome. In this work, CAF-associated signaling is shown to compromise therapy response. In the validation cohort, CAF-associated signaling is also associated with therapy failure in general EOC, possibly hinting towards a conserved mechanism. Therefore, it may be helpful to stratify HGSOC patients for CAF activity and consider alternative treatment options.

**Keywords: tumor microenvironment, epithelial ovarian cancer, high-grade serous ovarian cancer, cancer-associated fibroblasts, chemoresistance**

## 1 INTRODUCTION

According to the Global Cancer Statistics 2020 (GLOBOCAN), ovarian cancer ranks high as the deadliest tumor originating from gynecological sites, especially when comparing new cases (313.959) and disease-related deaths (207.252) (1). The staggering amount of patient deaths from this tumor type make it a serious health concern. Due to the lack of early symptoms, the disease is mostly discovered in advanced tumor stages with an extensive spread inside the peritoneal cavity (2). Epithelial ovarian cancer (EOC) is a heterogeneous disease, comprised of various subtypes. The four most prominent subtypes of EOC are clear cell, endometrioid, mucinous and serous ovarian cancer. The latter can be further subdivided into low-and high-grade serous ovarian cancer (3–5). In order to rate EOC subtypes regarding their proliferative and metastatic potential they can be differentiated as type I and type II EOC (6). Type 1 EOCs, encompassing endometrioid, clear cell and low-grade serous ovarian cancer, are characterized by slow progression and can often be discovered in early disease stages. Comparatively they have a better prognosis than type 2 EOCs (3, 5). High-grade serous ovarian cancer (HGSOC) is a type II EOC and the most prevalent EOC subtype, while also displaying a high proliferation rate and metastatic potential. Furthermore, HGSOC is mostly diagnosed at an advanced disease stage (3, 5). On a molecular level, DNA repair defects and p53 mutations are frequently encountered in HGSOC (4). Taken together, HGSOC is considered to have the poorest prognosis among the listed tumors and accounts for up to 80% of all deaths from EOCs (4, 7).

The two pillars of HGSOC therapy are cytoreductive surgery and adjuvant chemotherapy. The outcome is directly depended on disease stage (8). Since the 1980s platinum agents in combination with first cyclophosphamide and then paclitaxel are applied. The standard treatment consists of six cycles of carboplatinum and paclitaxel every three weeks (9, 10). In advanced stages, the anti-angiogenic agent bevacizumab may be added in addition to combined chemotherapy (10, 11). While most tumors regress initially after treatment, patients eventually face disease relapse, leading to the presumption that chemoresistance will develop eventually in the majority of cases (10, 12). From this point, patients are either defined as carrying a platinum-resistant or platinum-sensitive disease. Platinum-resistant patients present either with rapid progression after initial chemotherapy or a complete remission of the tumor mass, followed by a sudden relapse within six months after primary therapy has been completed. Similary, platinum-sensitive patients also display a complete remission after chemotherapy. However, disease relapse occurs later than in platinum-resistant patients (longer than six months after completing chemotherapy) (13–15).

In recurrent cases, platinum-based chemotherapy is also the treatment of choice for patients deemed platinum-sensitive. Moreover, platinum-sensitive tumors are especially vulnerable for treatment with Poly-ADP-Ribose-polymerase (PARP)-inhibitors in the first-line as well as the recurrent situation (16, 17). Platinum-resistant recurrent patients may also receive an alternative chemotherapeutic agent (cyclophophamide, doxorubicin, Pacitaxel or Topotecan) in combination with bevacizumab (18, 19).

One particular molecular subtype of HGSOC, the mesenchymal subtype is characterized by frequent generation of desmoplastic stroma. Mixed subtypes containing both epithelial and mesenchymal structures are also known. The occurrence of desmoplastic stroma in HGSOC is linked to decreased overall survival and resistance to platinum-based chemotherapy (20–22). This cancer-associated stroma is an important part of the tumor microenvironment. It may strongly influence tumor progression, invasion, metastasis, and angiogenesis (23, 24). A study by Zhang et al. (25) found increased expression of collagens (COL5A1, COL11A1), FAP, ACTA2 and p-SMAD2 within the stroma. FAP and ACTA2 (26, 27) are distinctive markers of a myofibroblast subtype, Cancer-associated fibroblasts (CAFs), which can reorganize the extracellular matrix to the tumors benefit or promote tumor-supportive inflammation (28, 29). Additionally, they secrete angiogenic factors (30). The constant reshuffling within the extracellular matrix triggers integrin-mediated activation of MAPK and PI3K-Akt signaling pathways, thereby enhancing cell proliferation and migration (31, 32).

Considering the abundance of CAFs in certain HGSOC subtypes and the link to dismal outcome, it seems very plausible that CAFs and associated stroma support tumor cells by paracrine signaling and providing a physical barrier, which facilitates the often-occurring platinum-resistance in HGSOC and decreased survival (33–35). We established a gene panel, encompassing various factors involved in prominent signaling pathways (TGF-β-, PI3K-Akt-, MAPK signaling) linked to desmoplastic stroma reaction (DSR). By analyzing the effects of paracrine CAF-signaling in a clinically well-defined and homogeneous collective of HGSOC patients, we intend to link it to impaired therapy outcome. Thereby, we also provide an mRNA-based expression signature, which may be helpful to stratify patients for application of platinum-based chemotherapy in the future.

## 2 MATERIAL AND METHODS

It should be noted that the following methods were applied as it was described in (36). However, in this study the gene panel is custom-designed in order to fit genes associated with DSR. This gene list derived from both previous research and current literature (37–40) includes key members of the canonical and non-canonical TGF-β signaling pathway, the PI3K pathway, WNT signaling, MAPK pathway, cell cycle progression, important growth factors and their respective receptors and well as main markers for activated myofibroblasts within the tumor (FAP, FN1, ACTA2/α-SMA).

## 2.1 Study and Cohort Design

### 2.1.1 Investigation Cohort

The retrospective investigation cohort encompassed 24 patients (**Figure 1**). They were diagnosed with high-grade serous ovarian cancer (HGSOC). The diagnosis was confirmed by an experienced pathologist according to the International Union Against Cancer (UICC), more specifically the 8th edition of TNM guidelines (41). Patients were included into the study based on the following criteria: confirmed HGSOC with the ovaries as primary site, treatment with platinum-based chemotherapy (adjuvant) only, and sufficient follow-up data. Tumor tissue from the omentum was excluded. Clinical data include patients' age, survival data (overall survival and recurrence-free survival) as well as tumor grading. DSR was identified in all 24 cases *via* staining of FAP, FN1 and ACTA2. Additionally, 7/24 patients had shown strong FAP positivity and extensive stroma remodeling. Based on recurrence-free survival (RFS), a binary outcome variable was defined that correlates to resistance against cisplatin. Patients displaying poor therapy outcome or therapy resistance were characterized by an RFS below 6 months after therapy completion, which conforms to the sources mentioned above (13–15). Median overall and recurrence-free survival for the investigation cohort were 35 and 9 months, respectively. All important clinical data from the investigation cohort are summarized in **Supplemental Table 1**.

### 2.1.2 Validation Cohort

A cohort (n=303) of epithelial ovarian cancers (EOC) served as a validation cohort for this study. Gene expression data (RNA Seq) and clinical data were obtained from The Cancer Genome Atlas (TCGA) database (National Cancer Institute, National Human Genome Research institute, Bethesda, MD, US). The primary site of tumors within the validation cohort were the ovaries, though three tumor samples were derived from the omentum. A key selection criterion was sufficient follow-up that allowed for calculation of therapy outcome after platinum treatment. Poor therapy outcome or therapy resistance was defined as it was described in 2.1.1 (RFS below 6 months after therapy completion) (13–15). Median overall and recurrence-free survival for the validation cohort were 44 and 18 months, respectively. All important clinical data from the validation cohort are summarized in **Supplemental Table 2**.

## 2.2 RNA Extraction and Quantity Measurement

### 2.2.1 Preparing Tissue Sections for RNA Isolation

Tumor tissue used for the study was formalin-fixed and paraffin-embedded (FFPE). All samples have been collected between 2005 and 2010. Only one tumor per patient was selected for further analysis. Each sample analyzed contained at least 85% tumor cells. All specimens have been stored at room temperature in the archives of the Institute of Pathology, University Hospital Essen. Tissue sections (thickness: 10 microns) were made using a "Microm HM340E" microtome (Thermo Fisher Scientific, Massachusetts, USA). The amount of sections was dependent on available tumor tissue (at least two sections per sample). The first tissue section from the surface layer has been discarded due to possible oxidation processes. In order to avoid loss of RNA yield, slides were stored by freezing (-20°C) until the RNA isolation procedure commenced.

### 2.2.2 RNA Isolation

RNA was isolated in a semi-automatic workflow with the help of the Maxwell® RSC Instrument (Promega, Wisconsin, USA) using a Maxwell® RSC RNA FFPE kit (AS1440, Promega, Wisconsin, USA). The process was conducted according to the

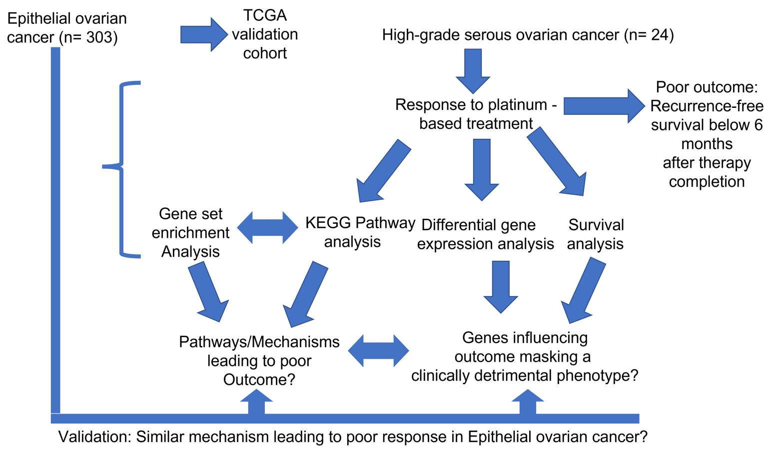

**FIGURE 1** | General methodical workflow of the study.

manufacturer's instructions. In the final step, RNA was eluted in 50 μL RNase-free water.

### 2.2.3 RNA Quantification

After the isolation process, RNA yield was quantified using a Qubit 2.0 fluorometer (Life Technologies, California, USA). Samples were prepared for Qubit measurement by utilizing an RNA broad-range assay kit (Invitrogen, Thermo Fisher Scientific, California, USA) according to the manufacturer's instructions. In short, the fluorometric quantification is based on linear regression using predefined standards provided within the kit.

## 2.3 Digital Gene Expression Analysis

Samples harboring sufficient RNA yield were analyzed on the NanoString nCounter MAX/FLEX platform. 100 ng total RNA were used for each reaction. Digital expression analysis of 221 genes associated with DSR, TGF-β-, PI3K-Akt and MAPK signaling was performed utilizing a customized panel encompassing key genes of those pathways (**Supplemental Table 3**). Hybridization of capture- and reporter probes, carrying the biotin-tag and the 6-digits fluorescence barcode, respectively, with sample RNA was carried out using a thermocycler (Eppendorf, Germany) at 65°C (72°C lid temperature) for 21h as mentioned in the manufacturer's protocol. After this stringent hybridization, post-hybridization processes including immobilization to the cartridge surface as well as clean-up of the hybridization products were conducted automatically on the NanoString nCounter Prep-Station according to the high sensitivity protocol. The cartridge was scanned directly after preparation on the NanoString nCounter Digital Analyzer with maximum sensitivity (555 fields of view).

## 2.4 NanoString Data Processing

Count data acquired by NanoString analysis were normalized and analyzed using the R statistical programming environment (The R Foundation for Statistical Computing, Institute for Statistics and Mathematics, Vienna, Austria; v. 4.0.3). Beside probes covering the target genes, a variety of technical and biological controls are included in the panel. First, eight different negative controls comprising probes with sequences not complimentary to the human transcriptome are included to estimate unspecific binding capability and identify potential alterations in the hybridization process. Second, six artificial RNA sequences with predefined concentration are included in the panel (technical positive controls). Those serve for detection of technical issues as well as to define the dynamic range of the assay and for calibration of linear regression, as those controls are diluted in a predefined manner and can be used as a standard curve. Samples without linear growth of those inherent positive controls indicating incomplete hybridization or elevated negative controls leading to decreased signal to noise ratio have been re-run. Third, nine reference genes for biological normalization purposes have been included in the panel, covering three high, three medium and three low expressed targets.

Technical normalization was performed by subtracting the mean counts from inherent negative controls plus two-times standard deviation from all target specific counts of each sample, while biological normalization was carried out using the geometric mean of included reference genes. In detail, a normalization factor has been calculated by dividing the geometric mean of all geometric means of the reference genes through the sample specific geometric mean of the reference genes. Afterwards, all target counts get multiplied by this normalization factor and afterwards mathematically rounded to integers. In addition to background subtraction, background noise was excluded by utilization of one-side Wilks *t*-test of negative controls and target specific counts in all samples to identify genes not relevantly expressed ($p < 0.05$) (36).

## 2.5 Statistical Analysis

Statistical and graphical analyses were also performed within the R statistical programming environment (v. 4.0.3)

First, the Shapiro–Wilks test was applied to test for normal distribution of data (42). For ordinal variables containing two groups, either the non-parametric Wilcoxon Mann-Whitney rank sum test or the parametric Student's *t*-test was utilized (43). If ordinal variables contained more than two groups, the ANOVA (Analysis of variance, parametric) or the Kruskal–Wallis test (non-parametric) was used instead (44). Double dichotomous contingency tables were analyzed using Fisher's exact test. To test dependency of ranked parameters with more than two groups the Pearson's Chi-squared test was used. Group differences between metric variables were either detected by Pearson product moment correlation or Spearman's rank correlation test (45). Quality control of run data was first performed by mean-vs-variance plotting to find outliers on target or sample level. True differences and clusters on both target and sample level were calculated by correlation matrices. To further specify the different candidate patterns, both unsupervised and supervised clustering, as well as principal component analysis were performed to overcome commonalities and differences. Sensitivity and specificity of markers were determined from receiver operating characteristic (ROC) curves illustrating their performance to discriminate the studied groups (46, 47). The bootstrap procedure (1000 iterations) was used for internal validation of the estimates in the ROC analyses. Pathway analysis is based on the KEGG database (Kyoto Encyclopaedia of Genes and Genomes) and was performed using the "pathview" package in R. Differences were specified by -log2 fold changes between means (parametric) or medians (non-parametric) of compared groups. Overall survival (OS) and RFS were calculated using single-factorial and combined fitting models. Survival analysis was done by Cox-regression (COXPH-model), and statistical significance was determined using likelihood ratio test, Wald test and Score (logrank) test. Kaplan-Meier curves and visualization *via* forest plots with a confidence interval of 95% (95% CI) were calculated based on existing survival data and combined survival curves. Beside p-value, hazard ratio (HR), time-dependent survival rate and median survival time have been calculated. Gene set enrichment analysis (GSEA) was performed using the WEB-based Gene SeT AnaLysis Toolkit (WebGestalt) website (48). In order to investigate certain signaling pathways, differential gene expression analysis was visualized on molecular network maps. These maps were provided by KEGG (49).

In order to overcome the problem of repeated statistical testing, p-values were corrected by utilizing the false discovery rate (FDR). Results were considered significant at $p < 0.05$ after adjustment (50).

# 3 RESULTS

## 3.1 Gene Expression in CAF-Associated Pathways Negatively Impact Patient's Overall Survival

Predictably, outcome after chemotherapy is linked to reduced overall survival ($p < 0.05$). However, in multivariate analysis, it turned out that this influence was independent of other clinical covariates like age at time of diagnosis, tumor grading or tumor stage ($p < 0.05$, **Supplemental Table 4**), thereby establishing therapy outcome as a sole determining factor influencing OS. Additionally, the influence of age, grading and stage on therapy outcome (RFS < 6 months after therapy completion) was also examined. None of those influenced therapy outcome in a multifactorial analysis, proving it an independent factor (**Supplemental Table 5**).

Genes associated with TGF-β or PI3K-Akt signaling were subjected to a cox proportional hazard model in order to assert their expressions' influence on either OS or RFS (**Figure 2A**). Overall, 13 genes were linked to reduced OS ($n = 9$) or RFS ($n = 6$). Of those genes only SMURF2 and RHOA overlapped between both survival variables (**Figure 2B**).

## 3.2 High Expression of CAF-Associated Genes Drives Therapy Failure, While Also Impacting Patients' Survival

While the expression of certain genes influences patients' survival, it may also be possible that specific genes may constitute a gene expression signature, which can be correlated to therapy outcome. As such, all genes involved in TGF-β and PI3K-Akt signaling were subjected to differential expression analysis in dependance of this outcome. All in all, six genes are linked to therapy failure ($p < 0.05$, **Table 1**). Furthermore, differential expression of those genes was analyzed whether they were not (Resistant, "R") or still responding to chemotherapy (ongoing response, "onR"). Strikingly, the expression of all genes was increased in patients without long-term response to chemotherapy (**Figure 3**).

Two genes were also linked to OS (CGA, $p= 0.018$) and RFS (MMP13, $p= 0.0074$). Group-based survival differences were asserted by cox proportional hazard models. The patient groups were separated based on whether genes displayed high or low expression rates. In either case, high expression of both MMP13 and CGA were detrimental to patients' survival (**Supplemental Figure 1**). Moreover, we validated the correlation between gene expression levels and the occurrence of desmoplastic tumor stroma. The presence of CAFs within the tumor, quantitatively depicted as FAP positivity, was strongly linked to the expression of MMP13, AKT1, TGFB3 and TGFBR2, among other factors (**Supplemental Table 6**).

## 3.3 Increased Activity of Signaling Pathways Involved in Growth Factor and Fibroblast Signaling Is Associated With Novel Cell Death Pathways and Cytokine-Cytokine Receptor Interactions

In the next step, single gene associations with outcome needed to be put into context with larger signaling pathways. For this purpose, a gene set enrichment analysis (GSEA) was performed (**Figure 4A**), followed by KEGG pathways analysis (**Figures 4B**, **5**). The latter allowed for accurate examination of differential expression, depending on durable therapy responses, in specific pathways.

According to GSEA, genes in association with worsen therapy outcome were highly expressed in signaling pathways linked to "Necroptosis", "Cytokine-cytokine receptor interaction" and "Alcoholism". However, they were barely expressed in signaling pathways linked to "Hypertrophic cardiomyopathy", "Malaria" and "Amoebiasis" (**Figure 4A**).

It is especially interesting that one of the top listed pathways regarding overexpression of genes correlated to poor outcome is "Cytokine-cytokine receptor interaction" (**Figure 4A**). This necessitated a more precise look into the underlaying pathways (**Figure 4B**). Apparently, ligands for alpha-and beta interferon receptors are highly expressed. Furthermore, TGFB1 and TGFBR2 were highly expressed as well, which indicates high TGF-β activity. Other factors, which also showed high expression were FASLG, IL-1A, CXCL-12, NODAL and GDF7. TGF-β signaling may also hint towards fibroblast activity which is underlined by looking at "Pathways in Cancer" (**Supplemental Figure 2**). Two important factors, often linked to fibroblast activity FGF and PDGF (and PDGFR) display strong expression in association with poor therapy outcome. Their downstream signaling *via* Ras finally leads to activation of matrix-metalloproteinases (MMPs) like MMP13. Other important signaling pathways, which are also linked to fibroblast activity are the TGF-β- (**Figure 5A**), PI3K-Akt- (**Figure 5B**), and MAPK (**Figure 5C**) signaling pathways. Most genes within those pathways display strong expression in case of therapy failure. It should be noted that TGF-β signaling is still partially carried out by canonical SMAD signaling, with SMAD2/SMAD3 still being active, while the inhibitory SMAD6/7 are seemingly not expressed in the group responding poorly to chemotherapy (**Figure 5A**). However, in comparison, genes linked to non-canonical TGF-β signaling (MAPK and PI3K-Akt signaling) are more strongly expressed as indicated by intensive red coloring (**Figures 5B, C**)

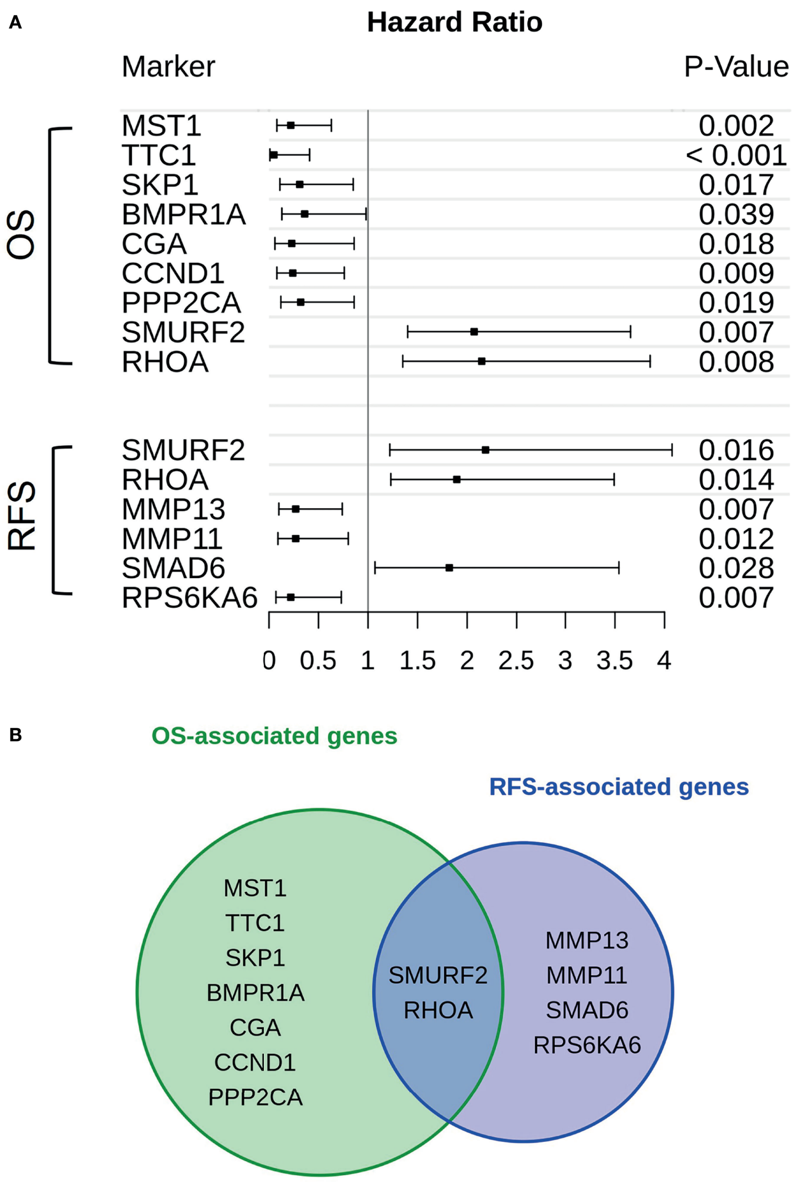

**FIGURE 2** | Genes in association with CAF-signaling impact patients' survival. **(A)** For every gene that is hinted to impact patients' overall survival (upper group) or recurrence-free survival (lower group) hazard ratios were calculated. The span of these values, including a risk estimate was visualized *via* forest plot. Of the original 24 patients available, only 19 were used in the calculations. Five patients were excluded due to missing survival data. The p-value was calculated by Score-logrank test. **(B)** Both groups of genes, either in association with overall survival (green) or recurrence-free survival (blue), were compared and overlaps between them were also highlighted.

**TABLE 1** | Genes associated with poor therapy outcome after chemotherapy ($p < 0.05$).

| Associated genes: | P-value: |
|---|---|
| MMP13 | 0.007 |
| EPHA3 | 0.044 |
| PSMD9 | 0.023 |
| PITX2 | 0.027 |
| PHLIPP1 | 0.0086 |
| CGA | 0.049 |

## 3.4 Pronounced Non-Canonical TGF-ß Signaling Can Be Found in Patients Responding Poorly to Chemotherapy Across Various Epithelial Ovarian Cancer Subtypes

Similar observations regarding those specific pathways have been made in the validation cohort. In contrast to the actual investigation cohort, the validation cohort was heterogenous

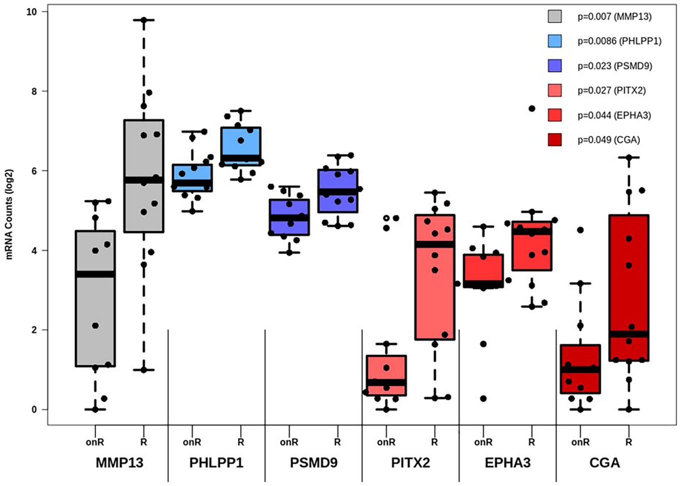

**FIGURE 3** | Differential expression analysis of genes affecting therapy outcome. For each gene the number of measured counts were compared between patients still responding to therapy (Ongoing Response, "onR") or not (Resistant, "R"). Group-based expression differences were visualized by p-value, which was calculated by Wilcoxon Mann-Whitney rank sum test.

(see *Study and Cohort Design*). Thus, it was composed of different malignant entities, including HGSOC. Similarly, TGF-β, MAPK-, PI3K-Akt activity was increased when correlated to therapy outcome (**Supplemental Figures 3–7**), thereby verifying the influence of CAF-associated signaling on outcome in EOC.

## 4 DISCUSSION

Among the four EOC subtypes mentioned in the introduction, HGSOC is the most aggressive (4, 7). Fortunately, its high proliferation makes HGSOC rather susceptible towards cytotoxic chemotherapy (3–5, 7). For this reason, chemotherapy has been a cornerstone in clinical HGSOC management for decades (8–10). One of the biggest problems, however, is the disease relapse of HGSOC after initial tumor regression upon receiving chemotherapy (10, 12). This occurs in the majority of patients, creating a crucial necessity to explore the mechanical background behind those relapses and also to provide biomarkers that help stratifying patients for chemotherapy (10, 12).

A detailed look into the activities of the tumor micro environment (TME) may be helpful to unveil reasons for poor therapy outcome in HGSOCs. As a key factor within TME, CAFs employ miscellaneous functions. One of their best-known functions is the generation of fibronectin and collagen, two substantial components of stroma tissue and the extracellular matrix. Simultaneously, they counterbalance this activity by production of matrix-metalloproteases (25, 28, 33). The amassment of stroma within tissue is also called desmoplasia or DSR, a process often encountered in tumors (51, 52). Besides organization of the extracellular matrix, CAFs employ humoral functions as well by releasing various cytokines. TGF-β is perhaps the most well-studied of them. It has a multitude of different functions like protecting cells from apoptosis and enabling cell cycle arrest. Furthermore, it regulates the immune system by inhibiting effector functions of CD8 positive lymphocytes, NK cells and dendritic cells, while simultaneously promoting regulatory T cells (53–55). All these effects can also benefit the tumor, thereby explaining TGF-βs' often perceived dual role in cancer (56). While many effects of TGF-β are mediated *via* the SMAD signaling cascade (56, 57), it may also initiate factors related to MAPK and PI3K-Akt signaling pathways (non-canonical TGF-β signaling) (58, 59). These pathways are linked with cell proliferation as well as migration, thereby also enhancing tumor progression (31, 32).

Based on histological and genetic subtyping, five variants of HGSOC can be distinguished. One of them is the mesenchymal subtype which is characterized by occurrence of DSR. Furthermore, this subtype is also associated with a poor survival prognosis (22, 25, 60). Therefore, we aimed to identify DSR in HGSOC patients and link it to poor outcome after platinum-based chemotherapy in patients, defined as having an RFS shorter than 6 months after therapy completion. DSR was supposed to be identified based on the expression of specific genes and activity of specific signaling pathways like MAPK, PI3K-Akt and TGF-β signaling.

Of the six genes associated with therapy failure, CGA and MMP13 are certainly the most outstanding, since they were also linked to reduced OS and RFS, respectively (**Supplemental Figure 1**). MMP13 plays a crucial role for epithelial-mesenchymal transition (EMT) and therefore for cancer progression (61). Furthermore, HIF-1a induced MMP13 expression appears to promote invasion and metastasis in ovarian cancer as well (62). CAFs can also induce EMT *via* secretion of TGF-β1, which then leads to invasion and metastasis (40). The secretion of TGF-β by CAFs additionally promote MMP13 activity (63, 64). CGA encodes for the conserved alpha chain of human gonadotropins (LH, FSH, hCG). In ovarian

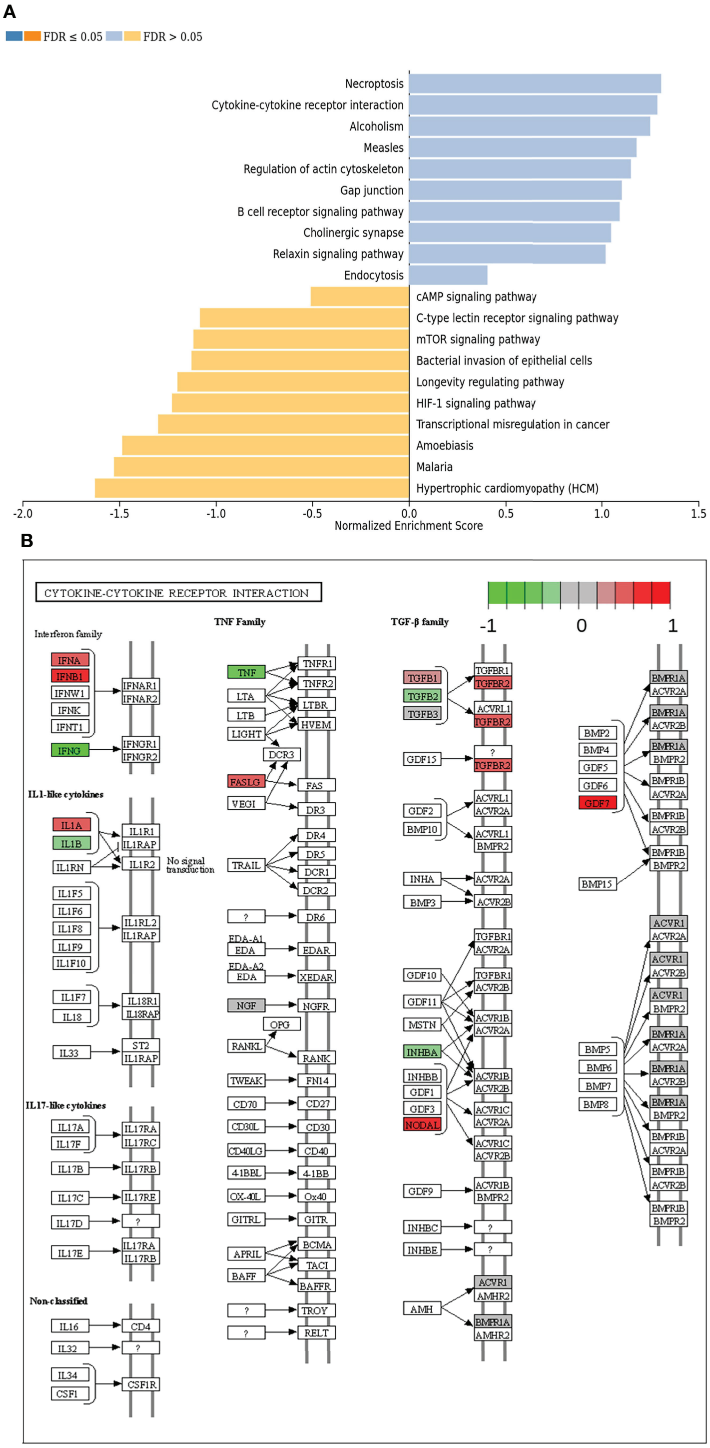

**FIGURE 4** | **(A)** Gene set enrichment analysis of differentially expressed genes regarding therapy outcome in various signaling pathways. Blue: Genes in association with therapy outcome are strongly expressed in those pathways. Yellow: Genes in association with therapy outcome are barely expressed in those pathways. FDR: False Discovery rate. Due to testing the expression of certain genes in specific pathways multiple times, the p-values are adjusted for the naturally occurring variance by the FDR method. **(B)** Genes expressed in association with "Cytokine-cytokine receptor interaction" and therapy failure in HGSOC. The color code indicates at differential gene expression whether the patients did not (red) or did respond well to chemotherapy (green). This molecular network map stems from the Kyoto Encyclopedia of Genes and Genomes (KEGG) database.

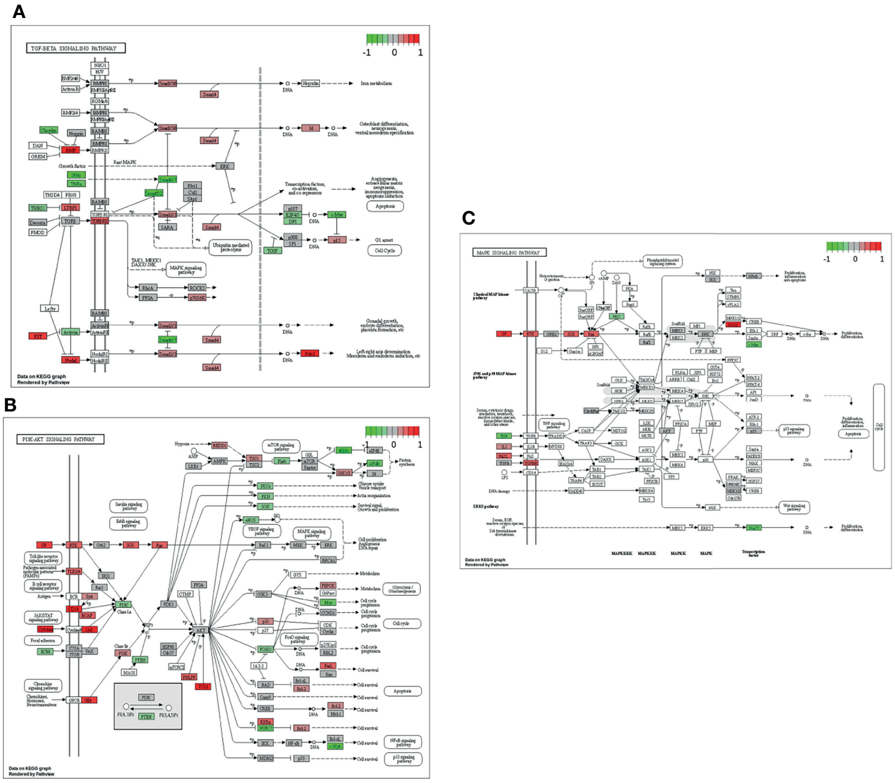

**FIGURE 5** | Genes expressed in association with the TGF-β **(A)**, PI3K-Akt **(B)** and MAPK **(C)** signaling pathways and therapy outcome in HGSOC. The color code indicates at differential gene expression whether the patients did not (red) or did respond well to chemotherapy (green). This molecular network map stems from the Kyoto Encyclopedia of Genes and Genomes (KEGG) database.

cancer, the levels of gonadotropins (LH/FSH) are increased. Additionally, it seems they are able to facilitate invasion and metastasis by overexpression of cyclooxygenase-2 (65). Chorionic gonadotropin levels are significantly increased when comparing benign and malignant tumors. Also, gonadotropin levels moderately correlate with tumor staging and grading (66). Taken together, both MMP13 and CGA are known to facilitate invasion and metastasis, which does explain their well-founded impact on patients' outcome (**Supplemental Figure 1**). MMP13 is also strongly linked to CAFs and TGF-β signaling (40, 63, 64).

EPHA3 is a receptor tyrosine-kinase that is involved in various cell-cell interactions. It is implicated to influence angiogenesis and metastasis among other factors in various malignancies (67), especially gastric cancer (68, 69). PSMD9 is a subunit of the 26s proteasome and is mainly known for regulatory functions. Low expression of PSMD9 was discussed as a biomarker to assess patients' suitability for radiation therapy in breast cancer, since cells with low expression were more vulnerable for radiation treatment (70). The transcription factor PITX2 has already been investigated in ovarian cancer (71, 72). This factor promotes tumor invasion and is activated by TGF-β and Activin-A (72). Apparently PITX2 is also an important instigator of epithelial-to-mesenchymal transition in ovarian cancer (72). PITX2 and EPH3, especially, are both linked to cancer progression and metastasis, thereby correlating with patients displaying poor therapy outcome. Additionally, PITX2 expression induced by CAFs can initiate EMT (40, 72). It is indicated, that PITX2 activity is enhanced by TGF-β *via* SMAD signaling in patients displaying poor therapy outcome within our cohort (**Figure 5A**).

Though TGF-β signaling, more specifically SMAD-mediated TGF-β signaling, may be considered to be strongly activated according to our results, it should be noted that all downstream components appear weakly expressed, when compared to Cytokine-Cytokine signaling, MAPK signaling or PI3K-Akt signaling (**Figures 4B, 5B, C**). This led us to the conclusion that TGF-β could function by non-canonical signaling *via* Ras, MAPK and PI3K-Akt. Facilitated by TGF-β, they also promote CAF activity (31, 32, 39, 40, 58, 59). **Supplemental Figure 2** displays a strong expression of FGF, PDGF and HGF in patients with poor therapy outcome. All three factors are strongly linked to CAF activity and DSR (39, 73). An enhanced DSR is also associated with resistance to chemotherapy as drug delivery is compromised by the physical barrier provided by the stroma (40, 74). Summing up, the correlation of MMP13 and PITX2 with poor therapy outcome (**Table 1**) as well the strong gene expression in CAF-associated pathways (**Supplemental Figure 2** and **Figures 4**, **5**) suggest an important role of DSR in patients responding poorly to chemotherapy. CAFs and associated processes have been studied extensively in EOCs (75–77) and even HGSOCs (78). Our study contributes to present knowledge by adding a direct comparison of

CAF-associated signaling pathways in both HGSOC and EOC in general. Taken together, our study underlines the prognostic value of CAFs and its importance for clinical decisions. As to this day poor response to platinum-based chemotherapy is a common problem in HGSOC, predictive biomarkers are urgently needed for the development of individualized treatment regimens. Patient stratification for occurrence of DSR or CAFs before platinum-based may be promising for development of models to predict patients' therapy response in the future.

## DATA AVAILABILITY STATEMENT

The original contributions presented in the study are included in the article/**Supplementary Material**. Further inquiries can be directed to the corresponding author.

## ETHICS STATEMENT

The studies involving human participants were reviewed and approved by Ethics Committee of the Medical Faculty of the University Duisburg-Essen (protocol no. 16-6916-BO). The patients/participants provided their written informed consent to participate in this study.

## AUTHOR CONTRIBUTIONS

Conceptualization: PB and FM. Methodology: MW, EM, SB, and FM. Software: MW and FM. Validation: EM, SB, AB, PM, PB, and FM. Formal analysis: MW, EM, SB, AB, PM, PB, and FM. Investigation: MW, EM, SB, AB, and PB. Resources: KS and RK. Data curation: MW, EM, SB, AB, PM, PB, and FM. Writing-original Draft preparation: MW, PB, and FM. Writing-review and editing: All authors. Visualisation: MW and FM. Supervision: FM. Project administration: KS, RK, PB, and FM. Funding acquisition: KS, RK, PB, and FM. All authors have read and agreed to the published version of the manuscript.

## SUPPLEMENTARY MATERIAL

The Supplementary Material for this article can be found online at: https://www.frontiersin.org/articles/10.3389/fonc.2022.798680/full#supplementary-material

## REFERENCES

1. Sung H, Ferlay J, Siegel RL, Laversanne M, Soerjomataram I, Jemal A, et al. Global Cancer Statistics 2020: GLOBOCAN Estimates of Incidence and Mortality Worldwide for 36 Cancers in 185 Countries. *CA: A Cancer J Clin* (2021) 71(3):209–49. doi: 10.3322/caac.21660
2. Jelovac D, Armstrong DK. Recent Progress in the Diagnosis and Treatment of Ovarian Cancer. *CA: Cancer J Clin* (2011) 61(3):183–203. doi: 10.3322/caac.20113
3. Koshiyama M, Matsumura N, Konishi I. Subtypes of Ovarian Cancer and Ovarian Cancer Screening. *Diagnostics (Basel Switzerland).* (2017) 7(1):12. doi: 10.3390/diagnostics7010012
4. Kurman RJ, Shih Ie M. The Dualistic Model of Ovarian Carcinogenesis: Revisited, Revised, and Expanded. *Am J Pathol* (2016) 186(4):733–47. doi: 10.1016/j.ajpath.2015.11.011
5. Cook DP, Vanderhyden BC. Ovarian Cancer and the Evolution of Subtype Classifications Using Transcriptional Profiling†. *Biol Reprod* (2019) 101 (3):645–58. doi: 10.1093/biolre/ioz099
6. Kurman RJC, Herrington ML, Simon C. World Health Organisation Classification of Tumours of the Female Reproductive Organs. *Int Agency Res Cancer* (2014) 6:316.
7. Bowtell DD, Böhm S, Ahmed AA, Aspuria PJ, Bast RC Jr., Beral V, et al. Rethinking Ovarian Cancer II: Reducing Mortality From High-Grade Serous Ovarian Cancer. *Nat Rev Cancer* (2015) 15(11):668–79. doi: 10.1038/nrc4019
8. Jayson GC, Kohn EC, Kitchener HC, Ledermann JA. Ovarian Cancer. *Lancet (London England)* (2014) 384(9951):1376–88. doi: 10.1016/S0140-6736(13) 62146-7
9. Markman M. Optimizing Primary Chemotherapy in Ovarian Cancer. *Hematology Oncol Clinics North America* (2003) 17(4):957–68, viii. doi: 10.1016/S0889-8588(03)00058-3
10. Matulonis UA, Sood AK, Fallowfield L, Howitt BE, Sehouli J, Karlan BY. Ovarian Cancer. *Nat Rev Dis Primers* (2016) 2:16061. doi: 10.1038/nrdp.2016.61
11. Oza AM, Cook AD, Pfisterer J, Embleton A, Ledermann JA, Pujade-Lauraine E, et al. Standard Chemotherapy With or Without Bevacizumab for Women With Newly Diagnosed Ovarian Cancer (ICON7): Overall Survival Results of a Phase 3 Randomised Trial. *Lancet Oncol* (2015) 16(8):928–36. doi: 10.1016/S1470-2045(15)00086-8
12. Bast RC Jr., Hennessy B, Mills GB. The Biology of Ovarian Cancer: New Opportunities for Translation. *Nat Rev Cancer* (2009) 9(6):415–28. doi: 10.1038/nrc2644
13. Kim S, Han Y, Kim SI, Kim H-S, Kim SJ, Song YS. Tumor Evolution and Chemoresistance in Ovarian Cancer. *NPJ Precis Oncol* (2018) 2(1):20. doi: 10.1038/s41698-018-0063-0
14. Glasgow MA, Argenta P, Abrahante JE, Shetty M, Talukdar S, Croonquist PA, et al. Biological Insights Into Chemotherapy Resistance in Ovarian Cancer. *Int J Mol Sci* (2019) 20(9):2131. doi: 10.3390/ijms20092131
15. Network NCC. *Ovarian Cancer Including Fallopian Tube Cancer and Primary Peritoneal Cancer (Version 3.2021)* (2021). Available at: https://www.nccn.org/professionals/physician_gls/pdf/ovarian.pdf.
16. Tomao F, Bardhi E, Di Pinto A, Sassu CM, Biagioli E, Petrella MC, et al. Parp Inhibitors as Maintenance Treatment in Platinum Sensitive Recurrent Ovarian Cancer: An Updated Meta-Analysis of Randomized Clinical Trials According to BRCA Mutational Status. *Cancer Treat Rev* (2019) 80:101909. doi: 10.1016/j.ctrv.2019.101909
17. Alkema NG, Wisman GBA, van der Zee AGJ, van Vugt MATM, de Jong S. Studying Platinum Sensitivity and Resistance in High-Grade Serous Ovarian Cancer: Different Models for Different Questions. *Drug Resist Updat* (2016) 24:55–69. doi: 10.1016/j.drup.2015.11.005
18. Barber EL, Zsiros E, Lurain JR, Rademaker A, Schink JC, Neubauer NL. The Combination of Intravenous Bevacizumab and Metronomic Oral Cyclophosphamide is an Effective Regimen for Platinum-Resistant Recurrent Ovarian Cancer. *J Gynecol Oncol* (2013) 24(3):258–64. doi: 10.3802/jgo.2013.24.3.258
19. Pujade-Lauraine E, Hilpert F, Weber B, Reuss A, Poveda A, Kristensen G, et al. Bevacizumab Combined With Chemotherapy for Platinum-Resistant Recurrent Ovarian Cancer: The AURELIA Open-Label Randomized Phase III Trial. *J Clin Oncol* (2014) 32(13):1302–8. doi: 10.1200/JCO.2013.51.4489
20. Tothill RW, Tinker AV, George J, Brown R, Fox SB, Lade S, et al. Novel Molecular Subtypes of Serous and Endometrioid Ovarian Cancer Linked to Clinical Outcome. *Clin Cancer Res: Off J Am Assoc Cancer Res* (2008) 14 (16):5198–208. doi: 10.1158/1078-0432.CCR-08-0196
21. Konecny GE, Wang C, Hamidi H, Winterhoff B, Kalli KR, Dering J, et al. Prognostic and Therapeutic Relevance of Molecular Subtypes in High-Grade Serous Ovarian Cancer. *J Natl Cancer Inst* (2014) 106(10):dju249. doi: 10.1093/jnci/dju249

22. Verhaak RG, Tamayo P, Yang JY, Hubbard D, Zhang H, Creighton CJ, et al. Prognostically Relevant Gene Signatures of High-Grade Serous Ovarian Carcinoma. *J Clin Invest* (2013) 123(1):517–25. doi: 10.1172/JCI65833
23. Multhaupt HAB, Leitinger B, Gullberg D, Couchman JR. Extracellular Matrix Component Signaling in Cancer. *Adv Drug Deliv Rev* (2016) 97:28–40. doi: 10.1016/j.addr.2015.10.013
24. Su S, Chen J, Yao H, Liu J, Yu S, Lao L, et al. CD10+GPR77+ Cancer-Associated Fibroblasts Promote Cancer Formation and Chemoresistance by Sustaining Cancer Stemness. *Cell* (2018) 172(4):841–56.e16. doi: 10.1016/j.cell.2018.01.009
25. Zhang Q, Wang C, Cliby WA. Cancer-Associated Stroma Significantly Contributes to the Mesenchymal Subtype Signature of Serous Ovarian Cancer. *Gynecol Oncol* (2019) 152(2):368–74. doi: 10.1016/j.ygyno.2018.11.014
26. Costa A, Kieffer Y, Scholer-Dahirel A, Pelon F, Bourachot B, Cardon M, et al. Fibroblast Heterogeneity and Immunosuppressive Environment in Human Breast Cancer. *Cancer Cell* (2018) 33(3):463–79.e10. doi: 10.1016/j.ccell.2018.01.011
27. Costa-Almeida R, Soares R, Granja PL. Fibroblasts as Maestros Orchestrating Tissue Regeneration. *J Tissue Eng Regen Med* (2018) 12(1):240–51. doi: 10.1002/term.2405
28. Kalluri R. The Biology and Function of Fibroblasts in Cancer. *Nat Rev Cancer* (2016) 16(9):582–98. doi: 10.1038/nrc.2016.73
29. Erez N, Truitt M, Olson P, Arron ST, Hanahan D. Cancer-Associated Fibroblasts Are Activated in Incipient Neoplasia to Orchestrate Tumor-Promoting Inflammation in an NF-kappaB-Dependent Manner. *Cancer Cell* (2010) 17(2):135–47. doi: 10.1016/j.ccr.2009.12.041
30. Kobayashi H, Enomoto A, Woods SL, Burt AD, Takahashi M, Worthley DL. Cancer-Associated Fibroblasts in Gastrointestinal Cancer. *Nat Rev Gastroenterol Hepatol* (2019) 16(5):282–95. doi: 10.1038/s41575-019-0115-0
31. Hastings JF, Skhinas JN, Fey D, Croucher DR, Cox TR. The Extracellular Matrix as a Key Regulator of Intracellular Signalling Networks. *Br J Pharmacol* (2019) 176(1):82–92. doi: 10.1111/bph.14195
32. Mieulet V, Garnier C, Kieffer Y, Guilbert T, Nemati F, Marangoni E, et al. Stiffness Increases With Myofibroblast Content and Collagen Density in Mesenchymal High Grade Serous Ovarian Cancer. *Sci Rep* (2021) 11(1):4219. doi: 10.1038/s41598-021-83685-0
33. Paraiso KH, Smalley KS. Fibroblast-Mediated Drug Resistance in Cancer. *Biochem Pharmacol* (2013) 85(8):1033–41. doi: 10.1016/j.bcp.2013.01.018
34. Özdemir BC, Pentcheva-Hoang T, Carstens JL, Zheng X, Wu CC, Simpson TR, et al. Depletion of Carcinoma-Associated Fibroblasts and Fibrosis Induces Immunosuppression and Accelerates Pancreas Cancer With Reduced Survival. *Cancer Cell* (2014) 25(6):719–34. doi: 10.1016/j.ccr.2014.04.005
35. Farmer P, Bonnefoi H, Anderle P, Cameron D, Wirapati P, Becette V, et al. A Stroma-Related Gene Signature Predicts Resistance to Neoadjuvant Chemotherapy in Breast Cancer. *Nat Med* (2009) 15(1):68–74. doi: 10.1038/nm.1908
36. Mairinger F, Bankfalvi A, Schmid KW, Mairinger E, Mach P, Walter RF, et al. Digital Immune-Related Gene Expression Signatures In High-Grade Serous Ovarian Carcinoma: Developing Prediction Models For Platinum Response. *Cancer Manage Res* (2019) 11:9571–83. doi: 10.2147/CMAR.S219872
37. Hanahan D, Weinberg RA. Hallmarks of Cancer: The Next Generation. *Cell* (2011) 144(5):646–74. doi: 10.1016/j.cell.2011.02.013
38. Räsänen K, Vaheri A. Activation of Fibroblasts in Cancer Stroma. *Exp Cell Res* (2010) 316(17):2713–22. doi: 10.1016/j.yexcr.2010.04.032
39. Heneberg P. Paracrine Tumor Signaling Induces Transdifferentiation of Surrounding Fibroblasts. *Crit Rev Oncol Hematol* (2016) 97:303–11. doi: 10.1016/j.critrevonc.2015.09.008
40. D'Arcangelo E, Wu NC, Cadavid JL, McGuigan AP. The Life Cycle of Cancer-Associated Fibroblasts Within the Tumour Stroma and its Importance in Disease Outcome. *Br J Cancer* (2020) 122(7):931–42. doi: 10.1038/s41416-019-0705-1
41. James D, Brierley MKG, Wittekind C. *TNM Classification of Malignant Tumours. 8th*. Hoboken, New Jersey: Wiley-Blackwell, Co-affiliated publisher, Union for International Cancer Control (UICC): Geneva, Switzerland (2017). 6th January 2017.
42. Royston JP. Algorithm AS 181: The W Test for Normality. *J R Stat Soc Ser C (Appl Statist)* (1982) 31(2):176–80. doi: 10.2307/2347986
43. Bauer DF. Constructing Confidence Sets Using Rank Statistics. *J Am Stat Assoc* (1972) 67(339):687–90. doi: 10.1080/01621459.1972.10481279
44. Tan JX, Dao FY, Lv H, Feng PM, Ding H. Identifying Phage Virion Proteins by Using Two-Step Feature Selection Methods. *Mol (Basel Switzerland).* (2018) 23(8):2000. doi: 10.3390/molecules23082000
45. Yin XH, Wang ZQ, Yang SZ, Jia HY, Shi M. Clinical Observation of Laparoscopic Radical Hysterectomy for Cervical Cancer. *Int J Clin Exp Med* (2014) 7(5):1373–7.
46. Yang L, Wang J, Wang H, Lv Y, Zuo Y, Jiang W. Analysis and Identification of Toxin Targets by Topological Properties in Protein-Protein Interaction Network. *J Theor Biol* (2014) 349:82–91. doi: 10.1016/j.jtbi.2014.02.001
47. Yang L, Wang J, Wang H, Lv Y, Zuo Y, Li X, et al. Analysis and Identification of Essential Genes in Humans Using Topological Properties and Biological Information. *Gene* (2014) 551(2):138–51. doi: 10.1016/j.gene.2014.08.046
48. Liao Y, Wang J, Jaehnig EJ, Shi Z, Zhang B. WebGestalt 2019: Gene Set Analysis Toolkit With Revamped UIs and APIs. *Nucleic Acids Res* (2019) 47(W1):W199–205. doi: 10.1093/nar/gkz401
49. Kanehisa M, Goto S. KEGG: Kyoto Encyclopedia of Genes and Genomes. *Nucleic Acids Res* (2000) 28(1):27–30. doi: 10.1093/nar/28.1.27
50. Long C, Li W, Liang P, Liu S, Zuo Y. Transcriptome Comparisons of Multi-Species Identify Differential Genome Activation of Mammals Embryogenesis. *IEEE Access* (2019) 7:7794–802. doi: 10.1109/ACCESS.2018.2889809
51. Zeltz C, Primac I, Erusappan P, Alam J, Noel A, Gullberg D. Cancer-Associated Fibroblasts in Desmoplastic Tumors: Emerging Role of Integrins. *Semin Cancer Biol* (2020) 62:166–81. doi: 10.1016/j.semcancer.2019.08.004
52. Whatcott CJ, Diep CH, Jiang P, Watanabe A, LoBello J, Sima C, et al. Desmoplasia in Primary Tumors and Metastatic Lesions of Pancreatic Cancer. *Clin Cancer Res: Off J Am Assoc Cancer Res* (2015) 21(15):3561–8. doi: 10.1158/1078-0432.CCR-14-1051
53. Batlle E, Massagué J. Transforming Growth Factor-β Signaling in Immunity and Cancer. *Immunity* (2019) 50(4):924–40. doi: 10.1016/j.immuni.2019.03.024
54. Flavell RA, Sanjabi S, Wrzesinski SH, Licona-Limón P. The Polarization of Immune Cells in the Tumour Environment by TGFbeta. *Nat Rev Immunol* (2010) 10(8):554–67. doi: 10.1038/nri2808
55. Sanjabi S, Oh SA, Li MO. Regulation of the Immune Response by TGF-β: From Conception to Autoimmunity and Infection. *Cold Spring Harbor Perspect Biol* (2017) 9(6):a022236. doi: 10.1101/cshperspect.a022236
56. Meulmeester E, Ten Dijke P. The Dynamic Roles of TGF-β in Cancer. *J Pathol* (2011) 223(2):205–18. doi: 10.1002/path.2785
57. Ábrigo J, Campos F, Simon F, Riedel C, Cabrera D, Vilos C, et al. TGF-β Requires the Activation of Canonical and non-Canonical Signalling Pathways to Induce Skeletal Muscle Atrophy. *Biol Chem* (2018) 399(3):253–64. doi: 10.1515/hsz-2017-0217
58. Lee MK, Pardoux C, Hall MC, Lee PS, Warburton D, Qing J, et al. TGF-Beta Activates Erk MAP Kinase Signalling Through Direct Phosphorylation of ShcA. *EMBO J* (2007) 26(17):3957–67. doi: 10.1038/sj.emboj.7601818
59. Heldin CH, Moustakas A. Signaling Receptors for TGF-β Family Members. *Cold Spring Harbor Perspect Biol* (2016) 8(8):a022053. doi: 10.1101/cshperspect.a022053
60. Chirshev E, Hojo N, Bertucci A, Sanderman L, Nguyen A, Wang H, et al. Epithelial/mesenchymal Heterogeneity of High-Grade Serous Ovarian Carcinoma Samples Correlates With miRNA Let-7 Levels and Predicts Tumor Growth and Metastasis. *Mol Oncol* (2020) 14(11):2796–813. doi: 10.1002/1878-0261.12762
61. Li RM, Nai MM, Duan SJ, Li SX, Yin BN, An F, et al. Down-Expression of GOLM1 Enhances the Chemo-Sensitivity of Cervical Cancer to Methotrexate Through Modulation of the MMP13/EMT Axis. *Am J Cancer Res* (2018) 8(6):964–80.
62. Zhang H, Yang Q, Lian X, Jiang P, Cui J. Hypoxia-Inducible Factor-1α (HIF-1α) Promotes Hypoxia-Induced Invasion and Metastasis in Ovarian Cancer by Targeting Matrix Metallopeptidase 13 (Mmp13). *Med Sci Monit: Int Med J Exp Clin Res* (2019) 25:7202–8. doi: 10.12659/MSM.916886
63. Delany AM, Canalis E. The Metastasis-Associated Metalloproteinase Stromelysin-3 is Induced by Transforming Growth Factor-β in Osteoblasts and Fibroblasts. *Endocrinology* (2001) 142(4):1561–6. doi: 10.1210/endo.142.4.8072

64. Overall C, Wrana J, Sodek J. Transcriptional and Post-Transcriptional Regulation of 72-kDa Gelatinase/Type IV Collagenase by Transforming Growth Factor-Beta 1 in Human Fibroblasts. Comparisons with collagenase and tissue inhibitor of matrix metalloproteinase gene expression. *J Biol Chem* (1991) 266(21):14064–71. doi: 10.1016/S0021-9258(18)92810-3
65. Feng D, Zhao T, Yan K, Liang H, Liang J, Zhou Y, et al. Gonadotropins Promote Human Ovarian Cancer Cell Migration and Invasion *via* a Cyclooxygenase 2-Dependent Pathway. *Oncol Rep* (2017) 38(2):1091–8. doi: 10.3892/or.2017.5784
66. Lenhard M, Tsvilina A, Schumacher L, Kupka M, Ditsch N, Mayr D, et al. Human Chorionic Gonadotropin and its Relation to Grade, Stage and Patient Survival in Ovarian Cancer. *BMC Cancer* (2012) 12(1):2. doi: 10.1186/1471-2407-12-2
67. Janes PW, Slape CI, Farnsworth RH, Atapattu L, Scott AM, Vail ME. EphA3 Biology and Cancer. *Growth Factors* (2014) 32(6):176–89. doi: 10.3109/08977194.2014.982276
68. Nasri B, Inokuchi M, Ishikawa T, Uetake H, Takagi Y, Otsuki S, et al. High Expression of EphA3 (Erythropoietin-Producing Hepatocellular A3) in Gastric Cancer is Associated With Metastasis and Poor Survival. *BMC Clin Pathol* (2017) 17:8. doi: 10.1186/s12907-017-0047-y
69. Lv XY, Wang J, Huang F, Wang P, Zhou JG, Wei B, et al. EphA3 Contributes to Tumor Growth and Angiogenesis in Human Gastric Cancer Cells. *Oncol Rep* (2018) 40(4):2408–16. doi: 10.3892/or.2018.6586
70. Langlands FE, Dodwell D, Hanby AM, Horgan K, Millican-Slater RA, Speirs V, et al. PSMD9 Expression Predicts Radiotherapy Response in Breast Cancer. *Mol Cancer* (2014) 13:73. doi: 10.1186/1476-4598-13-73
71. Frederic F, Chan D, Liu V, Leung T, Cheung A, Ngan H. Increased Expression of PITX2 Transcription Factor Contributes to Ovarian Cancer Progression. *PloS One* (2012) 7:e37076. doi: 10.1371/journal.pone.0037076
72. Basu M, Bhattacharya R, Ray U, Mukhopadhyay S, Chatterjee U, Roy SS. Invasion of Ovarian Cancer Cells is Induced Bypitx2-Mediated Activation of TGF-β and Activin-A. *Mol Cancer* (2015) 14:162. doi: 10.1186/s12943-015-0433-y
73. Wu F, Yang J, Liu J, Wang Y, Mu J, Zeng Q, et al. Signaling Pathways in Cancer-Associated Fibroblasts and Targeted Therapy for Cancer. *Signal Transduct Targeted Ther* (2021) 6(1):218. doi: 10.1038/s41392-021-00641-0
74. Alexander J, Cukierman E. Stromal Dynamic Reciprocity in Cancer: Intricacies of Fibroblastic-ECM Interactions. *Curr Opin Cell Biol* (2016) 42:80–93. doi: 10.1016/j.ceb.2016.05.002
75. Cai J, Tang H, Xu L, Wang X, Yang C, Ruan S, et al. Fibroblasts in Omentum Activated by Tumor Cells Promote Ovarian Cancer Growth, Adhesion and Invasiveness. *Carcinogenesis* (2012) 33(1):20–9. doi: 10.1093/carcin/bgr230
76. Wang L, Zhang F, Cui JY, Chen L, Chen YT, Liu BW. CAFs Enhance Paclitaxel Resistance by Inducing EMT Through the IL–6/JAK2/STAT3 Pathway. *Oncol Rep* (2018) 39(5):2081–90. doi: 10.3892/or.2018.6311
77. Zhang F, Cui J-y, Gao H-f, Yu H, Gao F-f, Chen J-l, et al. Cancer-Associated Fibroblasts Induce Epithelial-Mesenchymal Transition and Cisplatin Resistance in Ovarian Cancer *via* CXCL12/CXCR4 Axis. *Future Oncol* (2020) 16(32):2619–33. doi: 10.2217/fon-2020-0095
78. Gao Q, Yang Z, Xu S, Li X, Yang X, Jin P, et al. Heterotypic CAF-Tumor Spheroids Promote Early Peritoneal Metastatis of Ovarian Cancer. *J Exp Med* (2019) 216(3):688–703. doi: 10.1084/jem.20180765

**Conflict of Interest:** The authors declare that the research was conducted in the absence of any commercial or financial relationships that could be construed as a potential conflict of interest.

frontiers
in Oncology

METHODS
published: 23 March 2022
doi: 10.3389/fonc.2022.852772

# Effectiveness and Safety of Niraparib as Neoadjuvant Therapy in Advanced Ovarian Cancer With Homologous Recombination Deficiency (NANT): Study Protocol for a Prospective, Multicenter, Exploratory, Phase 2, Single-Arm Study

*Dongchen Zhou*[1,2†], *Jiahao Liu*[1,2†], *Ronghua Liu*[1,2†], *Huayi Li*[1,2], *Yi Huang*[3], *Ding Ma*[1,2], *Li Hong*[4*] *and Qinglei Gao*[1,2*]

*[1] Department of Gynecological Oncology, Tongji Hospital, Tongji Medical College, Huazhong University of Science and Technology, Wuhan, China, [2] National Clinical Research Center for Obstetrics and Gynecology, Cancer Biology Research Center (Key Laboratory of the Ministry of Education), Tongji Hospital, Tongji Medical College, Huazhong University of Science and Technology, Wuhan, China, [3] Department of Gynecological Oncology, Hubei Cancer Hospital, Tongji Medical College, Huazhong University of Science and Technology, Wuhan, China, [4] Department of Gynecology and Obstetrics, Renmin Hospital of Wuhan University, Wuhan, China*

**Edited by:**
*Xia Bai Rong,*
*The First Affiliated Hospital of University of Science and Technology of China Anhui Provincial Hospital, China*

**Reviewed by:**
*Barbara Costantini,*
*Agostino Gemelli University Polyclinic (IRCCS), Italy*
*Kyung Jin Eoh,*
*Yonsei University, South Korea*

***Correspondence:**
*Qinglei Gao*
*qingleigao@hotmail.com*
*Li Hong*
*drhongli77@163.com*

*[†]These authors have contributed equally to this work and share first authorship*

**Specialty section:**
*This article was submitted to Gynecological Oncology, a section of the journal Frontiers in Oncology*

**Received:** *11 January 2022*
**Accepted:** *28 February 2022*
**Published:** *23 March 2022*

**Citation:**
*Zhou D, Liu J, Liu R, Li H, Huang Y, Ma D, Hong L and Gao Q (2022) Effectiveness and Safety of Niraparib as Neoadjuvant Therapy in Advanced Ovarian Cancer With Homologous Recombination Deficiency (NANT): Study Protocol for a Prospective, Multicenter, Exploratory, Phase 2, Single-Arm Study. Front. Oncol. 12:852772. doi: 10.3389/fonc.2022.852772*

**Background:** Ovarian cancer (OC) is a heterogeneous gynecological malignancy with a poor prognosis as the majority of patients are diagnosed at an advanced stage. Neoadjuvant chemotherapy (NACT) followed by interval debulking surgery (IDS) is recommended for patients who cannot achieve optimal cytoreduction or cannot endure primary debulking surgery (PDS). As there is an increased risk of chemoresistance for platinum-based NACT, it is important to investigate an alternative option. A Poly (ADP-ribose) polymerase inhibitor (PARPi), niraparib, has shown high anti-tumor activity, especially in homologous recombination deficiency (HRD) positive patients with OC. Thus, niraparib as a neoadjuvant treatment agent may help improve surgery accessibility and create survival benefits.

**Methods:** This multicenter, prospective, single-arm, open-label, phase II study plans to recruit 53 patients (aged 18-75 years) with newly diagnosed HRD positive, unresectable (Fagotti score ≥ 8 or upper abdominal computed tomography [CT] score ≥ 3) International Federation of Gynecology and Obstetrics (FIGO) stage III-IV OC. The HRD status was detected by next-generation sequencing and HRD positive patients will be counseled for study participation. Enrolled patients will receive niraparib capsules QD (200mg or 300mg per day) for two cycles (4 weeks/cycle). After neoadjuvant niraparib treatment, patients exhibiting complete response (CR), partial response (PR), or stable disease (SD) will undergo tumor reduction surgery and subsequent standard carboplatin/paclitaxel-based chemotherapy. The primary objectives include the objective response rate (ORR) and R0 resection rate. The rate of treatment interruption/termination and progression-free survival (PFS) will be secondary objectives. The study uses Simon's optimal two-stage design (24 and 21 patients for the first and second stage respectively). The data manager will record all adverse events (AEs).

**Discussion:** This is the first prospective study to evaluate the effectiveness and safety of niraparib in neoadjuvant treatment for advanced OC. The result of this study will provide a solid base for further expanding the clinical applications of the PAPRi and exploring more therapeutic possibilities for patients with HRD positive advanced OC.

**Clinical Trial Registration**: https://clinicaltrials.gov/, identifier NCT04507841.

**Keywords: ovarian cancer, HRD, neoadjuvant therapy, niraparib, phase II study, single-arm**

## INTRODUCTION

Cancer statistics in China indicated that there is an increasing incidence and mortality due to cancer with about 55,342 (17.6%) new ovarian cancer (OC) cases and 37,519 (18.1%) deaths in 2020 (1). The world OC coalition 2020 reported China with the largest number of women with OC in terms of incidence and 5-year prevalence (2). The majority of OCs are at an advanced stage corresponding to stages II b to IV of the International Federation of Gynecology and Obstetrics (FIGO) classification, resulting in poor prognosis (3, 4). Advanced stage presentation has a 5-year relative survival rate of 29% (5). The size of the residual lesion after surgery is an important prognostic factor for survival, so the 5-year survival rate is even worse for those who cannot receive optimal resection.

Standard therapy as per NCCN guidelines for patients with OC (2021) includes surgical debulking or cytoreductive surgery (residual disease <1 cm [R1] and removal of macroscopic disease [R0]) followed by platinum-based chemotherapy (6, 7). If optimal resection (R0 and R1) cannot be achieved, platinum-based neoadjuvant chemotherapy (NACT) with interval debulking surgery (IDS) should be considered (6). Sub-optimal debulking and platinum resistance predominantly leads to treatment failure and high mortality. Hence, complete R0 resection and platinum sensitivity are important for prolonging survival (8). NACT increased the chances of complete resection thereby resulting in improved progression-free survival (PFS) and overall survival (OS) theoretically (9). However, according to previous reports, survival benefits brought by increased R0 resection rate may be diminished by NACT-induced platinum resistance. Evidence showed that NACT may enhance cancer cell stemness, which may lead to chemoresistance, and patients who underwent NACT may experience more platinum resistance and shorter platinum-free interval for recurrence (10, 11). As the platinum-containing regimen in NACT may induce resistance at a later stage, therefore it is important to use an alternative non-platinum-based NACT to avoid platinum chemoresistance and to produce complete R0 resection opportunity in patients with advanced OC.

Evidenced by multiple clinical trials, poly (ADP-ribose) polymerase (PARP) inhibitors (including olaparib, niraparib, veliparib, etc.) have revolutionized the treatment paradigm of OC by eliminating HRD positive or *BRCA 1/2* mutated tumors (12–15). The anti-cancer activities of PARP inhibitors have been confirmed step by step from the late-line to the front-line maintenance therapy (16). Among these drugs, niraparib, an efficient FDA (Food and Drug Administration)-approved *PARP 1/2* inhibitor, showed competence as monotherapy for the late-line treatment of OC, with an overall response rate of 28% in homologous recombination deficiency (HRD) positive patients (95% CI 15.6-42.6; one side P=0.00053) (17). Based on the QUADRA trial, the FDA approved niraparib to treat HRD positive ovarian cancer patients with platinum-sensitive relapse after ≥3 line chemotherapy. Thus, niraparib might serve as an alternative agent for platinum-based NACT in patients with HRD positive OC. Besides, chemotherapy-naïve OC was more sensitive to platinum, as compared to recurrent tumors, implying the potential for a better anti-cancer efficiency of niraparib if served as neoadjuvant therapy.

Therefore, it can be hypothesized that applying neoadjuvant niraparib could reduce platinum resistance and ensure maximum benefit from cytoreductive surgery and postoperative chemotherapy in ovarian cancer patients with HRD positive, unresectable or intolerable to surgery, and ultimately lead to improved prognosis. And the present study is conducted aiming

---

**Abbreviations:** OC, Ovarian cancer; FIGO, The International Federation of Gynecology and Obstetrics; NACT, Neoadjuvant chemotherapy; IDS, Interval debulking surgery; Poly (ADP-ribose) polymerase (PARP) inhibitors; FDA, Food and Drug Administration; HRD, Homologous recombination deficiency; ORR, Objective response rate; PFS, Progression-free survival; CR, Complete response; PR, Partial response; SD; Stable disease; AEs, Adverse events; OS, Overall survival; GCP, Good Clinical Practices; CT, Computed tomography; RECIST, Response Evaluation Criteria in Solid Tumors; CTCAE, Common Terminology Criteria for Adverse Events; DCR, Disease control rate; CA125, Cancer antigen 125; GCIC, Gynecologic Cancer Intergroup Consensus; CFI, Chemotherapy-free interval; TFST, Time to first subsequent therapy; QOL, Quality of life; PRO, Patient report outcome; FACT-O, Functional Assessment of Cancer Therapy-Ovarian; HADS, Hospital Anxiety and Depression Scale; ISI, Insomnia Severity Index; IPAQ, International Physical Activity Questionnaire; EQ-VAS, EuroQol-visual analog scales; LOH, Loss of heterozygosity; TAI, Telomeric allelic imbalance; LST, Large scale state transitions; CRF, Case report form.

to assess the efficiency and safety of niraparib in newly diagnosed advanced OC.

# METHODS

## Study Design

This multicenter, prospective, interventional, single-arm, open-label, phase II study plans to recruit 53 women from 10 centers from China. This study will be conducted in accordance with the protocol, the current version of the Declaration of Helsinki, Good Clinical Practices (GCP) guidelines and any local regulations. The study has been registered at ClinicalTrials.gov (NCT04507841) was approved by the China-South East and Middle Gynecological Oncology Group (CSEM GOG-017). This trial was also approved by the Research Ethics Commission of Tongji Medical College of Huazhong University of Science and Technology (2020-S122). Informed consents will be obtained from patients both before screening and before receiving niraparib treatment.

The study design is provided in **Figure 1**. Treatment-naïve patients (aged 18-75 years) with newly diagnosed, HRD positive, low likelihood of optimal cytoreduction by computed tomography evaluation ≥3 or Fogotti score ≥8, FIGO stage III-IV OC will be included. The detailed inclusion and exclusion criteria are provided in **Table 1**. Informed consent will be obtained before HRD testing and receiving niraparib treatment, and the choice of treatment will depend on patients' preferences. All enrolled patients will receive a minimum of 200mg or 300mg QD of niraparib as 100 mg capsules for 2 cycles each lasting for 28 days. The initial dose will be adjusted according to the baseline body weight and platelet count (≥77 kg and 150000/UL, 300 mg dose is recommended; otherwise 200 mg dose). After receiving niraparib for 2 cycles, abdominal computed tomography (CT) scan will be performed to classify objective remission status according to Response Evaluation Criteria in Solid Tumors (RECIST version 1.1). If patients achieve complete response (CR), partial response (PR) or stable disease (SD), they will receive open laparotomy IDS. Post-surgery, routine platinum-based chemotherapy will be given for 6 cycles, following which, niraparib will be given as maintenance therapy within 12 weeks up to 3 years or till disease progression or patient withdrawal from the study since they are high risk of recurrence and demonstrated efficacy in neoadjuvant therapy. However, patients with progression disease (PD) will receive NACT and follow-up therapy as recommended by the NCCN guidelines. In the case of grade 3-4 adverse events (AEs), the treatment should be suspended, and the AEs should be actively treated until returning to grade 1-2. The dose may be reduced in the next cycle of treatment depending on the decision of the investigators. If the toxicity does return to grade 1-2 or below within 28 days, no further reduction below 100mg/day will be allowed.

## Study Objectives and Endpoints

The primary objective is to evaluate objective response rate (ORR) and R0 resection rate after niraparib neoadjuvant treatment. ORR is defined by the rate of patients achieving CR or PR. The secondary endpoints will be to evaluate the number of patients with treatment-related AEs or serious AEs as assessed by Common Terminology Criteria for Adverse Events (CTCAE version 5.0). Furthermore, the rate of treatment interruption and termination caused by patients' intolerance of side effects, incidence of AEs at all levels during the course of the treatment, surgery and chemotherapy following treatment will also be determined. The secondary efficacy endpoints will be to determine disease control rate (DCR); pathologic complete response rate measured by Miller-Panye system; PFS; cancer antigen 125 (CA125) progression rate as per Gynecologic Cancer Intergroup Consensus (GCIC) guidelines; OS and long-term benefits including chemotherapy-free interval (CFI) and time

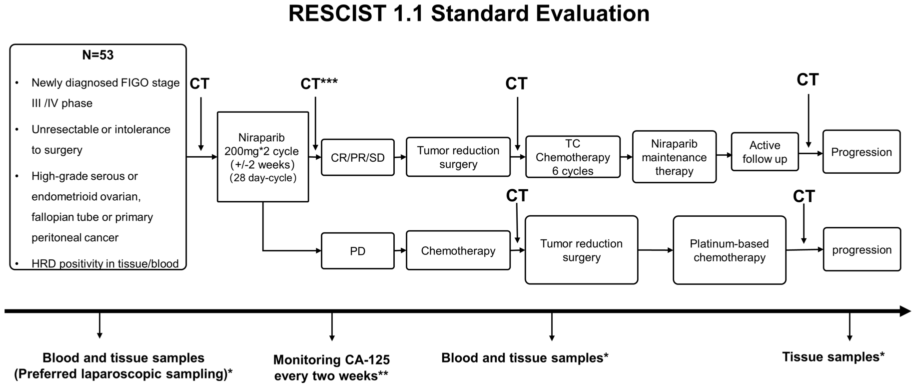

**FIGURE 1** | Study Design. *Blood and tissue samples were collected at various stages i.e., before and during treatment, disease progression/recurrence, during surgery and post-operative chemotherapy and follow-up. **CA-125 was determined as per Gynecologic Cancer Intergroup Consensus (GCIC) guidelines. ***Abdominal CT or laparoscopy is recommended to classify objective remission status. CA-125, cancer antigen-125; CR, complete response; CT, computed tomography; FIGO, International Federation of Gynecology and Obstetrics; HRD, homologous recombination deficiency; NACT, neoadjuvant chemotherapy; N, number; PD, progressive disease; PR, partial response; RECIST, Response Evaluation Criteria in Solid Tumors; SD, stable disease; TC, Paclitaxel and carboplatin regimen.

**TABLE 1 |** Key inclusion and exclusion criteria.

| Inclusion Criteria | Exclusion Criteria |
|---|---|
| Women patients aged 18-75 years | Personnel involved in the planning or implementation of the research |
| High-grade serous or endometrioid ovarian/peritoneal/fallopian tube cancer, FIGO stage III-IV confirmed by open or laparoscopic surgery or coarse needle aspiration biopsy | Patients participating in other clinical drug experiments or administering other research drugs or neoadjuvant therapies (chemo/radio/immuno therapies, TCM) at the same time as the study |
| HRD positive confirmed by tissue/blood samples | Allergy to niraparib or with similar chemical/biologic analogs |
| Consent for providing tissue/blood samples not only during the course of treatment but also for expanded gene/tumor markers related research studies | Dysphagia or any other GIT condition interfering with the ADME of the drug |
| At least one lesion measurable by CT/MRI | Previously received any treatment or PARPIs for ovarian cancer |
| Failure to achieve R0 tumor reduction (Fagotti score ≥8, upper abdominal CT score ≥3) or surgery intolerance (age ≥80 years, BMI ≥40, chronic diseases, malnutrition or hypoproteinemia, moderate to massive ascites, newly diagnosed venous thromboembolism, ECOG >2) | Simultaneous treatment of symptomatic or uncontrolled brain metastases requiring surgery, radiation and/or corticosteroids, or clinical manifestations of spinal cord compression |
| Expected survival time: >12 weeks | Non-recovery from a major surgery performed within 3 weeks before the start of the study |
| ECOG score: 0-2 | Previous or current diagnosis of MDS/AML or other primary malignancies, except for carcinoma *in situ* of the skin's basal and squamous, breast ductal, or cervix |
| Good organ function:<br>— Bone marrow (neutrophil count ≥1500/μL, platelet ≥100000/μL, Hb ≥10g/dL)<br>— Liver (Total bilirubin ≤1.5 times, direct bilirubin ≤1 time, AST and ALT ≤2.5 times, if liver metastasis exists ≤5 time of the upper limit of normal value)<br>— Renal (Serum creatinine ≤1.5 times the upper limit of normal value, or creatinine clearance rate ≥60 ml/min) | Disease or conditions exposing patients to high-risk toxicity, including HIV, hepatitis B and C; severe cardiovascular disease, intractable ventricular arrhythmias myocardial infarction in the last three months; uncontrolled epileptic grand mal seizure, unstable spinal cord compression or superior vena cava syndrome; psychiatric disorders affecting patients' informed consent; hypertension beyond drug control or unsuitable for participation in the study identified by researchers |
| Fertile women must have negative pregnancy tests, adequate contraception (except hormonal) within one week before enrolment and should be non-lactating; women without reproductive potential are also eligible (menopause/surgical sterilization) | Medical history or existing clinical evidence likely to interfere with study results or patients' compliance |
| Sound understanding and ability to comply with the procedures involved in study protocol such as treatment schedule, laboratory testing, imaging testing, follow-up and willingness to complete questionnaire survey of quality of life | Platelet or red blood cell transfusion within 3 days before the start of treatment of the study drug |
| Previous chemotherapy toxicity should be ≤ CTCAE 1 or baseline level, except for sensory neuropathy or alopecia with stable symptoms ≤ CTCAE grade 2 | Clinical unresolved toxicity ≥ grade 2, except neuralgia, lymphopenia, and depigmentation of skin |

*ADME, absorption distribution metabolism excretion; ALT, alanine aminotransferase; AML, acute myeloid leukemia; AST, aspartate aminotransferase; BMI, body mass index; CT, computed tomography; CTCAE, Common Terminology Criteria for Adverse Events; ECOG, Eastern Cooperative Oncology Group; FIGO, The International Federation of Gynecology and Obstetrics; GIT, gastrointestinal tract; Hb, hemoglobin; HIV, human immunodeficiency virus; HRD, homologous recombination deficiency; MDS, myelodysplastic syndrome; MRI, magnetic resonance imaging; PARPIs, Poly (ADP-ribose) polymerase inhibitors; TCM, traditional Chinese medicine.*

to first subsequent therapy (TFST). The definitions of primary secondary endpoints are provided in **Table 2**.

For assessing quality of life (QOL), validated patient report outcome (PRO) tools will be used namely, Functional Assessment of Cancer Therapy-Ovarian (FACT-O), Hospital Anxiety and Depression Scale (HADS), Insomnia Severity Index (ISI), International Physical Activity Questionnaire (IPAQ), EuroQol-visual analog scales (EQ-VAS).

The exploratory objectives will include changes in tumor biomarkers such as CA-125 during treatment, exploring

**TABLE 2 |** Primary and secondary endpoints.

| Primary endpoints | Definition |
|---|---|
| R0 resection rate* | The percentage of initially unresectable patients who successfully achieve R0 resection. |
| ORR | The percentage of patients who experienced complete or partial remission after niraparib neoadjuvant niraparib treatment with evaluated by the RECIST1.1 criteria. |
| **Secondary endpoints** | |
| PFS | Time from receiving Niraparib to tumor progression or cancer-related death as assessed by RECIST version 1.1. |
| DCR | The proportion of patients achieving CR, PR and SD. |
| OS | Time between receiving Niraparib and death by any cause. |
| pCR | Complete disappearance of the tumor cells in surgical specimens after niraparib neoadjuvant therapy. |

**R0 resection indicates microscopically margin-negative resection, in which no gross/microscopic tumor remains in the primary tumor bed.*

*CR, complete response; DCR, disease control rate; OS, overall survival; PFS, progression-free survival; PR, partial response; RECIST, Response evaluation criteria in solid tumors; SD, stable disease; pCR, complete pathologic response.*

biomarkers related to efficacy and patient prognosis and changes in gene mutation before and after treatment from tumor tissue and blood.

## Visiting Plan

HRD positive status will be screened by the next generation sequencing technology on peripheral blood and tumor tissue samples by using three classic indicators of genomic instability (LOH, loss of heterozygosity; TAI, telomeric allelic imbalance and LST, large scale state transitions). It takes 7 natural days from sampling to issuing the report, the same time as routine postoperative examination. Baseline data will be recorded at the screening visit, and it must be completed within 28 days before enrolment. Pre-assessment on the basis of parameters specified in **Figure 2** will be performed within 3 days before tumor reduction surgery.

Patients will be followed up every three months during the first two years of the treatment, every six months for 2-5 years, and every year thereafter. Information on disease progression, safety and complications will be collected during follow-up and further recorded in the case report form (CRF). The treatment and follow-up plan has been presented in **Figure 2**. Survival follow-up will be conducted every 90 days (± 7 days) after drug withdrawal. Moreover, information of patients receiving new chemotherapy for the first time after the end of this study will be collected. Treatment can be terminated at any point during the study due to any of the following reasons: serious/life-threatening or intolerable treatment-related AEs, risk to patients, protocol violation, withdrawal of consent, pregnancy, and disease progression. The end of treatment (EOT) and follow-up visit should be completed if the study is discontinued or in case of patient's withdrawal from the study. The following categories of concomitant medications are prohibited during the study period: granulocyte colony-stimulating factor (G-CSF), CYP1A2 sensitive substrates, anticoagulants and antiplatelet drugs,

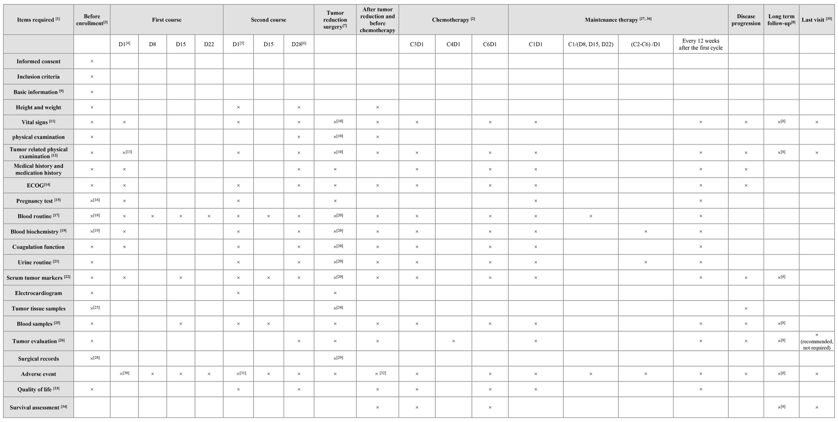

| Items required [1] | Before enrollment[3] | First course | | | | Second course | | | Tumor reduction surgery[7] | After tumor reduction and before chemotherapy | Chemotherapy [2] | | | Maintenance therapy [27, 36] | | | | Disease progression | Long term follow-up[8] | Last visit [35] |
|---|---|---|---|---|---|---|---|---|---|---|---|---|---|---|---|---|---|---|---|---|
| | | D1[4] | D8 | D15 | D22 | D1[5] | D15 | D28[6] | | | C3D1 | C4D1 | C6D1 | C1D1 | C1/(D8, D15, D22) | (C2-C6) /D1 | Every 12 weeks after the first cycle | | | |
| Informed consent | × | | | | | | | | | | | | | | | | | | | |
| Inclusion criteria | × | | | | | | | | | | | | | | | | | | | |
| Basic information [9] | × | | | | | | | | | | | | | | | | | | | |
| Height and weight | × | | | | | × | | × | | × | | | | | | | | | | |
| Vital signs [11] | × | × | | | | × | | × | ×[10] | × | × | | × | × | | | × | × | ×[8] | × |
| physical examination | × | | | | | | | × | ×[10] | × | | | | | | | | | | |
| Tumor related physical examination [12] | × | ×[13] | | | | × | | × | ×[10] | × | × | | × | × | | | × | × | ×[8] | × |
| Medical history and medication history | × | × | | | | | | × | × | | × | | × | × | | | × | × | | |
| ECOG[14] | × | × | | | | × | | × | × | × | × | | × | × | | | × | × | | |
| Pregnancy test [15] | ×[16] | × | | | | × | | | × | | | | | × | | | × | | | |
| Blood routine [17] | ×[18] | × | × | × | × | × | × | × | ×[20] | × | × | | × | × | × | | × | | | |
| Blood biochemistry [19] | ×[19] | × | | | | × | | × | ×[20] | × | × | | × | × | | × | × | | | |
| Coagulation function | × | × | | | | × | | × | ×[20] | × | × | | × | × | | | × | | | |
| Urine routine [21] | × | | | | | × | | × | ×[20] | × | × | | × | × | | × | × | | | |
| Serum tumor markers [22] | × | × | | × | | × | × | × | ×[20] | × | × | | × | × | | | × | × | ×[8] | |
| Electrocardiogram | × | | | | | × | | | × | | | | | | | | | | | |
| Tumor tissue samples | ×[23] | | | | | | | | ×[24] | | | | | | | | | × | | |
| Blood samples [25] | × | | | × | | × | × | | × | × | × | | × | × | | | × | × | ×[8] | |
| Tumor evaluation [26] | × | | | | | | | × | × | × | | × | | × | | | × | × | ×[8] | ×<br>(recommended, not required) |
| Surgical records | ×[28] | | | | | | | | ×[29] | | | | | | | | | | | |
| Adverse event | | ×[30] | × | × | × | ×[31] | × | × | × | × [32] | × | | × | × | × | × | × | × | ×[8] | × |
| Quality of life [33] | × | | | | | × | | × | | × | × | | × | × | | | × | | | |
| Survival assessment [34] | | | | | | | | | | × | × | | × | | | | | | ×[8] | × |

**FIGURE 2** | Follow-up plan. [1]In addition to the prescribed visit schedule, local researchers may conduct more frequent inspections as per patients' requirements, which may include blood and urine routine examination, blood biochemistry, ECG, CT, and serum tumor biomarker (within one week); [2]Refers to platinum-based chemotherapy post-surgery and included information collected from the patient's medical record; [3]It should not be completed >4 weeks before enrolment, excluding exceptional cases; [4]Required to be completed within 72 hours of the start of the cycle 1 ( ± 1D); [5]Required to be completed within 72 hours of the start of the cycle 2 ( ± 1D); [6]Required to be completed within 72 hours from the beginning of cycle 2 treatment D28 (± 1D); [7]Required to be completed within 3 days pre-operation; [8]Once every 12 weeks after maintenance treatment and once every 24 weeks after two years; [9]Includes name, age, gender, place of origin, contact details and date of admission; [10]Time interval from last inspection should be >7 days, otherwise the inspection shall be canceled; [11]Includes heart rate, blood pressure, pulse and respiration; [12]Records the tumor size at least; [13]Recommended, non-mandatory; [14]The United States Eastern Cooperative Oncology Group (ECOG) physical status scores; [15]Blood or urine β-HCG test; [16]Completed within two weeks before enrollment; [17]Includes neutrophil/platelet count, and Hb level; [18]Atleast 7 days before enrollment; [19]Includes measurement of serum creatinine and electrolytes, total bilirubin, ALT/AST; [20]Time interval from the last inspection should not be <1 week, otherwise the inspection shall be canceled; [21]Includes measurement of creatinine, urea nitrogen, and erythrocytes; [22]Includes testing of CA125, CA199, CEA, and HE4 related markers; [23]Biopsy done by laparoscopy, laparotomy, or coarse-needle aspiration; [24]Primary and metastatic tumor tissues obtained by laparotomy/laparoscopic tumor reduction surgery; [25]Samples in 2ml EDTA anticoagulant tube were used for HRD detection before enrollment and after two courses of treatment. Samples of 10ml Streck tube were collected before enrollment, D15 and D28 of the first course of chemotherapy, D15 of the second course of chemotherapy, and before tumor reduction surgery and subsequent therapy; [26]Abdominal CT or MRI is recommended for evaluation instead of ultrasound alone; [27]If blood routine tests are abnormal during maintenance treatment, then it should be carried out every 3 days and closely monitored until it becomes normal; [28]The operation record of the biopsy should be sent to the research center for record within 7 days; [29]Surgical records should be completed within 24 hours after the surgery and sent to the research center within 7 days for reference; [30]All adverse events to be documented from first day of receiving niraparib to post 30 days of treatment termination; [31]All adverse events to be documented from first day of receiving niraparib to post 30 days of treatment termination; [32]Postoperative adverse events (D1 to D28); [33]Includes FACT-O, HADS, ISI, IPAQ, and EQ-VAS; [34]Recurrence and time of recurrence, death and time of death, whether to continue follow-up and last follow-up time are recorded; [35]The last follow-up before withdrawal; [36]After the completion of first-line chemotherapy, patients will receive maintenance treatment with niraparib within 12 weeks. ALT/AST, alanine aminotransferase/aspartate aminotransferase; CA, cancer antigen; CEA, carcinoembryonic antigen; CT, computed tomography; D, day; ECOG, Eastern Cooperative Oncology Group; ECG, electrocardiogram; EDTA, ethylenediaminetetraacetic acid; EQ-VAS, EuroQol-visual analog scales; FACT-O, Functional Assessment of Cancer Therapy-Ovarian; HADS, Hospital Anxiety and Depression Scale; Hb, hemoglobin; β-HCG, β-human chorionic gonadotropin; HE4, human epididymis protein 4; HRD, homologous recombination deficiency; IPAQ, International Physical Activity Questionnaire; ISI, Insomnia Severity Index; MRI, magnetic resonance imaging.

systemic glucocorticoids, other PARPis, radiation therapy, vaccines and hormonal contraceptives.

## Effectiveness Evaluation

Computed tomography (CT) of the abdominal and pelvic cavity and other tumor areas with clinical indications will be performed at baseline and each follow-up (**Figure 2**). Tumor radiological imaging will use RECIST v1.1 criteria to classify objective remission status. Target lesions will be classified into CR, PR, SD, PD and non-evaluable (NE). Non-target lesions will be evaluated on the basis of CR, non-CR/non-disease progression (NN), PD, and NE.

Tumor response will be classified as PD for target lesions if there is ≥ 20% increase in the sum of the longest diameter of target lesions in comparison to the smallest sum longest diameter recorded in addition to an absolute increase of 5 mm whereas in case of non-target lesions, appearance of one or more new lesions or unequivocal progression of existing lesions will be considered as PD. New lesions refer to the appearance of new malignant lesions indicative of PD (18). In the case of PD, treatment should be terminated, and the follow-up should be continued. Target lesions of all patients will be measured by the same imaging technique and recorded in the CRF. Patients receiving at least two treatment cycles and one disease assessment or patients with early progression will be considered evaluable. Full analysis set (FAS) used for effectiveness evaluation will include all patients with primary gynecological malignancies (sub-grouped by tumor type), meeting the inclusion-exclusion criteria, with complete medical records.

## Data and Sample Collection, Management, and Monitoring

Recurrent tumor tissue and blood samples collected will be sent to Tongji central laboratory. A detailed sample collection process is presented in **Figure 3**. During the treatment period, patients will receive relevant examinations and are expected to complete questionnaires related to the QOL as per schedule. Post-treatment, patients will be subjected to follow-up examination and telephone follow-up. The detailed data obtained from the patients will be recorded in the CRF and kept strictly confidential in the research center. All study records and original documents will be maintained and stored according to relevant regulations and guidelines, or by the research institution's rules. The investigator will access the relevant raw data of the clinical study and will be responsible for reviewing CRF to determine completeness, accuracy, and consistency of the information with the source data. Moreover, CRF, raw laboratory data, and medical test results must be readily available for clinical inspectors, auditors, and health authorities.

## Safety Analysis

The most common adverse events observed in a previous study were Anemia, Nausea, Thrombocytopenia, etc. and the serious (grade ≥3) adverse events were anemia, thrombocytopenia and neutropenia (19). All AEs will be monitored 30 days after the last dose in this study. The research coordinator or data manager will summarize all serious AEs resulting in treatment withdrawal or deaths during or within 30 days of treatment termination on a per-patient basis. AEs will be coded in accordance with Medical

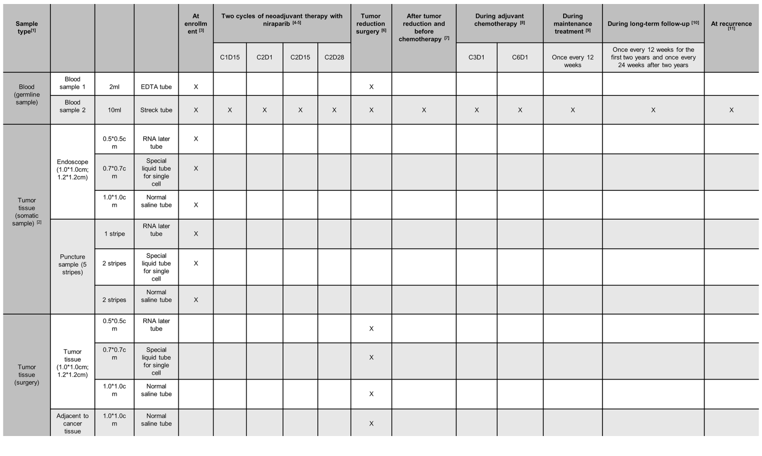

| Sample type[1] | | | | At enrollment [3] | Two cycles of neoadjuvant therapy with niraparib [4-5] | | | | Tumor reduction surgery [6] | After tumor reduction and before chemotherapy [7] | During adjuvant chemotherapy [8] | | During maintenance treatment [9] | During long-term follow-up [10] | At recurrence [11] |
|---|---|---|---|---|---|---|---|---|---|---|---|---|---|---|---|
| | | | | | C1D15 | C2D1 | C2D15 | C2D28 | | | C3D1 | C6D1 | Once every 12 weeks | Once every 12 weeks for the first two years and once every 24 weeks after two years | |
| Blood (germline sample) | Blood sample 1 | 2ml | EDTA tube | X | | | | | X | | | | | | |
| | Blood sample 2 | 10ml | Streck tube | X | X | X | X | X | X | X | X | X | X | X | X |
| Tumor tissue (somatic sample) [2] | Endoscope (1.0*1.0cm; 1.2*1.2cm) | 0.5*0.5cm | RNA later tube | X | | | | | | | | | | | |
| | | 0.7*0.7cm | Special liquid tube for single cell | X | | | | | | | | | | | |
| | | 1.0*1.0cm | Normal saline tube | X | | | | | | | | | | | |
| | Puncture sample (5 stripes) | 1 stripe | RNA later tube | X | | | | | | | | | | | |
| | | 2 stripes | Special liquid tube for single cell | X | | | | | | | | | | | |
| | | 2 stripes | Normal saline tube | X | | | | | | | | | | | |
| Tumor tissue (surgery) | Tumor tissue (1.0*1.0cm; 1.2*1.2cm) | 0.5*0.5cm | RNA later tube | | | | | | X | | | | | | |
| | | 0.7*0.7cm | Special liquid tube for single cell | | | | | | X | | | | | | |
| | | 1.0*1.0cm | Normal saline tube | | | | | | X | | | | | | |
| | Adjacent to cancer tissue | 1.0*1.0cm | Normal saline tube | | | | | | X | | | | | | |

**FIGURE 3** | Sample collection plan. [1]In addition to pathological sections, one copy of frozen, paraffin-embedded tissue for gene detection, and RNA preservation samples will be sent for sample retention. Also, samples in 2ml EDTA anticoagulant tube and in 10 ml streck tube should be sent to Tongji laboratory immediately for ctDNA sequencing; [2]Tissue sample specimens should first meet the requirements of normal histopathological examination, and the remaining samples should be subjected to gene detection and tissue preservation according to the sample collection process; [3]Tissue samples should be obtained at the time of biopsy. Sample in 2ml EDTA anticoagulant tube and in 10 ml streck tube should be sent to Tongji laboratory; [4]Blood samples should be obtained within 72 hours after two weeks of the first cycle of treatment; [5]Blood samples should be obtained within 72 hours on Day 1, 15 and the last day of the second course of treatment; [6]Tissue samples should be obtained intraoperatively and blood samples within 72 hours after operation; [7]Blood samples should be obtained once before adjuvant chemotherapy after tumor reduction surgery; [8]The third and sixth cycles of chemotherapy were obtained on Day 1; [9]During the maintenance treatment of niraparib, follow-up was conducted every 12 weeks to obtain blood samples; [10]During the long-term follow-up after the withdrawal of maintenance treatment, follow-up was conducted every 12 weeks, and evaluation was conducted every 24 weeks up to two years to obtain blood samples; [11]Tissue samples should be obtained at the time of biopsy, and blood samples should be obtained within one week after confirming recurrence.

Dictionary for Drug Regulatory Activities (MedDRA). Patient's survival and myelodysplastic syndrome/acute myeloid leukemia (MDS/AML) information will be collected every 8 weeks from the beginning of treatment up to 90 days after the end of the study. The safety set (SS) used for safety evaluation will include patients using niraparib at least once and with relatively complete medical records.

## Statistical Analysis

Hierarchical testing will be used to control the overall Type I error rate. First, ORR analysis will be conducted at the 1-sided alpha level of 0.05. If the result is positive, R0 resection rate analysis will be conducted with the 1-sided alpha level of 0.05. Descriptive measures will be used to summarize continuous variables (average value, standard deviation, median, maximum value, minimum value). Categorical variables will be expressed in frequency and percentage. The time to event analysis will be performed by the Kaplan Meier curve providing the median time to event. All data collected on CRF will be listed on a per-patient basis. Except for the date, the missing data will not be estimated. All statistical analysis will be calculated by SAS 9.4 statistical analysis software. Any deviations from the statistical methods given in the protocol will be reported in the final report as appropriate.

## Sample Size

Sample size will be determined based on an intended statistical power of 90% (one-sided test, significance level of 5%). ORR will be the first primary endpoint as it is more objective and better reflects the effectiveness of niraparib neoadjuvant therapy. Based on the assumption that niraparib will be considered ineffective if the ORR is ≤ 20% (P0), and effective if the ORR is ≥ 40% (P1), this study can further proceed to large-scale clinical trials. The proposed study will utilize Simon's two-stage design wherein in stage 1 a total of 24 patients will be enrolled. If the number of patients achieving objective response is >5, then the study will proceed to stage 2. In stage 2, a total of 21 patients were planned to be enrolled. A total of 53 patients will be included in the study, considering a possible 15% drop-out rate of patients. The intended ORR for achieving the primary endpoint in stage 2 will be >8 patients with objective response. Once the study achieves the first primary objective, the R0 resection rate of the second primary endpoint will be analyzed sequentially. Using 45 sample size, one-sided test, significance level of 5%, power was calculated to be 85.7%. Finally, the actual R0 resection rate and the confidence interval will be obtained according to statistical analysis of the data.

# DISCUSSION

To the best of our knowledge, this will be the first prospective multicenter study to evaluate the safety and effectiveness of niraparib alone as neoadjuvant treatment in advanced OC. The results from this study may propose a new treatment alternative for HRD positive patients with OC and extend the therapeutic applications of PARPi. Currently, not much is known about response of treatment-naïve patients to PARPi, and this long-lasting unsolved question has troubled many researchers.

So far, platinum-based chemotherapy is the only acceptable option for neoadjuvant treatment in patients with advanced OC (20). This study may extend the neoadjuvant treatment strategies in OC. Notably, the use of NACT for patients with OC increased from 17.6% in 2004 to 45.1% in 2016 (21). However, platinum- and paclitaxel-based NACT failed to grant any survival benefits in all existing randomized controlled trials (RCTs), leading to serious concerns on the effectiveness of NACT (10, 22). Oncogene targeted therapies have been proved to be more efficacious and safer than chemotherapy in serval other types of tumors, such as lung and breast cancer leading to a significantly improved prognosis and quality of life (23, 24). Similar therapies are rarely available for OC. Previously, ANTHALYA and GEICO 1205/NOVA clinical trials provided evidence on bevacizumab as a NACT in addition to chemotherapy in advanced OC, suggesting limited improvement in ORR (25). Most recently, the NUVOLA trial is recruiting patients to evaluate neoadjuvant olaparib and weekly TC (carboplatin plus paclitaxel) in unresectable OC (26). Therefore, it is imperative to explore more possibilities for neoadjuvant treatment in OC. Keeping in view the facts discussed above, our study was designed to find out whether niraparib neoadjuvant treatment could reduce surgical complexity and improve patients' prognosis in advanced OC. Besides, this study could provide a foundation for future RCTs aiming to evaluate the potential PFS improvement with neoadjuvant niraparib therapy in patients with HRD positive OC.

The primary endpoint chosen for this study will ensure the maximum clinical translational potential since it represents the neoadjuvant treatment response as well as the complexity of the debulking surgery. Meanwhile, ORR, PFS, and OS could depict the anti-tumor potential of niraparib comprehensively in the short- and long-term respectively. Additionally, the sample size was calculated using Simon's two-stage design. If niraparib was proven effective in a small population in the first stage, then only this study can proceed to the second stage and recruit more patients. More importantly, considering the safety concerns for the enrolled patients, serum CA125 levels will be measured biweekly. This will partially reflect the treatment responses and ensure patients with uncontrolled diseases withdrew from the experimental treatment on time. This design will not only secure the greatest clinical benefit to participants but also establish a scientifically reliable trial.

Several limitations of the study design can be acknowledged. Firstly, as of now, only Chinese patients will be included in the study. Secondly, no control group exists in this study, which should be notified during the result explanation and further appended in future studies.

Generally, this study may assess the potential of niraparib neoadjuvant treatment and IDS as a valid therapeutic strategy for patients with unresectable bulky tumors or poor general conditions. International investigators are welcome to contact and collaborate so that patients other than of Chinese origin can be enrolled in the study.

## DATA AVAILABILITY STATEMENT

The original contributions presented in the study are included in the article/supplementary material. Further inquiries can be directed to the corresponding authors.

## AUTHOR CONTRIBUTIONS

QG, DZ, and JL developed the study concept and protocol. HL and RL assisted in further development of the protocol. YH, LH, DM, and QG are responsible for the supervision of the clinical trial. QG has access to the final trial dataset. All authors contributed to the article and approved the submitted version.

## REFERENCES

1. Cao W, Chen HD, Yu YW, Li N, Chen WQ. Changing Profiles of Cancer Burden Worldwide and in China: A Secondary Analysis of the Global Cancer Statistics 2020. *Chin Med J (Engl)* (2021) 134(7):783–91. doi: 10.1097/CM9.0000000000001474
2. Reid F. *World Ovarian Cancer Coalition Atlas 2020*. (2020). p. 42. Available at: https://worldovariancancercoalition.org/global-charter/road-to-the-charter/(2020) [Accessed January 4, 2022].
3. Gadducci A, Guarneri V, Peccatori FA, Ronzino G, Scandurra G, Zamagni C, et al. Current Strategies for the Targeted Treatment of High-Grade Serous Epithelial Ovarian Cancer and Relevance of BRCA Mutational Status. *J Ovarian Res* (2019) 12(1):9. doi: 10.1186/s13048-019-0484-6
4. Takaya H, Nakai H, Takamatsu S, Mandai M, Matsumura N. Homologous Recombination Deficiency Status-Based Classification of High-Grade Serous Ovarian Carcinoma. *Sci Rep* (2020) 10(1):2757. doi: 10.1038/s41598-020-59671-3
5. Lheureux S, Gourley C, Vergote I, Oza AM. Epithelial Ovarian Cancer. *Lancet* (2019) 393(10177):1240–53. doi: 10.1016/S0140-6736(18)32552-2
6. Armstrong DK, Alvarez RD, Bakkum-Gamez JN, Barroilhet L, Behbakht K, Berchuck A, et al. NCCN Guidelines Insights: Ovarian Cancer, Version 1.2019. *J Natl Compr Canc Netw* (2019) 17(8):896–909. doi: 10.6004/jnccn.2019.0039
7. Armstrong DK, Alvarez RD, Bakkum-Gamez JN, Barroilhet L, Behbakht K, Berchuck A, et al. *NCCN Clinical Practice Guidelines in Oncology: Ovarian Cancer (version 3.2021)*. (2021). Available at: https://www.nccn.org [Accessed January 4, 2022].
8. Feng Z, Wen H, Li R, Liu S, Fu Y, Chen X, et al. Comparison of Survival Between Primary Debulking Surgery Versus Neoadjuvant Chemotherapy for Ovarian Cancers in a Personalized Treatment Cohort. *Front Oncol* (2020) 10:632195. doi: 10.3389/fonc.2020.632195
9. Al-Batran SE, Homann N, Pauligk C, Illerhaus G, Martens UM, Stoehlmacher J, et al. Effect of Neoadjuvant Chemotherapy Followed by Surgical Resection on Survival in Patients With Limited Metastatic Gastric or Gastroesophageal Junction Cancer: The AIO-FLOT3 Trial. *JAMA Oncol* (2017) 3(9):1237–44. doi: 10.1001/jamaoncol.2017.0515
10. Liu J, Jiao X, Gao Q. Neoadjuvant Chemotherapy-Related Platinum Resistance in Ovarian Cancer. *Drug Discov Today* (2020) 25(7):1232–8. doi: 10.1016/j.drudis.2020.04.015
11. Gee ME, Faraahi Z, McCormick A, Edmondson RJ. DNA Damage Repair in Ovarian Cancer: Unlocking the Heterogeneity. *J Ovarian Res* (2018) 11(1):50. doi: 10.1186/s13048-018-0424-x
12. Moore K, Colombo N, Scambia G, Kim BG, Oaknin A, Friedlander M, et al. Maintenance Olaparib in Patients With Newly Diagnosed Advanced Ovarian Cancer. *N Engl J Med* (2018) 379(26):2495–505. doi: 10.1056/NEJMoa1810858
13. Ray-Coquard I, Pautier P, Pignata S, Pérol D, González-Martín A, Berger R, et al. Olaparib Plus Bevacizumab as First-Line Maintenance in Ovarian Cancer. *N Engl J Med* (2019) 381(25):2416–28. doi: 10.1056/NEJMoa1911361

## FUNDING

This trial is funded by Pioneer Research Foundation of Tongji Hospital.

## ACKNOWLEDGMENTS

We thank Dr. Dharya Singh and Dr. Kaushik Subramanian of Indegene Pvt. Ltd, India for their help in language polishing. The abstract of this clinical trial was chosen as meeting posters in 2021 and 2022 (Oral Presentation) Society of Gynecologic Oncology (SGO) annual meetings.

14. González-Martín A, Pothuri B, Vergote I, DePont Christensen R, Graybill W, Mirza MR, et al. Niraparib in Patients With Newly Diagnosed Advanced Ovarian Cancer. *N Engl J Med* (2019) 381(25):2391–402. doi: 10.1056/NEJMoa1910962
15. Coleman RL, Fleming GF, Brady MF, Swisher EM, Steffensen KD, Friedlander M, et al. Veliparib With First-Line Chemotherapy and as Maintenance Therapy in Ovarian Cancer. *N Engl J Med* (2019) 381(25):2403–15. doi: 10.1056/NEJMoa1909707
16. Mirza MR, Coleman RL, González-Martín A, Moore KN, Colombo N, Ray-Coquard I, et al. The Forefront of Ovarian Cancer Therapy: Update on PARP Inhibitors. *Ann Oncol* (2020) 31(9):1148–59. doi: 10.1016/j.annonc.2020.06.004
17. Moore KN, Secord AA, Geller MA, Miller DS, Cloven N, Fleming GF, et al. Niraparib Monotherapy for Late-Line Treatment of Ovarian Cancer (QUADRA): A Multicentre, Open-Label, Single-Arm, Phase 2 Trial. *Lancet Oncol* (2019) 20(5):636–48. doi: 10.1016/S1470-2045(19)30029-4
18. Nishino M, Jagannathan JP, Ramaiya NH, Van den Abbeele AD. Revised RECIST Guideline Version 1.1: What Oncologists Want to Know and What Radiologists Need to Know. *AJR Am J roentgenol* (2010) 195(2):281–9. doi: 10.2214/AJR.09.4110
19. Berek JS, Matulonis UA, Peen U, Ghatage P, Mahner S, Redondo A, et al. Safety and Dose Modification for Patients Receiving Niraparib. *Ann Oncol* (2018) 29(8):1784–92. doi: 10.1093/annonc/mdy181
20. Wright AA, Bohlke K, Armstrong DK, Bookman MA, Cliby WA, Coleman RL, et al. Neoadjuvant Chemotherapy for Newly Diagnosed, Advanced Ovarian Cancer: Society of Gynecologic Oncology and American Society of Clinical Oncology Clinical Practice Guideline. *Gynecol Oncol* (2016) 143(1):3–15. doi: 10.1016/j.ygyno.2016.05.022
21. Knisely AT, St Clair CM, Hou JY, Collado FK, Hershman DL, Wright JD, et al. Trends in Primary Treatment and Median Survival Among Women With Advanced-Stage Epithelial Ovarian Cancer in the US From 2004 to 2016. *JAMA Netw Open* (2020) 3(9):e2017517. doi: 10.1001/jamanetworkopen.2020.17517
22. Dabi Y, Huchon C, Ouldamer L, Bendifallah S, Collinet P, Bricou A, et al. Patients With Stage IV Epithelial Ovarian Cancer: Understanding the Determinants of Survival. *J Transl Med* (2020) 18(1):134. doi: 10.1186/s12967-020-02295-y
23. Wang J, Xu B. Targeted Therapeutic Options and Future Perspectives for HER2-Positive Breast Cancer. *Signal Transduction Targeted Ther* (2019) 4:34. doi: 10.1038/s41392-019-0069-2
24. Falzone L, Salomone S, Libra M. Evolution of Cancer Pharmacological Treatments at the Turn of the Third Millennium. *Front Pharmacol* (2018) 9:1300. doi: 10.3389/fphar.2018.01300
25. Advani SH, Doval DC, Koppikar SB, Reddy PVA, Prasad S, Bapna A, et al. Use of Bevacizumab in Advanced Ovarian Cancer: Consensus From an Expert Panel Oncologists. *Indian J Gynecol Oncol* (2021) 19(1):8. doi: 10.1007/s40944-020-00485-6
26. Marchetti C, Tudisco R, Salutari V, Pietragalla A, Scambia G, Fagotti A. Neoadjuvant Chemoteraphy in Unresectable Ovarian Cancer With Olaparib and Weekly Carboplatin Plus Paclitaxel: A Phase II, Open Label Multicenter

Study (NUVOLA Trial). *Int J gynecological Cancer Off J Int Gynecological Cancer Soc* (2021) 31(8):1175–8. doi: 10.1136/ijgc-2021-002727

**Conflict of Interest:** The authors declare that the research was conducted in the absence of any commercial or financial relationships that could be construed as a potential conflict of interest.

frontiers | Frontiers in Oncology

ORIGINAL RESEARCH
published: 22 April 2022
doi: 10.3389/fonc.2022.754067

# A Preliminary Exploration Using Imaging Methods to Predict the Possibility of the Recurrence of Serous Ovarian Cancer in Patients Undergoing Total Resection

**Mengshi Fang[1], Shan Huang[2], Jiangning Dong[1]*, Hong Yan[3], Xin Fang[1], Ping Zhang[1], Feng Cao[1], Yulan Chen[1] and Qiujun Zhang[4]**

[1] Department of Radiology, The First Affiliated Hospital of USTC, Division of Life Sciences and Medicine, University of Science and Technology of China, Hefei, China, [2] Department of Nuclear Medicine, The Second Affiliated Hospital of Anhui Medical University, Hefei, China, [3] Department of Pathology, The First Affiliated Hospital of USTC, Division of Life Sciences and Medicine, University of Science and Technology of China, Hefei, China, [4] Department of Medical Oncology, The First Affiliated Hospital of USTC, Division of Life Sciences and Medicine, University of Science and Technology of China, Hefei, China

OPEN ACCESS

**Edited by:**
Gang Chen,
Huazhong University of Science and Technology, China

**Reviewed by:**
Clarissa Polen-De,
Mayo Clinic, United States
Xinming Zhao,
Chinese Academy of Medical Sciences and Peking Union Medical College, China

***Correspondence:**
Jiangning Dong
dongjn@163.com

**Specialty section:**
This article was submitted to Gynecological Oncology, a section of the journal Frontiers in Oncology

**Received:** 05 August 2021
**Accepted:** 29 March 2022
**Published:** 22 April 2022

**Citation:**
Fang M, Huang S, Dong J, Yan H, Fang X, Zhang P, Cao F, Chen Y and Zhang Q (2022) A Preliminary Exploration Using Imaging Methods to Predict the Possibility of the Recurrence of Serous Ovarian Cancer in Patients Undergoing Total Resection. Front. Oncol. 12:754067. doi: 10.3389/fonc.2022.754067

**Background:** The purpose of our research was to explore the value of preoperative CT and MRI examinations and clinical indicators in the prediction of recurrence of ovarian serous carcinoma in patients who underwent satisfactory staging surgery.

**Procedure:** Detailed inclusion and exclusion criteria were installed to screen all patients collected and the eligible patients were divided into two groups. The CT and MRI features and some clinical characteristics of two groups were analyzed, in addition, the apparent diffusion coefficient (ADC) value in tumor solid region was measured. Univariate analysis was used in this study.

**Results:** There were 78 patients with histologically proven ovarian serous carcinoma. According to the strict inclusion and exclusion criteria, we retained 29 patients (recurrence group: 11 patients, no recurrence group: 18 patients). For the peritoneal implantation metastasis in CT or MRI images and Ki67 proliferation index (Ki67 PI), the differences between two cohorts were statistically significant ($P < 0.05$). The rate of peritoneal metastasis in the recurrence cohort (10/11, 91%) was higher than that in the no recurrence cohort (7/18, 39%). Patients with high Ki67 PI expression had lower recurrence risk than those with low Ki67 PI expression, HR=0.172 (95%CI: 0.050-0.589, P=0.005), and patients without peritoneal planting had lower recurrence risk than those with it, HR=9.373 (95%CI: 1.194-73.551, P=0.033). For FIGO III patients, ipsilateral fallopian tube involvement was statistically significant between the two groups ($P < 0.05$). The differences in the other preoperative imaging characteristics of ovarian serous cancer, including the volume; capsule of the mass; main components; ADC value; cystic change; bleeding; degree of enhancement of the mainly solid region in 3 periods; and range of tumor involvement in the ovary, uterus, bladder, bowel, and pelvic wall, were not statistically significant. In addition, the differences in the other clinical indicators (i.e., age, FIGO stage) between the two cohorts were not statistically significant.

**Conclusions:** In CT and MRI examinations before surgery, peritoneal implantation metastasis was suggestive of the possibility of the recurrence of serous ovarian carcinoma in the near future. In addition to that, ipsilateral fallopian tube involvement and Ki67 PI may also indicate the possibility of recurrence (the former was only applicable to FIGO III patients).

**Keywords: ovarian cancer, recurrence, magnetic resonance imaging, diffusion-weighted imaging, apparent diffusion coefficient value, Ki67 proliferation index**

## INTRODUCTION

Epithelial ovarian carcinoma (EOC) is a malignant tumor with the highest mortality rate among gynecological malignant tumors (1). The clinical symptoms of ovarian cancer are insidious, and the early symptoms are not obvious. Approximately 2/3 of the patients are FIGO III or IV when they visit the doctor for the first time (2). According to the different pathological types of ovarian cancer, the five-year survival rates of these patients with FIGO III and IV were 23.9%~37.0% (2). Serous carcinoma is the most common type of EOC.According to the FIGO Cancer Report 2018, many cases of high-grade serous ovarian carcinoma and peritoneal carcinoma may originate in the tubal umbrella terminus (3). The lethality of EOC is mainly due to the higher risk of recurrence (4, 5). Recurrent ovarian cancers (ROCs) have a very poor prognosis, and most patients with ROC eventually develop resistance to chemotherapy drugs (6). Because of the complexity of the patients' situation, it is more difficult to choose treatment options for them. The prediction and earlier detection of ROC can help physicians intervene earlier in the treatment process of patients to better achieve individualized and accurate treatments. Imaging examinations can provide important value in the process of follow-up for ovarian carcinoma, but most studies on the risk of recurrence of ovarian carcinoma have mainly focused on clinical and hematological indicators and are relatively lacking in medical imaging data. The purpose of this research was to define the possibility of the use of imaging methods to analyze and predict the recent recurrence of ovarian serous carcinoma, especially for FIGO III patients, with the ultimate hope of helping clinicians to plan more suitable treatments.

## METHODS

### Patients and Clinical Information

Upon searching the Hospital Information System (HIS), between August 2015 and September 2019, there were 78 patients who had histologically proven ovarian serous carcinoma in our hospital. We retrospectively searched for these patients in the Picture Archiving and Communication System (PACS), and there were only 46 patients who underwent both pelvic MRI scan and abdominal CT examination before pelvic surgery. The inclusion criteria were as follows: 1) no obvious residual lesions were observed visually after staging operation (the diameter of the residual tumor was ≤1 cm); 2) the time periods between baseline imaging examination and surgery were not more than 7 days; 3) the progression-free survival of the tumor was not less than 6 months; 4) postoperative chemotherapy consisted of 4~6 courses, and the interval of each chemotherapy course was 21 days; 5) patients received first-line chemotherapy approximately 2 weeks after surgery and received first-line chemotherapy for ovarian cancer; 6) the follow-up plan should meet the following requirements: 1 year: once every 3 months, 2-3 years: once every 6 months, >3 years: once a year. Exclusion criteria were as follows: 1) failure to complete adequate and normal chemotherapy or loss to follow-up; 2) severe combined diseases (e.g., heart, lung, liver diseases or renal insufficiency); and 3) ovarian cancer combined with other malignant tumors.

Chemotherapy regimens were mainly included TC (paclitaxel +carboplatin) intravenous chemotherapy, TC+TP (paclitaxel +cisplatin) intraperitoneal intravenous chemotherapy, DC (docetaxel+carboplatin), and PC (cisplatin+cyclophosphamide). Although the longest follow-up time was 40.8 months, in order to avoid the influence of follow-up time on the recurrence of ovarian serous cancer, the follow-up time node was set as 20 months, so that the recurrence of the above patients were divided into two groups, namely the recurrence group and the non-recurrence group. During the follow-up period, patients were required gynecological examinations, ultrasound examinations, and serum tumor marker tests to assess whether the patient had relapsed. When suspicious indications of recurrence were found, patients were advised to have abdominal imaging examinations. Ovarian cancer recurrence was diagnosed when two or more of the following were present: 1) increased levels of tumor markers; 2) a mass found in imaging examination; 3) a mass found on physical examination; 4) hydrothorax and peritoneal fluid; 5) intestinal obstruction of unknown causes.

### CT Examination

CT examinations were carried out on a 64-Row CT scanner (Discovery CT750HD, fifth-generation spectral CT, GE Healthcare), The scanning range was from the upper margin of the diaphragm to the iliac crest. Abdominal plain scan and dynamic enhancement scans of 3 phases (arterial phase, portal phase, delay phase) were adopted. The parameter details were as follows: tube voltage (TV), 120 kV; tube current, 280 mA; frame rotation time, 0.8 s; pitch, 0.984:1; layer thickness, 5.0 mm; and reconstruction interval, 5.0 mm. A double-cylinder power injector (OptiVantage; Mallinckrodt; USA) was utilized to inject the contrast material (4.4 ml/s, 270 mgl/ml, Visipaque, General Electric Healthcare, USA) through peripheral veins.

## MRI Examination

MRI scanning was carried out on a 3.0T system (Signa HDXT, GE Healthcare, USA) equipped with an eight-channel torso array coil. For any larger mass that could not be fully accommodated in an axial plane, a sagittal or coronary scanning sequence was adopted to cover as much of the entire mass as possible. Routine MRI protocols were adopted for the examination of the adnexal lesions, which included axial fast spin echo (FSE) T1-weighted images (T1WI), axial FSE T2-weighted images (T2WI) and fat-suppressed T2WI (FS T2WI). An axial DWI sequence included an echo-planar imaging sequence with an array spatial-sensitivity-encoding technique (ASSET). The specific parameters of T1WI protocol were as follows: repetition time (TR), 500 ms; echo time (TE), 7.8 ms; thickness, 6.0 mm; layer spacing, 2.0 mm; and the number of excitations (NEX), 1. The specific T2WI parameters were TR, 4200 ms; TE, 68 ms; thickness, 6.0 mm; layer spacing, 2.0 mm; and NEX, 2. The parameter details of FS T2WI were similar to those of the T2WI sequence. The parameters of DWI were TR, 4000 ms; TE, 65 ms; thickness, 6.0 mm; layer spacing, 2.0 mm; NEX, 6; and b value = 0 and 1000 s/mm$^2$). Liver acquisition with a volume acceleration (LAVA) sequence was adopted for contrast-enhanced pelvic examination, and a power injector (Optistar LE; Mallinckrodt; USA) was performed to inject the contrast material (0.1 mmol/kg, Gadodiamide, General Electric Healthcare, USA). The specific parameters of LAVA MR were TR, 4.5 ms; TE, 1.3 ms; flip angle, 15°; layer spacing, 0 mm; NEX, 1; and band width, 166.67 kHz. The images were obtained from multiple phases after the injection of the contrast agent in the axial and sagittal planes (postcontrast at 20 s, 60 s, 120 s in the axial plane and 150 s in the sagittal plane).

## Radiological Evaluation

MRI and CT images were analyzed carefully on an Advantage Windows workstation 4.5 (AW 4.5 workstation, GE Healthcare, USA) by two radiologists with 31 and 29 years of experience in gynecological imaging. They were blinded to the pathological results, and from each other's results. The reader variability was evaluated. The average of the measurements for the quantitative data or the outcome of negotiations for the qualitative data acquired by these two radiologists was the final value. For the enrolled patients, the following MRI and CT characteristics were recorded: volume (if there was only one lesion, the maximum transverse diameter plus the maximum vertical diameter plus the maximum anteroposterior diameter/cm; if there were multiple lesions, the maximum lesion size was taken; if multiple lesions showed fusions, the size of all the lesions was taken); whether one or both ovaries was involved (single or bilateral); whether the capsule of mass was intact (yes or no); the presentation of the main components in the mass (type A: mural nodule, type B: solid mass, type C: loose tissue–similar to the spongy appearance); ADC value (Function Tool software was adopted to analyze the ADC value of the tumor, and the ROI was manually placed in the solid area of tumor, which corresponded to high signal intensity; we took 3 measurements at the same level, and the mean value was obtained in mm$^2$/s); cystic changes (present or not); the degree of cystic extent (graded as 0-3; grade 0: no sac change; grade 1: the area of cystic changes was less than 1/3; grade 2: 1/3~2/3; grade 3: more than 2/3); bleeding (present or not); the degree of enhancement of the mainly solid region in the arterial period (20 s), venous period (60 s) and the delayed period (120 s~) (mild: less than gluteal muscles; moderate: similar to gluteal muscles; severe: more than gluteal muscles); whether the ipsilateral fallopian tube was involved (yes or no); whether the uterine/bladder/bowel/pelvic wall was involved (yes or no); whether regional lymph node metastasis was found (yes or no, decision criteria: uneven lymph node signal, the disappearance of the lymph node hilum, lymph node short diameter > 1.0 cm); whether there were peritoneal implants; the degree of peritoneal thickening (the thickest point was measured, cm); ascites (present or not); and the deepest diameter of ascites in pelvic MR images (perpendicular to trunk level, cm). The above image indicators were required in the first preoperative examination. During postoperative follow-up, the radiologists judged whether the tumor recurred and the site of recurrence.

## Histopathological Evaluation

All surgical samples were fixed with 4% neutral formaldehyde and embedded with paraffin wax, and 4-μm sections were stained by hematoxylin and eosin (HE) and immunohistochemistry (EliVision). The main antibodies used included Ki67 PI, CAM5.2, EMA, CK7, Ber-EP4, p53, BRCA1, CA-125, WT1, ER, CD99, B72.3, CK20, vimentin, CEA, calretinin, CK5/6, and TTF-1. Antigen negative indicated that all tumor cells were negative, antigen positive indicated that more than 50% of tumor cells were positive, and 0-50% indicated focal positivity or negativity. Histological classification was estimated by two senior pathologists.

## Statistical Analysis

The measurement data with a normal distribution were presented as the "mean ± standard deviation (SD)", and the independent sample *t* test was used for comparisons between groups. Non-normally distributed measurement data were presented as the median (P25-P75), and we used the rank-sum test (Mann-Whitney U test) for comparisons between the two cohorts. Qualitative materials were statistically described by frequency and percentage (%), and the Fisher exact test was used for comparisons between the two cohorts. Intraclass correlation coefficients (ICCs) were used to evaluate the interobserver agreement in the measurement of volume, ADC values, degree of peritoneal thickening and the deepest diameter of ascites, respectively (ICC > 0.8 was indicative of an almost perfect agreement). Cohen's Kappa coefficients were used to analyze the consistency of the classification variables, respectively (Cohen's kappa > 0.8 was indicative of an almost perfect agreement). The test level α was 0.05. A *P* value of < 0.05 was considered statistically significant. SPSS version 20.0 was used to perform all the statistical analyses. The univariate analysis were performed for all parameters between the two groups. Due to the high proportion of FIGO III patients included, the above analysis were also performed for FIGO III patients. In addition, we conducted receiver operating characteristic (ROC) curve analysis on Ki67 PI, and obtained the most optimal cut-off value. Higher than the value was classified as high expression group, lower than the value was classified as low expression group. The survival of the two groups and progression-free survival period (month) were analyzed. Again, all patients were divided into positive and negative groups based on whether peritoneum was implanted and survival curves were analyzed.

## RESULTS

Based on the above inclusion and exclusion criteria, we removed 17 patients. In total, we retained 29 patients for the study (the progression-free survival period ranged from 6 to 40.8 months, with an average of (19.3 ± 9.7) months). All 29 patients underwent laparotomy, and the pathological results of 27 patients were confirmed to be high-grade serous carcinoma, while those of other 2 patients were confirmed to be low-grade serous carcinoma. According to the postoperative follow-up visits, the patients were divided into a recurrence group and a no recurrence group. There were 11 patients in the recurrence group, and 73% (8/11) patients had recurrent lesions in the peritoneum. In the remaining patients, lymph node abnormalities (e.g., inguinal area, adjacent to the iliac vessels, around the rectum, retroperitoneal area, and mesenteric area) were observed. In one patient, both peritoneal and lymph node abnormalities were found. There were 18 patients in the no recurrence group. Statistical analysis results showed that there was a significant difference in Ki67 PI (*P* < 0.05). The result was summarized in **Table 1**.

Regarding the presentation of the main components in the mass, 4 patients were classified as type-A (**Figures 1A, B**), 5 patients as type-B, and 2 patients as type-C. The degrees of cystic extent were as follows: 0 (n=0), 1 (n=4), 2 (n=2), and 3 (n=5) (**Figures 1A–C**). There were 6 patients who displayed high intensity in some cyst regions on T1WI, which may have been bleeding, but this sign did not appear in the remaining 5 patients. In the no recurrence cohort (n=18), there were 8 patients with intact capsules (**Figures 2A–C**). Regarding the presentation of the main components in the mass, 11 patients were classified as type-A (**Figure 2B**), 7 patients as type-B, and 0 patient as type-C. The degrees of cystic extent were 0 (n=1), 1 (n=7), 2 (n=4), and 3 (n=6) (**Figures 2A, B**). There were 7 patients who displayed high intensity in some cyst regions on T1WI that was low intensity on T2WI, indicating a bleeding signal (**Figures 2A, C**), but this feature was not observed in the remaining 11 patients. There were no significant differences in the above indicators (*P*>0.05).

**TABLE 1** | The statistical results of univariate analysis of the clinical characteristics of the recurrence and no recurrence groups.

| Indicators | Recurrence (n=11) | No recurrence (n=18) | Univariate analysis (*P*) |
|---|---|---|---|
| Age (y) | 53.0 ± 7.8 | 51.6 ± 8.4 | 0.742 |
| Surgical stage | | | 0.251 |
| FIGO I | 1 | 3 | |
| FIGO II | 0 | 4 | |
| FIGO III | 10 | 11 | |
| Ki67 PI (%) | 45.00 ± 24.39 | 62.78 ± 14.06 | **0.045** |

*Values in bold are statistically significant.*

The ADC value of the recurrence group was lower than that of the no recurrence group, but *P*>0.05. On the enhanced images of the arterial period in the recurrence cohort, 3 patients (3/11, 27%) displayed moderate enhancement, and 8 (8/11, 73%) patients displayed severe enhancement (**Figure 1D**), and in the no recurrence group, 5 (5/18, 28%) moderate enhancement (**Figure 2D**), and 12 (12/18, 66%) severe enhancement, *P*>0.05. In the venous period in the recurrence group, 9 (9/11, 82%) severe enhancement (**Figure 1E**), and in the no recurrence group, 16(16/18, 89%) patients severe enhancement (**Figure 2E**), *P*>0.05. In the delayed period, the same manifestation was observed in the recurrence group (**Figures 1F**, **2F**). These findings were shown in **Table 2**.

From the MR imaging findings, in the no recurrence group, there were 8 patients with bilateral ovarian involvement (**Figures 2A, B**). Regarding whether the uterus, bladder, bowel, or pelvic wall was involved, the result was yes in 7 (7/11, 64%) patients in the recurrence group, and the no recurrence group existed 6 (6/18, 33%) cases. However, none of these indicators mentioned above was statistically significant (*P*>0.05).

Lymph nodes were classified as metastatic lymph nodes when there were very typical signs of lymph node metastasis. The results showed that there were 4 (4/11, 36%) patients with lymph node metastasis in the recurrence cohort and 3 (3/18, 17%) patients in the no recurrence cohort (*P*>0.05), but the differences in peritoneal implants were significantly (*P* < 0.05). In the recurrence cohort, 10 (10/11, 91%) patients had peritoneal implants (**Figures 1F–I**), while in the no recurrence cohort, 7 (7/18, 39%) patients had peritoneal implants. With respect to the degree of peritoneal thickening in these two cohorts, the details were summarized in **Table 3** (*P*>0.05).

There was a good interobserver agreement between the two radiologists for the above imaging indicators, with ICCs and Cohen's kappa coefficients ranging within 0.81–0.92 and 0.87–0.99, respectively.

In addition, all indicators were compared between the two groups only for FIGO III patients, and the results were shown in **Table 4**. The results showed that Ki67 PI and ipsilateral fallopian tube involvement were statistically significant between the two groups (*P* < 0.05), while other indicators weren't statistically significant. These findings were shown in **Table 4**.

The optimal cut-off value obtained by ROC curve analysis of Ki67 PI was 35% (area under the curve was 0.765, 95% confidence

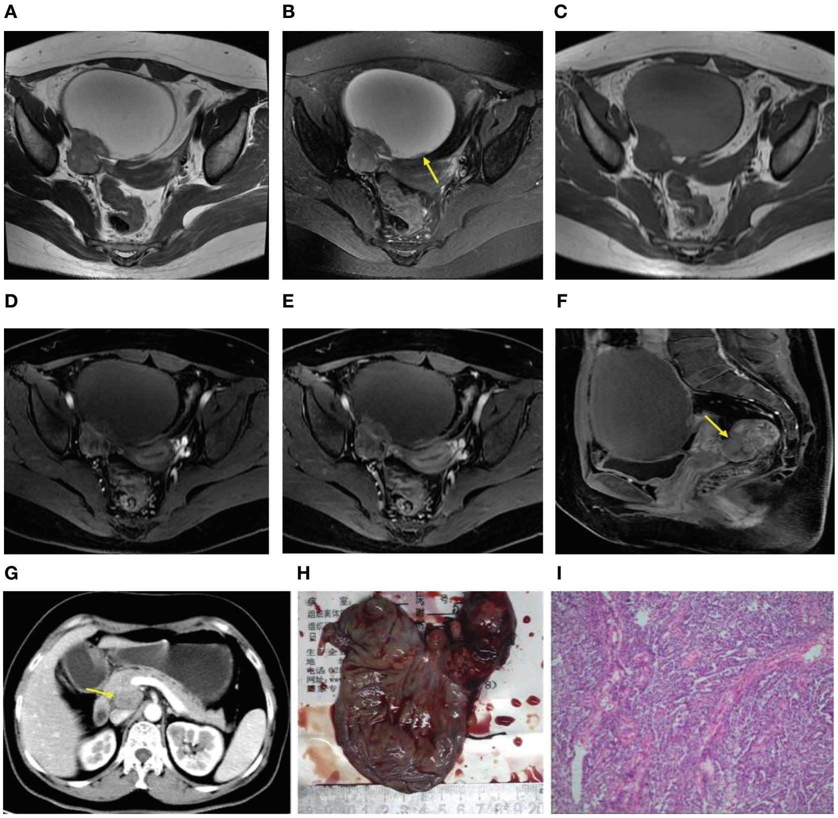

**FIGURE 1** | **(A–I)** Axial T2WI and FS T2WI showing a cystic solid mass with a capsule wall nodule [yellow arrow, **(B)**]. T1WI **(C)** displayed high signal in the liquid region of the mass. In the arterial, venous and delayed period, the solid region of the mass revealed severe enhancement, more than the gluteal muscle **(D–F)**. A metastatic nodule was seen in the rectouterine depression [yellow arrow,**(F)**]. Postoperative follow-up revealed a retroperitoneal metastatic lymph node [yellow arrow, **(G)**]. Postoperative gross specimen and HE staining at low magnification showed a high-grade serous carcinoma **(H, I)**.

interval(CI) was 0.585-0.945). 35% of Ki67 PI was used as a node to divide all patients into high expression group and low expression group. Survival analysis was conducted on the recurrence status of all patients, and the results were shown in **Figure 3A**. It showed that Ki67 PI was an important factor affecting the recurrence of ovarian serous cancer (P=0.005). Patients with high Ki67 PI expression had lower recurrence risk than those with low Ki67 PI expression, HR=0.172 (95%CI: 0.050-0.589). Similarly, whether peritoneum was implanted that was another important factor affecting the recurrence of ovarian serous cancer (P=0.033), and patients without peritoneal planting had lower recurrence risk than those with it, HR=9.373 (95%CI: 1.194-73.551), and the results were shown in **Figure 3B**.

## DISCUSSION

Ovarian cancer five-year overall survival in early FIGO stages is 90% vs 20–25% in advanced FIGO stages; however, 70% of patients are diagnosed in advanced FIGO stages (7). The high-grade serous subtype accounts for approximately 70% of cases (8). The treatment of ovarian cancer typically includes surgical treatment (staging or debulking) and intraperitoneal, intravenous, or combined chemotherapy (9). There is growing acceptance of the importance of a personalized approach to treatment in patients with ROC and the recognition of the complex interplay between patient- and tumor-related factors that impact the likelihood of patient prognosis (10). If it is possible to predict the likelihood of postoperative recurrence before the first treatment, this may assist in the selection of individualized treatment options. Currently, CA125 and human epididymis protein 4 (HE4) are the only two markers that have been approved by the FDA for monitoring treatment and detecting disease recurrence (7). However, imaging examinations are noninvasive and may be of some benefit to patients if they can help predict the prognosis of ovarian cancer.

Some past studies have suggested that surgical stage, lymph node metastasis, peritoneal implantation, and abdominal water volume played important roles in the prognosis of ovarian carcinoma (11–14). In our study, except for peritoneal implantation, all the other imaging indicators showed no statistical significance. The reasons are analyzed in detail below. First, as for surgical stage, there were more FIGO stage III patients in our study (21/29, 72.4%), while there were fewer FIGO stage I and II patients, which may cause a bias in the results. Second, regarding lymph node metastasis, our study described imaging results to assess lymph node metastasis,

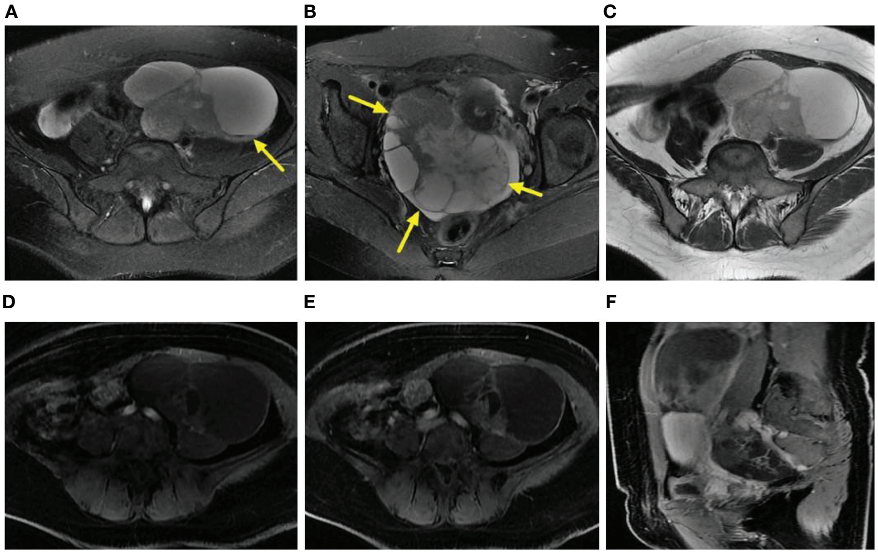

**FIGURE 2** | **(A–F)** Axial FS T2WI and T2WI showed multiple cystic solid masses in both ovaries [yellow arrow, **(B)**], and the liquid-liquid plane was visible in part of the capsule [yellow arrow, **(A)**]. In the arterial period, the solid region of the lesion revealed moderate enhancement (i.e., similar to that of the gluteal muscle) **(D)**. In the venous and delayed periods, the solid region of the lesion displayed severe enhancement (i.e., more than that of the gluteal muscle) **(E, F)**.

and previous studies have focused on the results of operations for lymph node metastasis to predict prognosis. These results may not exactly match, as conventional imaging of lymph node metastasis alone may not be able to assess small lymph node metastasis and distinguish it from lymph node reactive hyperplasia. Third, regarding abdominal water quantity, our study measured the deepest diameter perpendicular to the horizontal axis of the pelvic cavity to represent abdominal water quantity, but the results showed no statistical significance, possibly because the pelvic fluid depth could not completely reflect the total amount of fluid in the entire abdomen or pelvis, and some ascites were scattered in the middle and upper levels of the abdominal cavity. Fourth, regarding peritoneal implantation metastasis, our study suggests that preoperative imaging methods were used to assess the peritoneal metastasis in the recurrence group (10/11, 91%) and the no recurrence group (7/18, 39%), with statistical difference, at the same time, patients with peritoneal planting had higher recurrence risk than those without it. However, peritoneal implants were not statistically significant between the recurrent and non-recurrent FIGO III groups. Because peritoneal implants was histologically confirmed in all FIGO III patients, and most peritoneal implants could be recognized in preoperative imaging evaluation. A few could not be recognized, because the peritoneal implantation foci were very small. So for FIGO III patients, preoperative determination of radiographic implantation metastases in peritoneum should not be used to make inferences about patients' outcomes. In addition, our study further analyzed the degree of peritoneal thickening, but the results showed no statistical significance. This may imply that no matter how great the degree of peritoneal thickening, the patient's prognosis was affected as long as there was an implanted metastasis on CT or MRI. An interesting result was that for FIGO III patients, the imaging indicator of ipsilateral fallopian tube involvement was statistically significant between the two groups, and no imaging signs of fallopian tube involvement were observed in the recurrence group. This has not been reported in previous literature, and further study on large sample size or related mechanism is needed. In addition to the above indicators, Ki67 PI was statistically significant whether in large groups or in FIGO III groups, implying that it was not affected by uneven staging. The average Ki67 PI of the recurrence cohort was lower than that of the no recurrence cohort, and there was some overlap between the two groups. Previous studies have yielded mixed results for Ki67 PI for prognostic assessment, so the results require further verification with large sample data in the future.

**TABLE 2** | The statistical results of the univariate analysis of the ADC values and enhancement degrees of the recurrence and no recurrence groups.

| Indicators | Recurrence (n=11) | No recurrence (n=18) | Univariate analysis (*P*) |
|---|---|---|---|
| ADC ($\times 10^{-3}$mm$^2$/s) | 0.93 ± 0.27 | 1.02 ± 0.20 | 0.353 |
| Arterial period* | | | 1.000 |
| Mild | 0 | 1 | |
| Moderate | 3 | 5 | |
| Severe | 8 | 12 | |
| Venous period* | | | 0.622 |
| Mild | 0 | 0 | |
| Moderate | 2 | 2 | |
| Severe | 9 | 16 | |
| Delayed period* | | | 0.539 |
| Mild | 0 | 0 | |
| Moderate | 2 | 1 | |
| Severe | 9 | 17 | |

**Enhancement degree.*

**TABLE 3 |** The statistical results of univariate analysis of the main CT and MRI features of the recurrence and no recurrence groups.

| Indicators | Recurrence (n=11) | No recurrence (n=18) | Univariate analysis (*P*) |
|---|---|---|---|
| Volume (cm$^3$) | 788.34 ± 646.67 | 528.32 ± 380.65 | 0.245 |
| Capsule | | | 0.096 |
| Complete | 1 | 8 | |
| Incomplete | 10 | 10 | |
| Presentation of main components | | | 0.162 |
| A | 4 | 11 | |
| B | 5 | 7 | |
| C | 2 | 0 | |
| Degree of cystic extent | | | 1.000 |
| 0 | 0 | 1 | |
| 1 | 4 | 7 | |
| 2 | 2 | 4 | |
| 3 | 5 | 6 | |
| Bleeding | | | 0.466 |
| Yes | 6 | 7 | |
| No | 5 | 11 | |
| Ovarian involvement | | | 0.450 |
| Unilateral | 4 | 10 | |
| Bilateral | 7 | 8 | |
| Ipsilateral fallopian tube involvement | | | 0.096 |
| Yes | 1 | 8 | |
| No | 10 | 10 | |
| Uterus/bladder/bowel/pelvic wall involvement | | | 0.143 |
| Yes | 7 | 6 | |
| No | 4 | 12 | |
| The deepest diameter of ascites in pelvic MR images (cm) | 4.39 ± 3.27 | 6.78 ± 4.74 | 0.121 |
| Lymph node metastasis | | | 0.375 |
| Yes | 4 | 3 | |
| No | 7 | 15 | |
| Peritoneal implants | | | **0.008** |
| Yes | 10 | 7 | |
| No | 1 | 11 | |
| Degree of peritoneal thickening (cm) | 1.4 (0.5, 2.9) | 0 (0, 2) | 0.130 |

*Values in bold are statistically significant.*

In our study, the preoperative imaging characteristics of ovarian serous cancer were retrospectively analyzed in detail, including the volume; capsule of the mass; main components; ADC value; cystic change; bleeding; degree of enhancement of the mainly solid region in 3 periods; and range of tumor involvement in the ovary. These imaging characteristics were rarely observed in the past literature. Although the results were not statistically significant, the negative results are of some important clinical significance, namely, that the preoperative imaging characteristics may reflect only the localized characteristics of the tumor, and reliance on preoperative imaging features to estimate the tumor's recurrence is very difficult. A combination of imaging methods and clinical indicators to evaluate prognosis, is likely to achieve more meaningful results.

**TABLE 4 |** The univariate analysis of the ovarian serous carcinoma on FIGO III between the recurrence and no recurrence groups.

| Indicators | Recurrence (n=10) | No recurrence (n=11) | Univariate analysis (*P*) |
|---|---|---|---|
| Age (y) | 52.80 ± 8.15 | 50.73 ± 7.31 | 0.546 |
| Ki67 PI (%) | 44.50 ± 25.65 | 67.27 ± 11.04 | **0.023** |
| Volume (cm$^3$) | 824.23 ± 670.64 | 464.12 ± 336.06 | 0.150 |
| Capsule | | | 0.586 |
| Complete | 1 | 3 | |
| Incomplete | 9 | 8 | |
| Presentation of main components | | | 0.327 |
| A | 4 | 7 | |
| B | 4 | 4 | |
| C | 2 | 0 | |
| Degree of cystic extent | | | 0.792 |
| 0 | 0 | 1 | |
| 1 | 3 | 4 | |
| 2 | 2 | 3 | |
| 3 | 5 | 3 | |
| Bleeding | | | 1.000 |
| Yes | 5 | 5 | |
| No | 5 | 6 | |
| Ovarian involvement | | | 0.659 |
| Unilateral | 3 | 5 | |
| Bilateral | 7 | 6 | |
| Ipsilateral fallopian tube involvement | | | **0.004** |
| Yes | 0 | 7 | |
| No | 10 | 4 | |
| Uterus/bladder/bowel/pelvic wall involvement | | | 0.659 |
| Yes | 7 | 6 | |
| No | 3 | 5 | |
| The deepest diameter of ascites in pelvic MR images (cm) | 4.58 ± 3.38 | 7.79 ± 5.10 | 0.104 |
| Lymph node metastasis | | | 0.659 |
| Yes | 4 | 3 | |
| No | 6 | 8 | |
| Peritoneal implants | | | 0.090 |
| Yes | 10 | 7 | |
| No | 0 | 4 | |
| Degree of peritoneal thickening (cm) | 1.78 ± 1.20 | 1.88 ± 1.82 | 0.883 |
| ADC ($\times 10^{-3}$mm$^2$/s) | 0.95 ± 0.27 | 1.01 ± 0.21 | 0.604 |
| Arterial period* | | | 1.000 |
| Mild | 0 | 1 | |
| Moderate | 3 | 3 | |
| Severe | 7 | 7 | |
| Venous period* | | | 0.586 |
| Mild | 0 | 0 | |
| Moderate | 2 | 1 | |
| Severe | 8 | 10 | |
| Delayed period* | | | 0.586 |
| Mild | 0 | 0 | |
| Moderate | 2 | 1 | |
| Severe | 8 | 10 | |

**Enhancement degree.*
*Values in bold are statistically significant.*

Our study had several limitations. First, this study was retrospective, and the number of patients was relatively small. Second, the DWI model adopted in this study was a single index model, which could not eliminate the perfusion related information in ADC values and could not fully reflect the

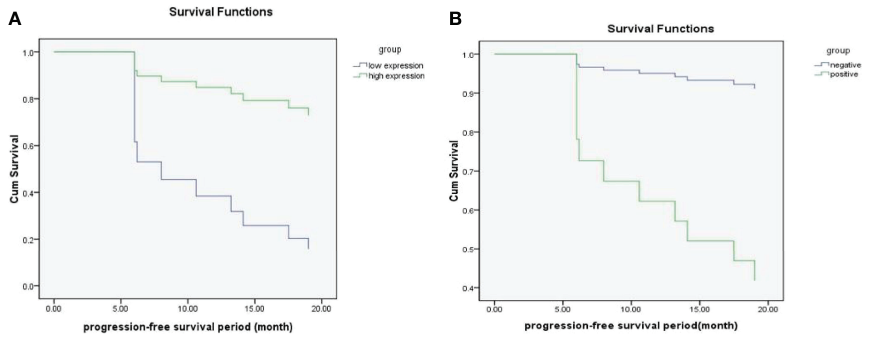

**FIGURE 3** | **(A, B)** The survival functions for Ki67 PI low-expression group and high-expression group **(A)**; The survival functions for positive group and negative group (whether peritoneal implantation metastasis was present) **(B)**.

diffusion of pure water molecules inside the tumor. However, intravoxel incoherent motion imaging may provide a more comprehensive analysis of a tissue's diffusion imaging data. In addition, the follow-up period was short, and the clinical endpoints were not evaluated based on overall survival. These limitations need to be addressed in the future.

In conclusion, in CT and MRI examinations before surgery, peritoneal implantation metastasis was suggestive of the possibility of the recurrence of serous ovarian carcinoma in the near future. In addition to that, ipsilateral fallopian tube involvement and Ki67 PI may also indicate the possibility of recurrence (the former was only applicable to FIGO III patients), but other imaging indexes show no obvious value for indicating the possibility of recurrence.

## DATA AVAILABILITY STATEMENT

The raw data supporting the conclusions of this article will be made available by the authors, without undue reservation.

## ETHICS STATEMENT

Written informed consent was obtained from the individual(s) for the publication of any potentially identifiable images or data included in this article.

## AUTHOR CONTRIBUTIONS

MF: Conceptualization, Methodology, Writing original draft preparation. SH: Software, Data curation, Visualization. J-ND: Supervision, Reviewing. HY: Investigation. XF and FC: Software. PZ and QZ: Validation. YC: Data curation. All authors contributed to the article and approved the submitted version.

## SUPPLEMENTARY MATERIAL

The Supplementary Material for this article can be found online at: https://www.frontiersin.org/articles/10.3389/fonc.2022.754067/full#supplementary-material

## REFERENCES

1. Siegel RL, Miller KD, Jemal A. Cancer Statistics, 2016. *CA Cancer J Clin* (2016) 66(1):7–30. doi: 10.3322/caac.21332
2. Heintz AP, Odicino F, Maisonneuve P, Quinn MA, Benedet JL, Creasman WT, et al. Carcinoma of the Ovary. FIGO 26th Annual Report on the Results of Treatment in Gynecological Cancer. *Int J Gynaecol Obstet* (2006) 95(Suppl 1):S161–192. doi: 10.1016/S0020-7292(06)60033-7
3. Bhatla N, Denny L. FIGO Cancer Report 2018. *Int J Gynecol Obstet* (2018) 143 (2):2–3. doi: 10.1002/ijgo.12608
4. Rizzuto I, Stavraka C, Chatterjee J, Borley J, Hopkins TG, Gabra H, et al. Risk of Ovarian Cancer Relapse Score: A Prognostic Algorithm to Predict Relapse Following Treatment for Advanced Ovarian Cancer. *Int J Gynecol Cancer* (2015) 25(3):416–22. doi: 10.1097/IGC.0000000000000361
5. Goode EL, Block MS, Kalli KR, Vierkant RA, Chen WQ, Fogarty ZC, et al. Dose -Response Association of CD8+ Tumor-Infiltrating Lymphocytes and Survival Time in High -Grade Serous Ovarian Cancer. *JAMA Oncol* (2017) 3 (12):e173290. doi: 10.1001/jamaoncol.2017.3290
6. Friedlander ML. Do All Patients With Recurrent Ovarian Cancer Need Systemic Therapy? *Cancer* (2019) 125:4602–8. doi: 10.1002/cncr.32476
7. Bonifácio VDB. Ovarian Cancer Biomarkers: Moving Forward in Early Detection. In: J Serpa, Editor. *Tumor Microenvironment, Advances in Experimental Medicine and Biology*, vol. 1219. Switzerland AG: Springer Nature (2020). p. 355–63.
8. Prat J, D'Angelo E, Espinosa I. Ovarian Carcinomas: At Least Five Different Diseases With Distinct Histological Features and Molecular. *Hum Pathol* (2018) 80:11–27. doi: 10.1016/j.humpath.2018.06.018
9. The US Preventive Services Task Force (USPSTF) members. Screening for Ovarian Cancer US Preventive Services Task Force Recommendation Statement. *JAMA* (2018) 319(6):588–94. doi: 10.1001/jama.2017.21926
10. Friedlander ML. Do All Patients With Recurrent Ovarian Cancer Need Systemic Therapy? *Cancer* (2019) 125:4602–8. doi: 10.1002/cncr.32476
11. Pereira A, Perez-Medina T, Magrina JF, Magtibay PM, Rodríguez-Tapia A, Cuesta-Guardiola T, et al. The Impact of Debulking Surgery in Patients With Node-Positive Epithelial Ovarian Cancer: Analysis of Prognostic Factors Related to Overall Survival and Progression-Free Survival After an Extended Long-Term Follow-Up Period. *Surg Oncol* (2016) 25(1):49–59. doi: 10.1016/j.suronc.2015.12.005
12. Chung HH, Lee M, Kim HS, Kim JW, Park NH, Song YS, et al. Prognostic Implication of the Metastatic Lesion-to -Ovarian Cancer Standardised Uptake

Value Ratio in Advanced Serous Epithelial Ovarian Cancer. *Eur Radiol* (2017) 27(11):4510–5. doi: 10.1007/s00330-017-4883-z

13. Xiaojing G, Yong Z, Zhi W. Influence of CT Manifestations, Tumor Marker Levels and Pathology on Ovarian Cancer Recurrence. *Chin J Med Imaging* (2016) 24(2):133–7. doi: 10.3969/j.issn.1005-5185.2016.02.013
14. Chen Y, Zhang L, Liu WX, Liu XY. Prognostic Significance of Preoperative Anemia, Leukocytosis and Thrombocytosis in Chinese Women With Epithelial Ovarian Cancer. *APJCP* (2014) 16(3):933–9. doi: \10.7314/apjcp.2015.16.3.933

**Conflict of Interest:** The authors declare that the research was conducted in the absence of any commercial or financial relationships that could be construed as a potential conflict of interest.

frontiers | Frontiers in Oncology

ORIGINAL RESEARCH
published: 29 April 2022
doi: 10.3389/fonc.2022.889862

# Survival Impacts of Perineural Invasion on Patients Under Different Radical Hysterectomies Due to Early Cervical Cancer

**Wei-wei Wei[†], Huihui Wang[†], Hong Zheng, Jiming Chen[*] and Ru-xia Shi[*]**

*Department of Gynecology, The Affiliated Changzhou No. 2 People's Hospital of Nanjing Medical University, Changzhou, China*

**Objective:** Cervical cancer is a common gynecological malignancy. In addition to the open radical hysterectomy (ORH) and laparoscopic radical hysterectomy (LRH), laparoscopic nerve-sparing radical hysterectomy (LNSRH) could be another treatment option since it could preserve urinary, colorectal, and sexual functions. However, LNSRH might result in early cancer metastasis and recurrence due to inadequate tumor resection. Additionally, whether LNSRH should be considered based on perineural invasion (PNI) status remains controversial. To assess different types of hysterectomy on the outcome of early cervical cancer with PIN.

**Methods:** A retrospective study was performed in early cervical cancer patients who received ORH, LRH, or LNSRH between January 2012 and December 2019. Age, FIGO cancer stages, histopathological types, tumor size, histological grade, invasion depth, lymph node metastasis, lymphovascular space invasion, and PNI were documented. Disease-free survival (DFS) and overall survival (OS) were recorded.

**Results:** A total of 174 patients were included, with 33, 69, and 72 patients received LRH, ORH, and LNSRH, respectively. Twenty-one patients (12.1%) had PNI. DFS ($P$ = 0.000) and OS ($P$ = 0.022) periods were shortened in positive PNI patients than in negative PNI patients ($P$ = 0.000 and 0.022, respectively). In patients with positive PNI, lymph node metastasis, but not the surgery type, was an independent risk factor for DFS and OS ($P$ = 0.000).

**Conclusion:** Early cervical cancer patients with PNI had shorter postoperative DFS and OS periods. In these patients, lymph node metastasis, but not the type of hysterectomy, was independently associated with DFS and OS.

**Keywords: perineural invasion, cervical cancer, nerve-sparing radical hysterectomy, laparoscopic surgery, survival impacts**

**Edited by:**
*Xia Bai Rong,*
*The First Affiliated Hospital of University of Science and Technology of China Anhui Provincial Hospital, China*

**Reviewed by:**
*Shengtao Zhou,*
*Sichuan University, China*
*Dongling Zou,*
*Chongqing University, China*

***Correspondence:**
*Jiming Chen*
*cjming@126.com*
*Ru-xia Shi*
*czeyfk@163.com*

[†]*These authors share first authorship*

**Specialty section:**
*This article was submitted to Gynecological Oncology, a section of the journal Frontiers in Oncology*

**Received:** *04 March 2022*
**Accepted:** *04 April 2022*
**Published:** *29 April 2022*

**Citation:**
*Wei W-w, Wang H, Zheng H, Chen J and Shi R-x (2022) Survival Impacts of Perineural Invasion on Patients Under Different Radical Hysterectomies Due to Early Cervical Cancer. Front. Oncol. 12:889862. doi: 10.3389/fonc.2022.889862*

## HIGHLIGHTS

What is already known on this topic

PNI exists in early cervical cancer and is a poor prognostic factor for patients with early cervical cancer.

Effect of nerve-sparing radical hysterectomy in early cervical cancer with perineural invasion is unknown.

What this study adds

In early cervical cancer patients with perineural invasion, lymph node metastasis was a risk factor for survival.

How this study might affect research, practice or policy

Physicians should evaluate lymph node metastasis when treating early cervical cancer with perineural invasion.

## INTRODUCTION

Cervical cancer is a common gynecological malignancy globally (1). Its main treatment modalities include surgery and adjuvant chemoradiation therapy. Traditionally, early cervical cancer was treated with open radical hysterectomy (ORH) with or without bilateral pelvic lymphadenectomy. Studies have confirmed that ORH could prolong the disease-free survival (DFS) and the overall survival (OS) in patients with early cervical cancer (2). Lately, a minimally invasive surgical procedure, laparoscopic radical hysterectomy (LRH), has been introduced. Compared with traditional ORH, LRH could be a less traumatic procedure in early cervical cancer patients but might result in a lower DFS and OS (3–6). Both ORH and LRH could negatively impact the quality of life. Moreover, these patients frequently develop severe postoperative urinary, colorectal, and sexual dysfunctions (7). Consequently, a new type of surgery, nerve-sparing radical hysterectomy (NSRH), was proposed, preserving essential visceral nerves to maintain normal physiological functions Clinical trials have shown the benefits of NSRH in cervical cancer patients (8).

However, since NSRH leaves the visceral nerves and adjacent tissue intact, it raises concerns about incomplete cancer resection, early recurrence, and an increased risk of metastasis (9, 10). For example, a malignant mass can spread cancer cells contiguously along the nerve fibers, called perineural invasion (PNI) (11). PNI is recognized as one of the routes of metastatic spread of primary cancer (12). Studies have suggested that the presence of PNI is correlated with a poor prognosis in early-stage cervical cancer patients (13, 14). A shorter DFS and OS were reported after radical hysterectomy in cervical cancer patients with PNI than those without PNI (15). However, there is a paucity of studies exploring the outcome of NSRH in early cervical cancer patients with PNI.

This study investigated the impact on the treatment outcome of early cervical cancer with PNI with LRH, ORH, or LNSRH. We recorded and analyzed the DFS and OS to ascertain the postoperative prognosis and quality of life.

## MATERIALS AND METHODS

### Study Design and Patient Selection

We conducted a retrospective study of histopathologically confirmed early cervical cancer patients who underwent surgical operations in Changzhou No. 2 People's Hospital, affiliated with the Nanjing Medical University, between January 2012 and December 2019. The hospital Institutional Review Board approved this study.

The inclusion criteria were: 1) patients with a confirmed histopathological diagnosis of cervical adenosquamous carcinoma, squamous cell carcinoma, or adenocarcinoma, 2) patients with preoperative early cervical cancer stages I A2– II A2 based on the International Federation of Gynecology and Obstetrics (FIGO) staging system (2018) and 3) patients who had ORH, LRH, or LNSRH with additional pelvic lymphadenectomy +/- removal of paraaortic lymph nodes. Patients with incomplete medical records or abnormal vital organ function were excluded.

This study was approved by the hospital ethics committee (approval number [2021] YLJSD015). All procedures performed in the present study were in accordance with the ethical standards of the institutional and/or national research committee and with the 1964 Helsinki declaration and its later amendments or comparable ethical standards.

### Data Collection

We recorded the participant's age and cervical cancer characteristics, including FIGO stage, pathological type, tumor size, histological grade, invasion depth, lymph node metastasis, lymphovascular space invasion (LVSI), and PNI.

All patients routinely had computed tomography (CT) of the abdomen and pelvis and/or magnetic resonance imaging (MRI) of the pelvis before surgery. These patients underwent ORH, LRH, or LNSRH with additional pelvic lymphadenectomy +/- removal of paraaortic lymph nodes. The indications for paraaortic lymphadenectomy included enlarged nodes on the CT or MRI examinations and a tumor diameter > 2 cm. Our LNSRH surgical procedure has been reported previously (16). In cervical cancer patients with signs of local extension, we tailored the surgical procedures to dissect the parametrial and paravaginal tissues. Since patients with parametrial tumor infiltration were not good candidates for the nerve-sparing procedure, we performed the partial nerve-sparing Kobayashi radical hysterectomy to preserve some portions of the inferior hypogastric plexus and the pelvic splanchnic nerves (9).

Postoperatively, patients received adjuvant radiotherapy if they had a risk of tumor recurrence. Risk factors for tumor recurrence included: 1) positive resection margins, parametrial invasion, and lymph node metastases; or 2) more than two of the following factors, including stromal invasion >1/2 of cervical wall thickness, tumor diameter > 4 cm, and LVSI (17–20).

Tumor tissue samples were obtained from the cervix and parametrial areas of invasion during surgery. They were fixed, embedded, and stained with hematoxylin-eosin (H&E). PNI was confirmed if the H&E staining showed that: 1) any layers of the nerve sheath, including the epineurium, perineurium, or endoneurium, were infiltrated by the cancer cells or 2) ≥ 33% of the nerve circumference was surrounded by the cancer cells (12, 21). An example of PNI is shown in **Figure 1**.

After the hospital discharge, patients were followed up by a telephone interview every three months. Follow-up information

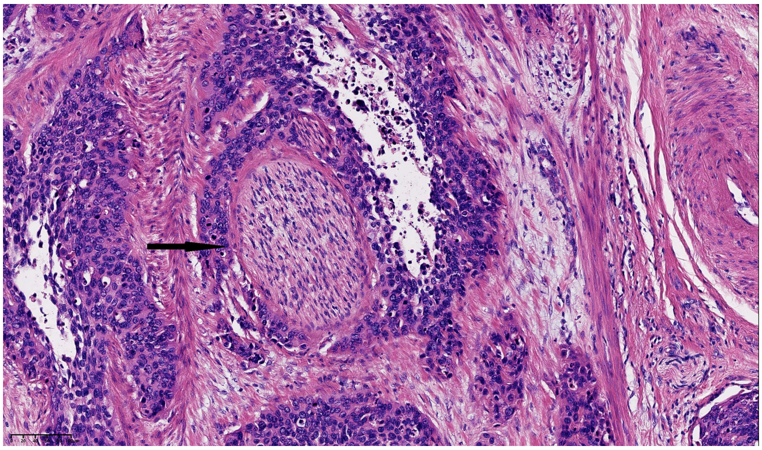

**FIGURE 1** | Histological image of perineural invasion (PNI) in cervical squamous cell carcinoma stained with Hematoxylin and eosin (H&E). PNI from small cancer cell clusters is indicated by arrows (magnification, x200). Scale bar: 20µm each grid.

collected included general health status, cancer recurrence, and mortality. The duration of the follow-up was also documented.

DFS was the period from the time point of surgery to the timepoint of cancer recurrence identified on repeat CT or MRI. If there was no cancer recurrence, the time point of the last follow-up examination or death was used. Overall survival (OS) was the period from the time point of surgery to death.

## Statistical Analysis

Multivariate logistic regression analyses were conducted to examine the factors related to DFS and OS. Continuous data are shown as mean ± standard deviation (SD) and compared by one-way ANOVA. Categorical data are presented as percentages and compared by the Chi-square test. The Kaplan–Meier analysis was used to examine the DFS and OS. The log-rank test was used to calculate each corresponding *P*-value. Statistical significance was considered with a $P < 0.05$. All analyses were performed in SPSS 20.0 (SPSS, IBM, New York, USA).

# RESULTS

## Participant Characteristic Comparisons

This study included 174 patients, with 33, 69, and 72 in the LRH, ORH, and LNSRH groups, respectively. We did not observe statistically significant differences in the FIGO stage, histopathological types, tumor size, histological grade, invasion depth, lymph node metastasis, and LVSI among the three groups (**Table 1**).

A total of 21 patients (12.1%) had PNI, with 2, 10, and 9 patients in the LRH, ORH, and LNSRH groups, but with no significant difference among them.

Postoperatively, 112 patients received adjuvant radiation therapy. Twelve patients rejected radiotherapy, with three in the LRH, six in the ORH, and three in the LRH group. Five of these 12 patients had cancer recurrences, with four in the ORH group, and one in the LNSRH group.

## Comparisons of Postoperative Survival Among the Three Groups

Twelve patients were lost to follow-up, while the remaining162 patients had a median postoperative follow-up time of 44.9 months (0 – 115 months).

The DFS rates were 87.9, 82.6, and 91.7%, and the OS rates were 97.0, 95.7, and 98.6% in the LRH, ORH, and LNSRH groups, respectively, with no statistically significant difference among the three groups ($P$ = 0.302 for DFS and 0.553 for OS, **Figures 2A, B**).

Patients were assigned into either the PNI positive or PNI negative groups. The PNI positive and PNI negative groups had DFS rates of 66.7 and 90.8% and OS rates of 90.5 and 98.0%, respectively. Positive PNI patients had significantly lower DFS ($P$ = 0.000) and OS ($P$ = 0.022) than the negative PNI patients (**Figures 2C, D**).

## Multivariate Regression Analyses

In 21 patients with positive PNI, multivariate logistic regression analysis revealed that lymph node metastasis, but not the type of surgery, was independently correlated with DFS and OS ($P$ = 0.000) (**Table 2**).

# DISCUSSION

Despite increased prevention and screening efforts, cervical cancer is still a common gynecological malignancy in women, with more than 300,000 deaths worldwide annually (1). Its management should consider the postoperative survival chance and the quality of life.

**TABLE 1 |** Clinical and histopathological characteristics of study participants.

| Characteristics | LRH group (N = 33) | ORH group (N = 69) | LNSRH group (N = 72) | P |
|---|---|---|---|---|
| Age, years (mean ± SD) | 52.8 ± 8.0 | 52.8 ± 9.1 | 53.2 ± 10.2 | 0.085 |
| FIGO stage, N (%) | | | | 0.920 |
| IA | 1 (3.0%) | 0 (0.0%) | 5 (6.9%) | |
| IB1 | 6 (18.2%) | 14 (20.3%) | 9 (12.5%) | |
| IB2 | 11 (33.3%) | 15 (21.8%) | 28 (38.9%) | |
| IB3 | 1 (3.0%) | 9 (13.0%) | 4 (5.5%) | |
| IIA1 | 2 (6.1%) | 7 (10.1%) | 9 (12.5%) | |
| IIA2 | 2 (6.1%) | 5 (7.2%) | 2 (2.8%) | |
| IIIC1 | 9 (27.3%) | 18 (26.1%) | 13 (18.1%) | |
| IIIC2 | 1 (3.0%) | 1 (1.5%) | 2 (2.8%) | |
| Pathology, N (%) | | | | 0.928 |
| Squamous cell carcinoma | 30 (90.9%) | 61 (88.4%) | 64 (88. 9%) | |
| Adeno/adenosquamous carcinoma | 3 (9.1%) | 8 (11.6%) | 8 (11.1%) | |
| Histological grade, N (%) | | | | 0.089 |
| Well-differentiated | 8 (24.2%) | 14 (20.3%) | 14 (19.4%) | |
| Moderately differentiated | 17 (51.5%) | 33 (47.8%) | 29 (40.3%) | |
| Poorly differentiated | 8 (24.2%) | 22 (31.9%) | 29 (40.3%) | |
| Tumor size, cm (mean ± SD) | 3.5 ± 1.1 | 3.8 ± 1.2 | 3.5 ± 1.3 | 0.642 |
| Depth of invasion | | | | 0.274 |
| <1/2 | 13 (39.4%) | 24 (34. 8%) | 30 (41. 7%) | |
| ≥1/2 | 20 (60.6%) | 45 (65.2%) | 42 (58.3%) | |
| LVSI | | | | 0.330 |
| Present | 9 (27.3%) | 26 (37.7%) | 29 (40.3%) | |
| Lymph node metastasis | | | | |
| Positive | 10 (30.3%) | 19 (27.5%) | 15 (20.8%) | 0.246 |
| Perineural invasion | | | | |
| Positive | 2 (6.1%) | 10 (14.5%) | 9 (12.5%) | 0.407 |
| Rejected adjuvant radiation therapy, N (%) * | 3 (14.3%) | 6 (12.0%) | 3 (5.7%) | 0.152 |
| Cancer recurrence | 0 (0.0%) | 4 (66.7%) | 1 (33.3%) | |

*LVSI, lymphovascular space invasion.*

**These patients were considered to have the risk of tumor recurrence and were offered the adjuvant radiation therapy. However, they refused the treatments.*

Surgical resection is the mainstay of treatment in early cervical cancer patients. ORH is the traditional surgical approach and was confirmed to improve the survival chance in cervical cancer patients. Recently, LRH was introduced as a new surgical modality, and early studies showed the benefits of LRH, including less trauma, fast recovery, and short hospital stays (22). However, more and more studies have demonstrated inferior surgical outcomes, including short OFS and OS and early cancer recurrence (3–6). Our study did not observe any statistically significant differences in the baseline characteristics between patients with early cervical cancer who underwent either ORH or LRH. Patients treated with LRH or ORH had no statistically significant differences in the OS and DFS. More studies to investigate the surgical outcomes and survival in patients treated with these two types of surgery are required.

Both ORH and LRH could also cause postoperative bladder, colorectal, and sexual dysfunction, and decreased quality of life in affected patients due to physical discomfort and mental stress (7). NSRH was proposed to preserve the visceral nerves to retain postoperative pelvic functions (9). Clinical evidence has demonstrated that NSRH could be a practical and safe procedure, that may improve the postoperative quality of life of women with cervical cancer (23). However, whether the NSRH could affect the postoperative survival outcomes and cancer recurrence is still under investigation since cancer could spread along the splanchnic nerve, which might be inadequately removed by the NSRH (9, 10).

PNI refers to cancer cell invasion of the nerve fibers. Recent studies have shown that cervical cancer could have PNI. PNI was correlated with poor postoperative survival and cancer recurrence. In cervical cancer patients with PNI, NSRH might leave the cancer cells in the nerve fibers intact. In addition, studies have shown that PNI could be associated with other pathology risk characteristics and poor prognosis (15, 24). Cervical cancer patients with PNI could thus have a high risk for postoperative cancer recurrence or metastasis. Some authors suggested that PNI should be a major consideration when selecting NRSH for patients with cervical cancer (10). However, preoperative determination of PNI could be difficult. Studies have suggested that preoperative pelvic MRI imaging and intraoperative frozen section examinations might help to define the PNI, but the results were not conclusive. More studies are required to find the methods that can provide an accurate preoperative diagnosis of PNI.

The objective of our study was to ascertain whether different types of surgery could affect the prognosis of early cervical cancer with PNI. In our study, 12.1% of patients with early cervical cancer had PNI, which was more than 8.6% reported by Zhu et al. (13). This percentage difference might be because our patients had slightly higher FIGO stages than their patients. Our study results

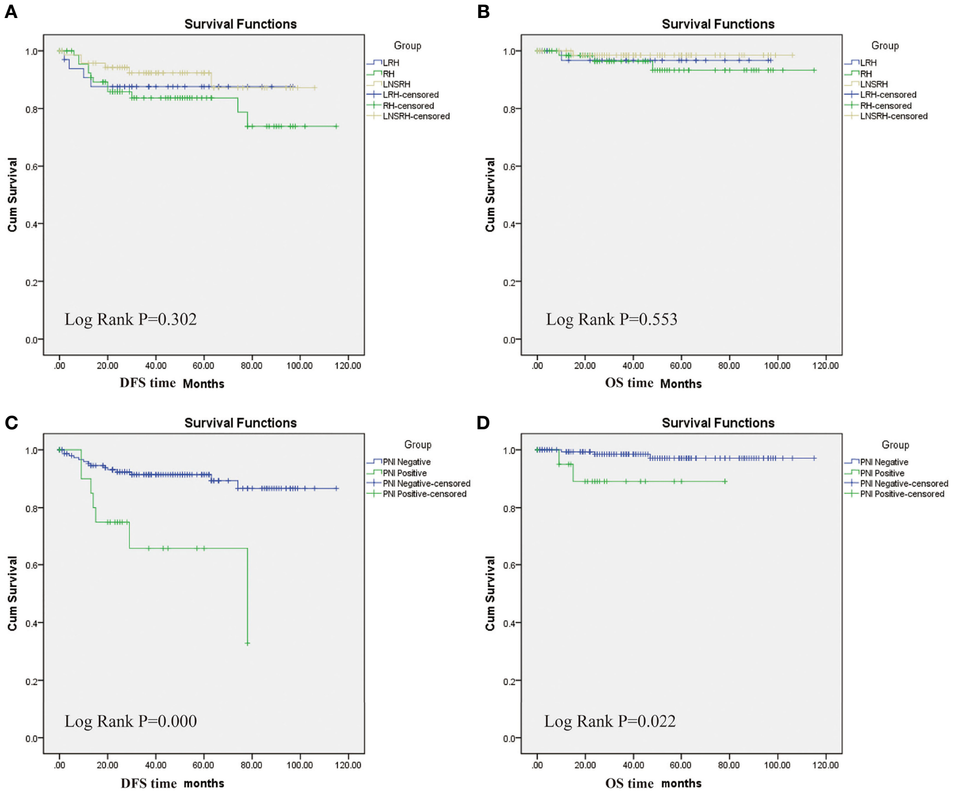

**FIGURE 2** | Kaplan-Meier survival analyses. **(A)** Comparisons of disease-free survival (DFS) periods among three groups. **(B)** Comparisons of overall survival (OS) periods among three groups. There was no statistically significant difference in DFS and OS among the three groups. **(C)** DFS periods between positive and negative PNI groups. **(D)** OS periods between positive and negative PNI groups. PNI positive group had lower DHS and OS than the PCI negative group.

**TABLE 2** | Multivariate analysis for disease-free survival and overall survival.

| **Variables** | **Disease-free survival time**<br>***P*** | **Overall survival time**<br>***P*** |
|---|---|---|
| FIGO stage, n (%) | 0.216 | 0.258 |
| Depth of invasion | 0.815 | 0.250 |
| LVSI | 0.652 | 0.146 |
| Lymph nodes metastases | 0.000 | 0.000 |
| Type of surgery* | 0.990 | 0.690 |

*LVSI, lymphovascular space invasion.*

**Types of surgery, open radical hysterectomy, laparoscopic radical hysterectomy, or laparoscopic nerve-sparing radical hysterectomy.*

showed that early cervical cancer patients with PNI had lower postoperative DFS and OS than those without PNI. This result is consistent with previous reports (14, 15). Multivariate regression analysis demonstrated that, in all patients with PNI, the lymph node metastasis, but not the type of surgery, was an independent risk factor impacting the DFS and OS. This finding implied that LNSRH probably has similar efficacy as LRH and ORH in treating early cervical cancer patients with PNI. Therefore, physicians should carefully consider lymph node metastasis and not the type of surgery when considering hysterectomy in these patients with PNI. Lymph node metastasis and not the type of hysterectomy would determine the length of postoperative survival.

In this retrospective study, we performed NSRH laparoscopically. The minimally invasive techniques could enhance postoperative recovery, decrease postoperative complications, and improve short-term prognosis compared with major gynecologic surgery, such as RH (25, 26). We did not identify a statistically significant DFS and OS difference among the three groups, but the DFS and OS were higher in the LNSRH group than in the other two groups. These findings suggest that LNSRH is a feasible, safe, and effective surgical option for treating early cervical cancer with PNI (23).

Additional benefits of LNSRH could be the earlier return of bladder function, allowing patients to undergo earlier postoperative adjuvant radiotherapy, and potentially improving the chances of survival.

Our study's strengths include its direct survival comparison among three different types of hysterectomy and relatively long-term follow-up periods. The study's limitations include the retrospective design, single-center study, and a very small sample size. We only studied the survivals, but not the postoperative complications and quality of life of these patients. Future prospective studies should be conducted to validate our findings and address these questions.

In conclusion, patients with early cervical cancer and PNI had shorter postoperative DFS and OS periods. In these patients, lymph node metastasis, but not the surgery types, was independently associated with the DFS and OS.

## DATA AVAILABILITY STATEMENT

The raw data supporting the conclusions of this article will be made available by the authors, without undue reservation.

## ETHICS STATEMENT

The studies involving human participants were reviewed and approved by Changzhou Second People's Hospital Ethics Committee. The patients/participants provided their written informed consent to participate in this study.

## AUTHOR CONTRIBUTIONS

W-WW: Data curation; Formal analysis; Funding acquisition; Investigation; Methodology; Writing - original draft. HW: Data collection; Methodology; Validation. HZ: Methodology; Validation; Software. JC: Resources; Supervision; Writing - review & editing. R-XS: Conceptualization; Methodology; Project administration. All authors contributed to the article and approved the submitted version.

## FUNDING

This work was supported by grants from the Changzhou Science & Technology Program (QN201931), the maternal and child health research project of Jiangsu Province ( F202138 ), the Scientific Research Support Program for Postdoctoral of Jiangsu Province(2019K064), and the Scientific Research Support Program for "333 Project" of Jiangsu Province (BRA2019161).

## REFERENCES

1. Arbyn M, Weiderpass E, Bruni L, de Sanjose S, Saraiya M, Ferlay J, et al. Estimates of Incidence and Mortality of Cervical Cancer in 2018: A Worldwide Analysis. *Lancet Glob Health* (2020) 8:e191–203. doi: 10.1016/S2214-109X(19)30482-6
2. Wenzel HHB, Smolders RGV, Beltman JJ, Lambrechts S, Trum HW, Yigit R, et al. Survival of Patients With Early-Stage Cervical Cancer After Abdominal or Laparoscopic Radical Hysterectomy: A Nationwide Cohort Study and Literature Review. *Eur J Cancer* (2020) 133:14–21. doi: 10.1016/j.ejca.2020.04.006
3. Ramirez PT, Frumovitz M, Pareja R, Lopez A, Vieira M, Ribeiro R, et al. Minimally Invasive Versus Abdominal Radical Hysterectomy for Cervical Cancer. *N Engl J Med* (2018) 379:1895–904. doi: 10.1056/NEJMoa1806395
4. Melamed A, Margul DJ, Chen L, Keating NL, Del Carmen MG, Yang J, et al. Survival After Minimally Invasive Radical Hysterectomy for Early-Stage Cervical Cancer. *N Engl J Med* (2018) 379:1905–14. doi: 10.1056/NEJMoa1804923
5. Smith AJB, Jones TN, Miao D, Fader AN. Minimally Invasive Radical Hysterectomy for Cervical Cancer: A Systematic Review and Meta-Analysis. *J Minim Invasive Gynecol* (2021) 28:544–55 e7. doi: 10.1016/j.jmig.2020.12.023
6. Nitecki R, Ramirez PT, Frumovitz M, Krause KJ, Tergas AI, Wright JD, et al. Survival After Minimally Invasive vs Open Radical Hysterectomy for Early-Stage Cervical Cancer: A Systematic Review and Meta-Analysis. *JAMA Oncol* (2020) 6:1019–27. doi: 10.1001/jamaoncol.2020.1694
7. Baessler K, Windemut S, Chiantera V, Kohler C, Sehouli J. Sexual, Bladder and Bowel Function Following Different Minimally Invasive Techniques of Radical Hysterectomy in Patients With Early-Stage Cervical Cancer. *Clin Transl Oncol* (2021) 23:2335–43. doi: 10.1007/s12094-021-02632-7
8. Ma L, Li Q, Guo Y, Tan X, Wang M, Qi Q. Laparoscopic Nervesparing Radical Hysterectomy for the Treatment of Cervical Cancer: A Meta-Analysis of Randomized Controlled Trials. *World J Surg Oncol* (2021) 19:301. doi: 10.1186/s12957-021-02408-x
9. Sakuragi N, Murakami G, Konno Y, Kaneuchi M, Watari H. Nerve-Sparing Radical Hysterectomy in the Precision Surgery for Cervical Cancer. *J Gynecol Oncol* (2020) 31:e49. doi: 10.3802/jgo.2020.31.e49
10. Zhu Y, Zhang GN, Shi Y, Cui L, Leng XF, Huang JM. Perineural Invasion in Cervical Cancer: Pay Attention to the Indications of Nerve-Sparing Radical Hysterectomy. *Ann Transl Med* (2019) 7:203. doi: 10.21037/atm.2019.04.35
11. Chen SH, Zhang BY, Zhou B, Zhu CZ, Sun LQ, Feng YJ. Perineural Invasion of Cancer: A Complex Crosstalk Between Cells and Molecules in the Perineural Niche. *Am J Cancer Res* (2019) 9:1–21.
12. Marchesi F, Piemonti L, Mantovani A, Allavena P. Molecular Mechanisms of Perineural Invasion, a Forgotten Pathway of Dissemination and Metastasis. *Cytokine Growth Factor Rev* (2010) 21:77–82. doi: 10.1016/j.cytogfr.2009.11.001
13. Zhu Y, Zhang G, Yang Y, Cui L, Jia S, Shi Y, et al. Perineural Invasion in Early-Stage Cervical Cancer and its Relevance Following Surgery. *Oncol Lett* (2018) 15:6555–61. doi: 10.3892/ol.2018.8116
14. Tang M, Liu Q, Yang X, Chen L, Yu J, Qi X, et al. Perineural Invasion as a Prognostic Risk Factor in Patients With Early Cervical Cancer. *Oncol Lett* (2019) 17:1101–7. doi: 10.3892/ol.2018.9674
15. Cui L, Shi Y, Zhang GN. Perineural Invasion as a Prognostic Factor for Cervical Cancer: A Systematic Review and Meta-Analysis. *Arch Gynecol Obstet* (2015) 292:13–9. doi: 10.1007/s00404-015-3627-z
16. Shi R, Wei W, Jiang P. Laparoscopic Nerve-Sparing Radical Hysterectomy for Cervical Carcinoma: Emphasis on Nerve Content in Removed Cardinal Ligaments. *Int J Gynecol Cancer* (2016) 26:192–8. doi: 10.1097/IGC.0000000000000577
17. Cho HC, Kim H, Cho HY, Kim K, No JH, Kim YB. Prognostic Significance of Perineural Invasion in Cervical Cancer. *Int J Gynecol Pathol* (2013) 32:228–33. doi: 10.1097/PGP.0b013e318257df5f
18. Je HU, Han S, Kim YS, Nam JH, Kim HJ, Kim JW, et al. A Nomogram Predicting the Risks of Distant Metastasis Following Postoperative Radiotherapy for Uterine Cervical Carcinoma: A Korean Radiation Oncology Group Study (KROG 12-08). *Radiother Oncol* (2014) 111:437–41. doi: 10.1016/j.radonc.2014.03.025
19. Monk BJ, Wang J, Im S, Stock RJ, Peters WA3rd, Liu PY, et al. Rethinking the Use of Radiation and Chemotherapy After Radical Hysterectomy: A Clinical-Pathologic Analysis of a Gynecologic Oncology Group/Southwest Oncology Group/Radiation Therapy Oncology Group Trial. *Gynecol Oncol* (2005) 96:721–8. doi: 10.1016/j.ygyno.2004.11.007

20. Rotman M, Sedlis A, Piedmonte MR, Bundy B, Lentz SS, Muderspach LI, et al. A Phase III Randomized Trial of Postoperative Pelvic Irradiation in Stage IB Cervical Carcinoma With Poor Prognostic Features: Follow-Up of a Gynecologic Oncology Group Study. *Int J Radiat Oncol Biol Phys* (2006) 65:169–76. doi: 10.1016/j.ijrobp.2005.10.019
21. Liebig C, Ayala G, Wilks JA, Berger DH, Albo D. Perineural Invasion in Cancer: A Review of the Literature. *Cancer* (2009) 115:3379–91. doi: 10.1002/cncr.24396
22. Backes FJ, Fowler JM. Hysterectomy for the Treatment of Gynecologic Malignancy. *Clin Obstet Gynecol* (2014) 57:115–27. doi: 10.1097/GRF.0000000000000006
23. Ceccaroni M, Roviglione G, Malzoni M, Cosentino F, Spagnolo E, Clarizia R, et al. Total Laparoscopic vs. Conventional Open Abdominal Nerve-Sparing Radical Hysterectomy: Clinical, Surgical, Oncological and Functional Outcomes in 301 Patients With Cervical Cancer. *J Gynecol Oncol* (2021) 32:e10. doi: 10.3802/jgo.2021.32.e10
24. Wei YS, Yao DS, Long Y. Evaluation of the Association Between Perineural Invasion and Clinical and Histopathological Features of Cervical Cancer. *Mol Clin Oncol* (2016) 5:307–11. doi: 10.3892/mco.2016.941
25. Chiva L, Zanagnolo V, Querleu D, Martin-Calvo N, Arevalo-Serrano J, Capilna ME, et al. SUCCOR Study: An International European Cohort Observational Study Comparing Minimally Invasive Surgery Versus Open Abdominal Radical Hysterectomy in Patients With Stage IB1 Cervical Cancer. *Int J Gynecol Cancer* (2020) 30:1269–77. doi: 10.1136/ijgc-2020-001506
26. Corrado G, Vizza E, Legge F, Pedone Anchora L, Sperduti I, Fagotti A, et al. Comparison of Different Surgical Approaches for Stage Ib1 Cervical Cancer Patients: A Multi-Institution Study and a Review of the Literature. *Int J Gynecol Cancer* (2018) 28:1020–8. doi: 10.1097/IGC.0000000000001254

**Conflict of Interest:** The authors declare that the research was conducted in the absence of any commercial or financial relationships that could be construed as a potential conflict of interest.

ORIGINAL RESEARCH
published: 29 April 2022
doi: 10.3389/fonc.2022.823956

# Low-Intensity Focused Ultrasound Targeted Microbubble Destruction Enhanced Paclitaxel Sensitivity by Decreasing Autophagy in Paclitaxel-Resistant Ovarian Cancer

**Gonglin Fan[1†], Jiale Qin[2†], Xiaofeng Fu[1], Xing Si[1], Liqiang Li[3], Keji Yang[3], Beibei Wang[4], Haiya Lou[1] and Jiang Zhu[2*]**

[1] Department of Ultrasound, Sir Run Shaw Hospital, Zhejiang University School of Medicine, Hangzhou, China, [2] Department of Ultrasound, Women's Hospital, Zhejiang University School of Medicine, Hangzhou, China, [3] State Key Laboratory of Fluid Power and Mechatronic Systems, School of Mechanical Engineering, Zhejiang University, Hangzhou, China, [4] Center of Cryo-Electron Microscope (CCEM), Zhejiang University, Hangzhou, China

**Edited by:**
Gang Chen,
Huazhong University of Science and Technology, China

**Reviewed by:**
Paul B. Fisher,
Virginia Commonwealth University, United States
Glaucia Maria Machado-Santelli,
Universidade de São Paulo, Brazil

***Correspondence:**
Jiang Zhu
zhujiang1046@zju.edu.cn

†These authors have contributed equally to this work and share first authorship

**Specialty section:**
This article was submitted to Gynecological Oncology, a section of the journal Frontiers in Oncology

**Received:** 28 November 2021
**Accepted:** 04 April 2022
**Published:** 29 April 2022

**Citation:**
Fan G, Qin J, Fu X, Si X, Li L, Yang K, Wang B, Lou H and Zhu J (2022) Low-Intensity Focused Ultrasound Targeted Microbubble Destruction Enhanced Paclitaxel Sensitivity by Decreasing Autophagy in Paclitaxel-Resistant Ovarian Cancer. Front. Oncol. 12:823956. doi: 10.3389/fonc.2022.823956

Ultrasound targeted microbubble destruction (UTMD) was introduced as a promising method to improve anti-tumor therapeutic efficacy, while minimizing side effects to healthy tissues. Nevertheless, the acoustical phenomenon behind the UTMD as well as the exact mechanisms of autophagy action involved in the increased anti-cancer response are still not fully understood. Therefore, we examined the drug resistance-reversing effects of low-intensity focused ultrasound with microbubble (LIFU+MB) in paclitaxel (PTX)-resistant ovarian cancer cells. Cell viability was evaluated using CCK8 (Cell Counting Kit-8), apoptosis was detected by flow cytometry, quantitative real-time PCR and Western blot were used to detect the expressions of mRNA and protein, and autophagy was observed by transmission electron microscopy (TEM). We revealed that the level of autophagy was increased ($p < 0.05$) in PTX-resistant ovarian cancer cells. Treatment of LIFU+MB combined with PTX can notably inhibit proliferation as well as increase apoptosis ($p < 0.01$) in drug-resistant cells. We proposed that LIFU+MB might affect the sensitivity of ovarian cancer cells to PTX by modulating autophagy. To verify the hypothesis, we analyzed the autophagy level of drug-resistant cells after the treatment of LIFU+MB and found that autophagy was significantly inhibited. Altogether, our findings demonstrated that LIFU+MB could reverse PTX resistance in ovarian cancer *via* inhibiting autophagy, which provides a novel strategy to improve chemosensitivity in ovarian cancer.

**Keywords: ovarian cancer, paclitaxel, resistance, autophagy, low-intensity focused ultrasound, microbubble**

## INTRODUCTION

Drug resistance is still a severe problem in the management of ovarian cancer all over the world (1). The standard postsurgical chemotherapy is the use of paclitaxel (PTX), a natural antimitotic agent, which has proven effective in many ovarian epithelial carcinomas (2). However, the treatment is often compromised by a high rate of relapse because of the development of drug resistance, which is a major obstacle in the management of ovarian cancer (3). Drug resistance has been linked to many mechanisms, including efflux transporters, apoptosis dysregulation, autophagy, cancer stem cells, epigenetics, and the epithelial–mesenchymal transition. Thus, it is key to developing and choosing effective therapies (4).

In recent years, therapeutic ultrasound, especially low-intensity focused ultrasound (LIFU), has received increasing attention due to its non-invasive nature, safety, and low cost (5). Ultrasound can cause physical and biochemical effects to affect tumor cell damage and apoptosis (6). A large number of recent studies have verified that ultrasound-targeted microbubble destruction (UTMD) technology can be applied for tumor-targeted therapy, providing a new treatment method for malignant tumors (7). Many UTMD-induced bioeffects have been reported already. For example, studies have shown that sonoporation can induce cellular stress, progression delays, endocytosis, actin cytoskeleton disruption, and membrane blebbing (8). However, the role of UTMD-induced autophagic changes in PTX-resistant cells remains unclear; thus, further studies are needed to elucidate its role.

Autophagy is an evolutionarily conserved indispensable catabolic process for the degradation of cytoplasmic components within lysosomes, which leads to organelle turnover and provides energy and macromolecular precursors (9). Autophagy frequently occurs during tumor growth and cancer chemotherapy (10). However, increasing evidence implicated that constructive autophagy usually functions to protect cancer cells during chemotherapy, leading to cancer drug resistance and refractory cancer (11). Recently, some studies have revealed that, under certain conditions, inhibiting autophagy can suppress cancer resistance (12).

Although the efficiency of UTMD-mediated cavitation in permeabilizing the biological barriers has been demonstrated, the exact mechanism behind the action of UTMD-induced autophagic changes has not been completely elucidated (13). Furthermore, the effect of UTMD in autophagy has not been tested yet. The main objective of this study was to explore the underlying mechanisms of clinically approved MB, in combination with LIFU in cancer therapy. Our data revealed that LIFU+MB was effective in cell apoptosis. The biological effects of LIFU+MB were significant determinants for the inhibition of cell proliferation, while we proposed that downregulated autophagy might be a contributing factor for improving chemosensitivity.

## MATERIALS AND METHODS

### Cell Culture

PTX-sensitive ovarian cell lines SKOV3 and A2780, and PTX-resistant cell lines SKOV3-TR and A2780-TR were gifts from Women's Reproductive Health Research Laboratory of Zhejiang Province (Hangzhou, China). A2780 and A2780-TR were cultured in RPMI 1640 media (Gibco, China) containing 10% fetal bovine serum (FBS, GIBCO or CellMax) and 1% penicillin/streptomycin (HyClone Laboratories, USA; 100 units/ml penicillin and 100 µg/ml streptomycin). SKOV3 and SKOV3-TR cells were cultured in McCoy's 5A medium (Boster Biological Technology Co., Wuhan, China) supplemented with 10% FBS and 1% penicillin/streptomycin. To maintain the drug-resistant phenotype, SKOV3-TR and A2780-TR cells were cultured in the presence of 10 nmol/L PTX (Bristol-Myers Squibb Pharmaceuticals Ltd., USA) and passaged for 1 week in a drug-free medium before the experiment. All cells were grown in an incubator with a humidified atmospheric air containing 5% $CO_2$ at 37°C. The cells were used for experiments on the logarithmic phase.

### Determination of the Inhibitory Concentration 50%

To identify the situation of the PTX resistance, cells were treated with increasing dosages of PTX for 48 h, and cell viability was tested by the Cell Counting Kit-8 (CCK-8, Dojindo Laboratories, Kumamoto, Japan) according to the manufacturer's instructions. The absorbance at 450 nm was measured by using a Versamax microplate reader (Thermo Varioskan Flash, USA). Absorption in the blank well was subtracted, and the control was set as 100%, and others were normalized accordingly. The $IC_{50}$ was calculated by the GraphPad Prism program.

### LIFU+MB Therapy System

The ultrasound probe system was developed and produced by our group (14, 15). We followed the best community-accepted practices in the tutorial papers as guidance (16, 17). The water tank type and the portable type are made using *in vitro* and *in vivo* experiments (**Figures 1A–E**). The system can deliver focused ultrasound energy (transducer's active diameter 67 mm, –6 dB focal diameter 2.44 mm, –6 dB focal length 5.0 mm). In *in vitro* experiments, acoustic absorbing layers were placed at the inner wall of the tank, consisting of a computer, a waveform generator (RIGOL DG1022U, Beijing RIGOL Technology Co., Ltd., China), a power amplifier (JYH-1000, JIE HUI Industry Co., Ltd., Shanghai, China), and a motion stage to allow for movement and positioning perpendicular to the ultrasound beam axis. The animal experiment was performed using a portable ultrasonic probe (the cover of the probe is made of a sound-absorbing material), which was also designed and produced by our group. The beam profiles were recorded using a needle hydrophone (HNR-0500; Onda, Sunnyvale, CA, USA) and an automated three-axis micro-positioner (ASTS-01; Onda Corporation). **Figures 2A, B** show the corresponding peak negative pressure on the hydrophone scan plane. **Figures 2C, D** show the simulation results of the temperature rise in the PVDF sensor when the ultrasound transducer worked for 1 s (15).

The SonoVue® microbubble contrast agent (Bracco S.p.A, Milan, Italy) was reconstituted in 5 ml of normal saline, a concentration of 10% (v/v) of which was used in each

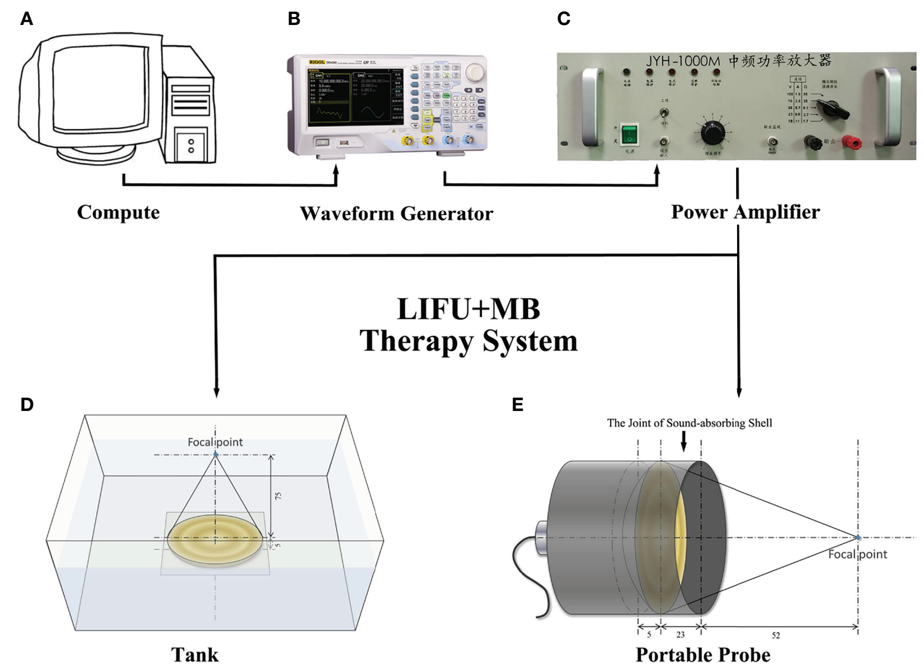

**FIGURE 1** | Design of acoustic exposure platform. Illustration of the entire platform setup that includes **(A)** compute, **(B)** waveform generator, **(C)** power amplifier, **(E)** transducer, and **(D)** the exposure platform immersed within a degassed water bath.

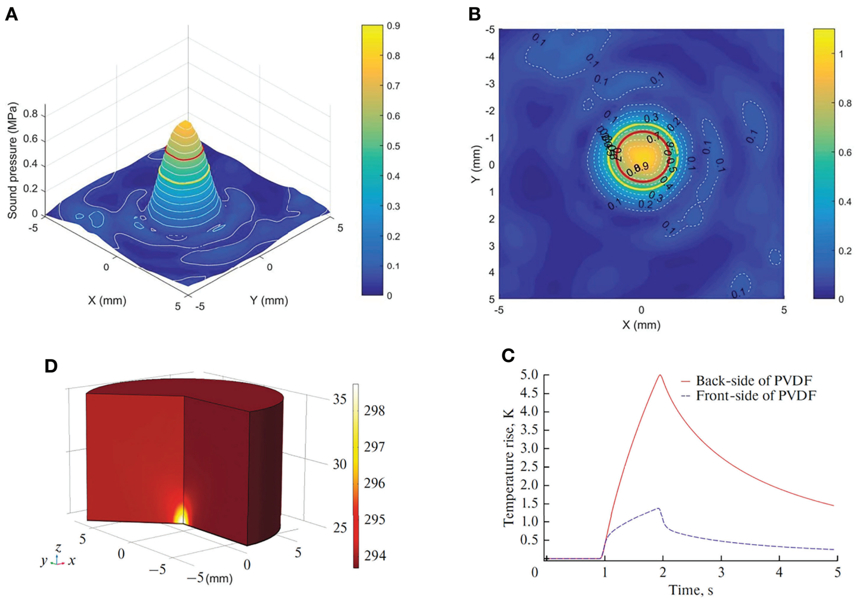

**FIGURE 2** | Characterization of the *in situ* ultrasound field and temperature change. **(A)** 3-D plot of the peak negative pressure on the hydrophone scan plane. **(B)** 2-D plot of the peak negative pressure. Red circle: –3 dB focal region. Yellow circle: –6 dB focal region. **(C)** Temperature rise in the sensor. **(D)** Temperature change at the front side and back side of PVDF.

experimental group. Once reconstituted, it can be chemically and physically stable for 6 h. Studies showed that SonoVue® microbubbles are safe and well tolerated when administered intravenously at 0.03 and 0.3 ml/kg, which are the expected clinical dose and 10 times the clinical dose, respectively. The extremely rapid pulmonary elimination of the compound would indicate that $SF_6$ does not accumulate in healthy subjects, even with repeated administration. SonoVue® microbubbles can also serve as artificial and preexisting nuclei for ultrasound-induced stable and inertial cavitation, which are considered to be the most important mechanism for therapeutic applications. The mean terminal half-life was 12 min (range, 2 to 33 min). More than 80% of the administered sulfur hexafluoride was recovered in exhaled air within 2 min after injection and almost 100% after 15 min (18).

The ultrasonic stimulation experiments were conducted in cells with and without microbubbles. **Figure 3** shows the relationship between SKOV3 cell viability and the concentration of SonoVue® microbubbles, treatment time, ultrasonic intensity, and duty factor. During the experiments, the system operating parameters were 1 MHz, 20% duty cycle (on 0.2 s, off 0.8 s), 3 min exposure duration, 0.42 MPa peak negative pressure, 3 W/cm$^2$ $I_{SPPA}$, 0.6 W/cm$^2$ $I_{SPTA}$, and 108.0 J/cm$^2$ with delivered acoustic energy density. The ultrasound beam propagates vertically into the target through an acoustically transparent sealed chamber (NUNC™ OptiCell®, cat. no. 155330; OptiCell® is a unique cell culture format for growing, monitoring, and transporting cells, which consists of two parallel gas-permeable and cell culture-treated polystyrene membranes), with acoustic coupling provided by degassed water.

## Cell Proliferation

The *in vitro* experiment included eight groups: (1) Blank, (2) LIFU alone, (3) MB alone, (4) LIFU+MB, (5) PTX (200 nM), (6) PTX (200 nM)+LIFU, (7) PTX (200 nM)+MB, and (8) PTX (200 nM)+LIFU+MB. For the Blank and LIFU alone groups, an equivalent volume of medium was used instead of MB or PTX. After 0 h, 12 h, 24 h, 48 h, and 72 h, the medium was exchanged and cell viability was determined as mentioned above. All assays were replicated three times.

## Cell Apoptosis Analysis

Apoptosis of the cells was measured by an Annexin V-fluorescein isothiocyanate (FITC)/propidium iodide (PI) apoptosis detection kit (MultiSciences Biotechnology, Zhejiang, China) according to the manufacturer's instruction. The cells were randomly divided into the aforementioned eight treatment groups. In brief, cells were harvested after 24 h and double-stained with Annexin V-FITC and PI for 15 min in the dark and then analyzed using a FACSCalibur flow cytometer (BD LSRFortessa, USA). The experiments were replicated at least three times.

## Western Blot Analysis

Cultured cells were harvested and lysed in RIPA buffer (Beyotime Biotechnology, Shanghai, China) containing 1%

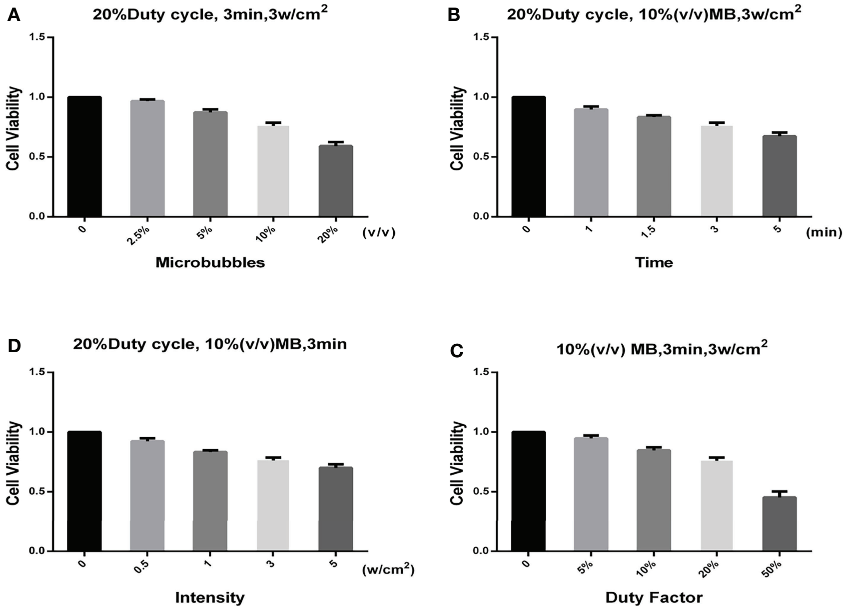

**FIGURE 3** | Relationship between different parameters and the cell viability. **(A)** Relationship between the SonoVue® microbubble concentration and the cell viability. The frequency, duty factor, treatment time, and ultrasonic intensity were 1 MHz, 20%, 3 min, and 3 W/cm$^2$, respectively. **(B)** Relationship between the treatment time and the cell viability. The frequency, duty factor, SonoVue® microbubble concentration, and ultrasonic intensity were 1 MHz, 20%, 10% (v/v), and 3 W/cm$^2$, respectively. **(C)** Relationship between the ultrasonic intensity and the cell viability. The frequency, duty factor, SonoVue® microbubble concentration, and treatment time were 1 MHz, 20%, 10% (v/v), and 3 min, respectively. **(D)** Relationship between the duty factor and the cell viability. The frequency, SonoVue® microbubble concentration, treatment time, and ultrasonic intensity were 1 MHz, 10% (v/v), 3 min, and 3 W/cm$^2$, respectively.

protease inhibitor and separated by electrophoresis, transferred to membranes, and subjected to Western blot according to the standard procedure. The following antibodies were used: Anti-LC3B (ab192890, 1:1,000) was purchased from Abcam (Cambridge, MA, USA), anti-SQSTM1/p62 (#8025, 1:1,000) was purchased from Cell Signaling Technology (Danvers, MA, USA), and anti-GAPDH (AF0006, 1:1,000), used as the internal control, was purchased from Beyotime Biotechnology (Beyotime Biotechnology, Shanghai, China). After incubation with the appropriate secondary antibody, results were detected using ECL detection reagents. Immunoreactive bands were quantified by densitometry using ImageJ software.

## Transmission Electron Microscopy

The cells were collected after centrifugation at 1,000*g* for 5 min. Subsequently, the cells were washed twice with cold phosphate-buffered saline (PBS) and fixed with 2.5% glutaraldehyde overnight at 4°C. Then, cells were dehydrated in a graded ethanol series and embedded by epoxy resin. After mounting on copper grids, the ultrathin sections were double-stained with uranyl acetate and lead citrate. The samples were examined and imaged with a TECNAI 10 or 12 transmission electron microscope (Philips, Holland).

## RNA Preparation and Quantitative Real-Time PCR

Total RNA was extracted using TRIzol reagent (Invitrogen, USA), and RT-PCR was performed according to the manufacturer's instructions. cDNA was synthesized using the PrimeScript RT reagent Kit (Code No. RR047A, Takara, Dalian, China). RT-PCR was performed using the Roche LightCycler 480 and TB Green™ Fast qPCR Mix (Code No. RR820A, Takara, Dalian, China). The primer sequences are listed in **Table 1**. All reactions were run in triplicate. The expression level was normalized to the GAPDH control, and relative expression values were determined against the control using the $2^{-\Delta\Delta CT}$ method.

## Animal Experiment

Animal experiments were approved by the medical experimental animal care commission of Zhejiang University. Female nude mice, aged 4–6 weeks, weighing 18–20 g, were purchased from the Animal Experiment Center (Shanghai SLRC Experimental Animal Co., Ltd., China) and were maintained under controlled conditions of temperature (20 ± 1°C, relative humidity 50%–80%) and illumination (12-h light, 12-h dark). All mice had free access to a standard diet and water.

Approximately $1\times10^7$ A2780-TR cells in 200 µl of serum-free medium and Matrigel solution were injected directly into the flank of each mouse. The tumor-induced nude mice were randomly divided into four groups, with four mice in each of the following groups: the control group, the PTX (10 mg/kg)-treated group, the LIFU+MB-treated group, and the PTX (10 mg/kg)+LIFU+MB-treated group. When the tumor volume reached 150 $mm^3$, the mice received a corresponding treatment. The therapeutic transducer was positioned on top of the tumor. An acoustic absorbing pad was placed under the animal to prevent standing waves from developing. PTX injection is a sterile, stabilized solution of PTX, suitable for dilution for intravenous administration. All the mice were anesthetized with intraperitoneal injections of 1% sodium pentobarbital (6.25 ml/kg), and different suspensions (0.2 ml) were administered *via* the lateral tail vein catheterized with a 26-gauge angio-catheter (Angiocath, Becton Dickinson, UT). For ultrasound stimulation experiments, the animals were exposed to tumor-directed acoustic insonation immediately after injection. The acoustic setup and insonation parameters are described as before. The mice were treated, the long and short diameters of the tumor were measured, and the tumor volumes (TV, TV = $0.5 \times \text{length} \times \text{width}^2$) were calculated every 3 days. The tumor growth curve was drawn according to the measured TV values. After 18 days of treatment, the nude mice were sacrificed by cervical dislocation, and the tumor mass was removed and weighed.

## Contrast-Enhanced Ultrasound Imaging Technique

In a preliminary study, contrast-enhanced ultrasound (CEUS) was performed in mice. The examinations were performed using a GE LOGIQ 9 unit (GE Healthcare, Waukesha, USA) and a linear probe (9L), adjusted to examinations using a microbubble contrast agent. SonoVue® was used at a dose of 0.1 ml, immediately followed by an injection of 0.1 ml of normal saline. Images were recorded for 3 min after contrast agent injection.

## Histological Analysis and Immunohistochemistry

Tumor tissues from the control and LIFU+MB groups were embedded in paraffin and cut into 4 µm-thick sections. Then, the sections were stained with hematoxylin and eosin (H&E). For immunohistochemical staining, the sections were incubated with Anti-LC3B antibodies at 4°C overnight. The subsequent sections were exposed to HRP-antibody colored with diaminobenzidine (DAB), and visualized by microscopy (DM 2500, Leica, Germany).

## Statistical Analysis

All statistical analyses were performed using SPSS 19.0 software (SPSS Inc., Chicago, IL, USA). Data were presented as mean ±

**TABLE 1** | Sequences of primers for quantitative real-time PCR.

| Gene Name | Forward Primer Sequence (5′→3′) | Reverse Primer Sequence (5′→3′) |
|---|---|---|
| GAPDH | GGAGCGAGATCCCTCCAAAAT | GGCTGTTGTCATACTTCTCATGG |
| p62(SQSTM1) | AAGCCGGGTGGGAATGTTG | CCTGAACAGTTATCCGACTCCAT |
| LC3B-II | GATGTCCGACTTATTCGAGAGC | TTGAGCTGTAAGCGCCTTCTA |

standard deviation. One-way analysis of variance (ANOVA) was used to analyze the differences among groups. The Student's *t*-test and Mann–Whitney *U*-test were used to compare the means of the two continuous data. All contingency tables and multiple parameters were assessed using the chi-squared test. **p*-values < 0.05, ***p* < 0.01, or ****p* < 0.001 (two-tailed) were considered as statistically significant. Images were processed using GraphPad Prism 6 (GraphPad Software, La Jolla, CA, USA) and Adobe Photoshop CS5 (Adobe, San Jose, CA, USA).

# RESULTS

## The Sensitivity of PTX in Human Ovarian Cancer Cell Lines SKOV3, A2780, SKOV3-TR, and A2780-TR

SKOV3, SKOV3-TR, A2780, and A2780-TR cells were treated with increasing concentrations of PTX for 48 h (**Figures 4A, B**). Then, CCK-8 assay was used to detect the cells' viability. Cell survival was decreased in a dose-dependent manner in all cell lines. As expected, the SKOV3-TR and A2780-TR cells were more resistant under different concentrations of PTX, as compared with the SKOV3 and A2780 parental cells ($p < 0.05$). $IC_{50}$ values confirmed these results (**Figure 4C**). The $IC_{50}$ values of PTX for SKOV3 vs. SKOV3-TR and A2780 vs. A2780-TR cells were 206.6 ± 28.9 vs. 7,914.1 ± 675.5 and 47.4 ± 3.9 vs. 3,538.0 ± 363.9 nM, respectively.

## The Increasing Autophagy Status in Cell Lines SKOV3-TR and A2780-TR

To determine the contributions of autophagy to cell chemosensitivity, the autophagy level was evaluated in SKOV3, SKOV3-TR, A2780, and A2780-TR cells. Compared with the PTX-sensitive cells, PTX-resistant cells showed higher LC3B-II protein level in Western blot analysis. For the change of p62/SQSTM1, it was inconsistent in two cell lines, which increased in A2780 but declined in SKOV3 (**Figures 5A–C**). Furthermore, autophagic flux was measured by assessing LC3B-II and p62/SQSTM1 in the presence of BafA1, an inhibitor that blocks the lysosomal degradation of autophagosomes. Consistently, PTX-resistant cells had higher levels of autophagic flux compared with the sensitive cells (**Figures 5A–C**). The RT-PCR results showed that the LC3B-II expression level was decreased, while the p62/SQSTM1 expression level was increased in the PTX-sensitive cell lines compared with the PTX-resistant cell lines. These results indicated that autophagy activity was higher in PTX-resistant cells than that in PTX-sensitive cells (**Figures 5D, E**). As expected, transmission electron microscopy (TEM) revealed the increasing number of autophagosomes in the SKOV3-TR and A2780-TR cells compared to the SKOV3 and A2780 cells (**Figures 5F–H**). Therefore, these results suggested that the higher level of autophagy in SKOV3-TR and A2780-TR cells might associate with the drug resistance character.

## LIFU+MB Recovered the Chemosensitivity of SKOV3-TR and A2780-TR Cells to PTX

Cell viability assays demonstrated that the treatment of LIFU and MB alone did not influence cell growth, but LIFU+MB inhibited cell proliferation to some extent. PTX+LIFU and PTX+MB treatments were unable to enhance chemosensitivity, while the PTX+LIFU+MB combination can distinctly inhibit cell growth of SKOV3-TR and A2780-TR cells (**Figures 6A, B**). In addition, the enhancement effect of LIFU+MB on the cells is short term.

To determine whether LIFU+MB treatment exerted a pro-apoptotic effect on cells, flow cytometry analysis *via* Annexin V-FITC/PI staining was performed. The results demonstrated that apoptotic cell death was induced upon LIFU+MB treatment while US and MB treatment did not. Consistent with these results, PTX+LIFU+MB significantly induced apoptosis compared with PTX treatment (**Figures 6C–F**). These results suggested that LIFU+MB treatment was able to enhance drug-induced apoptosis.

## LIFU+MB Decreased Autophagy Status of SKOV3-TR and A2780-TR Cells

To further figure out the major factors of LIFU+MB treatment-induced chemosensitivity, we tested the autophagic rate after treatment. SKOV3-TR and A2780-TR cells were pretreated with autophagy inhibitor Baf A1 for 1 h, treated with LIFU+MB, and cultured for 24 h; the autophagic rate was detected later. Western blot analyses demonstrated that LC3B-II expression levels were decreased in the treatment group, and p62/SQSTM1 expression level was increased in A2780-TR but decreased in SKOV3-TR

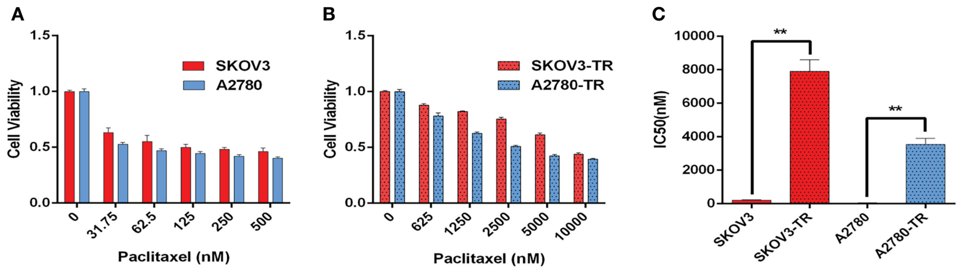

**FIGURE 4** | Paclitaxel inhibits ovarian cancer cell viability. **(A, B)** Viability of paclitaxel-resistant (SKOV3-TR and A2780-TR) and paclitaxel-sensitive (SKOV3 and A2780) cell lines in response to different concentrations of paclitaxel measured by the CCK-8 assay. **(C)** $IC_{50}$ values of paclitaxel for SKOV3, A2780, SKOV3-TR, and A2780-TR cells. The $IC_{50}$ values are calculated by SPSS 19.0 software. (**p < 0.01, n = 3, student t-test, means ± 95% CI).

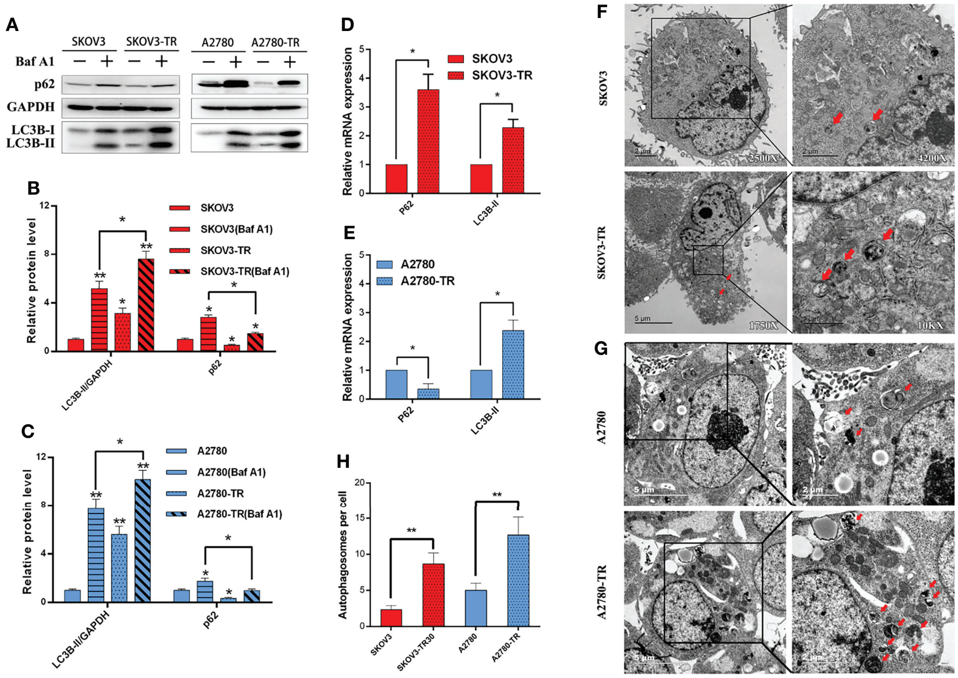

**FIGURE 5** | Autophagy detection in SKOV3, A2780, SKOV3-TR, and A2780-TR cells. **(A–C)** Western blot showed p62(SQSTM1) and LC3B levels in SKOV3, A2780, SKOV3-TR, and A2780-TR cells. The densitometric evaluations are calculated by ImageJ. **(D, E)** The expression of autophagy was determined by real-time PCR. **(F–H)** The autophagic vacuoles (autophagosomes) were detected in SKOV3, SKOV3-TR, A2780, and A2780-TR by transmission electron microscopy (TEM). The representative TEM images are shown and the typical autophagosomes are marked with red arrows. The number of autophagosomes per cell was calculated by counting the number of double-membrane organelles in 10 cells. (*p < 0.05, **p < 0.01, n = 3, student t-test, means ± 95% CI).

(**Figures 7A–C**). In the presence of Baf A1, the LIFU+MB group had lower levels of autophagy compared with the control. These observations were independently validated using TEM. LIFU+MB treatment strikingly decreased the number of autophagosomes in both SKOV3-TR and A2780-TR cells with or without BafA1 (**Figures 7F–H**). In addition, mRNA levels were also detected by qRT-PCR, and the data showed that LC3B-II expression level was decreased, while the p62/SQSTM1 expression level was increased after treatment (**Figures 7D, E**). These results suggested that downregulated autophagy of LIFU+MB treatment could contribute to chemosensitivity.

## LIFU+MB Improved PTX Efficiency in Ovarian Cancer *In Vivo*

The tumors showed complete hyperenhancement during the arterial phase in a preliminary experiment (**Figure 8A**). During the late phase, the tumors were also hypo-enhanced (**Figure 8B**). Next, the effects of LIFU+MB treatment on PTX efficiency were tested *in vivo*. The results showed that PTX and LIFU+MB treatment slightly suppressed tumor growth, whereas the LIFU +MB and PTX combination significantly enhanced the effect of PTX, suppressing tumor growth (**Figures 8C, D**). Immunohistochemical analyses showed that LIFU+MB decreased LC3B expression levels (**Figures 8E, F**). Our findings indicated that LIFU+MB treatment could sensitize ovarian cancer cells with PTX resistance *in vivo*.

# DISCUSSION

Drug resistance is a major problem in chemotherapy for ovarian cancer (19). Numerous studies have found that autophagy dysregulation might play important roles in chemoresistance (20). Autophagy has dual roles in cancer. It may allow cells to survive under unfavorable conditions. Paradoxically, it may also emerge as a tumor suppressor and eventually kill cancer cells (21). In this study, we observed that the autophagy levels of PTX-resistant cell lines SKOV3-TR and A2780-TR were higher than their parental cells, SKOV3 and A2780 ($p < 0.05$), indicating that autophagy may play a pro-survival role here, consistent with the report from Zhang et al. (22). As a further layer of complexity, upregulation of autophagy may lead cancer cells to a non-proliferative dormant state that protects the cells from toxic injuries while preserving their stem-like properties (23).

In this study, we designed and constructed a LIFU therapeutic system, aiming to explore the efficacy and mechanisms responsible for the enhancement of combining UTMD+PTX treatment for refractory ovarian cancer. Early studies showed that UTMD could increase the permeability of the plasma membrane, and the mechanical and cavitation effects were considered responsible for the low-intensity ultrasound bio-effects (6). Cavitation divides into two different physical processes, stable and inertial, that affect cells in different ways (24). Stable cavitation refers to the periodic expansion and

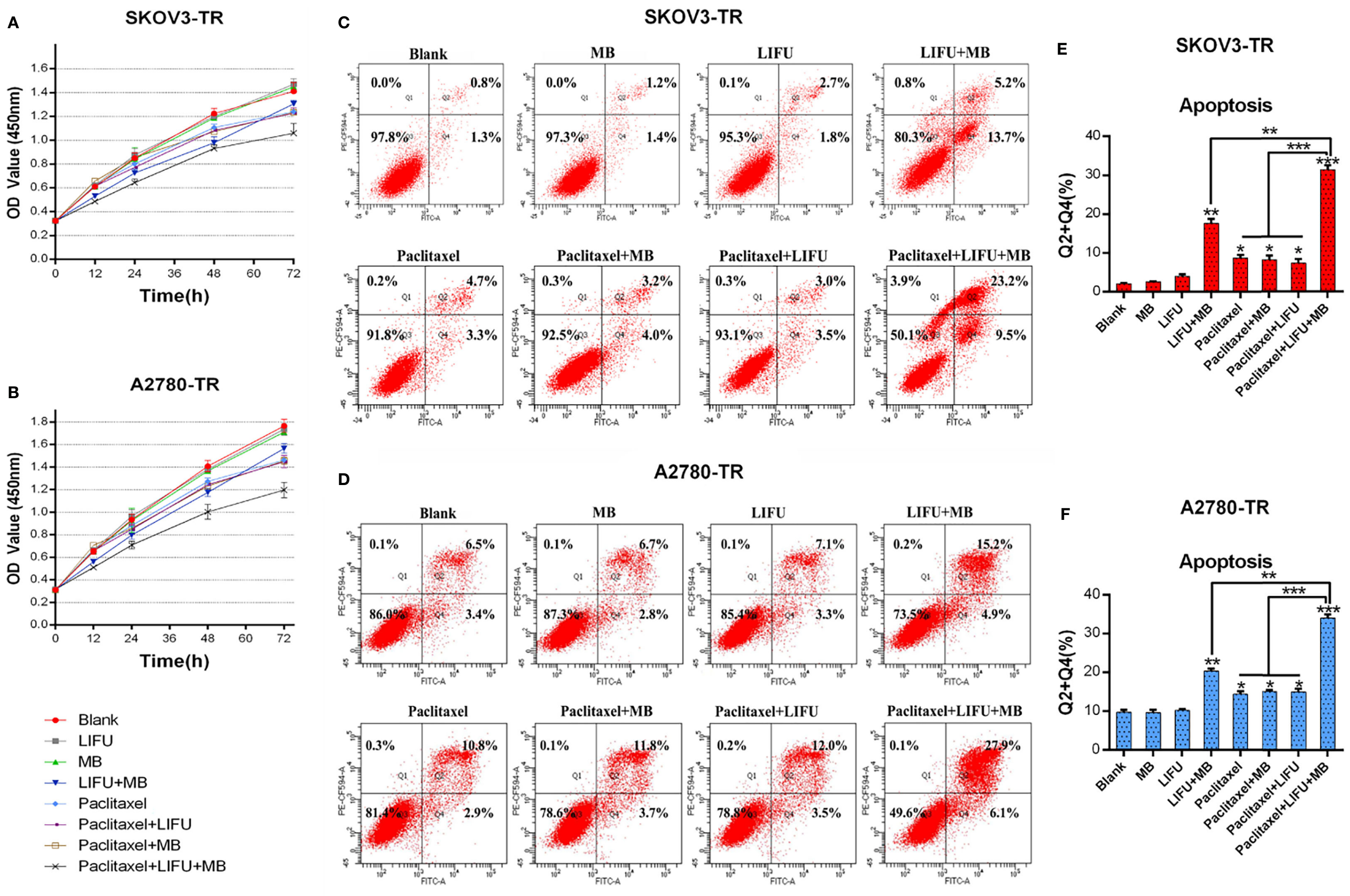

**FIGURE 6** | LIFU+MB enhanced the chemosensitivity of SKOV3-TR and A2780-TR cells to paclitaxel. **(A, B)** OD values were assessed by the CCK-8 method in response to different treatment for different times. **(C–F)** Analysis of apoptosis rates by flow cytometry and quantified after different treatment. (*p < 0.05, **p < 0.01, ***p < 0.001, n = 3, student t-test, means ± 95% CI).

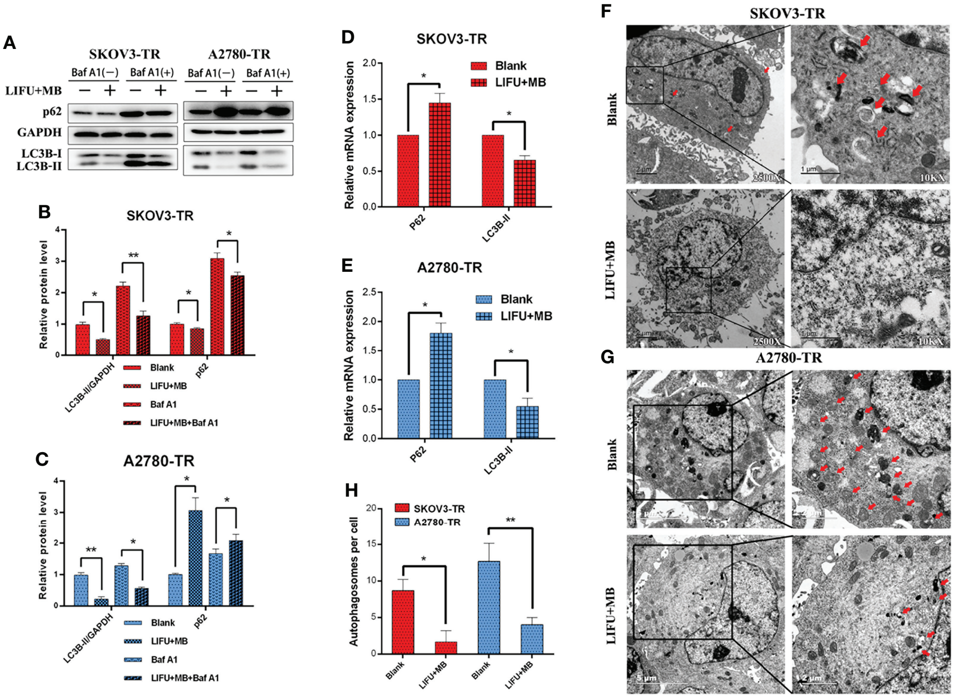

**FIGURE 7** | Autophagy detection in SKOV3-TR and A2780-TR cells after LIFU+MB. **(A–C)** Western blot showed p62(SQSTM1) and LC3B levels in SKOV3-TR and A2780-TR cells. **(D, E)** The expression of autophagy was determined by qRT-PCR. **(F–H)** Analysis of autophagy after LIFU+MB in SKOV3-TR and A2780-TR cells. (*p < 0.05, **p < 0.01, n = 3, student t-test, means ± 95% CI).

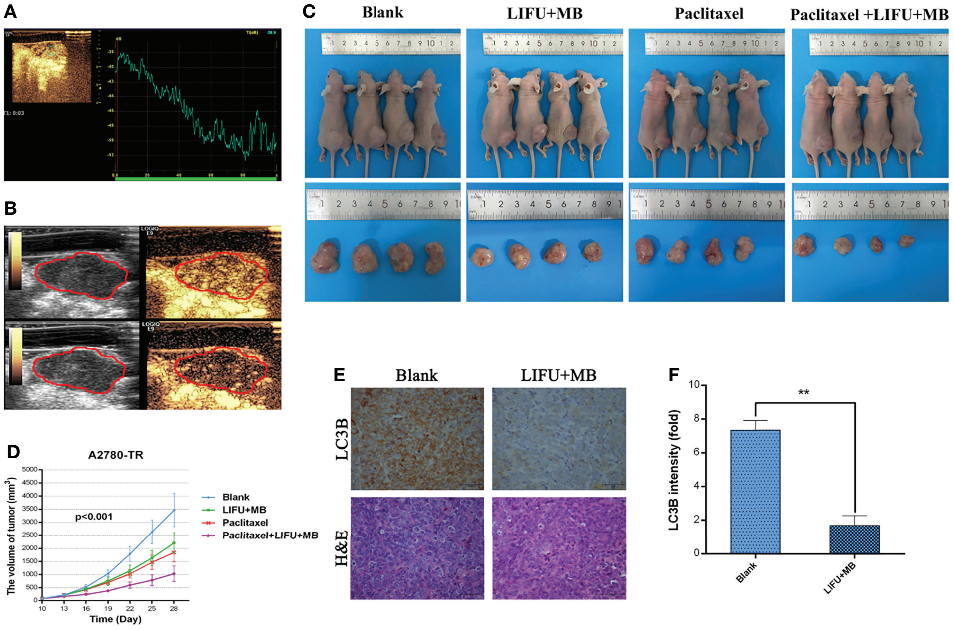

**FIGURE 8** | The effects of different treatments on the tumor-induced nude mice. **(A)** Contrast-enhanced ultrasound with time–intensity curve. **(B)** Preliminary assessment of tumors in mice, images at 15 s and 2 min after administration of 0.1 ml microbubble. **(C)** LIFU+MB significantly inhibited subcutaneous tumor growth in mice treated with paclitaxel. **(D)** Growth curve of A2780-TR subcutaneous xenograft tumors. **(E, F)** LC3B expression analyzed by immunohistochemistry in tumor tissues and quantified. Scale bar: 50 μm (×400). (**p < 0.01, n = 3, student t-test, means ± 95% CI).

contraction of microbubbles around their equilibrium radius in a low-pressure sound field. Inertial cavitation refers to the large expansion and rapid collapse of microbubbles in a high-pressure sound field, and may trigger sonochemical reactions, generate reactive oxygen species, and cause sonoluminescence (25, 26). However, in our experiment, only LIFU (1 MHz, 3 W/cm$^2$, 20% duty cycle) had little influence for cells, indicating that the inertial cavitation (LIFU+MB) may be a key factor.

To further explore the association between LIFU+MB and the level of autophagy, apoptosis and autophagy were evaluated in this study. Our results showed the increasing apoptosis rate of PTX-resistant cells, but the expression of LC3B-II decreased after treatment of LIFU+MB ($p < 0.05$). These results suggested that the LIFU+MB-induced cell death is achieved by inducing apoptosis. Indeed, therapies such as chemotherapy can induce stress, and the metabolic contributions from autophagy can help ameliorate the detrimental cellular effects (27). High-density stress conditions such as LIFU+MB may disrupt these metabolic compensations and induce apoptosis (28). Others, such as LIFU+MB-induced stress response, resembles cellular responses to electroporation and pore-forming toxins in membrane repair, thus restoring cellular homeostasis, and may lead to cell death (29). We also noticed that the effect of LIFU +MB did not last long *in vitro*. Thus, to enhance the effect of LIFU+MB treatment, the tumors were treated every 3 days *in vivo*.

During autophagy, the adaptor protein p62/SQSTM1 is consumed, and LC3B conversion is promoted. LC3B has two forms in cells: LC3B-I and LC3B-II, which is the central protein in the autophagy pathway. LC3B-I residing in the cytosol is converted to the membrane-bound LC3B-II during autophagosome formation (30). Thus, initiative autophagic flux can be indicated by LC3B-II amount and the accomplishment of p62/SQSTM1 degradation status, respectively (31). In this study, we found that LC3B-II expression level decreased after LIFU+MB treatment, suggesting that LIFU+MB could inhibit LC3B-mediated autophagy in PTX-resistant ovarian cancer cells. Nevertheless, further work needs to be performed to detect autophagy with the LIFU+MB and PTX combination.

Paradoxically, we found that basal p62/SQSTM1 expression was higher in SKOV3-TR cell lines, which is fundamentally different from what we found in A2780-TR cells. Following treatment with LIFU+MB, the level of p62/SQSTM1 decreased in SKOV3-TR cells while it increased in A2780 cells. Interestingly, qPCR revealed that the level of p62/SQSTM1 increased in two cell lines. In a previous study, p62/SQSTM1 was related to the resistant mechanism of SKOV3 cells, not only PTX but also other drugs (32). A possible explanation was that ovarian cancer is a heterogeneous disease in which different histological types may result from different origins and distinct genetic patterns (33). Because p62 contains several interaction domains to many signaling molecules for their proteasomal degradation, monitoring p62 degradation thus cannot accurately evaluate the exact autophagic flux or autophagy outcome (34). Moreover, whether downregulating the expression of p62/SQSTM1 can effectively sensitize PTX-resistant tumor is also not known (32, 35).

*In vivo*, we believe that the therapeutic efficacy observed can be attributed to not only the potential decrease of autophagic level in the tumor, but also other pathways. It is known that ultrasound in combination with microbubbles can increase the fenestration size of tumor's vascular wall, allowing deeper drug penetration. (36). It can also disrupt the tumor microenvironment and can affect many aspects of tumor biology such as hypoxia, vascular permeability, and interstitial fluid pressure (37). Nevertheless, further work needs to be performed to ascertain the true mechanisms behind the improved therapeutic efficacy in tumor tissue (38).

However, our studies have some limitations. First, cavitation is typically evaluated on a cell monolayer, allowing direct contact between the target cell line and microbubbles *in vitro*. Second, further experiments are needed to better understand the upstream regulation of autophagy and the related pathways in ovarian cancer. Moreover, whether the method presented here is effective in other refractory tumors is not known and require additional work.

## CONCLUSIONS

We have studied the efficacy and potential mechanism of UTMD+PTX treatment on refractory ovarian carcinoma. Our study indicated that LIFU+MB could enhance the localized anticancer effect of PTX *via* inhibiting autophagy. Hence, reversal of drug resistance is significantly improved by low-intensity focused ultrasound with microbubbles. In a more general sense, the combined LIFU+MB+chemotherapy drug treatment might offer an innovative way to effectively reduce the drug dosage so as to minimize the side effects of conventional chemotherapy.

## DATA AVAILABILITY STATEMENT

The raw data supporting the conclusions of this article will be made available by the authors, without undue reservation.

## ETHICS STATEMENT

The animal study was reviewed and approved by the medical experimental animal care commission of Zhejiang University.

## AUTHOR CONTRIBUTIONS

JZ and JQ designed research, revised the manuscript, and revised the final version of the manuscript. GF performed the experiments and drafted the article. LL, KY, XF, XS, and BW helped perform the research, contributed new reagents/analytic tools, and analyzed data. All authors contributed to the article and approved the submitted version.

## FUNDING

This work was supported by the National Natural Science Foundation of China (grant numbers: 81974470 to JZ, and 81601515 and 82171939 to JQ) and the Natural Science Foundation of Zhejiang Province of China (LY18H180001 to JZ and LY16H180003 to HL).

## ACKNOWLEDGMENTS

We thank Beibei Wang from the Center of Cryo-Electron Microscope (CCEM), Zhejiang University for her technical assistance on transmission electron microscopy.

## REFERENCES

1. Siegel RL, Miller KD, Jemal A. Cancer Statistics, 2019. *CA Cancer J Clin* (2019) 69(1):7–34. doi: 10.3322/caac.21551
2. Coleman RL, Monk BJ, Sood AK, Herzog TJ. Latest Research and Treatment of Advanced-Stage Epithelial Ovarian Cancer. *Nat Rev Clin Oncol* (2013) 10 (4):211–24. doi: 10.1038/nrclinonc.2013.5
3. Richardson DL, Sill MW, Coleman RL, Sood AK, Pearl ML, Kehoe SM, et al. Paclitaxel With and Without Pazopanib for Persistent or Recurrent Ovarian Cancer: A Randomized Clinical Trial. *JAMA Oncol* (2018) 4(2):196–202. doi: 10.1001/jamaoncol.2017.4218
4. Miller EM, Samec TM, Alexander-Bryant AA. Nanoparticle Delivery Systems to Combat Drug Resistance in Ovarian Cancer. *Nanomedicine* (2021) 31:102309. doi: 10.1016/j.nano.2020.102309
5. Daecher A, Stanczak M, Liu JB, Zhang J, Du S, Forsberg F, et al. Localized Microbubble Cavitation-Based Antivascular Therapy for Improving HCC Treatment Response to Radiotherapy. *Cancer Lett* (2017) 411:100–5. doi: 10.1016/j.canlet.2017.09.037
6. Hu Z, Lv G, Li Y, Li E, Li H, Zhou Q, et al. Enhancement of Anti-Tumor Effects of 5-Fluorouracil on Hepatocellular Carcinoma by Low-Intensity Ultrasound. *J Exp Clin Cancer Res* (2016) 35:71. doi: 10.1186/s13046-016-0349-4
7. Kopechek JA, Carson AR, McTiernan CF, Chen X, Hasjim B, Lavery L, et al. Ultrasound Targeted Microbubble Destruction-Mediated Delivery of a Transcription Factor Decoy Inhibits STAT3 Signaling and Tumor Growth. *Theranostics* (2015) 5(12):1378–87. doi: 10.7150/thno.12822
8. Joiner JB, Pylayeva-Gupta Y, Dayton PA. Focused Ultrasound for Immunomodulation of the Tumor Microenvironment. *J Immunol* (2020) 205(9):2327–41. doi: 10.4049/jimmunol.1901430
9. Eisenberg-Lerner A, Bialik S, Simon HU, Kimchi A. Life and Death Partners: Apoptosis, Autophagy and the Cross-Talk Between Them. *Cell Death Differ* (2009) 16(7):966–75. doi: 10.1038/cdd.2009.33
10. Huang Z, Zhou L, Chen Z, Nice EC, Huang C. Stress Management by Autophagy: Implications for Chemoresistance. *Int J Cancer* (2016) 139 (1):23–32. doi: 10.1002/ijc.29990
11. Peng X, Gong F, Chen Y, Jiang Y, Liu J, Yu M, et al. Autophagy Promotes Paclitaxel Resistance of Cervical Cancer Cells: Involvement of Warburg Effect Activated Hypoxia-Induced Factor 1-Alpha-Mediated Signaling. *Cell Death Dis* (2014) 5:e1367. doi: 10.1038/cddis.2014.297
12. DeVorkin L, Hattersley M, Kim P, Ries J, Spowart J, Anglesio MS, et al. Autophagy Inhibition Enhances Sunitinib Efficacy in Clear Cell Ovarian Carcinoma. *Mol Cancer Res* (2017) 15(3):250–8. doi: 10.1158/1541-7786.MCR-16-0132
13. Fan P, Yang D, Wu J, Yang Y, Guo X, Tu J, et al. Cell-Cycle-Dependences of Membrane Permeability and Viability Observed for HeLa Cells Undergoing Multi-Bubble-Cell Interactions. *Ultrasonics Sonochemistry* (2019) 53:178–86. doi: 10.1016/j.ultsonch.2019.01.005
14. Wang Y, Sun M, Cao Y, Zhu J. Application of Optical Interferometry in Focused Acoustic Field Measurement. *J Sound Vibration* (2018) 426:234–43. doi: 10.1016/j.jsv.2018.04.023
15. Cao Y, Chen Q, Zheng H, Lu L, Wang Y and Zhu J. Study on the Mechanism of Ultrasonic Power Measurement Sensor Based on Pyroelectric Effect. *Pleiades Publishing* (2018) 64(6):789–95. doi: 10.1134/S1063771018060015
16. Duan X, Yu ACH, Wan JMF. Cellular Bioeffect Investigations on Low-Intensity Pulsed Ultrasound and Sonoporation: Platform Design and Flow Cytometry Protocol. *IEEE Trans Ultrason Ferroelectr Freq Control* (2019) 66 (9):1422–34. doi: 10.1109/TUFFC.2019.2923443
17. ter Haar G, Shaw A, Pye S, Ward B, Bottomley F, Nolan R, et al. Guidance on Reporting Ultrasound Exposure Conditions for Bio-Effects Studies. *Ultrasound Med Biol* (2011) 37(2):177–83. doi: 10.1016/j.ultrasmedbio.2010.10.021
18. Electronic Medicines Compendium (emc). *SonoVue* (2021). Available at: https://www.medicines.org.uk/emc/product/1539 (Accessed Dec 15, 2021).
19. Matulonis UA, Sood AK, Fallowfield L, Howitt BE, Sehouli J, Karlan BY. Ovarian Cancer. *Nat Rev Dis Primers* (2016) 2:16061. doi: 10.1038/nrdp.2016.61
20. Pan X, Chen Y, Shen Y and Tantai J. Knockdown of TRIM65 Inhibits Autophagy and Cisplatin Resistance in A549/DDP Cells by Regulating miR-138-5p/ATG7. *Cell Death Dis* (2019) 10(6):429. doi: 10.1038/s41419-019-1660-8
21. Amaravadi RK, Kimmelman AC, Debnath J. Targeting Autophagy in Cancer: Recent Advances and Future Directions. *Cancer Discov* (2019) 9(9):1167–81. doi: 10.1158/2159-8290.CD-19-0292
22. Zhang SF, Wang XY, Fu ZQ, Peng QH, Zhang JY, Ye F, et al. TXNDC17 Promotes Paclitaxel Resistance *via* Inducing Autophagy in Ovarian Cancer. *Autophagy* (2015) 11(2):225–38. doi: 10.1080/15548627.2014.998931
23. Ferraresi A, Girone C, Esposito A, Vidoni C, Vallino L, Secomandi E, et al. How Autophagy Shapes the Tumor Microenvironment in Ovarian Cancer. *Front Oncol* (2020) 10:599915. doi: 10.3389/fonc.2020.599915
24. Gourevich D, Volovick A, Dogadkin O, Wang L, Mulvana H, Medan Y, et al. *In Vitro* Investigation of the Individual Contributions of Ultrasound-Induced Stable and Inertial Cavitation in Targeted Drug Delivery. *Ultrasound Med Biol* (2015) 41(7):1853–64. doi: 10.1016/j.ultrasmedbio.2015.03.016
25. Zou P, Li M, Wang Z, Zhang G, Jin L, Pang Y, et al. Micro-Particle Image Velocimetry Investigation of Flow Fields of SonoVue Microbubbles Mediated by Ultrasound and Their Relationship With Delivery. *Front Pharmacol* (2019) 10:1651. doi: 10.3389/fphar.2019.01651
26. Choi V, Rajora MA, Zheng G. Activating Drugs With Sound: Mechanisms Behind Sonodynamic Therapy and the Role of Nanomedicine. *Bioconjug Chem* (2020) 31(4):967–89. doi: 10.1021/acs.bioconjchem.0c00029
27. Kimmelman AC, White E. Autophagy and Tumor Metabolism. *Cell Metab* (2017) 25(5):1037–43. doi: 10.1016/j.cmet.2017.04.004
28. Jin SV, White E. Tumor Suppression by Autophagy Through the Management of Metabolic Stress. *Autophagy* (2008) 4(5):563–6. doi: 10.4161/auto.5830
29. Hausge R, Langer A, Murvold ET, Costea DE, Gjertsen BT, Gilja OH, et al. Low-Intensity Sonoporation-Induced Intracellular Signalling of Pancreatic Cancer Cells, Fibroblasts and Endothelial Cells. *Pharmaceutics* (2020) 12 (11):1058. doi: 10.3390/pharmaceutics12111058
30. Tang J, Zhu J, Ye Y, Liu Y, He Y, Zhang L, et al. Inhibition LC3B Can Increase Chemosensitivity of Ovarian Cancer Cells. *Cancer Cell Int* (2019) 19:199. doi: 10.1186/s12935-019-0921-z
31. Hurley JH, Young LN. Mechanisms of Autophagy Initiation. *Annu Rev Biochem* (2017) 86:225–44. doi: 10.1146/annurev-biochem-061516-044820
32. Yan XY, Zhang Y, Zhang JJ, Zhang LC, Liu YN, Wu Y, et al. P62/SQSTM1 as an Oncotarget Mediates Cisplatin Resistance Through Activating RIP1-NF-kappaB Pathway in Human Ovarian Cancer Cells. *Cancer Sci* (2017) 108 (7):1405–13. doi: 10.1111/cas.13276
33. Kuo CL, Jiang ZY, Wang YW, Lin TY, Huang WL, Wu FJ, et al. *In Vivo* Selection Reveals Autophagy Promotes Adaptation of Metastatic Ovarian

Cancer Cells to Abdominal Microenvironment. *Cancer Sci* (2019) 110 (10):3204–14. doi: 10.1111/cas.14162

34. Zhang W, Zhang S, Guan W, Huang Z, Kong J, Huang C, et al. Poly C Binding Protein 1 Regulates P62/SQSTM1 mRNA Stability and Autophagic Degradation to Repress Tumor Progression. *Front Genet* (2020) 11:930. doi: 10.3389/fgene.2020.00930
35. Wang J, Garbutt C, Ma H, Gao P, Hornicek FJ, Kan Q, et al. Expression and Role of Autophagy-Associated P62 (SQSTM1) in Multidrug Resistant Ovarian Cancer. *Gynecol Oncol* (2018) 150(1):143–50. doi: 10.1016/j.ygyno.2018.04.557
36. Zhao YZ, Lin Q, Wong HL, Shen XT, Yang W, Xu HL, et al. Glioma-Targeted Therapy Using Cilengitide Nanoparticles Combined With UTMD Enhanced Delivery. *J Control Release* (2016) 224:112–25. doi: 10.1016/j.jconrel.2016.01.015
37. Zhang Q, Jin H, Chen L, Chen Q, He Y, Yang Y, et al. Effect of Ultrasound Combined With Microbubble Therapy on Interstitial Fluid Pressure and VX2 Tumor Structure in Rabbit. *Front Pharmacol* (2019) 10:716. doi: 10.3389/fphar.2019.00716
38. Dimcevski G, Kotopoulis S, Bjanes T, Hoem D, Schjott J, Gjertsen BT, et al. A Human Clinical Trial Using Ultrasound and Microbubbles to Enhance Gemcitabine Treatment of Inoperable Pancreatic Cancer. *J Control Release* (2016) 243:172–81. doi: 10.1016/j.jconrel.2016.10.007

**Conflict of Interest:** The authors declare that the research was conducted in the absence of any commercial or financial relationships that could be construed as a potential conflict of interest.

frontiers | Frontiers in Oncology

ORIGINAL RESEARCH
published: 10 May 2022
doi: 10.3389/fonc.2022.897751

**Edited by:**
Xia Bai Rong,
The First Affiliated Hospital of University of Science and Technology of China Anhui Provincial Hospital, China

**Reviewed by:**
Lihuan Zhu,
Fujian Provincial Hospital, China
Ning Pu,
Fudan University, China

***Correspondence:**
Zhiyao Chen
chenzyaoo@sina.com
Zhijun Huang
huangzj@fjmu.edu.cn
Jianqing Lin
ljq13905977336@163.com

[†]These authors share first authorship

**Specialty section:**
This article was submitted to Gynecological Oncology, a section of the journal Frontiers in Oncology

**Received:** 16 March 2022
**Accepted:** 04 April 2022
**Published:** 10 May 2022

**Citation:**
Su X, Xue C, Xie C, Si X, Xu J, Huang W, Huang Z, Lin J and Chen Z (2022) lncRNA-LET Regulates Glycolysis and Glutamine Decomposition of Esophageal Squamous Cell Carcinoma Through miR-93-5p/miR-106b-5p/SOCS4. Front. Oncol. 12:897751. doi: 10.3389/fonc.2022.897751

# lncRNA-LET Regulates Glycolysis and Glutamine Decomposition of Esophageal Squamous Cell Carcinoma Through miR-93-5p/miR-106b-5p/SOCS4

*Xincheng Su[1†], Cong Xue[1†], Chengke Xie[1], Xianzhe Si[1], Jie Xu[1], Wenbo Huang[1], Zhijun Huang[1*], Jianqing Lin[2*] and Zhiyao Chen[1*]*

*[1] Department of Gastrointestinal and Esophageal Surgery, The 2nd Affiliated Hospital of Fujian Medical University, Quanzhou, China, [2] Department of Oncology, The 2nd Affiliated Hospital of Fujian Medical University, Quanzhou, China*

**Background:** Dysregulated non-coding RNAs exhibit critical functions in various cancers. Nonetheless, the levels and corresponding functions of circCSNX14 in esophageal squamous cell carcinoma (ESCC) yet remain to be elucidated.

**Methods:** Initially, the aberrant low levels of lncRNA-LET within ESCC tissues are validated *via* qRT-PCR observations. Moreover, the effects of lncRNA-LET upregulation on cell proliferation *in vitro* are determined. In addition, a series of assays determining the mechanistic views related to metabolism is conducted. Furthermore, the effects of lncRNA-LET in affecting tumor growth are investigated *in vivo* in a mouse model. Moreover, the interactions between lncRNA-LET and its networks are predicted and determined by RNA immunoprecipitation-assisted qRT-PCR as well as luciferase reporter assays.

**Results:** The downregulation of lncRNA-LET is correlated to the poor prognosis of ESCC patients. Moreover, the upregulated expression of lncRNA-LET could have reduced the cell viability. *In vivo* tumor inhibition efficacy assays showed that an increase of lncRNA-LET presented excellent inhibitory effects on cancer proliferation as reflected by tumor weight and volume in mice. Finally, the mechanistic views regarding the effects of miR-106b-5p or miR-93-5p and SOCS4 on ESCC are related to the feedback of lncRNA-LET.

**Conclusion:** Collectively, this study suggested that lncRNA-LET miR-93-5p or the miR-106b-5p–SOCS4 axis may provide great potential in establishing ESCC therapy.

**Keywords: esophageal squamous cell carcinoma, lncRNA-LET, miR-93-5p, miR-106b-5p, SOCS4**

# INTRODUCTION

Esophageal squamous cell carcinoma (ESCC), a primary esophageal cancer subtype, has remained as one of the significant healthcare challenges globally (1). Despite several advancements in treatment options and the development of various medical technologies, the treatment against ESCC remains highly challenging due to its location, which significantly hampers early prognosis and ease of surgical sectioning (2). Moreover, understanding the underlying mechanism is another highly challenging task in developing therapeutics against this malignant disease (3).

In addition to various attributes of increased glucose uptake and lactate production, the intrinsically available long non-coding ribose nucleic acids (lncRNAs) offer various essential functions in cancer prognosis (4, 5). Interestingly, several reports indicated the association of lncRNAs with cancer cell survival and proliferation through cell metabolic activities (6). In a case, lncRNA UCA1 enhanced tumorigenesis in bladder cancer through the upregulation of HK2, a key enzyme for metabolism (7). In another case, the downregulation of lncRNA DUXAP8 markedly inhibited the expression of HK2 and LDHA and thus decreased the glucose uptake in NSCLC cells (8).

Similarly, abnormal lncRNA levels have been identified in ESCC, which could assist in understanding the origin and proliferation of cancer cells towards early prognosis and the development of therapeutic options—for instance, it was reported that lncRNA POU3F3 could be beneficial for the early screening of ESCC (9). Moreover, lncRNA HCG22 could prevent the migration of cells in ESCC (8). In addition, lncRNA-uc002yug.2 could improve the RUNX1 combination with MALAT1, PEG10, and CASC9, showing an association with ESCC (10). These findings, based on lncRNA levels, would undoubtedly offer great potential in the early diagnosis or prognosis of ESCC. However, the critical and targeted functionalities of lncRNA-LET in ESCC cells still remain unclear. Furthermore, abnormally expressed miRNAs have been reported within various cancers (11), for instance, miR-185-5p serves as a tumor-promoting gene (11), and KLF3 plays critical biological impacts on cancer apoptosis (12).

In general, lncRNAs serve as the spongers of microRNAs (miRNAs) that are abnormally expressed in various tumors (13, 14), affecting other target genes *via* base pairing (15),—for instance, it was reported that the miR-548k in ESCC exerted oncogenic functions through downregulating the lncRNA-LET expression (16). On the contrary, upregulation of miR-93-5p and miR-106b-5p within esophageal carcinoma has been reported in the literature (17, 18). In another instance, the suppressors of cytokine signaling (SOCS-1 and SOCS-3) were revealed to be implicated in ESCC progression (19). Moreover, the association of lncRNA TUSC7, miR-616, and SOCS4 has been revealed in endometrial carcinoma (16, 20). Notably, miR-1290 was abnormal in lung adenocarcinoma, contributing to cancer progression through targeting SOCS4 (21). Inspired by these facts, herein we intend to detect the levels and functions of lncRNA-LET and its network in ESCC cancers. Moreover, the underlying regulated gene and protein expressions were also investigated to thoroughly understand the function of lncRNA-LET.

# EXPERIMENTAL SECTION

## Specimen Collection, Cell Culture, and Transfection

In total, 80 ESCC and matched non-carcinoma samples were altogether collected in cases from the 2nd Affiliated Hospital of Fujian Medical University (FMU). The patients who underwent chemotherapy or radiotherapy were excluded from our work to avoid affecting the gene expression. Each case had provided informed consent. Our study protocols gained approval from the medical ethics committee of the 2nd Affiliated Hospital of FMU.

The ESCC cells (KYSE0, TE-1, KYSE150, KYSE410, and Eca-109) were provided by the American Type Culture Collection (Manassas, VA, USA) and cultured within Dulbecco's modified Eagle's medium (Gibco, Grand Island, NB, USA) containing 8% or 10% fetal bovine serum (Gibco) and 1% penicillin-streptomycin (Gibco).

The complementary deoxyribose nucleic acid (cDNA) plasmids of lncRNA-LET were purchased from Genomeditech Co, Ltd. (Shanghai, China). Puromycin (2 μg/ml, Solarbio Co., Ltd., Beijing, China) was used to select stable transfection cell lines. The miR-106b-5p mimics, miR-93-5p, and corresponding controls were provided by GeneChem Co., Ltd. (Shanghai, China), which were transfected into cells with Lipofectamine 2000 (Invitrogen, NY, USA). The pcDNA-lncRNA-LET and controls were provided by GenePharma (Shanghai, China) and transfected using Lipofectamine 2000. Then, the pcDNA-(SOCS4) vectors were designed and synthesized by Biovector Science Inc. (Beijing, China):

lncRNA-LET WT: 5′-UACUUUGCCAAAUAGCACUUUA-3′
lncRNA-LET MUT: 5′-UACCCAGCUAGGCCCACGUAGA-3′
hsa-miR-93-5p: 5′-GAUGGACGUGCUUGUCGUGAAAC-3′
hsa-miR-106b-5p: 5′-UAGACGUGACAGUCGUGAAAU-3′
SOCS4 WT: 5′-AGAAGUAGACAAUUGCCACUUUU-3′
SOCS4 MUT: 5′-AGAAGUAGACAAUUGCAGCGACU-3′

## Cell Proliferation

The cell counting kit (CCK)-8 (Solarbio, Beijing, China) was adopted for examining cell proliferation. Briefly, non-treated or treated cells ($5 \times 10^3$/well) were inoculated into 96-well plates for incubation. Each well was added with CCK-8 solution (10 μl) for another 2 h of incubation. Finally, the plate was scanned using a multiple-microplate reader (Bio-rad, Shanghai, China) at 450 nm.

## RNA Extraction and qRT-PCR Assay

Initially, RNAstorm™ Kit (#CD501, Biotium, Fremont, USA) was adopted for extracting total RNA, which was later prepared into cDNA with miRNA Reverse Transcription Kit from Qiagen

(Hilden, Germany). Next, cDNA amplification was performed by 7500 Fast Real-Time System (Bio-Rad) after mixing with SYBR Green PCR Master Mix. The relative RNA expression was obtained with the standard $2^{-\Delta\Delta Ct}$ method, in which β-actin and U6 were applied as the endogenous references. The primer sequences are as follows:

- β-Actin
  F: 5′-AGCTCTGTAACCACAGGTTC-3′
  R: 5′-GGGCGGTTGTTGGTCACAGA-3′
- U6
  F: 5′-GCGCGCAACGGCGACTCA-3′
  R: 5′-GAGGTAGGCGCTCCAGACGA-3′
- hsa-miR-93-5p
  F: 5′-GCCGTTAAAGTCGTGTTC-3′
  R: 5′-CAGAGCAGGGATCGATCTA-3′
- hsa-miR-106b-5p
  F: 5′-TCCCGACAAACGAGCTTTGA-3′
  R: 5′-AGGCAATGATCAGCGAATTC-3′
- SOCS4
  F: 5′-GGGCACGGACAGCATGTTGC-3′
  R: 5′-CCGTGAGTTAATGCTGCCTGGG-3′

## Dual-Luciferase Reporter Assay

We obtained lncRNA-LET and miRNA targets from the sRNA target dataBase (https://www.hsls.pitt.edu/obrc/index.php?page=URL20110217163843). From the starBase analyses, the binding sites of miR-106b-5p and miR-93-5p within the non-coding region of the SOCS4 gene were observed. Primarily, the mutant (SOCS4 MUT) and wild type (WT) of SOCS4 were prepared *via* Genomeditech Co., Ltd. (Shanghai, China), which were later inserted in the respective vector. Then, miR-106b-5p and miR-93-5p or control mimics were transfected into cells and then treated with pRL-SV40 (Promega). Finally, an analytical assay exploring the luciferase activities was conducted with the luciferase reporter assay kit (Solarbio).

## RNA Immunoprecipitation–qRT-PCR

RNA Immunoprecipitation Kit (Sigma, St. Louis, USA) was adopted for RNA immunoprecipitation (RIP) assay. Initially, cell lysates were obtained using the abovementioned RNA extraction kit and subjected to centrifugation. The magnetic beads pre-treated with anti-IgG (ab1-470, Abcam, Cambridge, UK) or anti-AGO2 (ab2-81, Abcam) were incubated with the obtained supernatant. Subsequently, qRT-PCR was employed to determine the enrichment of lncRNA-LET, miR-93-5p, and miR-106b-5p.

## Western Blotting

Initially, RIP assay lysis buffer was used to obtain total protein from cellular lysates, and then the protein was quantified with the Bradford method. Subsequently, the total denatured protein was scattered with 10 or 12% SDS-PAGE and then transferred onto nitrocellulose membranes (Sigma). Then, 5% bovine serum albumin (BSA) was used to block the membranes and incubated using anti-SOCS4, anti-HK2, anti-LDHA, anti-amino acid transporter-2 (ASCT2), and anti-glutaminase 1 (GLS1) primary antibodies, respectively. β-Actin was applied as a loading control. Then, horseradish peroxidase (HRP)-labeled anti-rabbit IgG antibody (#7074, CST, USA) or HRP-labeled anti-mouse IgG antibody (#7076, CST, USA) was adopted for incubating the membranes. The blots were visualized by enhanced chemiluminescence substrates. All reagents, except antibodies, are obtained from Beyotime (Shanghai, China).

## Determination of Glucose Uptake, Lactate, ATP Production, Glutamine, and α-KG

Initially, controls or lncRNA-LET-overexpressed plasmids were utilized to transfect the ESCC cells for a 48-h period. Furthermore, the corresponding colorimetric assay kits (BioVision, CA, USA) were used to determine the glucose and lactate concentrations. The ATP levels in each group were detected by an ATP colorimetric/fluorometric assay kit (Sigma). The contents of glutamine and α-KG were detected with a glutamine/glutamate determination kit (Sigma). Finally, similar detections were conducted after the transfection with miRNA mimics.

## *In Vivo* Investigations

The *in vivo* investigations using mice were conducted strictly following the Institutional Animal Care and Use Committee guidelines from the 2nd Affiliated Hospital of FMU. The animals were raised under a 12-h light/dark cycle room in an SPF environment. To establish the tumor model, BALB/c nude mice (age, 6 weeks old) were given an injection of Eca-109 cells transfected with normal vector or lncRNA-LET pcDNA vector (200 μl of $1 \times 10^6$ cells/mouse) on the dorsal side of the animal. Furthermore, the tumor volume was calculated using the following equation: volume = $(\text{length} \times \text{width}^2)/2$, in which length indicates the longest dimension, while width represents the shortest dimension of the tumor. Finally, the mice were euthanized with $CO_2$ inhalation, and the excised tumors were weighed accurately.

## Immunohistochemistry Assay

Initially, the excised tumor tissues from nude mice were prepared as paraffin slides, followed by antigen retrieval. Furthermore, 5% BSA was adopted for blocking the tissue sections for a 1-h period, followed by incubation using antibodies against anti-Ki67, SOCS4, HK2, LDHA, ASCT2, and GLS1, respectively (Cell Signaling Technology, Danvers, MA, USA). Finally, the slides were observed using a microscope.

## Statistical Analysis

The experimental results are displayed as mean ± SD. The statistical analysis was performed, using GraphPad Prism 9.0, through one-way ANOVA or Student's *t*-test plus Tukey's *post-hoc* test at a defined statistical significance of $P < 0.05$ ($^*P < 0.05$, $^{**}P < 0.01$, and $^{***}P < 0.001$). Associations among lncRNA-LET and clinical features were analyzed through chi-square test. The correlation between lncRNA-LET miR-93-5p/miR-106b-5p and SOCS4 was examined by Pearson's correlation test.

# RESULTS

## lncRNA-LET Profiles in ESCC Tissues

Initially, cancerous and paracancerous ESCC tissues were analyzed by qRT-PCR to explore the clinical functionality of lncRNA-LET. It was observed that lncRNA-LET was expressed significantly lower ($P < 0.001$) in ESCC tissues compared to the paracancerous tissues (**Figure 1A**). Then, the relationship between lncRNA-LET and the prognosis of ESCC was established by the overall survival rate evaluation (**Figure 1B**). The overall survival time in patients with low levels of lncRNA-LET indicated poor prognosis, demonstrating the anti-cancer potential of lncRNA-LET. The lncRNA-LET decreased with an increase of clinical T stage in ESCC patients ($P < 0.001$) (**Figure 1C**), and lncRNA-LET in clinical LN-negative was expressed significantly higher than that in clinical LN-positive ($P < 0.001$) (**Figure 1D**). Owing to a wide variety of cells in the tumor microenvironment, several other cell lines were selected to more precisely characterize the expression levels of lncRNA-LET in cancer cells. As depicted in **Figure 1E**, lncRNA-LET was downregulated within the ESCC cell lines compared to the paracancerous samples, indicating the anti-cancer efficacy of lncRNA-LET. Furthermore, the overall survival time in patients with high levels of SOCS4 indicated good prognosis (**Figure 1F**).

Taking the median expression value of lncRNA-LET in the 80 cases of ESCC (**Figure 1A**) as a cutoff value, the patients were randomly distributed into two groups as low and high lncRNA-LET expression groups ($n$ = 40). Based on the relationship of lncRNA-LET with clinical features, the lncRNA-LET levels were firmly related to the tumor size and differentiation, TNM stage, and lymph node metastasis. However, it should be noted that the obtained results were independent of the age and gender of the patients (**Table 1**).

## Influence of lncRNA-LET on Proliferation, Glycolysis, and Glutamine Decomposition of ESCC Cells

Based on the results displayed in **Figure 1C**, two kinds of ESCC cells, *i.e.*, Eca-109 and KYSE410, were selected due to the extremely low expression of lncRNA-LET. As depicted in **Figure 2A**, lncRNA-LET plasmid pcDNA overexpression could significantly increase the expression of lncRNA-LET in Eca-109 and KYSE410 lines. The transfection would substantially inhibit the viabilities of Eca-109 and KYSE410 cells (**Figure 2B**). Owing to the engagement of lncRNAs in the metabolism of cancer cells *via* regulating transporters and enzymes (7), in this study, the glucose content, lactate generation, and ATP after the transfection of the lncRNA-LET plasmid were evaluated. It was observed that the overexpression of lncRNA-LET presented an apparent inhibition of glucose intake, ATP generation, and lactate generation within both cell lines (**Figures 2C–E**). Moreover, two crucial enzymes (HK2 and LDHA) for glycolysis were markedly decreased with the overexpression of lncRNA-LET (**Figure 2F**). Collectively, we confirm that the upregulation of lncRNA-LET had significantly repressed the glycolysis process intracellularly. Furthermore, the glutamine, α-glutamine, and glutamic acid levels in Eca-109 and KYSE410 cells were determined by an α-ketoglutarate (α-KG) detection kit. Glutamate, glutamine, and α-KG within cells transfected with the lncRNA-LET plasmid were significantly decreased (**Figures 2G–I**), suggesting the inhibition of

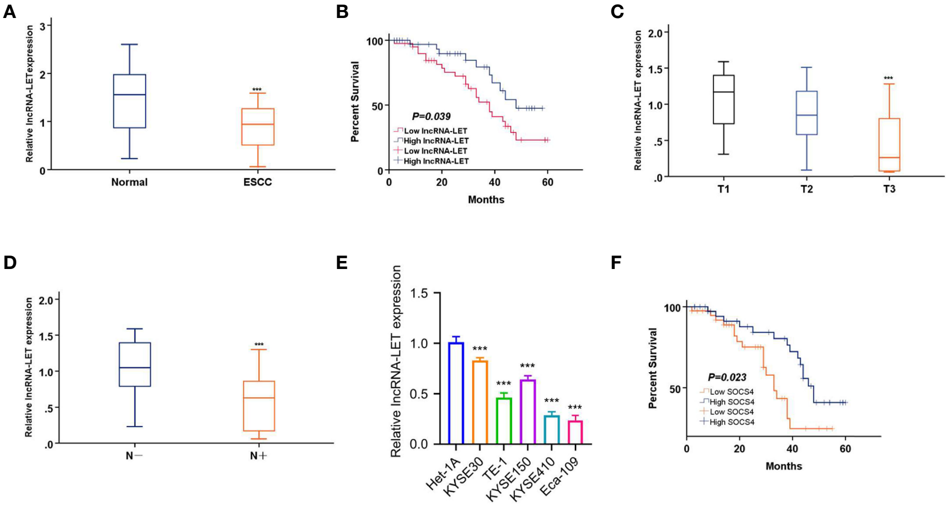

**FIGURE 1** | **(A)** lncRNA-LET expression within esophageal squamous cell carcinoma (ESCC) and matched non-carcinoma samples was measured by qRT-PCR. **(B)** The overall survival (OS) rate in cases showing lncRNA-LET downregulation ($n$ = 40) and lncRNA-LET upregulation ($n$ = 40) was analyzed by the Kaplan–Meier plot. **(C)** lncRNA-LET expression in different clinical T stages was measured by qRT-PCR. **(D)** lncRNA-LET expression within clinical LN-negative and LN-positive was measured by qRT-PCR. **(E)** lncRNA-LET expression in ESCC cell lines and the normal cell het-1a was measured by qRT-PCR. **(F)** The OS rate in cases showing SOCS4 downregulation ($n$ = 40) and SOCS4 upregulation ($n$ = 40) was analyzed by the Kaplan–Meier plot. ***$P < 0.001$.

**TABLE 1** | The relationship between lncRNA-LET and the clinical features of patients.

| Clinical characteristics | High lncRNA-LET (*n* = 40) | Low lncRNA-LET (*n* = 40) | *P*-value |
|---|---|---|---|
| Age | | | 0.3705 |
| ≥60 years | 21 | 17 | |
| <60 years | 19 | 23 | |
| Gender | | | 0.1432 |
| Female | 15 | 9 | |
| Male | 25 | 31 | |
| Tumor size | | | 0.0389 |
| ≤3 cm | 29 | 20 | |
| >3 cm | 11 | 20 | |
| Differentiation degree | | | 0.0452 |
| High/moderate | 33 | 25 | |
| Low | 7 | 15 | |
| Lymph node metastasis | | | 0.0322 |
| Positive | 35 | 27 | |
| Negative | 5 | 13 | |
| Clinical stage | | | 0.0125 |
| I–II | 22 | 11 | |
| III–IV | 18 | 29 | |

lncRNA-LET on metabolism. In addition, the expression levels of GLS1 and ASCT2 protein related to glutamine uptake and metabolism were decreased with the overexpression of lncRNA-LET in both cell lines (**Figure 2J**) (22, 23).

## lncRNA-LET Sponge miR-106b-5p and miR-93-5p

The starBase database was employed to analyze the miRNA binding site of lncRNA-LET (**Figure 3A**) to elucidate the aspects of targeted miRNA. It was observed that the lncRNA-LET wild type could bind to miR-106b-5p and miR-93-5p. Eca-109 and KYSE410 cells were subjected to miR-93-5p mimic treatment or non-treatment to confirm the prediction accuracy. To explore these aspects, miRNA expression was determined through qRT-PCR. From **Figure 3B**, miR-93-5p mimic transfection could remarkably increase the expression of miR-93-5p ($P < 0.001$) in both selected cell lines. Similarly, miR-106b-5p mimic transfection markedly increased miR-106b-5p expression compared to miR-nc in both selected cell lines ($P < 0.001$, **Figure 3C**). Then, the luciferase reporter gene experiment was performed in Eca-109 and KYSE410 cells. In comparison to miR-nc, the overexpressed miR-93-5p or miR-106b-5p could have significantly decreased the wild-type lncRNA-LET vector luciferase activity in Eca-109 and KYSE410 cells. Contrarily, the inhibition was retracted with the mutation of the predicted binding sites of miR-106b-5p or miR-93-5p (**Figure 3D**). Subsequently, we carried out the RNA pull-down assay by the biotin-labeled lncRNA-LET probe. As depicted in **Figure 3E**, it was confirmed that lncRNA-LET cells directly sponge mir-106b-5p or miR-93-5p. Furthermore, the RIP–qRT-PCR assay observations presented that the Ago2 group enriched more lncRNA-LET and miR-106b-5p/miR-93-5p, suggesting an interaction of lncRNA-LET with miR-106b-5p/mir-93-5p (**Figure 3F**). To verify the oriented association of lncRNA-LET with miR-93-5p/miR-106b-5p, the miR-106b-5p and miR-93-5p levels in Eca-109 and KYSE410 cells after lncRNA-LET overexpression derived from the use of pcDNA were detected. Compared with a vector, the overexpression of lncRNA-LET substantially downregulated the miR-106b-5p and miR-93-5p expression (**Figure 3G**). Then, the miR-93-5p (**Figure 3H**) and miR-106b-5p (**Figure 3I**) expressions within 80 ESCC subjects and matched non-carcinoma samples were detected, in which their expression in ESCC was remarkably elevated within cancer tissues. Moreover, a correlation between the relative expressions of miR-93-5p and miR-106b-5p in the patient samples was established (**Figure 3J**). In addition, negative correlations between lncRNA-LET and miR-93-5p (**Figure 3K**) or (**Figure 3L**) expression were demonstrated by Pearson correlation coefficient analysis. Furthermore, the miR-93-5p (**Figure 3M**) and miR-106b-5p (**Figure 3N**) expressions were increased within the ESCC cell lines (KYSE150, KYSE410, Kyse 0, TE-1, and Eca-109).

## lncRNA-LET Targets miR-93-5p/miR-106b-5p to Regulate Glycolysis and Glutamine Decomposition in ESCC Cells

To explore the effects of miR-93-5p or miR-106b-5p on lncRNA-LET-induced metabolism inhibition and tumor inhibition effects on ESCC cells, the cell viability of Eca-109 and KYSE410 cells was determined after treating with a vector, lncRNA-LET, and co-transfection (lncRNA-LET+miR-93-5p and lncRNA-LET+miR-106b-5p) (**Figure 4A**). Notably, it was observed that the cell proliferation ability in the selected cell lines was significantly reduced in the overexpression of the lncRNA-LET treatment group. In contrast, cell viability was increased after co-incubation of miR-106b-5p or miR-93-5p. In addition, the overexpression of lncRNA-LET inhibited the glucose contents, lactate generation, and ATP production intracellularly (**Figures 4B–D**). In contrast, the co-transfection of miR-106b-5p or miR-93-5p with lncRNA-LET partially increased the glucose contents, lactate generation, and ATP production, suggesting the tumor promotion roles of miR-106b-5p or miR-93-5p, along with their negative correlation with lncRNA-LET. The HK2 and ldhA protein levels in different groups of Eca-109 and KYSE410 cells revealed that the overexpression of lncRNA-LET had decreased the levels of HK2 and ldhA proteins in cells. Simultaneously, miR-106b-5p or miR-93-5p co-transfection partially recovered the HK2

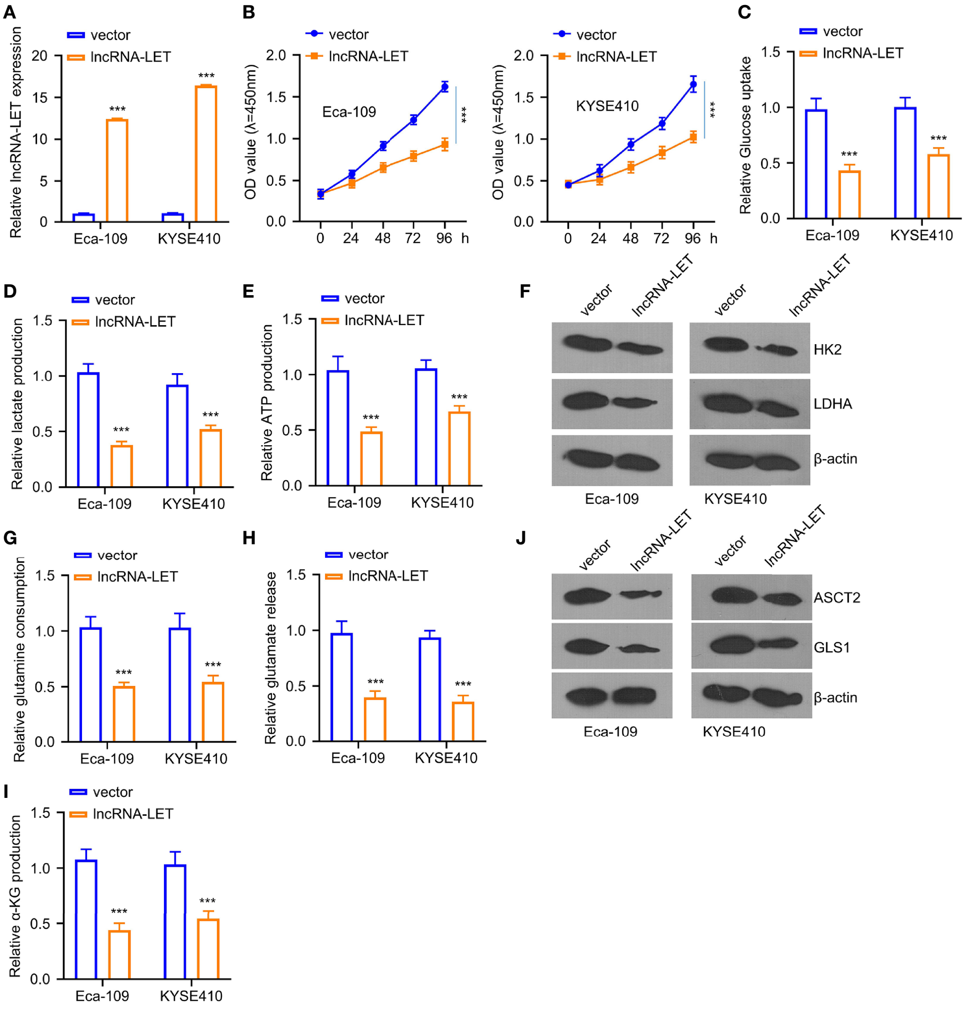

**FIGURE 2** | **(A)** The transfection efficiency of plasmid pcDNA lncRNA-LET was determined through qRT-PCR. **(B)** Cell viabilities in Eca-109 and KYSE410 cells transfected with or without lncRNA-LET pcDNA at 0, 24, 48, 72, and 96 h were measured through CCK-8 assay. **(C–E)** The levels of glucose, lactate, and ATP production were detected by the glycolysis kit. Western blotting was used to detect **(F)** the expressions of HK2 and ldhA proteins in Eca-109 and KYSE410 cells with or without lncRNA-LET transfection. **(J)** ASCT2 and gls1 protein levels in different groups (vector, lncRNA-LET). **(G–I)** The levels of glutamine, glutamic acid, and α-glutamine in cells after control vector or lncRNA-LET pcDNA transfection were detected by α-KG detection kit. ***$P < 0.001$.

and ldhA protein levels in ESCC cells (**Figure 4E**). As depicted in **Figures 4F–H**, the overexpressed lncRNA-LET inhibited glutamine, glutamate, and α-KG levels, while the co-incubation of miR-106b-5p or miR-93-5p partially abrogated the inhibition effect of lncRNA-LET. In contrast, the levels of ASCT2 and gls1 proteins in different groups of Eca-109 and KYSE410 cells showed different trends (**Figure 4I**). With the single transfection of lncRNA, the levels of ASCT2 and gls1 protein in cells were decreased, while the miR-106b-5p or miR-93-5p co-transfection partially increased the ASCT2 and gls1 protein levels in cells.

## Both miRNAs Target SOCS4

To investigate the downregulated miR-93-5p/miR-106b-5p expression, we analyzed their binding sites by starBase online database. It was observed from the experimental results that miR-106b-5p and miR-93-5p were associated with SOCS4. Furthermore, miR-106b-5p or miR-93-5p overexpression could inhibit SOCS4 in Eca-109 and KYSE410 cells (**Figure 5A**). However, no inhibition was observed in the SOCS4 mutant group. As shown in Western blotting, the expression of SOCS4 protein in Eca-109 and KYSE410 cells was decreased in the cases of pre-treatment by miR-106b-5p or miR-93-5p mimics (**Figures 5B, C**). Unlike the negative regulation of miR-106b-5p or miR-93-5p to SOCS4, lncRNA-LET overexpression increased the expression levels of SOCS4 protein, while less SOCS4 protein was detected in the co-transfection group (**Figures 5D, E**).

## The Effects of SOCS4 on the Inhibition of Glycolysis and Glutamine Decomposition

Furthermore, the levels of SOCS4 in clinical samples were measured *via* qRT-PCR and immunohistochemistry to define

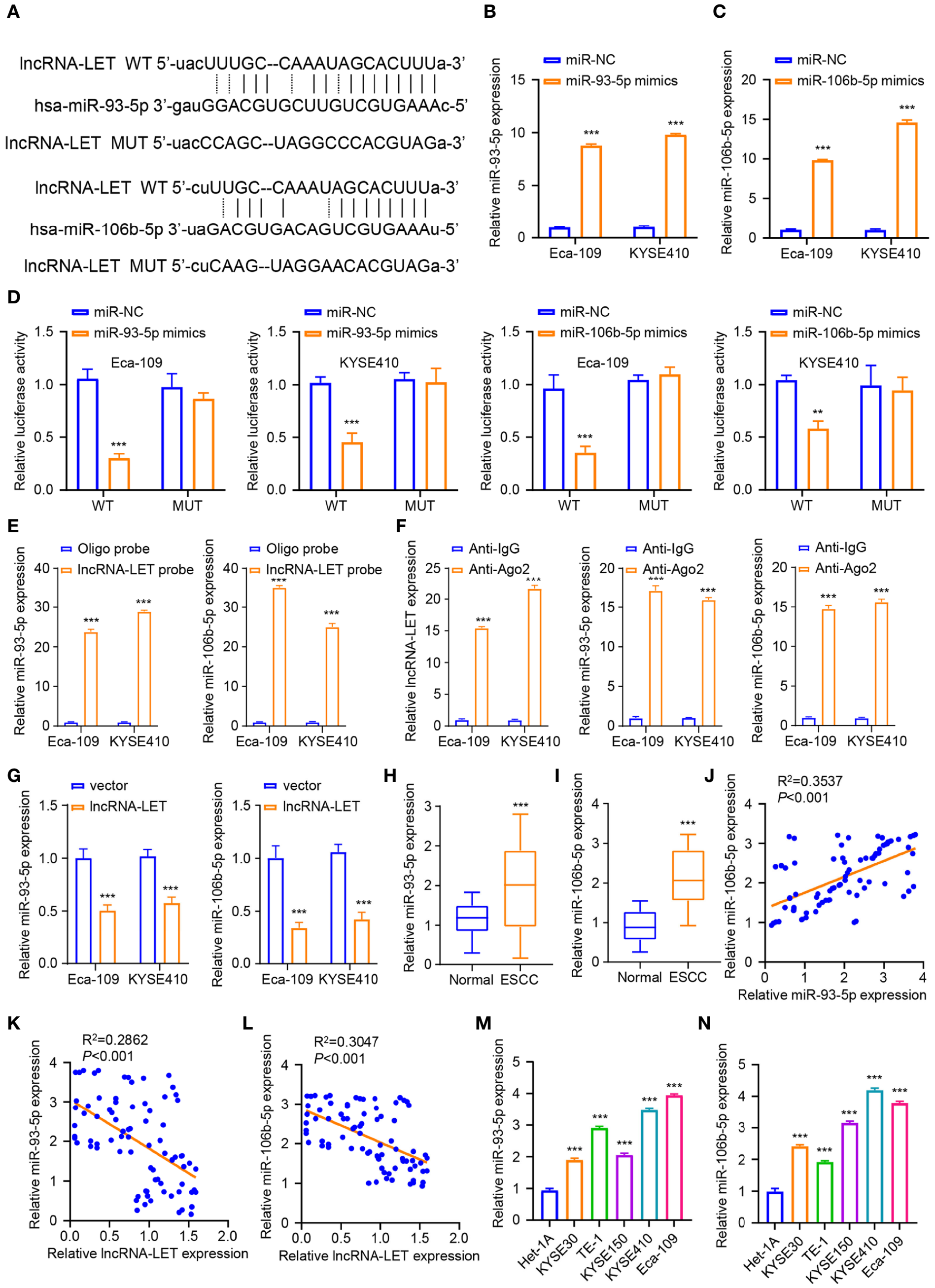

**FIGURE 3** | **(A)** The binding sites for miR-106b-5p and miR-93-5p predicted on lncRNA-LET were checked by starBase database. We conducted qRT-PCR to measure the **(B)** miR-93-5p levels after miR-nc mimic or miR-93-5p mimic transfection. **(C)** The miR-106b-5p level with miR-93-5p mimic or miR-nc mimic transfection. **(D)** Wild-type lncRNA-LET plasmid or binding site mutant plasmid luciferase activity affected by miR-106b-5p or miR-93-5p mimic transfection was detected by dual-luciferase activities. **(E)** The interaction of lncRNA-LET and with miR-93-5p/miR-106b-5p was verified through RNA pull-down assay. **(F)** The enrichment of lncRNA-LET, miR-93-5p, and miR-106b-5p was performed through RNA immunoprecipitation–qRT-PCR. **(G)** The miR-93-5p and miR-106b-5p levels within Eca-109 and KYSE410 cells after lncRNA-LET transfection were measured through qRT-PCR. We conducted qRT-PCR for detecting **(H, I)** miR-106b-5p and miR-93-5p expression within clinical tissue samples. **(L)** The miR-93-5p level and **(M)** miR-106b-5p level within esophageal squamous cell carcinoma (ESCC) cell and healthy esophageal epithelial cell line het-1a. **(J)** The correlation between the relative expressions of miR-106b-5p and miR-93-5p in the patient samples. **(K, L)** The association of lncRNA-LET with miR-93-5p/miR-106b-5p expressions. **(M, N)** The expressions of miR-93-5p and miR-106b-5p within ESCC cells (KYSE150, KYSE410, Kyse 0, TE-1, and Eca-109). *$P < 0.05$, **$P < 0.01$, and ***$P < 0.001$.

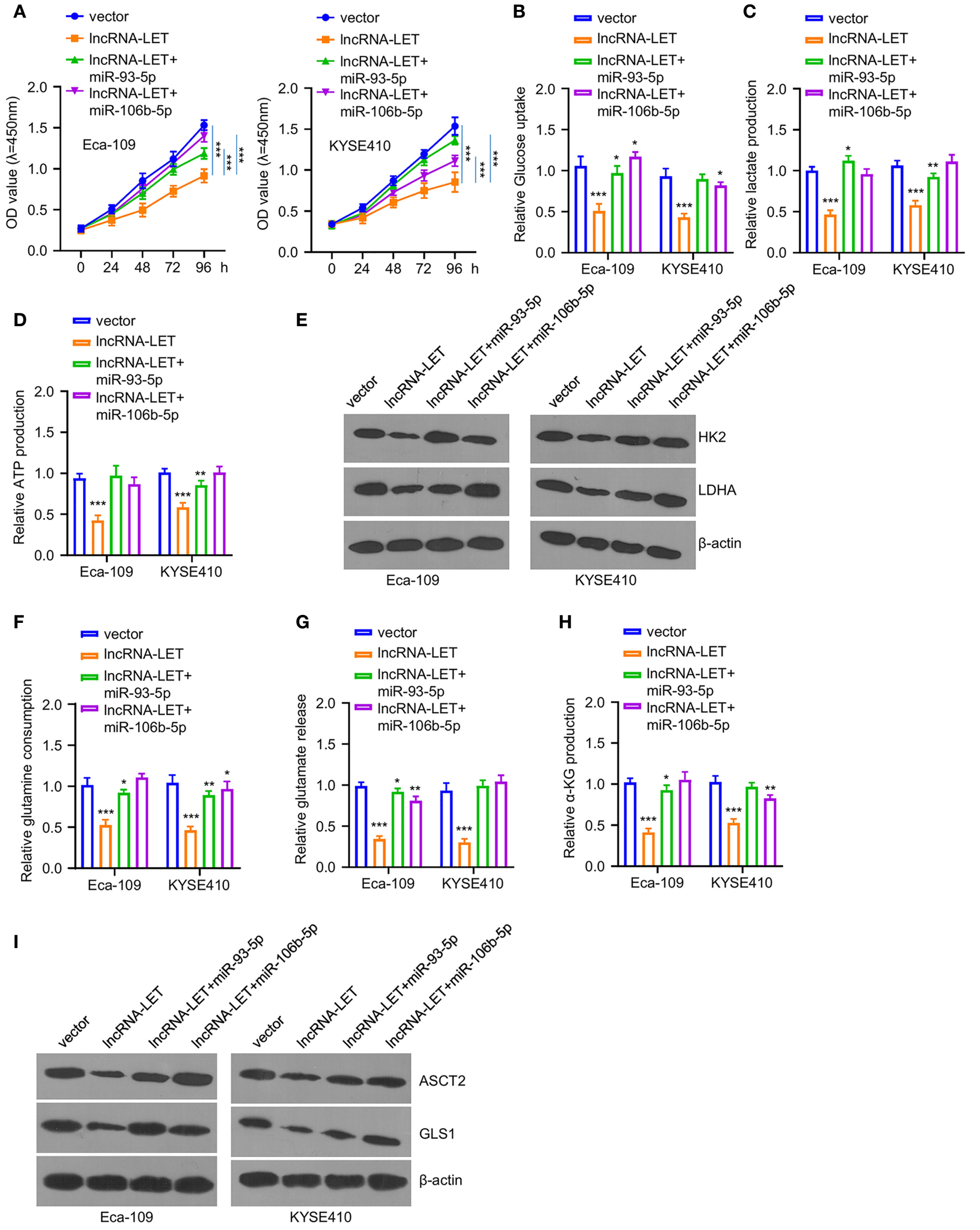

**FIGURE 4 |** **(A)** Cell viability in cells after lncRNA-LET transfection or lncRNA-LET and miR-93-5p or miR-106b-5p transfection was measured with CCK-8 kit. **(B–D)** Glucose consumption, lactate production, and ATP generation within cells after lncRNA-LET transfection or lncRNA-LET and miR-93-5p or miR-106b-5p transfection were defined by a glycolysis kit. We performed Western blotting for detecting **(E)** hK2 and ldhA protein expression within cells after lncRNA-LET transfection or lncRNA-LET and miR-106b-5p or miR-93-5p transfection and **(I)** ASCT2 and gls1 protein levels within cells after lncRNA-LET transfection or lncRNA-LET and miR-106b-5p or miR-93-5p co-transfection. **(F–H)** The glutamine, glutamate, and α-KG levels within cells after lncRNA-LET transfection or lncRNA-LET and miR-106b-5p or miR-93-5p co-transfection were measured through α-KG detection kit. *$P < 0.05$, **$P < 0.01$, and ***$P < 0.001$.

the roles of SOCS4 in glycolysis and glutamine decomposition. As displayed in **Figures 6A, B**, the SOCS4 levels were dramatically reduced within ESCC tissues compared to the adjacent non-carcinoma samples. Furthermore, the SOCS4 protein expression levels were significantly lower within various ESCC cell lines of KYSE 0, TE-1, KYSE150, KYSE410, and Eca-109 than those of healthy human immortal esophageal epithelial cells (het-1a) (**Figure 6C**). Accordingly, Eca-109 and KYSE410 cell lines with the lowest SOCS4 expression levels were used to determine the roles of SOCS4. Compared with a vector, SOCS4 plasmid transfection can effectively overexpress the SOCS4 protein level in both cell lines (**Figure 6D**). Unlike the

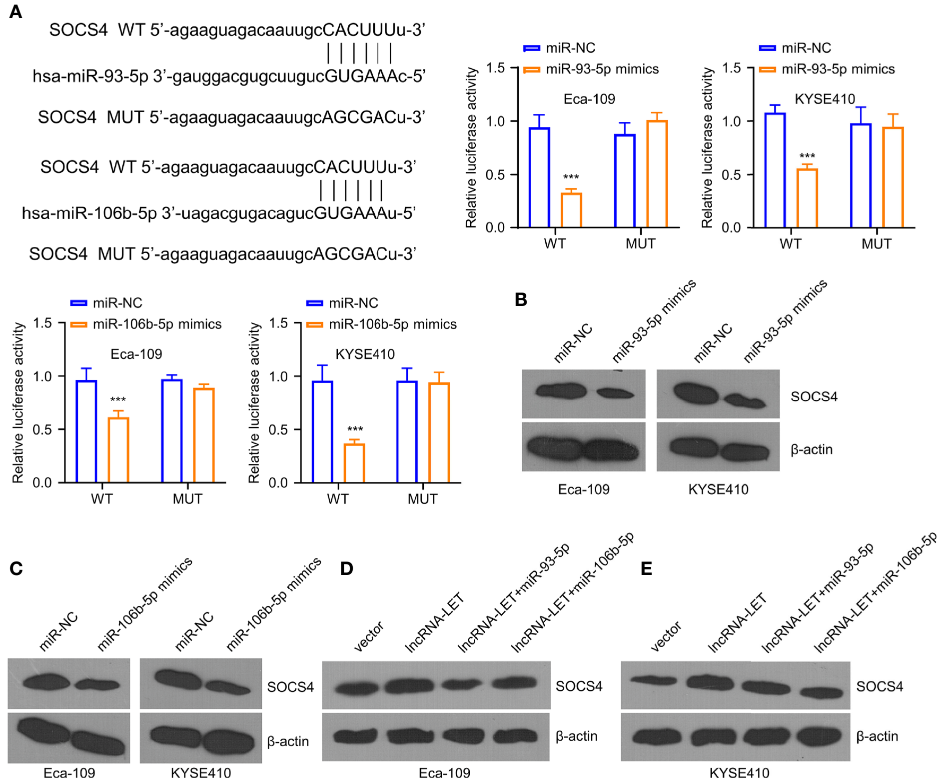

**FIGURE 5** | miR-93-5p/miR-106b-5p regulate the levels of SOCS4. **(A)** The predicted binding sites for SOCS4 gene on miR-93-5p and miR-106b-5p were analyzed by the starBase database. Western blotting was used to determine **(B, C)** SOCS4 protein in cells subjected to miR-93-5p or miR-106b-5p transfection and **(D, E)** in cells transfected with vector, lncRNA-LET, or lncRNA-LET+miR-106b-5p or miR-93-5p, respectively. **P* < 0.05, ***P* < 0.01, and ****P* < 0.001.

tumor-promoting roles of miR-106b-5p or miR-93-5p, SOCS4 overexpression dramatically inhibited cell proliferation (**Figure 6E**). Moreover, the regulatory role of SOCS4 in cell metabolism was similar to that of lncRNA-LET (**Figures 6F–H**). In addition, the overexpression of SOCS4 inhibited glucose uptake and lactate generation, together with ATP generation, while SOCS4 upregulation decreased the levels of HK2 and ldhA protein in the selected cells (**Figure 6I**). The obligatory increase of SOCS4 levels inhibited the glutamine, glutamate, and α-KG levels (**Figures 6J–L**) as well as resulted in the reduction of the expression levels of ASCT2 and gls1 proteins in various ESCC cells (**Figure 6M**).

## lncRNA-LET Upregulation Inhibited ESCC Cell Proliferation *In Vivo*

Finally, the Eca-109 tumor mice model was established for evaluating the influence of lncRNA-LET levels *in vivo*. Eca-109 cells transfected with or without lncRNA-LET were given into the dorsal side of nude mice *via* subcutaneous injection. As observed, the mice in the lncRNA-LET transfected group had a remarkably decreased tumor volume than those in the vector treatment group (**Figure 7A**). Correspondingly, the subcutaneous tumor weight in the lncRNA-LET-overexpression treatment group was lighter than those in the normal vector group (**Figure 7B**). The tumor tissues in the lncRNA-LET-overexpressed treatment group showed a lesser Ki-67 (proliferative marker) positive rate than the control vector group (**Figure 7C**). Notably, all cell metabolic markers (HK2, ldhA, ASCT2, and gls1) were downregulated in the lncRNA-LET treatment group. Contrarily, the positive trend of SOCS4 was observed in the lncRNA-LET tumor model, which was consistent with the positive correlation between lncRNA-LET and SOCS4. Finally, the miR-106b-5p and miR-93-5p within subcutaneous tumors of different groups were determined, indicating that their expression decreased in the lncRNA-LET group (**Figure 7D**).

## DISCUSSION

ESCC is one of the life-threatening malignant tumors affecting numerous patients globally, requiring the exploration of the underlying mechanisms and subsequent development of treatment options. In this vein, the lncRNAs could regulate cancer progression through interacting with biological factors (24–26). Initially, we observed that lncRNA-LET was expressed lower in the ESCC cancer tissues compared to the paracancerous tissues. With the lncRNA-LET pcDNA transfection, the lncRNA-LET level was dramatically elevated, giving rise to the

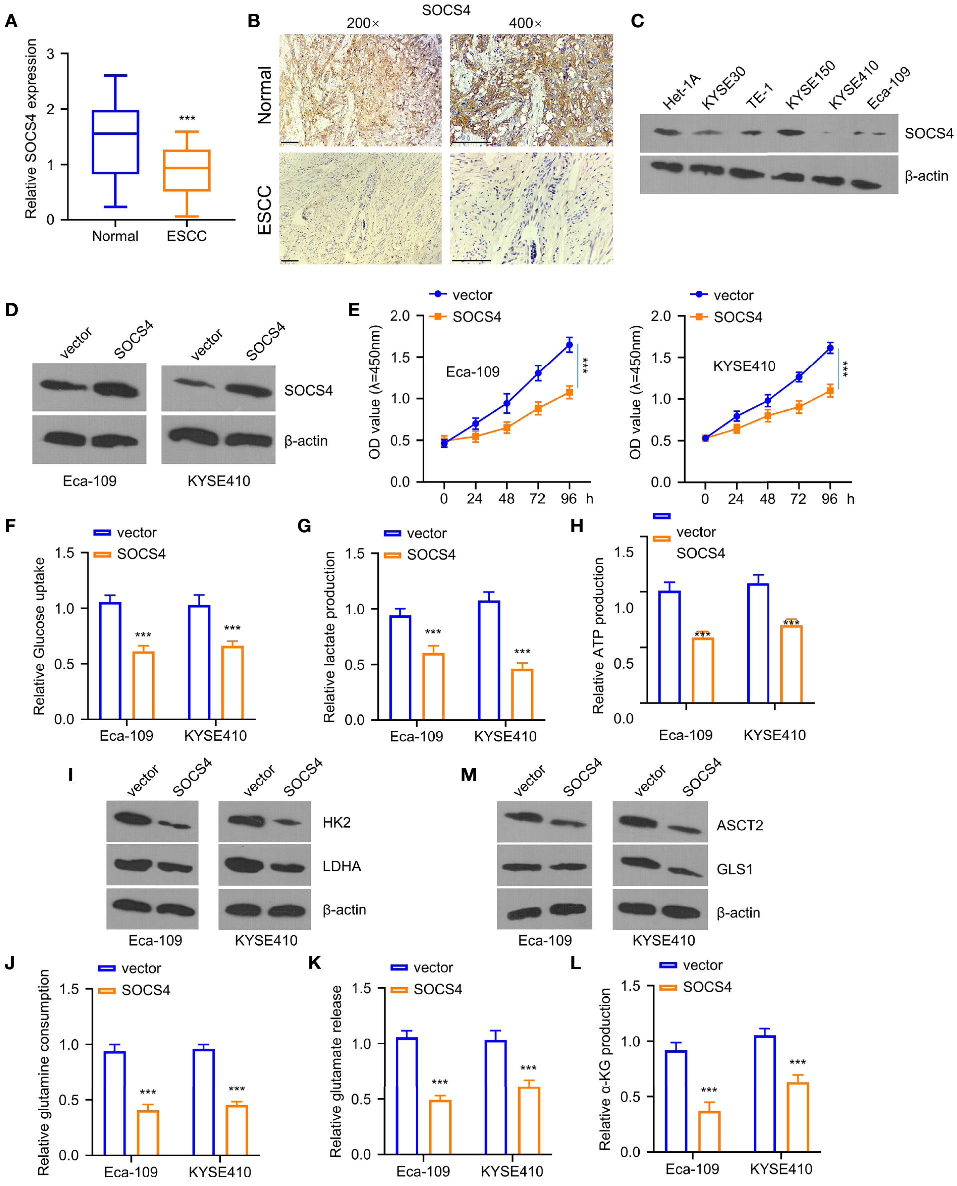

**FIGURE 6** | Overexpression of SOCS4 inhibited glycolysis and glutamine decomposition of esophageal squamous cell carcinoma (ESCC) cells. Western blotting (WB) **(A)** and immunohistochemistry **(B)** were used for determining SOCS4 expression within 80 ESCC and matched non-carcinoma samples. **(C)** SOCS4 protein levels within ESCC cells and healthy cells (het-1a) and **(D)** the overexpression of SOCS4 efficiency were detected by the WB method. **(E)** The cell viability of Eca-109 and KYSE410 cells at 0, 24, 48, 72, and 96 h was detected by the CCK-8 kit. **(F–H)** The glucose consumption, lactate production, and ATP in different groups (vector, SOCS4) of Eca109 and KYSE410 cells were defined by the glycolysis kit. **(I)** The levels of hK2 and ldhA protein in different groups (vector, SOCS4) of Eca-109 and KYSE410 cells and **(M)** gls1 and ASCT2 protein levels within cells with or without SOCS4 transfection. **(J–L)** Glutamate, glutamine, and α-KG expression in cells transfected with/without SOCS4 transfection was detected by α-KG detection kit. *$P < 0.05$, **$P < 0.01$, and ***$P < 0.001$.

markedly reduced cell viability, which suggested the tumor inhibition function of lncRNA-LET. Moreover, it should be noted that the lncRNAs were involved in various metabolic processes (27). Thus, the levels of various metabolic substances reflected that overall glycolytic flux and mitochondrial oxidative respiration were obtained. As shown in **Figure 2**, data on the levels of glucose, lactate, and ATP indicated augmented lncRNA-LET levels, reducing intracellular glycolysis. Furthermore, the expressions of HK2 and LDHA in ESCC cells with the transfection of lncRNA-LET were measured *via* the Western blotting method. The HK2 and LDHA levels dramatically decreased due to lncRNA-LET overexpression. We further explore the roles of lncRNA-LET on metabolic transporters (ASCT2) responsible for glutamine transportation and enzymes (GLS1) involved in the TCA cycle *via* converting glutamate into α-KG (23, 28). We altogether firmly believe

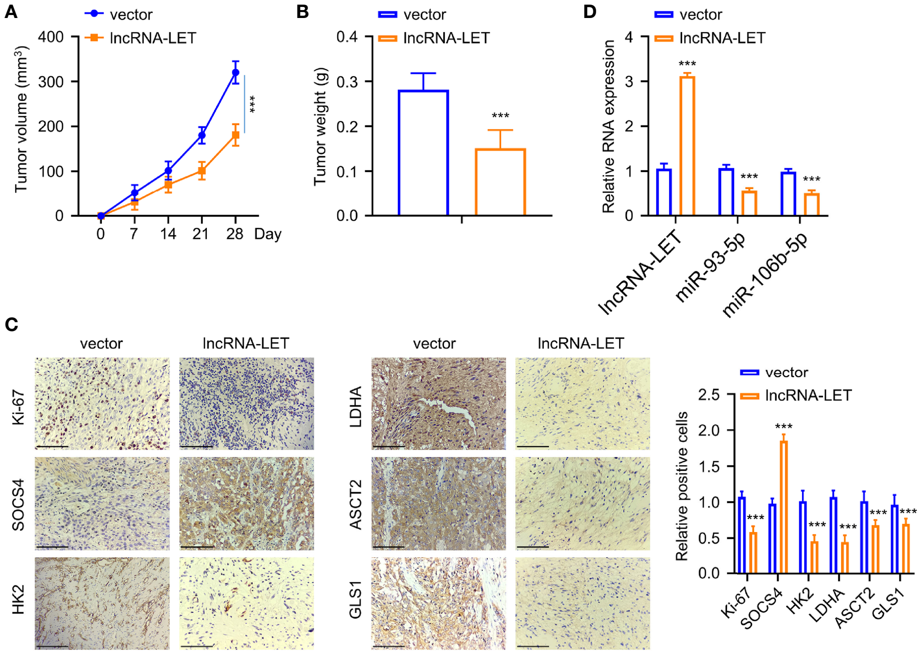

**FIGURE 7** | An increase of lncRNA-LET inhibited esophageal squamous cell carcinoma cell proliferation *in vivo*. **(A)** The subcutaneous tumor volume in the tumor xenograft model. **(B)** The tumor weights in different groups. **(C)** The expression of Ki-67, SOCS4, hK2, ldhA, ASCT2, and gls1 proteins in subcutaneous tumor tissues was detected by immunohistochemistry. **(D)** lncRNA-LET, miR-106b-5p, and miR-93-5p expression within subcutaneous tumor tissues were detected through qRT-PCR. $^{*}P < 0.05$, $^{**}P < 0.01$, and $^{***}P < 0.001$.

that lncRNA-LET played a critical role in cell glycolysis and the TCA cycle.

To this end, miRNAs play important roles in various cancers, exhibiting tumor-promoting or tumor-inhibiting effects (29–32). In this context, the expressions of miR-106b-5p and miR-93-5p were abnormal within ESCC tissues. The cell viability assay revealed that miR-106b-5p and miR-93-5p showed tumor promotion efficiency. In addition, the overexpression of these two miRNAs significantly affected the glucose uptake, ATP generation, and lactate generation, indicating their roles in regulating the metabolism in Eca-109 and KYSE410 cells. In addition, a reduction in HK2 and ldhA protein expressions in cells transfected with a single lncRNA-LET plasmid was observed. However, increased HK2 and ldhA expressions were observed in the co-transfection treatment group.

In humans, the SOCS family affects the release of cytokines and the downregulation of SOCS activity, resulting in excessive cytokine generation and promoting cancer development (24). Despite their importance, only a few reports concerning SOCS4 have been published to date (33). Subsequently, herein, we observed that miR-106b-5p and miR-93-5p harbored the binding sites of SOCS4. The tumor inhibitory roles of SOCS4 similar to lncRNA-LET were also demonstrated with functional and metabolic assays. Moreover, miR-106b-5p and miR-93-5p affected the SOCS4 levels, inducing a decrease of SOCS4 and reversing the functions of miR-106b-5p and miR-93-5p in cancer progression.

As lncRNA-LET was downregulated within ESCC cells and tissues, we increased the lncRNA-LET levels, in which inhibition of the proliferation, glycolysis, and glutamine decomposition of ESCC cells was observed. Subsequently, it was revealed that lncRNA-LET targeted miR-106b-5p and miR-93-5p, affecting glycolysis and the glutamine decomposition of ESCC cells. As the SOCS4 proteins are downstream targets of both miRNAs, the overexpression of SOCS4 correspondingly inhibited the glycolysis and glutamine decomposition of ESCC cells. In addition, lncRNA-LET overexpression inhibited ESCC cell proliferation *in vivo*. The interactions of lncRNA-LET, miR-106b-5p, miR-93-5p, and SOCS4 were altogether investigated, and hopefully, this axis could be a promising target for ESCC.

## CONCLUSION

In summary, our findings revealed the role of lncRNA-LET in repressing tumor cell survival *in vitro* and *in vivo*. In addition, lncRNA-LET could affect miR-106b-5p and miR-93-5p, while SOCS4 affected cell metabolism, thus inhibiting tumor progression. Our results altogether indicated that lncRNA-LET, miR-106b-5p, or the miR-93-5p–SOCS4 axis might contribute to ESCC treatment.

## DATA AVAILABILITY STATEMENT

The raw data supporting the conclusions of this article will be made available by the authors without undue reservation.

## ETHICS STATEMENT

The studies involving human participants were reviewed and approved by the medical ethics committee of the 2nd Affiliated Hospital of FMU. The patients/participants provided their written informed consent to participate in this study. The animal study was reviewed and approved by the medical ethics committee of the 2nd Affiliated Hospital of FMU.

## AUTHOR CONTRIBUTIONS

ZC, ZH, and JL contributed to the conception of the study. XSu and CXu performed the data analyses and wrote the manuscript. CXi and XSi performed the research and collected data. JX and WH helped performed the analysis with constructive discussions. All authors contributed to the article and approved the submitted version.

## FUNDING

This study was supported by the Natural Science Foundation of Fujian Province (2019J01476 and 2021J01273), the Medical Innovation Foundation of Fujian (2019-CXB-19), and Quanzhou High-Level Talent Plan (2020C003R).

## SUPPLEMENTARY MATERIAL

The Supplementary Material for this article can be found online at: https://www.frontiersin.org/articles/10.3389/fonc.2022.897751/full#supplementary-material

## REFERENCES

1. Kamangar F, Dores GM, Anderson WF. Patterns of Cancer Incidence, Mortality, and Prevalence Across Five Continents: Defining Priorities to Reduce Cancer Disparities in Different Geographic Regions of the World. *J Clin Oncol* (2006) 24(14):2137–50. doi: 10.1200/JCO.2005.05.2308
2. Zhihua Z, Weiwei W, Lihua N, Jianying Z, Jiang G. P53-Induced Long non-Coding RNA PGM5-AS1 Inhibits the Progression of Esophageal Squamous Cell Carcinoma Through Regulating miR-466/PTEN Axis. *IUBMB Life* (2019) 71(10):1492–502. doi: 10.1002/iub.2069
3. Song Y, Li L, Ou Y, Gao Z, Li E, Li X, et al. Identification of Genomic Alterations in Oesophageal Squamous Cell Cancer. *Nature* (2014) 509 (7498):91–5. doi: 10.1038/nature13176
4. Michelini F, Pitchiaya S, Vitelli V, Sharma S, Gioia U, Pessina F, et al. Damage-Induced lncRNAs Control the DNA Damage Response Through Interaction With DDRNAs at Individual Double-Strand Breaks. *Nat Cell Biol* (2017) 19(12):1400–11. doi: 10.1038/ncb3643
5. Wang Z, Yang B, Zhang M, Guo W, Wu Z, Wang Y, et al. lncRNA Epigenetic Landscape Analysis Identifies EPIC1 as an Oncogenic lncRNA That Interacts With MYC and Promotes Cell-Cycle Progression in Cancer. *Cancer Cell* (2018) 33(4):706–20.e9. doi: 10.1016/j.ccell.2018.03.006
6. Mondal T, Juvvuna PK, Kirkeby A, Mitra S, Kosalai ST, Traxler L, et al. Sense-Antisense lncRNA Pair Encoded by Locus 6p22. 3 Determines Neuroblastoma Susceptibility via the USP36-CHD7-SOX9 Regulatory Axis. *Cancer Cell* (2018) 33(3):417–434.e7. doi: 10.1016/j.ccell.2018.01.020
7. Fan C, Tang Y, Wang J, Xiong F, Guo C, Wang Y, et al. Role of Long non-Coding RNAs in Glucose Metabolism in Cancer. *Mol Cancer* (2017) 16 (1):130. doi: 10.1186/s12943-017-0699-3
8. Yin D, Hua L, Wang J, Liu Y, Li X. Long non-Coding RNA DUXAP8 Facilitates Cell Viability, Migration, and Glycolysis in non-Small-Cell Lung Cancer via Regulating HK2 and LDHA by Inhibition of miR-409-3p. *OncoTargets Ther* (2020) 13:7111. doi: 10.2147/OTT.S243542
9. Sun Y. Tumor Microenvironment and Cancer Therapy Resistance. *Cancer Lett* (2016) 380(1):205–15. doi: 10.1016/j.canlet.2015.07.044
10. Shen W-J, Zhang F, Zhao X, Xu J. LncRNAs and Esophageal Squamous Cell Carcinoma-Implications for Pathogenesis and Drug Development. *J Cancer* (2016) 7(10):1258. doi: 10.7150/jca.14869
11. Pei K, Zhu JJ, Wang CE, Xie QL, Guo JY. MicroRNA-185-5p Modulates Chemosensitivity of Human non-Small Cell Lung Cancer to Cisplatin via Targeting ABCC1. *Eur Rev Med Pharmacol Sci* (2016) 20(22):4697–704. https://pubmed.ncbi.nlm.nih.gov/27906433/.
12. Pearson RC, Funnell AP, Crossley M. The Mammalian Zinc Finger Transcription Factor Krüppel-Like Factor 3 (KLF3/BKLF). *IUBMB Life* (2011) 63(2):86–93. doi: 10.1002/iub.422
13. Pa M, Naizaer G, Seyiti A, Kuerbang G. Long Noncoding RNA MALAT1 Functions as a Sponge of MiR-200c in Ovarian Cancer. *Oncol Res* (2021). doi: 10.3727/096504017X15049198963076
14. Smith-Vikos T, Slack FJ. MicroRNAs and Their Roles in Aging. *J Cell Sci* (2012) 125(1):7–17. doi: 10.1242/jcs.099200
15. Felekkis K, Touvana E, Ch S, Deltas C. microRNAs: A Newly Described Class of Encoded Molecules That Play a Role in Health and Disease. *Hippokratia* (2010) 14(4):236. https://pubmed.ncbi.nlm.nih.gov/21311629/.
16. Lin J, Chen Z, Wu S, Huang W, Chen F, Huang Z. An NF90/long Noncoding RNA-LET/miR-548k Feedback Amplification Loop Controls Esophageal Squamous Cell Carcinoma Progression. *J Cancer* (2019) 10(21):5139. doi: 10.7150/jca.30816
17. Cai Y, Ruan W, Ding J, Wei N, Wang J, Zhang H, et al. Mir−93−5p Regulates the Occurrence and Development of Esophageal Carcinoma Epithelial Cells by Targeting Tgfβr2. *Int J Mol Med* (2021) 47(3):1–1. doi: 10.3892/ijmm.2020.4836
18. Zhang J, Chen D, Liang S, Wang J, Liu C, Nie C, et al. miR-106b Promotes Cell Invasion and Metastasis via PTEN Mediated EMT in ESCC. *Oncol Lett* (2018) 15(4):4619–26. doi: 10.3892/ol.2018.7861
19. Tischoff I, Hengge UR, Vieth M, Ell C, Stolte M, Weber A, et al. Methylation of SOCS-3 and SOCS-1 in the Carcinogenesis of Barrett's Adenocarcinoma. *Gut* (2007) 56(8):1047–53. doi: 10.1136/gut.2006.111633
20. Wu X, Cai D, Zhang F, Li M, Wan Q. Long Noncoding RNA TUSC7 Inhibits Cell Proliferation, Migration and Invasion by Regulating SOCS4 (SOCS5) Expression Through Targeting miR-616 in Endometrial Carcinoma. *Life Sci* (2019) 231:116549. doi: 10.1016/j.lfs.2019.116549
21. Xiao X, Yang D, Gong X, Mo D, Pan S, Xu J. miR-1290 Promotes Lung Adenocarcinoma Cell Proliferation and Invasion by Targeting SOCS4. *Oncotarget* (2018) 9(15):11977. doi: 10.18632/oncotarget.24046
22. Metallo CM, Gameiro PA, Bell EL, Mattaini KR, Yang J, Hiller K, et al. Reductive Glutamine Metabolism by IDH1 Mediates Lipogenesis Under Hypoxia. *Nature* (2012) 481(7381):380–4. doi: 10.1038/nature10602
23. DeBerardinis RJ, Cheng T. Q's Next: The Diverse Functions of Glutamine in Metabolism, Cell Biology and Cancer. *Oncogene* (2010) 29(3):313–24. doi: 10.1038/onc.2009.358
24. O'Sullivan LA, Sullivan LA, Liongue C, Lewis RS, Stephenson SE, Ward AC. Cytokine Receptor Signaling Through the Jak–Stat–Socs Pathway in Disease. *Mol Immunol* (2007) 44(10):2497–506. doi: 10.1016/j.molimm.2006.11.025
25. Luan X, Wang Y. LncRNA XLOC_006390 Facilitates Cervical Cancer Tumorigenesis and Metastasis as a ceRNA Against miR-331-3p and miR-338-3p. *J Gynecol Oncol* (2018) 29(6):e95. doi: 10.3802/jgo.2018.29.e95
26. Xu M, Chen X, Lin K, Zeng K, Liu X, Xu X, et al. lncRNA SNHG6 Regulates EZH2 Expression by Sponging miR-26a/B and miR-214 in Colorectal Cancer. *J Hematol Oncol* (2019) 12(1):3. doi: 10.1186/s13045-018-0690-5
27. Tan YT, Lin JF, Li T, Li JJ, Xu RH, Ju HQ. LncRNA-Mediated Posttranslational Modifications and Reprogramming of Energy Metabolism in Cancer. *Cancer Commun* (2021) 41(2):109–20. doi: 10.1002/cac2.12108
28. Kim HM, Koo JS. Expression of Glutamine Metabolism-Related and Amino Acid Transporter Proteins in Adrenal Cortical Neoplasms and Pheochromocytomas. *Dis Markers* (2021) 2021. doi: 10.1155/2021/8850990

29. Wang W, Luo Y-p. MicroRNAs in Breast Cancer: Oncogene and Tumor Suppressors With Clinical Potential. *J Zhejiang University-Sci B* (2015) 16 (1):18–31. doi: 10.1631/jzus.B1400184
30. Mei L-L, Qiu YT, Zhang B, Shi ZZ, et al. MicroRNAs in Esophageal Squamous Cell Carcinoma: Potential Biomarkers and Therapeutic Targets. *Cancer Biomarkers* (2017) 19(1):1–9. doi: 10.3233/CBM-160240
31. Liang S, Gong X, Zhang G, Huang G, Lu Y, Li Y, et al. The lncRNA XIST Interacts With miR-140/miR-124/iASPP Axis to Promote Pancreatic Carcinoma Growth. *Oncotarget* (2017) 8(69):113701–18. doi: 10.18632/oncotarget.22555
32. Jia J, Zhang X, Zhan D, Li J, Li Z, Li H, et al. LncRNA H19 Interacted With miR-130a-3p and miR-17-5p to Modify Radio-Resistance and Chemo-Sensitivity of Cardiac Carcinoma Cells. *Cancer Med* (2019) 8(4):1604–18. doi: 10.1002/cam4.1860
33. Kobayashi D, Nomoto S, Kodera Y, Fujiwara M, Koike M, Nakayama G, et al. Suppressor of Cytokine Signaling 4 Detected as a Novel Gastric Cancer Suppressor Gene Using Double Combination Array Analysis. *World J Surg* (2012) 36(2):362–72. doi: 10.1007/s00268-011-1358-2

**Conflict of Interest:** The authors declare that the research was conducted in the absence of any commercial or financial relationships that could be construed as a potential conflict of interest.

frontiers | Frontiers in Oncology

ORIGINAL RESEARCH
published: 24 June 2022
doi: 10.3389/fonc.2022.779356

# Transcriptome Analysis Reveals the Immune Infiltration Profiles in Cervical Cancer and Identifies KRT23 as an Immunotherapeutic Target

*Xia Li*[1*], *Yan Cheng*[1], *Yanmei Cheng*[2] *and Huirong Shi*[2]

[1] *Gynecological Oncology Radiotherapy Ward, The First Affiliated Hospital of Zhengzhou University, Zhengzhou, China,*
[2] *Department of Gynecology and Obstetrics, The First Affiliated Hospital of Zhengzhou University, Zhengzhou, China*

Cervical cancer (CC) is one of the most common malignancies in women worldwide. Dismal prognosis rates have been associated with conventional therapeutic approaches, emphasizing the need for new strategies. Recently, immunotherapy has been used to treat various types of solid tumors, and different subtypes of the tumor microenvironment (TME) are associated with diverse responses to immunotherapy. Accordingly, understanding the complexity of the TME is pivotal for immunotherapy. Herein, we used two methods, "ssGSEA" and "xCell," to identify the immune profiles in CC and comprehensively assess the relationship between immune cell infiltration and genomic alterations. We found that more adaptive immune cells were found infiltrated in tumor tissues than in normal tissues, whereas the opposite was true for innate cells. Consensus clustering of CC samples based on the number of immune cells identified four clusters with different survival and immune statuses. Then, we subdivided the above four clusters into "hot" and "cold" tumors, where hot tumors exhibited higher immune infiltration and longer survival time. Enrichment analyses of differentially expressed genes (DEGs) revealed that the number of activated immune signaling pathways was higher in hot tumors than that in cold tumors. Keratin, type I cytoskeletal 23 (KRT23), was upregulated in cold tumors and negatively correlated with immune cell infiltration. *In vitro* experiments, real-time reverse transcription-quantitative polymerase chain reaction, cytometric bead arrays, and ELISA revealed that knockdown of KRT23 expression could promote the secretion of C-C motif chemokine ligand-5 and promote the recruitment of CD8$^+$ T cells. We also constructed a model based on DEGs that exhibited a high predictive power for the survival of CC patients. Overall, our study provides deep insights into the immune cell infiltration patterns of CC. Moreover, KRT23 has huge prospects for application as an immunotherapeutic target. Finally, our model demonstrated a good predictive power for the prognosis of CC patients and may guide clinicians during immunotherapy.

**Keywords: cervical cancer, hot and cold tumor, KRT23, prediction model, tumor microenvironment**

**Edited by:**
*Gang Chen,*
*Huazhong University of Science and Technology, China*

**Reviewed by:**
*Komsun Suwannarurk,*
*Thammasat University, Thailand*
*Ihtisham Bukhari,*
*Henan Provincial People's Hospital, China*
*Yujia Zheng,*
*Chinese Academy of Medical Sciences and Peking Union Medical College, China*

***Correspondence:**
*Xia Li*
*lixia86519@126.com*

**Specialty section:**
*This article was submitted to Gynecological Oncology, a section of the journal Frontiers in Oncology*

**Received:** *18 September 2021*
**Accepted:** *23 May 2022*
**Published:** *24 June 2022*

**Citation:**
*Li X, Cheng Y, Cheng Y and Shi H (2022) Transcriptome Analysis Reveals the Immune Infiltration Profiles in Cervical Cancer and Identifies KRT23 as an Immunotherapeutic Target. Front. Oncol. 12:779356. doi: 10.3389/fonc.2022.779356*

## INTRODUCTION

Cancer is widely acknowledged to pose the highest clinical, social, and economic burden in terms of cause-specific disability-adjusted life years (1). Cervical cancer (CC) is ranked fourth for incidence and mortality in women worldwide (2). Invasion and metastasis by CC cells are associated with a poor prognosis, representing the most prevalent cause of cancer-associated deaths (3, 4). Current evidence suggests that surgery, chemotherapy, and radiotherapy yield satisfactory efficacy for early-stage and low-risk CC (5–7). However, the reported 5-year survival for metastatic cervical cancer is only 16.5% (8). In addition, side effects caused by chemotherapy and radiotherapy limit their clinical use. Accordingly, the exploration of the biological mechanisms and the development of new therapeutic targets and strategies for CC patients are essential.

In recent years, many emphases have been placed on the crucial role of immunotherapy in CC. Given the high expression of programmed cell death-1 (PD-1) and programmed cell death ligand-1(PD-L1) in advanced CC, an increasing body of evidence suggests that pembrolizumab (a humanized monoclonal anti-PD-1 antibody) yields substantial antitumor activity and exhibits a good biosafety profile in clinical trials during the treatment of recurrent CC or metastatic CC (mCC) (9–11). Even immunotherapy has achieved remarkable efficacy. Accumulated data in recent years have demonstrated that many patients experience minimal or no clinical benefit if provided with identical treatment. This phenomenon has been attributed to the complexity and uniqueness of the tumor microenvironment (TME).

The TME is a complex, plastic, and dynamic system sculpted by tumor cells and other surrounding cells (12, 13). Cells from the innate immune system and adaptive immune system, representing important components of the tumor stroma, can be reprogrammed according to the TME and may be involved in the survival and progression of tumor cells (14, 15). For example, tumor-associated macrophages (TAMs) represent the largest population of infiltrating myeloid cells in most solid tumors (16). It has been established that TAMs display a high degree of functional plasticity when exposed to various microenvironmental conditions and can be classified as "M1-like" (pro-inflammatory and usually antitumor) or "M2-like" (anti-inflammatory and protumor) (17, 18). Accumulating evidence substantiates the critical roles of the TME in promoting tumor progression. However, it remains unclear how the TME affects the efficacy of immunotherapy in CC. It is well-recognized that immunotherapy harnesses or restores the immune system to kill tumor cells, but this process requires the infiltration of immune cells in the tumor site. Many studies have demonstrated that different types of TMEs are associated with diverse degrees of clinical efficacy with immunotherapy. In this regard, a "hot" tumor with sufficient tumor-infiltrating lymphocytes and antigen-presenting cells can robustly respond to immunotherapy. In contrast, a "cold" tumor lacking immune cells, in general, cannot elicit an effective response to immunotherapy (19). Therefore, understanding and distinguishing the unique classes of the TME are useful for predicting and guiding immunotherapy.

Herein, we undertook a comprehensive analysis to explore the infiltration of immune cells in CC using two different methods and constructed a prediction model. We observed that CC patients with greater immune cell infiltration survived longer times. To uncover the underlying mechanisms of immune cell infiltration, we subdivided CC tumors into hot and cold types and ascertained the differentially expressed genes (DEGs) between them. Then, we identified Keratin, type I cytoskeletal 23 (KRT23), as a immunotherapeutic target. In addition, our model exhibited good predictive power for the overall survival (OS) of CC patients.

## MATERIALS AND METHODS

### Ethics Statement

Primary CC specimens were obtained after surgery and were frozen in the biobank of the First Affiliated Hospital of Zhengzhou University; some specimens have received neoadjuvant therapy. All participants provided written informed consent for their specimens to be used in this study. The study protocol was approved by the Ethics Committee of the First Affiliated Hospital of Zhengzhou University.

### Cell Culture

A human cervical cell line (HeLa) was purchased from the Institute of Biochemistry and Cell Biology of the Chinese Academy of Sciences (Shanghai, China). Cells were cultured in RPMI1640 medium with 5% fetal bovine serum and an atmosphere of 5% $CO_2$ in a humidified incubator at 37°C.

### Acquisition and Normalization of Data

Level-2 mRNA sequencing data (fragment per kilobase of transcript per million mapped reads) of CC were downloaded from The Cancer Genome Atlas (TCGA) database (https://portal.gdc.cancer.gov/) and transformed to transcripts per million for further analyses. The clinical data of CC were downloaded from the University of California Santa Cruz Xena (http://xena.ucsc.edu/). The GSE78220 dataset was downloaded from the Gene Expression Omnibus database (https://www.ncbi.nlm.nih.gov/geo/). A dataset of patients with metastatic urothelial cancer treated with anti-PD-L1 agents downloaded from the online website is supplied in the article (http://research-pub.gene.com/IMvigor210CoreBiologies/).

### Estimation of the Immune Profile

The immune profile (i.e., the number and type of immune cells) was estimated by the R packages "ssGSEA" and "xCell" (R Institute for Statistical Computing, Vienna, Austria). For xCell analysis, we selected samples with $p < 0.05$ and only included immune cells for further analyses. The Immune Score, Stromal Score, and tumor purity were calculated by the R package "ESTIMATE."

### Identification and Functional Annotation of Differentially Expressed Genes

Tumor samples were divided into "cold" and "hot" subtypes. DEGs were calculated by the R package "Limma" and visualized by volcano plots using the R package "ggplot2." DEGs with log fold change >1 and $p < 0.05$ were selected for annotation using the Kyoto Encyclopedia of Genes and Genomes (KEGG; https://www.genome.jp/) and Gene Ontology (GO; http://geneontology.org/) databases using the R package "clusterprofile." A protein–protein interaction (PPI) network was constructed using Search Tool for the Retrieval of Interacting Genes/Proteins (STRING; www.string-db.org/) and visualized by Cytoscape v3.6.1 (https://cytoscape.org/).

## Correlation and Survival Analyses

The R package "corrplot" was used to analyze the correlation of immune cells. The correlation of KRT23 and C-X-C motif chemokine ligand 9 (CXCL9) and CXCL10 and C-C motif chemokine ligand 5 (CCL5) in TCGA dataset was analyzed through cbioportal (www.cbioportal.org/). The correlation of KRT23 and immune cells as well as KRT23 expression in the pan-cancer dataset was determined by the online website TIMER (https://cistrome.shinyapps.io/timer/). Correlation analysis in tumor tissues from patients was conducted by Prism7 (GraphPad, San Diego, CA, USA). For survival analyses, samples were divided into four clusters or "hot" and "cold" tumor. The R package "survival" was used to assess the survival difference using the log-rank test.

## Real-Time Reverse Transcription-Quantitative Polymerase Chain Reaction

Total RNA was extracted by TRIzol®Reagent according to the manufacturer's (TaKaRa Biotechnology, Shiga, Japan) instructions, and the concentration was measured using a spectrophotometer (NanoDrop™ 2000; Thermo Fisher, Waltham, MA, USA). RNA (1 μg) was used to reverse DNA using the PrimeScript™ RT Reagent kit (TaKaRa Biotechnology). The primers for KRT23 were constructed by PrimerBank (https://pga.mgh.harvard.edu/primerbank/index.html/) and synthesized by Sangon Biotech (Shanghai, China) (**Supplementary Table S1**). Glyceraldehyde-3-phosphate dehydrogenase was used for data normalization.

## Small Interfering RNA Transfection

Knockdown of KRT23 expression was achieved using the jetPRIME® Transfection Reagent kit (Polyplus-transfection, Illkirch-Graffenstaden, France). HeLa cells ($1 \times 10^5$) were seeded in six-well plates with RPMI1640 medium. Before transfection, the small interfering RNA (siRNA) of KRT23 was diluted to 20 μM according to the manufacturer's instructions. Then, 200 μl of transfection buffer and 4 μl of jetPRIME reagents were mixed and incubated for 10 s at room temperature. Subsequently, 50 nM of siRNA was added and incubated for 15 min at room temperature. siRNA efficacy was analyzed by real-time reverse transcription-quantitative polymerase chain reaction (RT-qPCR) after 48 h. The sequence of siRNA synthesized by Gene Pharma (Shanghai, China) is listed in **Supplementary Table S2.**

## Transwell™ Assay

Migration of CD8$^+$ T cells was analyzed through the Transwell assay. CD8$^+$ T cells ($2 \times 10^4$) isolated by microbeads from healthy donors were activated with CD3/CD28 beads and seeded in the upper chamber of the Transwell apparatus with serum-free medium (Millipore, Billerica, MA, USA). HeLa cells ($2 \times 10^4$) were seeded in the lower chamber with RPMI1640 medium. The number of CD8$^+$ T cells was calculated using flow cytometry.

## Enzyme-Linked Immunosorbent Assay

Tumor cells were transfected with siRNA for 48 h. Then, supernatants were collected and centrifuged (1,500 rpm, 5 min) to remove debris. The CCL5 concentration was measured by the LEGEND MAX™ Human CCL5 (regulated upon activation normal T cell expressed and secreted factor, RANTES) ELISA kit according to the manufacturer's (Biolegend, San Diego, CA, USA) instructions. Briefly, standard dilutions and samples were prepared, followed by the addition of 50 μl of Assay Buffer B to each well. Then, 50 μl of the standard or sample was added to the appropriate well, followed by incubation at room temperature for 2 h with agitation at 200 rpm. Then, 100 μl of Human CCL5 Detection Antibody solution was added to each well, followed by 100 μl of Avidin-HRP A solution. Results were read at an optical density of 450 nm.

## Detection of Multiple Chemokines

We used the LEGENDplex™ kit (BioLegend) to detect the chemokines secreted by tumor cells. First, 25 μl of assay buffer was added to the standard or sample in each tube. Then, we added 25 μl of mixed beads (A and B) and incubated at room temperature for 2 h with agitation at 500 rpm. Subsequently, we added 25 μl of antibodies to each tube and incubated at room temperature for 1 h with agitation at 500 rpm. Next, we added 25 μl of SA-PE to each tube and washed it with washing buffer. The fluorescence intensity was detected by a flow cytometer and analyzed by LEGENDplex v8.0.

## Statistical Analyses

Statistical analyses were undertaken using Prism 7 (GraphPad) and R 3.6.3. Two-tailed unpaired *t*-tests and the Wilcoxon test were used to compare the difference between the two groups. Spearman's rank correlation coefficient was used to evaluate the correlation. A *p*-value <0.05 was statistically significant.

# RESULTS

## Infiltration Pattern of Immune Cells in Tumor and Adjacent Normal Tissue

We carried out a multistep analysis to explore the infiltration of immune cells into CC (**Figure 1**). First, we estimated the number of immune cells in each sample between tumor and adjacent normal tissues by Single sample gene set enrichment analysis (ssGSEA) and xCell algorithms. ssGSEA and xCell consistently showed that the number of each cell type that infiltrated into the TME was different, revealing the complexity of the TME. In general, the number of adaptive immune cells, such as activated CD4$^+$ T cells, effector memory CD4$^+$ T cells, type-17 T-helper (Th17) cells, and Th2 cells, in tumor tissue was higher than that

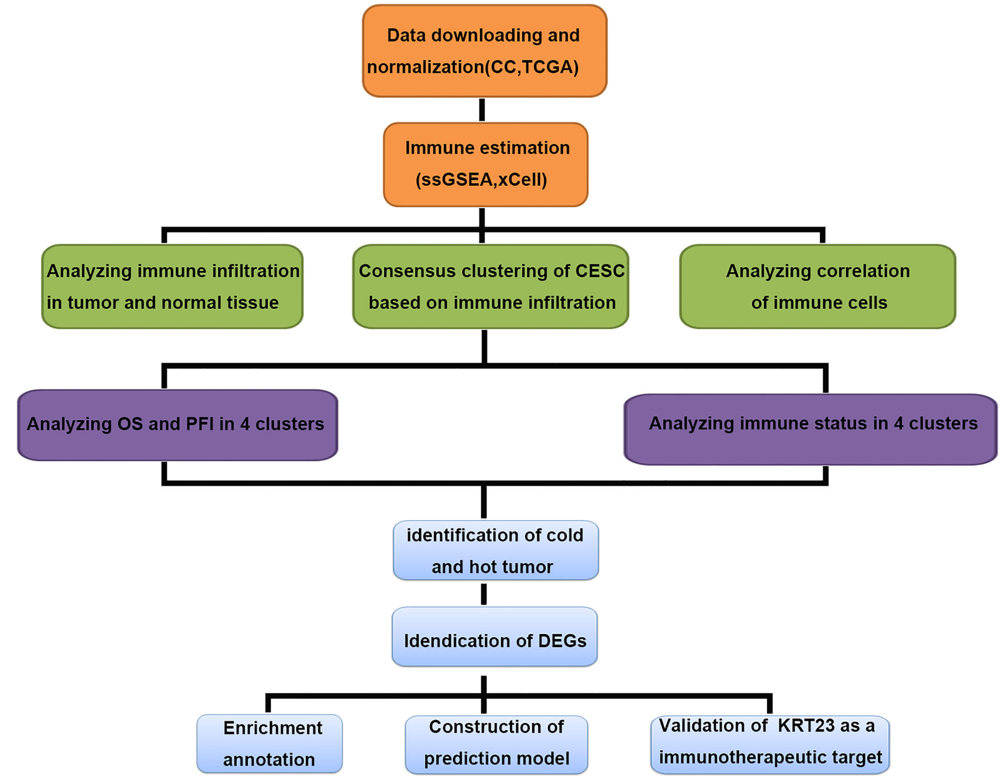

**FIGURE 1** | Multiple-step analysis of this study.

in adjacent normal tissue, which indicated an activated immune response in tumor tissue. The number of CD8$^+$ T cells was higher in tumor tissues, but the difference was not statistically significant. Cells from the innate immune system were significantly infiltrated in normal tissues (**Figures 2A, B**). Tumor tissues had a lower Immune Score, but the difference in Stromal Score was not significant (**Figures 2C, D**). We also compared the difference in immune cells in patients who received radiotherapy. After radiotherapy, pro-B cells and Th1 cells accumulated in tumor tissue (**Supplemetary Figures S1A, B**) . Overall, the above results revealed distinct adaptive and innate immune cell infiltration patterns.

## Characterization of Immune Clusters in Cervical Cancer Tissues

It is widely acknowledged that an efficient antitumor immune response requires the synergistic action of multiple cells. To explore the relationships between different cell types, we performed a correlation analysis of infiltrating cells in tumor tissues. Most infiltrating cells showed a high correlation with each other, especially activated CD8$^+$, CD4$^+$ T, dendritic, and B cells. We observed a high correlation between immunosuppressive and immune cells, such as regulatory T cells, myeloid-derived suppressor cells, and M2 macrophages, which suggested that immune suppression was induced by tumor cells after activation of the immune system. The innate immune system cells, such as monocytes, neutrophils, and natural killer cells, exhibited a weak association with other cells, demonstrating a unique antitumor immune process (**Figures 3A, B**).

Next, we performed consensus clustering of all samples based on the proportions of immune cells to identify the subtypes of infiltrating immune cells. The consensus matrix heatmap showed four distinct groups estimated by two methods (**Figures 3C, D**). We observed a gradual increase in immune cell infiltration in tumor tissue from groups 1–4. Groups 1 and 2 demonstrated little infiltration of immune-related cells, group 3 had modest infiltration levels, and group 4 demonstrated high levels of immune cells (**Supplemetary Figures S2A, B**) . Consistently, group 4 had the highest Immune Score (**Supplementary Figures S2C, D**) . To further characterize the clusters of CC cells, we intersected each group obtained from the two methods and denoted them as clusters 1–4 (**Supplementary Figure S3A**) . In accordance with the results stated above, cluster 4 had a high Immune Score (**Figure 4A**). Next, we analyzed the expression of genes involved in the immune response, immune tolerance, and antigen presentation in the four clusters. The expression of immune checkpoint-related genes (*CD276*, *CD274*, *CD40*, *CTLA4*, *HAVCR2*, *LAG3*, *PDCD1*), antigen presentation-related genes (*B2M*, *HLA-B*, *HAL-C*, *HLA-DQA1*, *TAP1*, *TAP2*, *HLA-DQA2*), cytokine-related genes (*GZMB*, *GZMH*, *IFNG*, *PRF1*, *TNF*), and chemokine-related genes (*CCL5*, *CXCL10*, *CXCL13*, *CXCL9*) increased gradually from cluster 1 to cluster

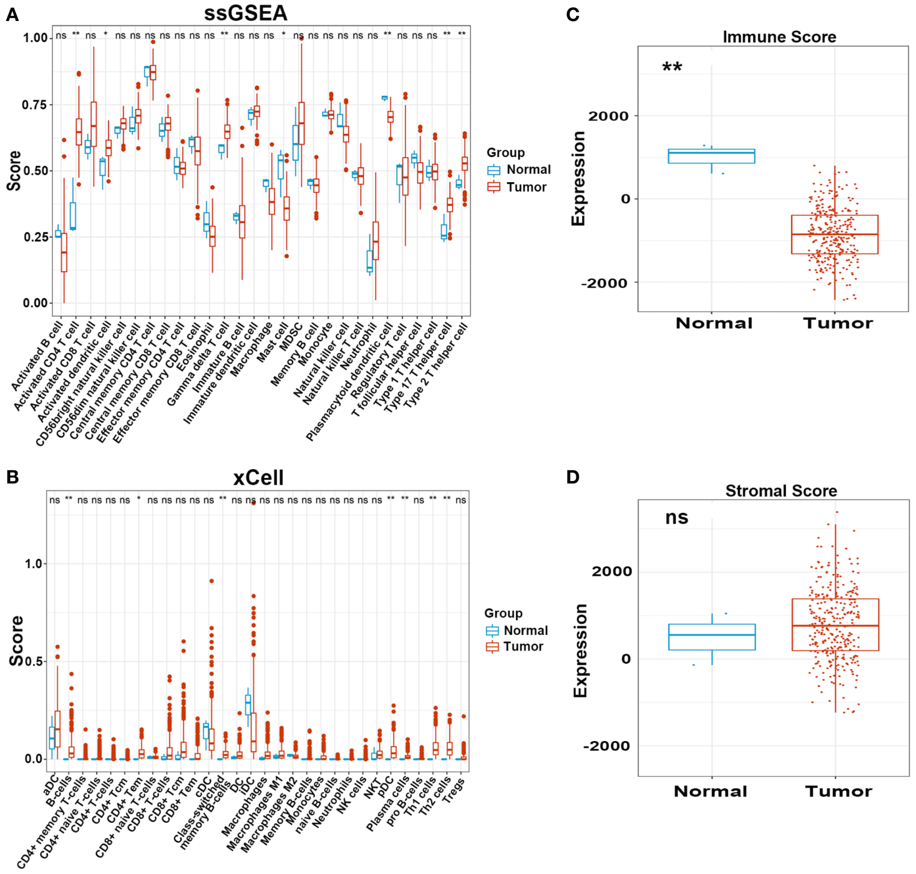

**FIGURE 2** | Infiltration pattern of immune cells in adjacent normal and tumor tissues. **(A, B)** Level of immune cells in normal and tumor tissues estimated by ssGSEA and xCell. **(C, D)** Immune and Stromal score in normal and tumor tissues estimated by ESTIMATE. ns, not significant; *$p \leq 0.05$, **$p \leq 0.01$.

4 (**Figure 4B**; **Supplementary Figures S3B–D**) . Survival analyses revealed that cluster 4 had the longest survival relative to clusters 1, 2, and 3 in terms of OS and progression-free interval (PFI) and have potential trends of a higher percentage of patients with low stages, although there was inconsistency with grade (**Figures 4C, D**; **Supplementary Figures S4A, B**) .

## Survival Status and Signaling Alterations Between Hot Tumors and Cold Tumors

To further explore the mechanisms of immune cell infiltration, we redefined cluster 1, cluster 2, and cluster 3 as cold tumors and cluster 4 as a hot tumor based on infiltration of immune cells and survival status. Hot tumors had longer OS and PFI than those in cold tumors (**Figures 5A, B**). Next, we analyzed the difference between the two groups at the transcriptional level. Hot and cold tumors showed different transcription patterns according to volcano plots (**Figure 5C**). In this study, 657 and 55 mRNAs were upregulated in hot and cold tumors, respectively. To further explore the function of DEGs, functional enrichment analyses were conducted using GO and KEGG. The GO analysis revealed that DEGs in cold tumors were significantly enriched in the "apical part of cell," "actin-based cell projection," and "apical plasma membrane" (**Figure 5D**), while those in hot tumors were primarily enriched in "T cell activation," "regulation of lymphocyte activation," "leukocyte cell–cell adhesion," "regulation of T cell activation," and "leukocyte proliferation" (**Figure 5E**). KEGG analyses of enrichment of DEGs revealed that DEGs in hot tumors were enriched mainly in "cytokine–cytokine receptor interaction," "chemokine signaling pathway," and "cell adhesion molecules," which indicated an active immune response in hot tumors (**Figures 5F**); none of the KEGG annotations were enriched in cold tumors. These results suggested that the immune system was activated in hot tumors, especially the T cell-mediated immune response. Finally, the PPI networks revealed that the DEGs of hot tumors were mainly immune-related chemokines and cytokines, and DEGs of cold tumors were metabolic genes and Keratin family (**Supplementary Figures S5A, B**) .

## Inhibition of KRT23 Expression Promotes Infiltration of CD8$^+$ T Cells

The above results revealed a correlation between immune cell infiltration and longer survival, suggesting that inducing immune cell infiltration in cold tumors may enhance antitumor immunity and prolong survival time. Among the DEGs between cold and hot tumors, we found that KRT23 was most significantly

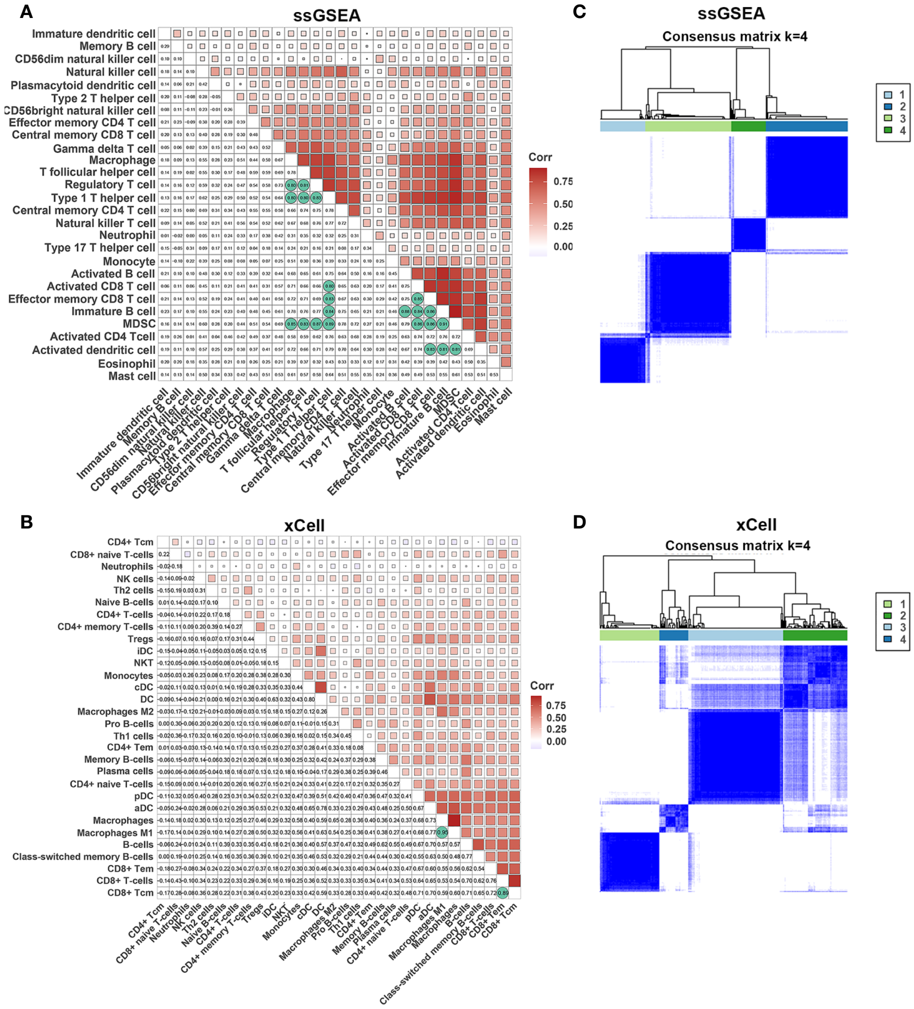

**FIGURE 3** | Correlations of immune cells. **(A, B)** Correlation of immune cells in tumor tissues estimated by ssGSEA and xCell. **(C, D)** The heatmap shows the consensus clustering of CC based on levels of immune cells estimated by ssGSEA and xCell.

expressed in cold tumors than in hot tumors. Pan-cancer analysis revealed that KRT23 has a higher expression in tumor tissues in most types of cancers (**Supplementary Figure S6A**) . Functional enrichment analyses using the KEGG and GO databases revealed that KRT23-related genes were negatively correlated with immune response (**Figures 6A, B**). Knockdown of KRT23 expression in HeLa cells inhibited cell proliferation (**Figures 6C, D**), which suggested an important role of KRT23. To explore how KRT23 affected immune cell infiltration, we used cytometric bead arrays to detect the chemokines derived from tumor cells with KRT23 knockdown. Results revealed that the secretion of $CD8^+$ T cell-related chemokines (CCL5, CXCL9, and CXCL10) was increased in the knockdown group (**Figure 6E**). Then, we quantified the expression of KRT23 and $CD8^+$ T cell-related chemokines in clinical tumor samples; the detailed information of patients was listed in **Table 1**. Results showed that KRT23 expression was negatively correlated with these chemokines, and this result was confirmed using TCGA database (**Figure 6F**; **Supplementary Figure S6B**) . We further found that KRT23 was negatively correlated with $CD8^+$ T cells (**Supplementary Figure S6C**) . In addition, we validated the CCL5 expression because CCL5 changed most obviously after knocking down KRT23. Results revealed that the knockdown of KRT23 expression increased CCL5 secretion (**Figure 6G**). Transwell assays further indicated that knockdown of KRT23 promoted the recruitment of $CD8^+$ T cells (**Figure 6H**).

## Construction and Validation of a Prediction Model Based on Differentially Expressed Genes

Next, we used DEGs to construct a prediction model. We performed a univariate Cox analysis followed by a Least absolute shrinkage and selection operator (LASSO) regression analysis (**Supplementary Figure S7A**) . To optimize the model, we carried out multivariate Cox analysis and finally identified 11 genes to construct our model (**Supplementary Figure S7B**) .

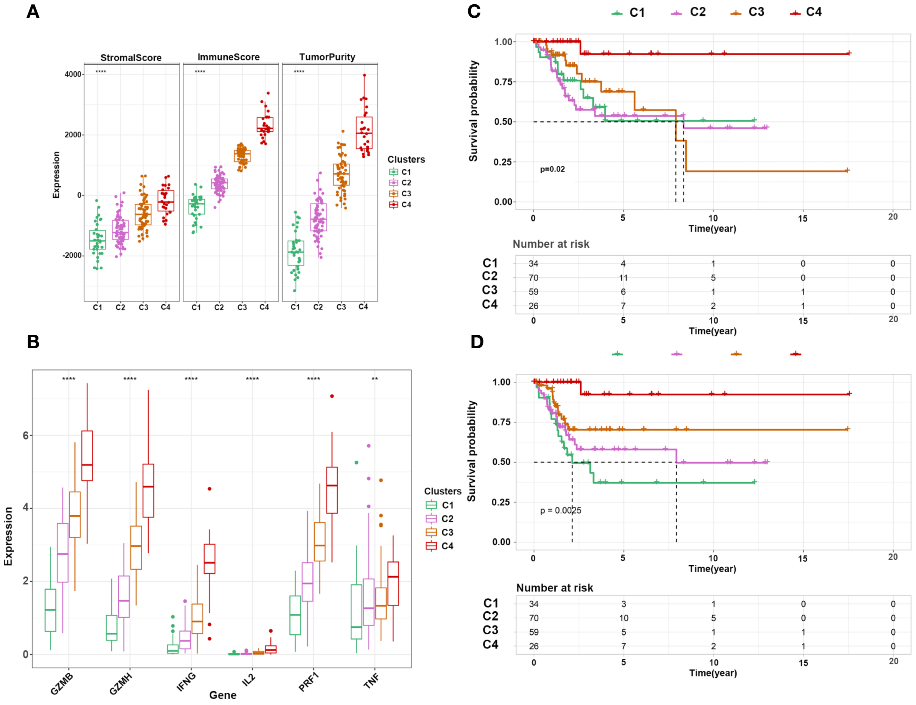

**FIGURE 4** | Characterization of immune clusters of CC. **(A)** Expression of immune score, stromal score, and tumor purity in the four subtypes. **(B)** Expression of cytotoxicity-related cytokines in the four subtypes. **(C, D)** Kaplan–Meier curve shows the OS and PFI of 4 clusters. $^{**}p \le 0.01$, $^{****}p \le 0.0001$.

Heatmaps were generated to reveal the expression of these genes in high- and low-risk groups in the training and internal test cohorts; the detailed information of patients was listed in **Table 2**. Survival analyses showed that patients with a high risk had shorter survival in the training and test cohorts (**Figures 7A, B**). To explore the accuracy of our model, we analyzed receiver operating characteristic (ROC) curves in the training and test cohorts at 1, 3, and 5 years. Our model yielded high area under the ROC curve (AUC) values (**Figures 7C, D**). Given that our model was established based on DEGs in hot and cold tumors, we hypothesized that this model could also predict tumor response to immunotherapy. Hence, we used two external cohorts of CC patients treated with immunotherapy. The results demonstrated that patients with a high risk had shorter survival in both cohorts (**Figures 7E, F**), suggesting that our model could predict the survival of patients who respond to immunotherapy.

## DISCUSSION

Up to now, there is ample evidence suggesting that chemotherapy for CC is associated with limited efficacy. The optimal regimen against recurrent CC or mCC includes a combination of cisplatin, paclitaxel, and bevacizumab, associated with an overall response rate of 48% and a median survival of 17 months (20). Moreover, the side effects associated with radiotherapy limit their clinical application in CC (21), highlighting the need for new and efficient therapeutic strategies. In recent years, immunotherapy has demonstrated sustainable clinical response and is the first-line treatment for various tumors (22). "Cancer immunotherapy" is a general term that is described as harnessing a patient's immune system to elicit antitumor effects (23). Antibodies against PD-1 and PD-L1 are commonly used for cancer immunotherapy. Their mechanism involved releasing the "inhibitory brakes" of T cells, resulting in robust activation of the antitumor immune response (24).

As previously stated, the major risk factor for CC is Human Papilloma Virus (HPV) infection (25), and the retained viral antigens in CC make immunotherapy an attractive option because they could be recognized as foreign. This rationale has led to the development of antibodies against PD-1 or PD-L1 assessed in several ongoing clinical trials (23, 26). Effective immunotherapy is contingent on the infiltration of lymphocytes and antigen-presenting cells. In general, the TME can be divided into two broad phenotypes: "T cell-inflamed" and "non-T cell-inflamed" (27). Several methods have been used to estimate the immune profile in the TME, encompassing ssGSEA, CIBERSORT, TIMER, MCP-counter, and xCell (28–32). ssGSEA and MCP-Counter use specific cell-maker genes and score the immune profile through the expression of these genes. CIBERSORT focuses on the ratios of each cell type using Nu-support vector regression. xCell integrates these methods and expands the cells that can be evaluated to 64 types. To more accurately reflect the level of immune cells in the TME of CC, we used two different methods. The comparison between tumor and adjacent normal tissues and correlation analysis of estimated

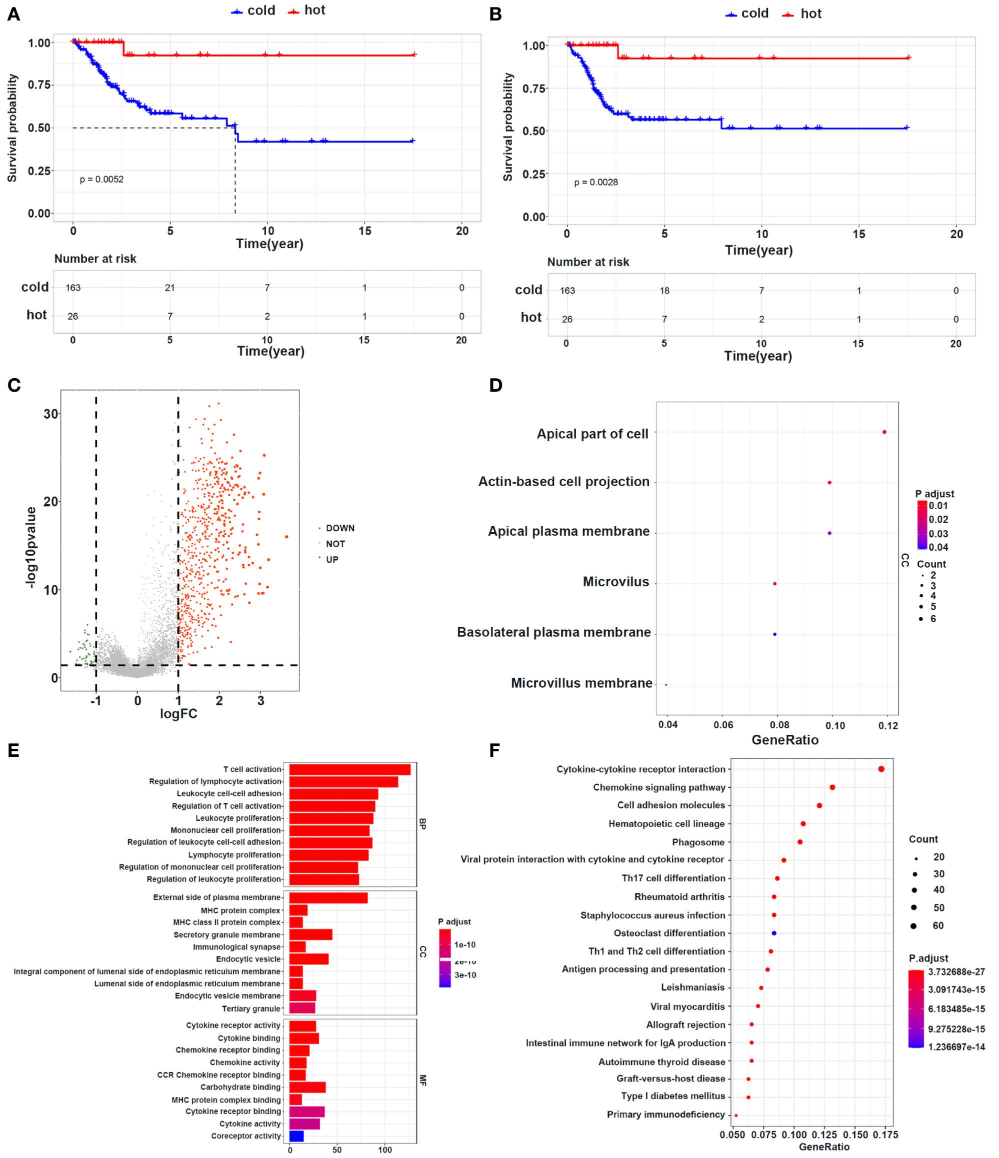

**FIGURE 5** | Survival and transcriptome characteristics of cold and hot tumors. **(A, B)** Kaplan–Meier curve shows the OS and PFI of cold and hot tumors. **(C)** Volcano plot shows the difference of gene expression in cold and hot tumors. **(D)** GO enrichment analysis in cold tumors. **(E)** GO enrichment analysis in hot tumors. **(F)** KEGG enrichment analysis in hot tumors.

immune cells yielded consistent findings, suggesting that these two methods can be used to estimate immune levels. We found that CC could be divided into 4 clusters based on consensus clustering, and clusters with higher immune infiltration yielded better survival rates. In a study by Wang et al. (33), CIBERSORT showed that CD4$^+$ T cells represent an independent prognostic factor of CC. Meanwhile, immune cell infiltration has also been correlated with the response to chemotherapy (34).

In this study, we further redivided the 4 clusters into 2 subtypes: “hot” and “cold” tumors based on the immune levels. “Hot” tumors exhibited a T cell-inflamed phenotype, and “cold” tumors acted as a non-T cell-inflamed phenotype. Pathway enrichment analysis confirmed that “hot” tumors were associated with an active immune response. Cold tumors are characterized by the infiltration of few immune cells and are hence the most challenging to eradicate, accounting for their poor prognoses (35). Several strategies have been used to convert cold tumors to hot tumors: radiotherapy, chemotherapy, targeted therapy, and adoptive-cell therapy (36–40). In this study, we analyzed the differences between hot and cold tumors and identified *KRT23* as the most significantly upregulated gene in cold tumors. Keratin is the main component of epithelial cells, and malignant tumor cells originate from these epithelial cells. *KRT23* is a newly identified gene in the KRT family (41, 42). Studies have reported that KRT23 overexpression promotes the migration of ovarian cancer cells *via* epithelial–mesenchymal transition. Interestingly, KRT23 could

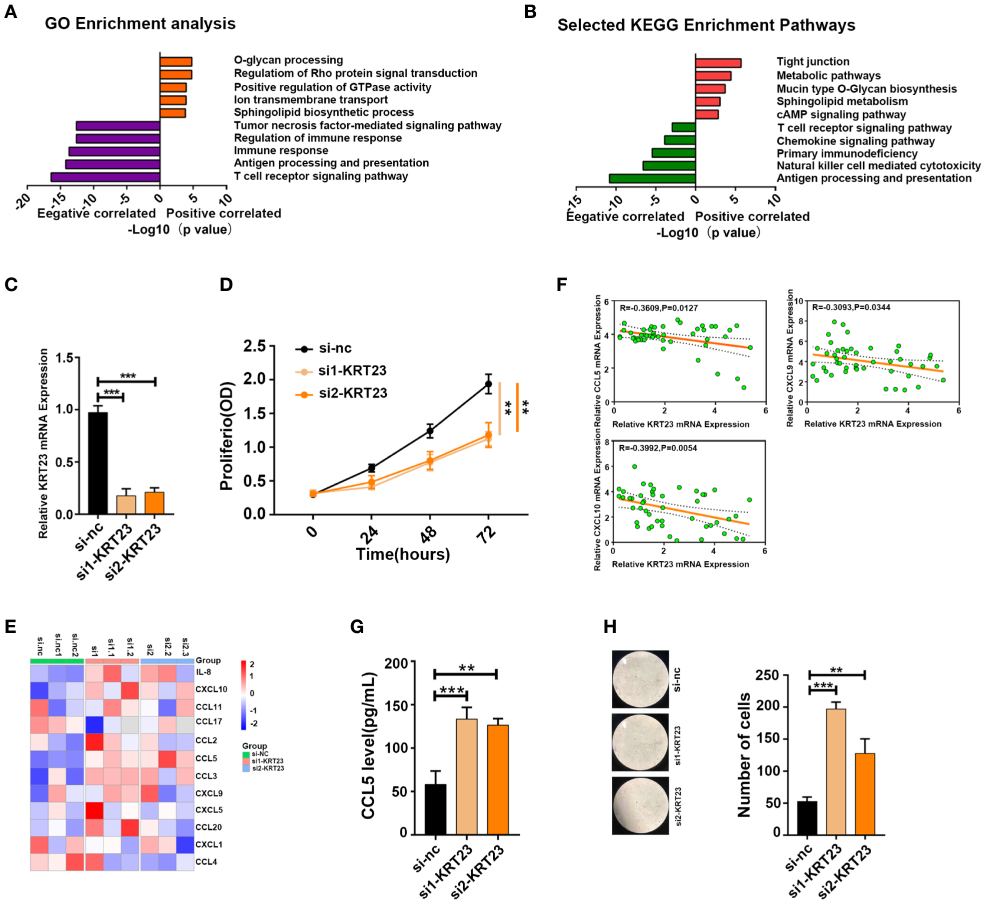

**FIGURE 6** | KRT23 promotes CD8$^+$ T cell recruitment. **(A, B)** GO and KEGG analysis of KRT23-related genes. **(C)** qPCR analysis shows the knockdown efficacy of KRT23. **(D)** Proliferating rate of tumor cells with knockdown of KRT23. **(E)** The heatmap shows the concentration of cytokine and chemokine secreted by tumor cells with knockdown of KRT23. **(F)** Correlation of KRT23 and CCL5, CXCL9, and CXCL10 in tumor tissues of CC. **(G)** ELISA shows the CCL5 secretion by tumor cells with knockdown of KRT23. **(H)** Number of CD8$^+$ T cells recruited by conditioned medium derived from tumor cells with knockdown of KRT23. $^{**}p \le 0.01$, $^{***}p \le 0.001$.

promote the proliferation of colorectal tumor cells by increasing telomerase reverse transcriptase expression (43). Although the oncogenic role of KRT23 has been explored, it remains unclear how KRT23 affects the immune response. We found that KRT23 expression was negatively correlated with the immune response. Knockdown of KRT23 expression in tumor cells resulted in increased secretion of CCL5 and inhibited tumor cell proliferation. Our results corroborate that the inhibition of KRT23 expression enhances the antitumor response. Hence, a potential combination strategy of targeting KRT23 and immunotherapy could be a rational approach against CC.

The large difference in survival between hot and cold tumors inspired us to construct a prediction model based on the DEGs between the two types of CC tumors. This model performed well in the training cohort and internal and external validation cohorts. Hence, our model was reliable and could be used to guide clinical treatment. Over the years, several prediction models for CC have been documented in the literatures. Mei et al. (44) conducted immune profiling by ssGSEA and identified four immune-related prognostic gene signatures. Chen et al. (45) constructed a TME-related signature to predict the prognosis of CC. The results from those studies further substantiate our findings. Moreover, Ding et al. (46) screened survival-related immune genes and constructed a prediction model containing 13 genes. In addition, Yang et al. (47) constructed a prediction model based on ferroptosis-related genes. Of note, our model exhibited a high predictive power for the survival of patients with melanoma and urothelial cancer receiving immunotherapy.

However, there are some limitations in this study. First, we did not explore the effect of KRT23 on migration or apoptosis of tumor cells. Second, the prediction model lacks validation using clinical specimens.

## CONCLUSIONS

In the present study, we undertook a comprehensive analysis of the infiltration of immune cells in CC. We identified hot and cold

**TABLE 1 |** Clinicopathological parameters of patients with cervical cancer in our cohort in the study.

| Characteristic | Number |
|---|---|
| **Histological type** | |
| Cervical squamous cell carcinoma | 42 |
| Non- squamous cell carcinoma | 5 |
| **History of neoadjuvant treatment** | |
| No | 35 |
| Yes | 12 |
| **Sample type** | |
| Primary | 47 |
| Metastatic | 0 |
| **Age at initial diagnosis** | |
| ≥60 | 21 |
| <60 | 26 |
| **Clinical stage** | |
| I | 9 |
| II | 22 |
| III | 11 |
| IV | 5 |
| **HPV infection** | |
| Yes | 19 |
| No | 2 |
| NA | 26 |
| **Differentiation** | |
| Low | 15 |
| Moderate | 28 |
| High | 4 |

**TABLE 2 |** Clinicopathological parameters of patients with cervical cancer in TCGA dataset in the study.

| Characteristic | Number |
|---|---|
| **Histological type** | |
| Cervical squamous cell carcinoma | 235 |
| Non- squamous cell carcinoma | 50 |
| **History of neoadjuvant treatment** | |
| No | 285 |
| Yes | 0 |
| **Sample type** | |
| Primary | 283 |
| Metastatic | 2 |
| **Age at initial diagnosis** | |
| ≥60 | 227 |
| <60 | 58 |
| **Clinical stage** | |
| I | 154 |
| II | 64 |
| III | 39 |
| IV | 22 |
| NA | 6 |
| **Histologic grade** | |
| G1 | 17 |
| G2 | 124 |
| G3 | 116 |
| G4 | 1 |
| GX | 27 |
| **HPV infection** | |
| Yes | 20 |
| NA | 265 |

tumors of CC; the former was associated with a more favorable outcome. Moreover, we demonstrated that KRT23 is a negative regulator of the immune response, and knockdown of KRT23 expression could promote CCL5 secretion. In addition, a prediction model based on DEGs between the two types of CC was established. This model performed well in predicting the survival of CC patients receiving immunotherapy. Overall, our findings provided novel insights into immune cell infiltration in

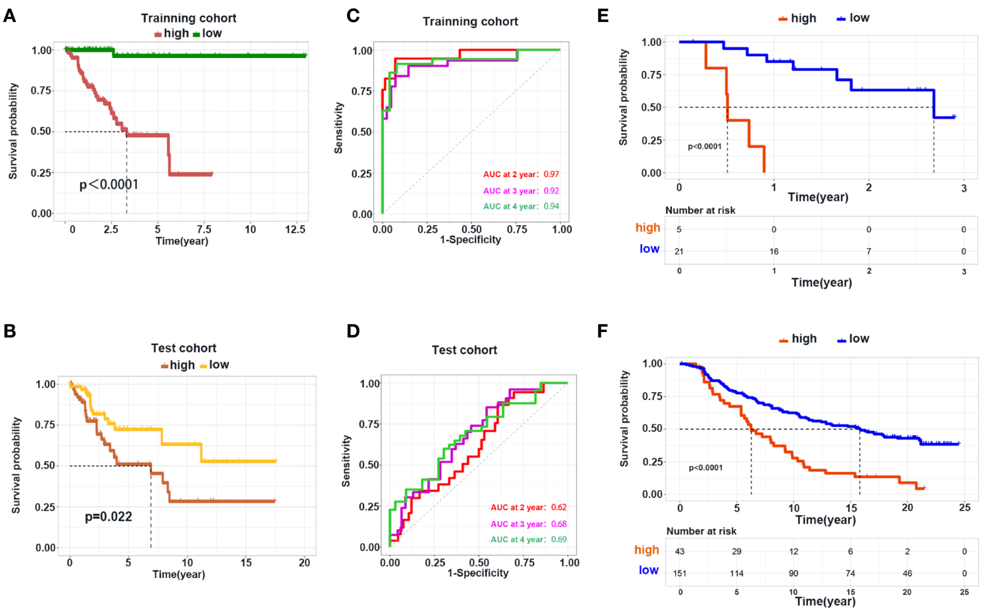

**FIGURE 7 |** Construction and validation of the prediction model. **(A, B)** Kaplan–Meier curve shows the OS in the high- and low-risk group in the training and test cohorts. **(C, D)** ROC curve analysis shows the AUC of the prediction model in the training and test cohorts. **(E, F)** Validation of the prediction model using the dataset of patients with metastatic melanoma and urothelial cancer receiving immunotherapy treatment.

CC and highlighted KRT23 as a potential target to enhance immunotherapy against CC.

## DATA AVAILABILITY STATEMENT

The datasets used and/or analyzed during the current study are available from the corresponding author on reasonable request. The data that support the findings of this study are openly available on the online website UCSCXena (https://xenabrowser.net/). GSE77280 are available from the GEO database (https://www.ncbi.nlm.nih.gov/geo/), and data of patients with metastatic urothelial cancer treated with anti-PD-L1 agents were downloaded from the online website supplied in the article (http://research-pub.gene.com/IMvigor210CoreBiologies/).

## ETHICS STATEMENT

The studies involving human participants were reviewed and approved by the ethics committee of the First Affiliated Hospital of Zhengzhou University. The patients/participants provided their written informed consent to participate in this study.

## AUTHOR CONTRIBUTIONS

XL designed the experiments, performed the experiments, and analyzed the data. YMC performed the experiments and analyzed the data. HS analyzed the data. YC designed the study and revised the article. All authors critically revised the article, approved the final version, and agreed to be accountable for all aspects of the article.

## FUNDING

This study was supported by the Henan Medical Science and Technology Project (Grant No.: LHGJ2090116).

## SUPPLEMENTARY MATERIAL

The Supplementary Material for this article can be found online at: https://www.frontiersin.org/articles/10.3389/fonc.2022.779356/full#supplementary-material

**Supplementary Figure 1 |** the level of immune cells in tumor tissues that received radiotherapy or not. **(A-B)** Comparison of immune cells estimated by ssGSEA and xCell in tumor tissues with radiotherapy or not. ns: not significant, $^{*}p \leq 0.05$, $^{**}p \leq 0.01$.

**Supplementary Figure 2 |** Immune infiltration of 4 groups. **(A-B)** Infiltration of immune cells estimated by ssGSEA and xCell in 4 groups. **(C-D)** Expression of immune score, stromal score and tumor purity in 4 groups.$^{****}p \leq 0.0001$.

**Supplementary Figure 3 |** Immune profiles in 4 clusters.**(A)** Venn plot shows intersecting of samples in each cluster based on immune infiltration estimated by ssGSEA and xCell.**(B)**Expression profiles of antigen presentation-related genes in 4 clusters. **(C)**Expression profiles of chemokines in 4 clusters.**(D)**Expression profiles of checkpoints in 4 clusters.$^{**}$ $p \leq 0.01$, $^{***}p \leq 0.001$, $^{****}p \leq 0.0001$.

**Supplementary Figure 4 |** Comparison of clinical parameters among the 4 clusters. **(A,B)** Bar charts shows the percentage of clinical stage and histologic grade among 4 clusters.

**Supplementary Figure 5 |** PPI network of DEGs. **(A)** PPI netwok of genes upregulated in cold tumor. **(B)** PPI netwok of genes upregulated in hot tumor.

**Supplementary Figure 6 |** Correlation of KRT23 and immune level. **(A)** Box plot shows the expression of KRT23 between tumor and normal tissue in pan-cancer dataset. **(B)** Correlation of KRT23 and CCL5,CXCL9 and CXCL10.**(C)** Correlation of KRT23 and immune cells.$^{***}p \leq 0.001$.

**Supplementary Figure 7 |** Selection of genes for constructing prediction model. **(A)** Partial likelihood deviance plot. **(B)** Multi-Cox of selected genes by LASSO.**(C-D)** Heatmap showing gene expression of genes in prediction model in training and test cohort.

## REFERENCES

1. Mattiuzzi C, Lippi G. Current Cancer Epidemiology. *J Epidemiol Glob Health* (2019) 9(4):217–22. doi: 10.2991/jegh.k.191008.001
2. Meads MB, Gatenby RA, Dalton WS. Environment-Mediated Drug Resistance: A Major Contributor to Minimal Residual Disease. *Nat Rev Cancer* (2009) 9(9):665–74. doi: 10.1038/nrc2714
3. Lopez MS, Baker ES, Maza M, Fontes-Cintra G, Lopez A, Carvajal JM, et al. Cervical Cancer Prevention and Treatment in Latin America. *J Surg Oncol* (2017) 115(5):615–8. doi: 10.1002/jso.24544
4. Shi X, Wang J, Dai S, Qin L, Zhou J, Chen Y. Apolipoprotein C1 (APOC1): A Novel Diagnostic and Prognostic Biomarker for Cervical Cancer. *Onco Targets Ther* (2020) 13:12881–91. doi: 10.2147/OTT.S280690
5. Somashekhar SP, Ashwin KR. Management of Early Stage Cervical Cancer. *Rev Recent Clin Trials* (2015) 10(4):302–8. doi: 10.2174/1574887110666150923113629
6. Brucker SY, Ulrich UA. Surgical Treatment of Early-Stage Cervical Cancer. *Oncol Res Treat* (2016) 39(9):508–14. doi: 10.1159/000448794
7. Falcetta FS, Medeiros LR, Edelweiss MI, Pohlmann PR, Stein AT, Rosa DD. Adjuvant Platinum-Based Chemotherapy for Early Stage Cervical Cancer. *Cochrane Database Syst Rev* (2016) 11(11):Cd005342. doi: 10.1002/14651858.CD005342.pub4
8. Ferlay J, Steliarova-Foucher E, Lortet-Tieulent J, Rosso S, Coebergh JW, Comber H, et al. Cancer Incidence and Mortality Patterns in Europe: Estimates for 40 Countries in 2012. *Eur J Cancer* (2013) 49(6):1374–403. doi: 10.1016/j.ejca.2012.12.027
9. Chung HC, Ros W, Delord JP, Perets R, Italiano A, Shapira-Frommer R, et al. Efficacy and Safety of Pembrolizumab in Previously Treated Advanced Cervical Cancer: Results From the Phase II KEYNOTE-158 Study. *J Clin Oncol* (2019) 37(17):1470–8. doi: 10.1200/JCO.18.01265
10. Frenel JS, Le Tourneau C, O'Neil B, Ott PA, Piha-Paul SA, Gomez-Roca C, et al. Safety and Efficacy of Pembrolizumab in Advanced, Programmed Death Ligand 1-Positive Cervical Cancer: Results From the Phase Ib KEYNOTE-028 Trial. *J Clin Oncol* (2017) 35(36):4035–41. doi: 10.1200/JCO.2017.74.5471
11. Youn JW, Hur SY, Woo JW, Kim YM, Lim MC, Park SY, et al. Pembrolizumab Plus GX-188E Therapeutic DNA Vaccine in Patients With HPV-16-Positive or HPV-18-Positive Advanced Cervical Cancer: Interim Results of a Single-Arm, Phase 2 Trial. *Lancet Oncol* (2020) 21(12):1653–60. doi: 10.1016/S1470-2045(20)30486-1
12. Hinshaw DC, Shevde LA. The Tumor Microenvironment Innately Modulates Cancer Progression. *Cancer Res* (2019) 79(18):4557–66. doi: 10.1158/0008-5472.CAN-18-3962

13. Arneth B. Tumor Microenvironment. *Medicina (Kaunas)* (2019) 56(1):15. doi: 10.3390/medicina56010015
14. Hanahan D, Weinberg RA. Hallmarks of Cancer: The Next Generation. *Cell* (2011) 144(5):646–74. doi: 10.1016/j.cell.2011.02.013
15. Grivennikov SI, Greten FR, Karin M. Immunity, Inflammation, and Cancer. *Cell* (2010) 140(6):883–99. doi: 10.1016/j.cell.2010.01.025
16. Vitale I, Manic G, Coussens LM, Kroemer G, Galluzzi L. Macrophages and Metabolism in the Tumor Microenvironment. *Cell Metab* (2019) 30(1):36–50. doi: 10.1016/j.cmet.2019.06.001
17. Cassetta L, Pollard JW. Targeting Macrophages: Therapeutic Approaches in Cancer. *Nat Rev Drug Discovery* (2018) 17(12):887–904. doi: 10.1038/nrd.2018.169
18. Xue J, Schmidt SV, Sander J, Draffehn A, Krebs W, Quester I, et al. Transcriptome-Based Network Analysis Reveals a Spectrum Model of Human Macrophage Activation. *Immunity* (2014) 40(2):274–88. doi: 10.1016/j.immuni.2014.01.006
19. Haanen J. Converting Cold Into Hot Tumors by Combining Immunotherapies. *Cell* (2017) 170(6):1055–6. doi: 10.1016/j.cell.2017.08.031
20. Tewari KS, Java JJ, Gatcliffe TA, Bookman MA, Monk BJ. Chemotherapy-Induced Neutropenia as a Biomarker of Survival in Advanced Ovarian Carcinoma: An Exploratory Study of the Gynecologic Oncology Group. *Gynecol Oncol* (2014) 133(3):439–45. doi: 10.1016/j.ygyno.2014.03.013
21. Tan Mbbs Mrcp Frcr Md LT, Tanderup Ph DK, Kirisits Ph DC, de Leeuw Ph DA, Nout Md Ph DR, Duke Mbbs Frcr S, et al. Image-Guided Adaptive Radiotherapy in Cervical Cancer. *Semin Radiat Oncol* (2019) 29(3):284–98. doi: 10.1016/j.semradonc.2019.02.010
22. Bagchi S, Yuan R, Engleman EG. Immune Checkpoint Inhibitors for the Treatment of Cancer: Clinical Impact and Mechanisms of Response and Resistance. *Annu Rev Pathol* (2021) 16:223–49. doi: 10.1146/annurev-pathol-042020-042741
23. Kagabu M, Nagasawa T, Sato C, Fukagawa Y, Kawamura H, Tomabechi H, et al. Immunotherapy for Uterine Cervical Cancer Using Checkpoint Inhibitors: Future Directions. *Int J Mol Sci* (2020) 21(7):2335. doi: 10.3390/ijms21072335
24. Perez-Ruiz E, Melero I, Kopecka J, Sarmento-Ribeiro AB, Garcia-Aranda M, De Las Rivas J. Cancer Immunotherapy Resistance Based on Immune Checkpoints Inhibitors: Targets, Biomarkers, and Remedies. *Drug Resist Update* (2020) 53:100718. doi: 10.1016/j.drup.2020.100718
25. Walboomers JM, Jacobs MV, Manos MM, Bosch FX, Kummer JA, Shah KV, et al. Human Papillomavirus is a Necessary Cause of Invasive Cervical Cancer Worldwide. *J Pathol* (1999) 189(1):12–9. doi: 10.1002/(SICI)1096-9896(199909)189:1<12::AID-PATH431>3.0.CO;2-F
26. Mayadev JS, Enserro D, Lin YG, Da Silva DM, Lankes HA, Aghajanian C, et al. Sequential Ipilimumab After Chemoradiotherapy in Curative-Intent Treatment of Patients With Node-Positive Cervical Cancer. *JAMA Oncol* (2020) 6(1):92–9. doi: 10.1001/jamaoncol.2019.3857
27. Trujillo JA, Sweis RF, Bao R, Luke JJ. T Cell-Inflamed Versus Non-T Cell-Inflamed Tumors: A Conceptual Framework for Cancer Immunotherapy Drug Development and Combination Therapy Selection. *Cancer Immunol Res* (2018) 6(9):990–1000. doi: 10.1158/2326-6066.CIR-18-0277
28. Aran D, Hu Z, Butte AJ. Xcell: Digitally Portraying the Tissue Cellular Heterogeneity Landscape. *Genome Biol* (2017) 18(1):220. doi: 10.1186/s13059-017-1349-1
29. Becht E, Giraldo NA, Lacroix L, Buttard B, Elarouci N, Petitprez F, et al. Erratum to: Estimating the Population Abundance of Tissue-Infiltrating Immune and Stromal Cell Populations Using Gene Expression. *Genome Biol* (2016) 17(1):249. doi: 10.1186/s13059-016-1113-y
30. Li T, Fan J, Wang B, Traugh N, Chen Q, Liu JS, et al. TIMER: A Web Server for Comprehensive Analysis of Tumor-Infiltrating Immune Cells. *Cancer Res* (2017) 77(21):e108–10. doi: 10.1158/0008-5472.CAN-17-0307
31. Newman AM, Liu CL, Green MR, Gentles AJ, Feng W, Xu Y, et al. Robust Enumeration of Cell Subsets From Tissue Expression Profiles. *Nat Methods* (2015) 12(5):453–7. doi: 10.1038/nmeth.3337
32. Subramanian A, Tamayo P, Mootha VK, Mukherjee S, Ebert BL, Gillette MA, et al. Gene Set Enrichment Analysis: A Knowledge-Based Approach for Interpreting Genome-Wide Expression Profiles. *Proc Natl Acad Sci USA* (2005) 102(43):15545–50. doi: 10.1073/pnas.0506580102
33. Wang J, Li Z, Gao A, Wen Q, Sun Y. The Prognostic Landscape of Tumor-Infiltrating Immune Cells in Cervical Cancer. *BioMed Pharmacother* (2019) 120:109444. doi: 10.1016/j.biopha.2019.109444
34. Galon J, Bruni D. Approaches to Treat Immune Hot, Altered and Cold Tumours With Combination Immunotherapies. *Nat Rev Drug Discov* (2019) 18(3):197–218. doi: 10.1038/s41573-018-0007-y
35. Zhang Y, Yu M, Jing Y, Cheng J, Zhang C, Cheng L, et al. Baseline Immunity and Impact of Chemotherapy on Immune Microenvironment in Cervical Cancer. *Br J Cancer* (2021) 124(2):414–24. doi: 10.1038/s41416-020-01123-w
36. Demaria S, Coleman CN, Formenti SC. Radiotherapy: Changing the Game in Immunotherapy. *Trends Cancer* (2016) 2(6):286–94. doi: 10.1016/j.trecan.2016.05.002
37. Gomes-Silva D, Ramos CA. Cancer Immunotherapy Using CAR-T Cells: From the Research Bench to the Assembly Line. *Biotechnol J* (2018) 13(2):10.1002/biot.201700097. doi: 10.1002/biot.201700097
38. Morgan JB, Wheeler TL, Koohmaraie M, Crouse JD, Savell JW. Effect of Castration on Myofibrillar Protein Turnover, Endogenous Proteinase Activities, and Muscle Growth in Bovine Skeletal Muscle. *J Anim Sci* (1993) 71(2):408–14. doi: 10.2527/1993.712408x
39. Obeid M, Tesniere A, Ghiringhelli F, Fimia GM, Apetoh L, Perfettini JL, et al. Calreticulin Exposure Dictates the Immunogenicity of Cancer Cell Death. *Nat Med* (2007) 13(1):54–61. doi: 10.1038/nm1523
40. Zitvogel L, Kepp O, Kroemer G. Decoding Cell Death Signals in Inflammation and Immunity. *Cell* (2010) 140(6):798–804. doi: 10.1016/j.cell.2010.02.015
41. Kurokawa I, Takahashi K, Moll I, Moll R. Expression of Keratins in Cutaneous Epithelial Tumors and Related Disorders–Distribution and Clinical Significance. *Exp Dermatol* (2011) 20(3):217–28. doi: 10.1111/j.1600-0625.2009.01006.x
42. Zhang JS, Wang L, Huang H, Nelson M, Smith DI. Keratin 23 (K23), a Novel Acidic Keratin, is Highly Induced by Histone Deacetylase Inhibitors During Differentiation of Pancreatic Cancer Cells. *Genes Chromosomes Cancer* (2001) 30(2):123–35. doi: 10.1002/1098-2264(2000)9999:9999<::AID-GCC1070>3.0.CO;2-W
43. Ren M, Gao Y, Chen Q, Zhao H, Zhao X, Yue W. The Overexpression of Keratin 23 Promotes Migration of Ovarian Cancer *via* Epithelial-Mesenchymal Transition. *BioMed Res Int* (2020) 2020:8218735. doi: 10.1155/2020/8218735
44. Mei J, Xing Y, Lv J, Gu D, Pan J, Zhang Y, et al. Construction of an Immune-Related Gene Signature for Prediction of Prognosis in Patients With Cervical Cancer. *Int Immunopharmacol* (2020) 88:106882. doi: 10.1016/j.intimp.2020.106882
45. Chen Q, Qiu B, Zeng X, Hu L, Huang D, Chen K, et al. Identification of a Tumor Microenvironment-Related Gene Signature to Improve the Prediction of Cervical Cancer Prognosis. *Cancer Cell Int* (2021) 21(1):182. doi: 10.1186/s12935-021-01867-2
46. Ding H, Fan GL, Yi YX, Zhang W, Xiong XX, Mahgoub OK. Prognostic Implications of Immune-Related Genes' (IRGs) Signature Models in Cervical Cancer and Endometrial Cancer. *Front Genet* (2020) 11:725. doi: 10.3389/fgene.2020.00725
47. Yang X, Yin F, Liu Q, Ma Y, Zhang H, Guo P, et al. Ferroptosis-Related Genes Identify Tumor Immune Microenvironment Characterization for the Prediction of Prognosis in Cervical Cancer. *Ann Transl Med* (2022) 10(2):123. doi: 10.21037/atm-21-6265

**Conflict of Interest:** The authors declare that the research was conducted in the absence of any commercial or financial relationships that could be construed as a potential conflict of interest.

The reviewer IB declared a shared parent affiliation with the authors to the handling editor at the time of review.

frontiers | Frontiers in Oncology

ORIGINAL RESEARCH
published: 29 June 2022
doi: 10.3389/fonc.2022.846786

# Identification of Novel Tumor Microenvironment Regulating Factor That Facilitates Tumor Immune Infiltration in Cervical Cancer

*Jingjing Xu*[1,2,3], *Zhe Huang*[4], *Yishu Wang*[5], *Zhenxian Xiang*[1,2,3] *and Bin Xiong*[1,2,3]*

*[1] Department of Gastrointestinal Surgery & Department of Gastric and Colorectal Surgical Oncology, Zhongnan Hospital of Wuhan University, Wuhan, China, [2] Hubei Key Laboratory of Tumor Biological Behaviors, Wuhan, China, [3] Hubei Cancer Clinical Study Center, Wuhan, China, [4] Department of Electrical and Computer Engineering, University of Illinois at Urbana-Champaign, Urbana, IL, United States, [5] Department of Legal English and TOEIC, Adelaide University, North Terrace, SA, Australia*

Cervical cancer is one of the most common gynecologic malignancies and one of the leading causes of cancer-related deaths in women worldwide. There are more than 30 categories of human papillomavirus infections in the genital tract. The recently discovered immune checkpoint suppression is a potential approach to improve clinical outcomes in these patients by altering immune cell function. However, many questions remain unanswered in terms of this method. For example, the proportion of responders is limited and the exact mechanism of action is uncertain. The tumor microenvironment (TME) has long been regarded as having nonnegligible influence on effectiveness of immunotherapy. The programmed cell death protein 1 (PD-1) pathway has received much attention due to its involvement in activating T-cell immune checkpoint responses. Since tumor cells may evade immune detection and become highly resistant to conventional treatments, anti-PD-1/PD-L1 antibodies are preferred as a kind of cancer treatment and many have just been licensed. To provide a theoretical basis for the development of new therapies, investigating the effect of tumor microenvironment on the prognosis of cervical cancer is necessary. In this work, immunological scores obtained from the ESTIMATE algorithm were used to differentiate between patients with high and low immune cell infiltration. We identified 11 immunologically significant differentially expressed genes (DEGs). For example, CXCR3 was found to be an important factor in $CD8^+$ T cell recruitment and tumor immunological infiltration in cervical cancer. These results may lead to novel directions of understanding complex interactions between cancer cells and the tumor microenvironment, as well as new treatment options for cervical cancer.

**Keywords: CXCR3, tumor microenvironment, estimate, CIBERSORT, PD-1, cervical cancer**

**Edited by:**
*Gang Chen,*
*Huazhong University of Science and Technology, China*

**Reviewed by:**
*Arutha Kulasinghe,*
*The University of Queensland, Australia*
*Saumya Pandey,*
*IndiraIVF Hospital, India*

***Correspondence:**
*Bin Xiong*
*binxiong1961@whu.edu.cn*

**Specialty section:**
*This article was submitted to Gynecological Oncology, a section of the journal Frontiers in Oncology*

**Received:** *31 December 2021*
**Accepted:** *02 June 2022*
**Published:** *29 June 2022*

**Citation:**
*Xu J, Huang Z, Wang Y, Xiang Z and Xiong B (2022) Identification of Novel Tumor Microenvironment Regulating Factor That Facilitates Tumor Immune Infiltration in Cervical Cancer. Front. Oncol. 12:846786. doi: 10.3389/fonc.2022.846786*

---

**Abbreviations:** TME, tumor microenvironment; CESC, cervical squamous cell carcinoma and endocervical adenocarcinoma; PPI, protein–protein interaction; DEG, differentially expressed gene; CXCR3, CXC chemokine receptor-3; GSEA, Gene Set Enrichment Analysis; TIC, tumor-infiltrating immune cell; TIL, tumor-infiltrating lymphocyte.

# INTRODUCTION

Cervical cancer is a type of gynecological cancer very harmful to women's health (1, 2). Human papillomavirus (HPV) infection, smoking, and a compromised immune system are all risk factors for cervical cancer (3, 4). Because persistent HPV infection is associated with immune system dysfunction and the development of cervical cancer (5), cervical cancer is a promising target audience for treatment through the use of immunotherapeutic means (6). Various immunomodulatory therapies, such as bacterial vaccine vectors and T-cell therapies, have been investigated. In the case of recurrence or metastasis, immune checkpoint inhibition in combination with chemoradiotherapy for definitive treatment shows potential (7, 8). Therefore, it is crucial to investigate the oncogenic process and treatment of cervical cancer.

The significance of the tumor microenvironment (TME) in tumor development is evidenced by an increasing number of studies (6). Collaboration between cancer cells and their supporting cells, such as immortal proliferation, resistance to apoptosis, and evasion of immune surveillance, influences the malignant phenotype of cancer (9). Thus, TME has a significant impact on the therapeutic response and clinical prognosis of cancer patients (10, 11). Cervical cancer is a HPV-related cancer, and the tumor microenvironment (TME) plays an important role in its progression. Tumor epithelial cells and other tumor-supporting cells such as immune cells, fibroblasts, immunosuppressive cells, adipocytes, endothelial cells, and pericytes constitute the tumor microenvironment, which is a complex and dynamic biome (12). To promote tumor angiogenesis, proliferation, invasion, and metastasis, and to dictate treatment-resistant activities, cancer cells rapidly attract supporting cells from the surrounding endogenous host stroma (13). Tumor-infiltrating immune cells (TICs) are promising prognostic indicators because they are closely associated with tumor growth (14). TICs are crucial in cervical cancer prognosis and are associated with overall survival (15). The CXCL10/CXCR3 signaling pathway regulates leukocyte trafficking and angiogenesis through paracrine interactions between tumor and stromal cells (16). Through the JAK and STAT signaling pathways, CXCL10-CXCR3 is hypothesized to regulate PD-L1 synthesis in fibroblasts (17). Activation of PD-L1/PD-1 poses great difficulties for cancer therapy (18), which is often associated with cytotoxic T lymphocyte malfunction. In patients with gynecologic malignancies, elevated PD-L1 expression may be a useful biomarker for predicting clinical outcomes (19, 20). Based on these findings, adaptive immunity in the tumor microenvironment is crucial for cervical cancer treatment. Therefore, it is difficult to find precise genetic tests to determine the dynamic regulation of immune and stromal components in the TME.

How different cell types affect regulation of TME was highlighted by transcriptome sequencing patterns and functional genomics analysis. The number of TICs and the proportion of immune and stromal components in CESC samples from The Cancer Genome Atlas (TCGA) database were calculated using ESTIMATE and CIBERSORT algorithms in the R software. A predictive biomarker, CXC chemokine receptor-3 (CXCR3), was identified. The chemokine receptor CXCR3 has three different ligands. Three alternative CXCLs exist, which are CXCL9, CXCL10, and CXCL11 (21). In the tumor microenvironment, CXCL10 has been revealed to have anti-malignant properties. According to the recent study, elevated PD-L1 expression *via* the CXCL10-CXCR3 axis improves viral latency and immune evasion of fibroblasts (17). Therefore, CXCR3 may participate in CESC TME and immunotherapy. By examining differentially expressed genes (DEGs) generated by immune and stromal components in CESC samples, we found that CXCR3 may be a viable biomarker for TME alteration and immunotherapeutic status in CESC. The tumor microenvironment is largely thought of as immunosuppressive, leading to $CD8^+$ T lymphocyte dysfunction and thus promoting tumor development. The presence of high concentrations of $CD8^+$ T cells in tumor tissue is a positive prognostic indicator in many cancers. Blockade of the suppressive programmed cell death 1 (PD-1) pathway produces a therapeutic response in a variety of tumor types (22). At the same time, the majority of patients do not respond or have disease recurrence, necessitating additional studies (23). Recent studies found the CXCR3 chemokine system is a biomarker of PD-1 blockade sensitivity, and increasing the intratumoral activity of this chemokine system may improve treatment efficacy (24). However, only a proportion of patients respond to PD-1 immune checkpoint blockade, emphasizing the need for a better understanding of the underlying mechanisms of PD-1-inhibitor-mediated enhancement of the anti-tumor $CD8^+$ T cell response (25). Finding new ways to understand how cancer interacts with the tumor microenvironment can lead to discoveries which can be used to generate prognostic assessments and clinical treatment options.

# MATERIALS AND METHODS

## Raw Data

The TCGA database was accessed to obtain transcriptomic RNA-seq data and clinical data from 309 CESC patients (normal samples, 3 cases; tumor samples, 306 cases). (https://portal.gdc.cancer.gov/).

## Generation of ImmuneScore, StromalScore, and ESTIMATEScore

The ESTIMATE algorithm uses the estimation package installed in R language version 4.1.0 to estimate the immune and stromal components of the TME for each sample, expressed as three scores. The total proportion of immune, stromal and both components of the TME was positively correlated with Immunocore, StromalScore, and ESTIMATEScore, which means the higher the correlation value, the higher the proportion of the corresponding component of the TME.

## Survival Analysis

Analyses were performed using the survival and survminer packages loaded with the R language, as well as the Kaplan-

Meier plotter website (https://kmplot.com/analysis/index.php?p=service&cancer=pancancer_rnaseq). For survival analysis, exact survival ranging from 0 to 17.6 years was recorded for all tumor samples. Statistical significance was determined using the log-rank test, and $p<0.05$ was considered significant. To create survival curves, the Kaplan-Meier method was utilized, and the log-rank test was performed to determine statistical significance.

### Generation of DEGs Between High-Score and Low-Score Groups Regarding ImmuneScore and StromalScore

The dataset of 306 tumor samples were classified as high or low scoring based on comparison with the median immune and stromal scores. Differential gene expression analysis was performed using the limma package, and DEGs were constructed by comparing samples with high and low scores. After logarithmic (high group/low group) transformation, DEGs with a change greater than 1 and false discovery rate (FDR) less than 0.05 were judged to be significant.

### Heatmaps

The pheatmap package in the R language was used to construct heatmaps of stromal and immune DEGs.

### Difference Analysis of Scores With Clinical Stages

The TCGA database was used to collect the clinicopathological characteristics of the CESC samples. The study was carried out in the R language. Depending on the number of clinical stages, the Wilcoxon rank-sum or the Kruskal-Wallis rank-sum test was used to determine significance.

### GO and KEGG Enrichment Analysis and PPI Network Construction of DEGs

GO and KEGG enrichment analysis was performed on 425 DEGs using R language with packages clusterProfiler, enrichplot, and ggplot2. Results were considered significantly enriched at a significance threshold p of 0.05. The STRING database (https://string-db.org/) was used for online PPI network analysis. These protein interaction data were imported using Cytoscape version 3.8.0. Nodes with an interaction confidence level greater than 0.95 were used to build the network.

### COX Regression Analysis

Survival package for univariate COX regression are available in R. Univariate Cox regression analysis was conducted to explore the impact of each gene on overall survival. The top 114 genes for univariate COX are displayed in the graph, arranged by p-value from the lowest to the highest.

### Gene Set Enrichment Analysis

Gene Set Enrichment Analysis (GSEA) is a method for interpreting biological meaning of a list of genes by the analysis of the overlaps with various previously defined gene sets (26). Kegg.v7.3.symbols.gmt were downloaded from Molecular Signatures Database as the target sets using the software GSEA 4.0.3 downloaded from Broad Institute. Only the gene sets with NOM $p<0.05$ were considered to be significant after the whole transcriptome of all tumor samples were applied by GSEA.

### TICs Profile

Using the CIBERSORT, a method for characterizing the abundances of member cell types in a mixed cell population from their gene expression profiles (27), the TIC abundance profiles of all tumor samples were analyzed, and only 250 tumor samples with a $p<0.05$ were chosen for further investigation using quality filtering.

## RESULTS

### Analysis Process of This Study

**Figure 1** depicts the analytical approach in our study. To assess the proportion of TICs and the number of immune and stromal components in the CESC samples, we extracted transcriptomic RNA-seq data from the TCGA database for 309 patients using the CIBERSORT and ESTIMATE techniques. The ESTIMATE algorithm is a method for estimating the proportion of TICs and the amount of immune and stromal component in CESC samples. A PPI network and univariate COX regression analysis were created using DEGs shared by ImmuneScore and StromalScore, and intersection analysis were performed using the core nodes of the PPI network and the top prognostic genes obtained from the univariate COX regression analysis. After obtaining 11 genes, we conducted a series of studies on CXCR3, including survival and COX regression, Gene Set enrichment analysis (GSEA), as well as association with TICs.

### Scores Were Correlated With the Survival of CESC Patients

To study the correlation between immune and stromal component ratios and the survival rate, survival analysis was used for ImmuneScore, StromalScore, and ESTIMATEScore respectively. The estimated higher score in ImmuneScore or StromalScore represents the larger amount of the immune or stromal component ratios in TME. ESTIMATEScore is the sum of ImmuneScore and StromalScore denoting the comprehensive component ratio of both of them in TME. As shown in **Figures 2A, B**, ESTIMATEScore and StromalScore had no significant correlation with the overall survival rate. ESTIMATEScore still showed positive correlation with the survival rate (**Figure 2C**). These results implied that the immune and stromal components in TME were significant for indicating the prognosis of CESC patients.

### Scores Were Associated With the Clinicopathological Features of CESC Patients

Clinical data from CESC patients in the TCGA database were analyzed to study the correlation between immune and stromal component ratios and clinicopathological features. We analyzed the correlation of grade, TNM stages M classification, N classification, age, as well as T classification with

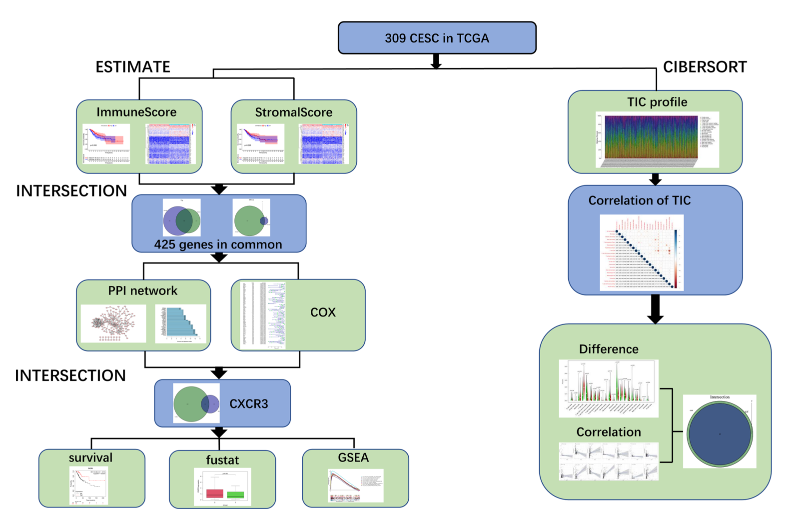

**FIGURE 1** | Analysis workflow of this study.

ImmuneScore (**Figures 3A–E**), StromalScore (**Figure 3F–J**) and ESTIMATEScore (**Figures 3K–O**). StromalScore and ESTIMATEScore were found to be negatively correlated with M classification of TNM stages (**Figure 3G**, p=0.046 and **Figure 3L**, p=0.022, respectively). The ratio of immunological and stromal components was related to the development of CESC, such as invasion and metastasis, as shown in **Figures 3G, L** (p=0.046 and p=0.022, respectively).

## Identification and Functional Analysis of DEGs

The specific alterations of gene profiles associated with immunological and stromal components in TME were discovered by a comparative investigation of high-scoring and low-scoring samples. In contrast to the median, ImmuneScore (high vs. low scoring samples) yielded a total of 1067 DEGs, with 643 genes upregulated and 424 genes downregulated (**Figures 4A–D**). Similarly, StromalScore identified 947 genes, of which 917 were up-regulated and 30 were down-regulated (**Figures 4A–D**). The Venn diagram's intersection analysis shows that 408 up-regulated genes had higher ImmuneScore and higher StromalScore, whereas 17 down-regulated genes had lower scores. These DEGs may be used to assess the status (425 genes in total). These results closely matched immune-related GO terms, such as the interaction of hematopoietic cell lines and viral proteins with cytokines and cytokine receptors, according to gene ontology (GO) enrichment analyses (**Figure 4E**). Natural killer cell-mediated cytotoxicity, S. aureus infection, B-cell receptor signaling pathways, and T-cell receptor signaling pathways were also discovered by KEGG enrichment analysis (**Figure 4F**). As a result, overall function of DEGs appears to engage in immune-related activities, showing that immunological factors are a key aspect of TME in CESC.

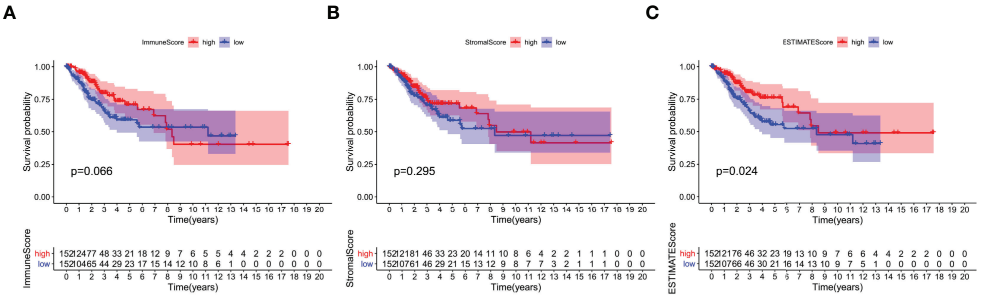

**FIGURE 2** | Correlation of scores with the survival of patients with CESC. **(A)** Kaplan–Meier survival analysis for CESC patients grouped into high or low score in ImmuneScore determined by the comparison with the median. p = 0.066 by log-rank test. **(B)** Kaplan–Meier survival curve for StromalScore with p = 0.0295 by log-rank test. **(C)** Survival analysis with Kaplan–Meier method for CESC patients grouped by ESTIMATEScore (p = 0.024 by log-rank test).

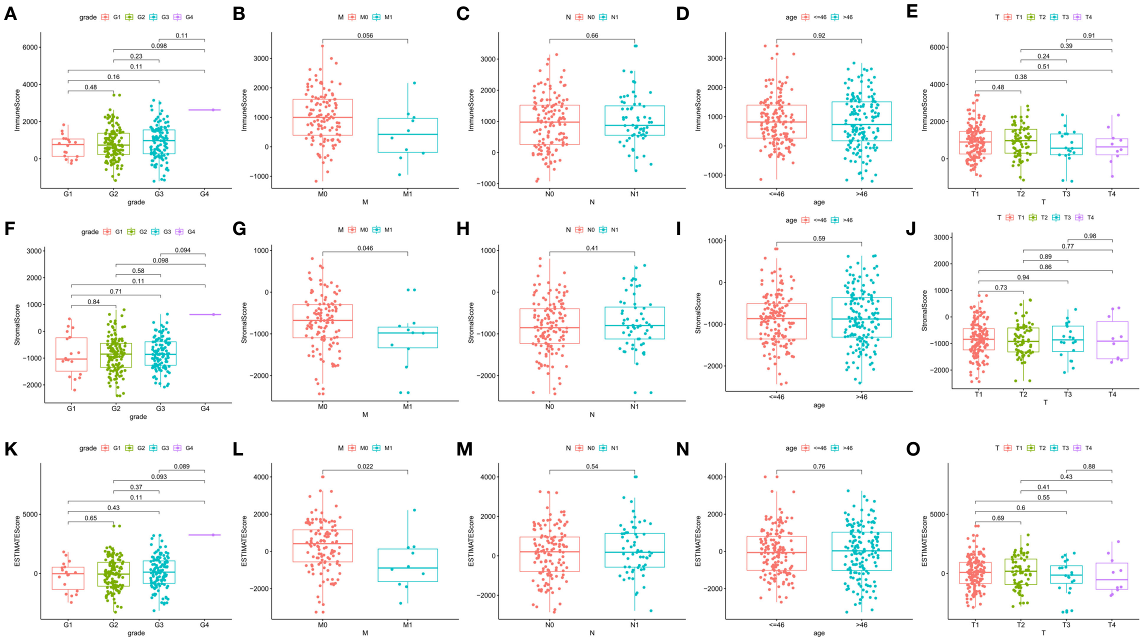

**FIGURE 3** | Correlation of ImmuneScore and StromalScore with clinicopathological staging characteristics. **(A–E)** Distribution of ImmuneScore in grade, M, N, age, and T classification. The p value is calculated by Kruskal–Wallis rank sum test. **(F–J)** Distribution of StromalScore in grade, M, N, age, and T classification. The p value is calculated by Kruskal–Wallis rank sum test. **(K–O)** Distribution of ESTIMATEScore in grade, M, N, age, and T classification. The p value is calculated by Kruskal–Wallis rank sum test.

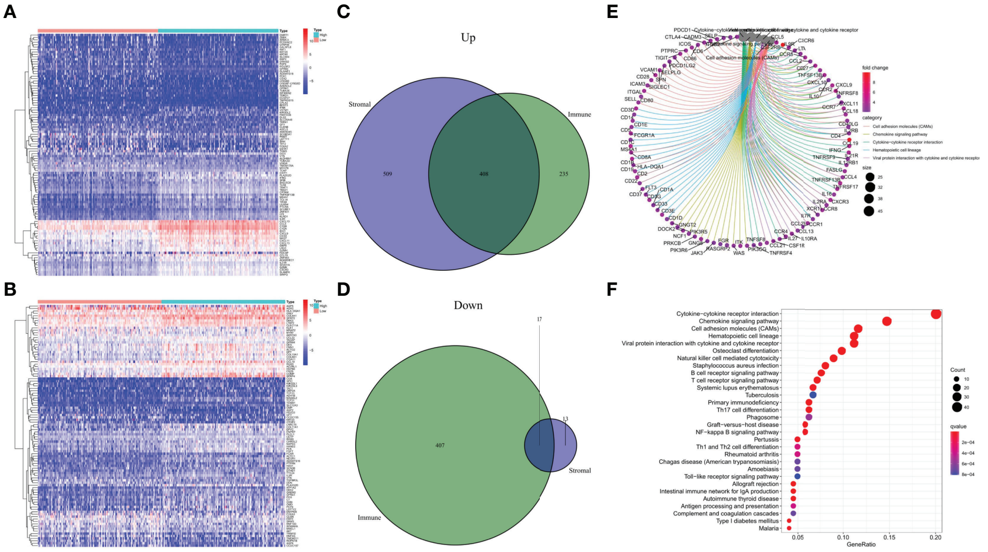

**FIGURE 4** | Heatmaps, Venn plots, and enrichment analysis of GO and KEGG for DEGs. **(A)** Heatmap for DEGs generated by comparison of the high score group vs. the low score group in ImmuneScore. Row name of heatmap is the gene name, and column name is the ID of samples which not shown in plot. Differentially expressed genes were determined by Wilcoxon rank sum test with q = 0.05 and fold-change>1 after log2transformation as the significance threshold. **(B)** Heatmap for DEGs in StromalScore, similar with **(A)**. **(C, D)** Venn plots showing common up-regulated and down-regulated DEGs shared by ImmuneScore and StromalScore, $p < 0.05$ and fold-change>1 after $\log_2$ transformation as the DEGs significance filtering threshold. **(E, F)** GO and KEGG enrichment analysis for 425 DEGs, terms with $p < 0.05$ were believed to be enriched significantly.

## Intersection Analysis of PPI Network and Univariate COX Regression

To examine the underlying mechanisms of the correlation of the genes, we used Cytoscape software to establish a PPI network based on the STRING database. As shown in **Figure 5A**, 425 genes interacted with each other, and the top 30 genes, ranked by several nodes, are represented as a histogram (**Figure 5B**). We used univariate COX regression analysis on the survival of CESC patients to find the top prognostic genes among the 425 DEGs (**Figure 5C**). Only 11 genes, CD3E, CCR2, CD28, BTK, CD3D, CD79A, CD79B, CXCR3, ITK, CCR7, and CD3G, were identified to overlap in a intersection analysis between the leading nodes in the PPI network and the top 104 genes ordered by p-value in the univariate COX model (**Figure 5D**).

## The Correlation of CXCR3 Expression With the Survival in CESC Patients and the Potential to Be an Indicator of TME Modulation

The tumor microenvironment is immunosuppressive, and contributes to tumor growth by causing the malfunction of CD8$^+$ T cells. According to CXCR3 analysis, CXCR3 expression was significantly higher in tumor samples than in normal samples (**Figure 6A**). Based on the median CXCR3 expression, all CESC samples were divided into two groups, high expression of CXCR3 and low expression of CXCR3. According to our study, CESC patients with high CXCR3 expression lived longer than those with low CXCR3 expression (**Figure 6B**). The final clinical characterization study yielded similar results, with greater CXCR3 expression in patients who were alive (**Figure 6C**). According to the results of the study, CXCR3 expression in TME was associated with a better prognosis in CESC patients. This may be due to the anti-tumor response of CXCR3-signaling CD8$^+$ T cells in the tumor microenvironment, which leads to a better prognosis of patients (23). This may explain why CXCR3 expression is higher in cervical cancer, but it may also indicate a better prognosis for patients with cervical cancer. Since the level of CXCR3 was favorably associated with the survival of CESC patients, GSEA was used to respectively compare the samples of CXCR3 expression in the high and low expression groups. As shown in **Figure 6D**, the CXCR3 high presentation group was enriched in antigen processing and presentation, B-cell receptor signaling, chemokine signaling, natural killer cell-mediated cytotoxicity, T-cell receptor signaling, and toll-like receptor signaling. In the CXCR3 low expression group, genes related to metabolic pathways such as biosynthesis of unsaturated fatty acids, glycosaminoglycan biosynthesis, keratin sulfate, and O-glycan biosynthesis were identified (**Figure 6E**). These results suggest that CXCR3 may be used as an indicator of TME status.

## Correlation of CXR3 With the Proportion of TICs

The fraction of tumor-infiltrating immune subpopulations was determined using CIBERSORT, and 21 different types of immune cells in tumor tissues were created to further support the link between CXCR3 expression and the TME (**Figure 7**). As detailed below, the differences and correlations were studied.

According to differential and correlation analyses, CXCR3 expression was linked to a total of 13 TICs (**Figure 8**). M1 macrophages, resting mast cells, plasma cells, activated memory CD4$^+$ T cells, CD8$^+$ T cells, T follicular helper cells, gamma-delta

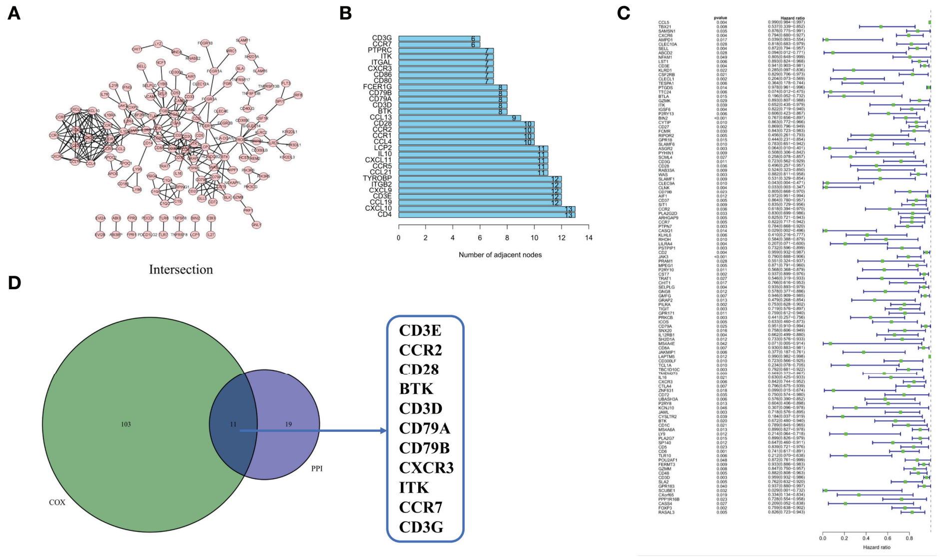

**FIGURE 5** | Protein–protein interaction network and univariate COX. **(A)** Interaction network constructed with the nodes with interaction confidence value > 0.95. **(B)** The top 30 genes ordered by the number of nodes. **(C)** Univariate COX regression analysis with 425 DEGs, listing the top significant factors with p < 0.05. **(D)** Venn plot showing the common factors shared by leading 30 nodes in PPI and top significant factors in univariate COX.

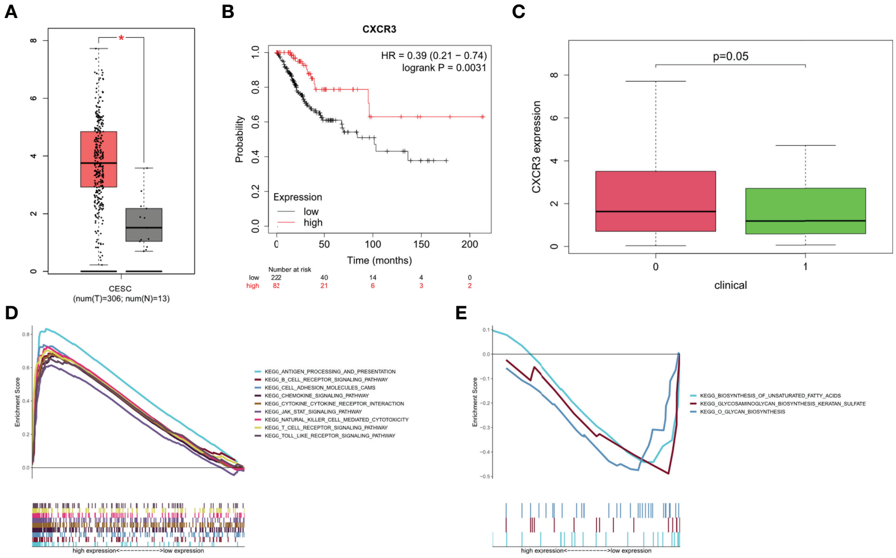

**FIGURE 6** | Survival analysis, clinical characteristics and GSEA for samples with high CXCR3 expression and low expression of CESC patients. **(A)** Differentiated expression of CXCR3 in the normal and tumor sample. **(B)** Survival analysis for CESC patients with different CXCR3 expression. Patients were labeled with high expression or low expression. **(C)** The correlation of CXCR3 expression with survival stage(fustat: 0 = survival, 1 = death). **(D)** Enriched gene sets in KEGG of high CXCR3 expression. Only several leading gene sets are shown in plot. **(E)** Enriched gene sets in KEGG by the low CXCR3 expression.

(γδ) T cells, and regulatory T cells (Tregs) were found to be positively correlated with CXCR3 expression. Five TICs, including activated dendritic cells, eosinophils, M0 macrophages, activated mast cells, and resting memory CD4$^+$T cells, were found to be negatively correlated with CXCR3 expression. These findings back up the hypothesis that CXCR3 levels impact TME immune activation.

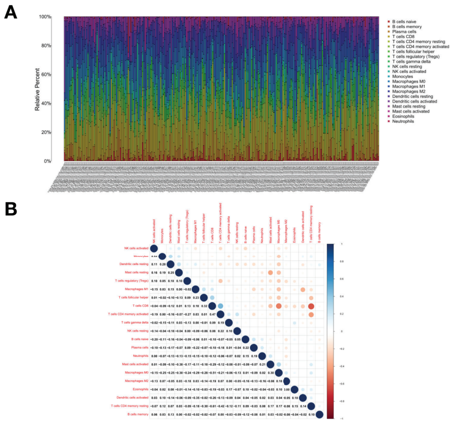

**FIGURE 7** | TIC profile in tumor samples and correlation analysis. **(A)** Barplot showing the proportion of 21 kinds of TICs in CESC tumor samples. Column names of plot were sample ID. **(B)** Heatmap showing the correlation between 21 kinds of TICs and numeric in each tiny box indicating the p value of correlation between two kinds of cells. The shade of each tiny color box represented corresponding correlation value between two cells, and Pearson coefficient was used for significance test.

## DISCUSSION

The purpose of this study is to seek for genes associated with TME that affect survival and TNM staging in CESC patients in the TCGA database. Based on a series of bioinformatic studies, CXCR3 may be an indicator of TME status in CESC patients. The immune system function is associated with CXCR3 (28). Future work can be focused on helping modify the therapeutic purpose of TME and the relationship between TME and tumors (29). The role of the immune microenvironment in cancer has been demonstrated in several studies. According to our transcriptome analysis on the CESC data in the TCGA database, the immune component of TME has an impact on patient prognosis. In particular, the ratio of immune and stromal components in TME was found to be strongly associated with the development of CESC including invasion and metastasis. These findings shed light on the importance of studying tumor-immune cell interactions as they provide new insights into how to develop more effective therapeutic options (30).

It is crucial to have a comprehensive understanding of the complex interplay of receptors-cell death cascades in inflammatory tumor microenvironment in cervical cancer (31). Previous research has shown that immunogenic cell death and cancer stem cells-related innovative clinical and translational research provided patients a boon in targeted immunotherapy in gynecologic malignancies including cervical cancer as well as other inflammatory cancers (32, 33). PD-L1 is an important suppressive immune receptor involved in the immunosuppression of cancer (34). Recent studies have found that PD-L1 is overexpressed in cervical cancer and its knockdown reduces the proliferation, invasiveness, and

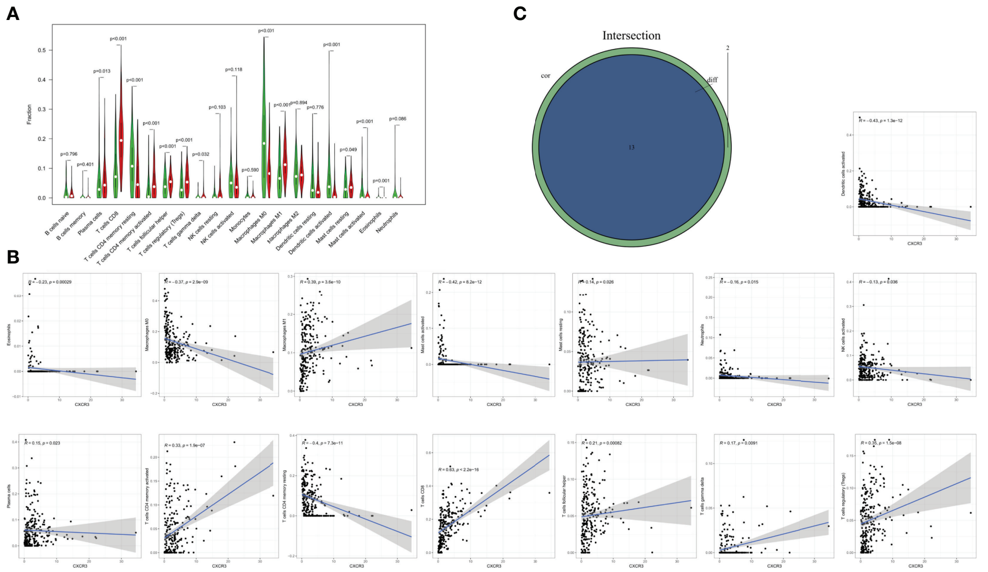

**FIGURE 8** | Correlation of TICs proportion with CXCR3 expression. **(A)** Violin plot showed the ratio differentiation of 21 kinds of immune cells between CESC tumor samples with low or high CXCR3 expression relative to the median of CXCR3 expression level, and Wilcoxon rank sum was used for the significance test. **(B)** Scatter plot showed the correlation of 15 kinds of TICs proportion with the CXCR3 expression ($p<0.05$). The blue line in each plot was fitted linear model indicating the proportion tropism of the immune cell along with CXCR3 expression, and Pearson coefficient was used for the correlation test. **(C)** Venn plot displayed 13 kinds of TICs correlated with CXCR3 expression codetermined by difference and correlation tests displayed in violin and scatter plots, respectively.

oncogenicity of cervical cancer cells (35). Three chemokine ligands of CXCR3 are CXCL9, CXCL10, and CXCL11 (21). CXCL10 has been regarded as having an anti-malignant role in the tumor microenvironment (36). According to recent work, the CXCL10-CXCR3 axis enhances viral latency and immune evasion of fibroblasts through upregulation of PD-L1 expression (17). Thus, CXCR3 may be a part of CESC TME and immunotherapy. The CXCR3 chemokine system was found to be a biomarker of PD-1 blockade sensitivity in recent studies, and therapeutic efficacy may be improved by enhancing the intratumoral activity of this chemokine system (24). Therefore, we investigated the association between CXCR3 expression and TME. According to GSEA data, immune-related signaling pathways were significantly enriched in the CXCR3 high expression group, including natural killer cell-mediated cytotoxicity, S. aureus infection, B-cell receptor signaling pathway, and T-cell receptor signaling pathway. The CXCR3 low expression group regarding unsaturated fatty acid production, glycosaminoglycan biosynthesis, keratin sulfate, and O-glycan biosynthesis were enriched. Based on these findings, we argue that CXCR3 may function in the immunity and metabolism of TME.

In this work, a fraction of TICs was analyzed using CIBERSORT, and a good association between CD8$^+$ T cells and CXCR3 expression was found in CESC patients. For some malignancies, the presence of a high number of CD8$^+$ T lymphocytes in the tumor tissue is a good prognostic signal (37). There are some studies focused on the application of prognostic and therapeutic TILs in cervical cancer. A study compared lymphocytes in cervical tissues from 19 patients with CIN and from 20 patients with normal cervices. The proportion of CD8$^+$ T cells is significantly increased in the dysplastic tissue, which clearly indicates that a higher density of CD8$^+$ TILs are positively associated with the progress of cervical cancer (38). A systematic review with meta-analysis on the prognostic significance of TILs showed that CD8$^+$ lymphocytes had a positive effect on patient overall survival (OS) of cervical cancer with a hazard ratio (HR) of 0.71, indicating that CD8$^+$ TILs have prognostic values for not only cancer progression but also patient OS (39). A finding from phase II trials indicates that TILs therapy may prove an efficacious option for cervical cancer. The treatment was among 27 patients with metastatic cervical carcinoma refractory to the standard of care. This response was seen sustainedly in patients whose disease was refractory to standard treatment (40, 41). CXCR3 seems to be important for maintaining the immune activity of TME, as there is a positive correlation between CD8$^+$ T cell numbers and CXCR3 expression in CESC patients (42). Based on the increase in CD8$^+$ T cells, CXCR3 may have antitumor efficacy in CESC. These molecular analyses at the tissue and cell level could reveal the cellular status of TME, but information related to spatial-level cellular distribution, co-organization, and cell-cell interaction is insufficient in the TME (43). Deep spatial analysis is capable of unraveling tumor evolutionary trajectories as well as geospatial evolution in cell populations and their expression signatures (44). In cervical tumors, spatial analysis data could map the spatial relationships between different cell phenotypes. Spatial analysis is able to distinguish different cell populations that play specific roles in activation and regulation close to the malignant cells, suggesting that those cells can play specific roles according to their distribution. As is reported in lung adenocarcinoma, the close proximity and interaction between malignant cells and T-cells expressing PD-L1 and PD-1 suggest that cytotoxic T-cells actively interface with the malignant cells and may increase the risk of tumor recurrence in those patients (45). Recent study provides functional and spatial analysis of immune cells in the Lymphocyte-rich classic Hodgkin lymphoma (LR-CHL) microenvironment at single-cell resolution. It identifies a unique $CD4^{+}PD\text{-}1^{+}CXCL13^{+}CXCR5^{-}$ TFH-like subset that surrounds Hodgkin Reed-Sternberg (HRS) cells, appears in close proximity to $CXCR5^{+}$ B cells, and is associated with poor clinical outcome. This finding suggests the pathogenic mechanism of the CXCL13/CXCR5 axis and $PD\text{-}1^{+}CXCL13^{+}$ T cells as a treatment target in LR-CHL. This reveals that the expression profiles of CXC motif cytokines and their receptors have a crucial impact in the TME and patient prognosis at the tumor spatial-level. Several studies showed that checkpoint blockades targeting PD-1/PD-L1 pathways have achieved efficient clinical responses by suppressing cancer progression and improving survival in cervical cancer (46). We can infer that CXCL10/CXCR3 axis and $PD\text{-}1^{+}CXCL10^{+}$ T cells may also play specific roles corresponding to their distribution in cervical cancer. Therefore, more studies are needed to determine the precision of combining CXCR3 expression, tumor-infiltrating T-cell isoforms, and anti-PD-1/PD-L1 treatment response in patients with cervical cancer. In addition, we need to validate the findings of the study through experiments *in vitro* and *in vivo*. We also should admit that the TCGA data has limitations. The TCGA isoform expression quantification data annotation errors and batch effects may occur due to the fact that the data was collected not only at different times but also by different institutions (47).

## DATA AVAILABILITY STATEMENT

The original contributions presented in the study are included in the article/supplementary materials. Further inquiries can be directed to the corresponding author.

## ETHICS STATEMENT

This study was approved by the Zhongnan Hospital of Wuhan University ethics committee.

## AUTHOR CONTRIBUTIONS

JX designed the research, completed data analysis and completed the manuscript. ZH and YW helped to revise the manuscript. JX, ZX and BX helped with the final correction. All authors approved the final version.

## REFERENCES

1. Liu S, Yuan Z, Qiao X, Liu Q, Song K, Kong B, et al. Light Scattering Pattern Specific Convolutional Network Static Cytometry for Label-Free Classification of Cervical Cells. *Cytometry A* (2021) 99(6):610–21. doi: 10.1002/cyto.a.24349
2. Sun H, Ma H, Zhang H, Ji M. Up-Regulation of MELK by E2F1 Promotes the Proliferation in Cervical Cancer Cells. *Int J Biol Sci* (2021) 17(14):3875–88. doi: 10.7150/ijbs.62517
3. Burd EM. Human Papillomavirus and Cervical Cancer. *Clin Microbiol Rev* (2003) 16(1):1–17. doi: 10.1128/CMR.16.1.1-17.2003
4. Waggoner SE. Cervical Cancer. *Lancet* (2003) 361(9376):2217–25. doi: 10.1016/S0140-6736(03)13778-6
5. Pandey S, Chandravati. Autophagy in Cervical Cancer: An Emerging Therapeutic Target. *Asian Pac J Cancer Prev* (2012) 13(10):4867–71. doi: 10.7314/APJCP.2012.13.10.4867
6. Borcoman E, Le Tourneau C. Pembrolizumab in Cervical Cancer: Latest Evidence and Clinical Usefulness. *Ther Adv Med Oncol* (2017) 9(6):431–9. doi: 10.1177/1758834017708742
7. Feng CH, Mell LK, Sharabi AB, McHale M, Mayadev JS. Immunotherapy With Radiotherapy and Chemoradiotherapy for Cervical Cancer. *Semin Radiat Oncol* (2020) 30(4):273–80. doi: 10.1016/j.semradonc.2020.05.003
8. Shekarian T, Sivado E, Jallas AC, Depil S, Kielbassa J, Janoueix-Lerosey I, et al. Repurposing Rotavirus Vaccines for Intratumoral Immunotherapy Can Overcome Resistance to Immune Checkpoint Blockade. *Sci Transl Med* (2019) 11(515):1–17. doi: 10.1126/scitranslmed.aat5025
9. Zhang Y, Zhang Z. The History and Advances in Cancer Immunotherapy: Understanding the Characteristics of Tumor-Infiltrating Immune Cells and Their Therapeutic Implications. *Cell Mol Immunol* (2020) 17(8):807–21. doi: 10.1038/s41423-020-0488-6
10. Bi KW, Wei XG, Qin XX, Li B. BTK Has Potential to Be a Prognostic Factor for Lung Adenocarcinoma and an Indicator for Tumor Microenvironment Remodeling: A Study Based on TCGA Data Mining. *Front Oncol* (2020) 10:424. doi: 10.3389/fonc.2020.00424
11. Quail DF, Joyce JA. Microenvironmental Regulation of Tumor Progression and Metastasis. *Nat Med* (2013) 19(11):1423–37. doi: 10.1038/nm.3394
12. Cheng HS, Lee JXT, Wahli W, Tan NS. Exploiting Vulnerabilities of Cancer by Targeting Nuclear Receptors of Stromal Cells in Tumor Microenvironment. *Mol Cancer* (2019) 18(1):51. doi: 10.1186/s12943-019-0971-9
13. Bussard KM, Mutkus L, Stumpf K, Gomez-Manzano C, Marini FC. Tumor-Associated Stromal Cells as Key Contributors to the Tumor Microenvironment. *Breast Cancer Res* (2016) 18(1):84. doi: 10.1186/s13058-016-0740-2
14. Wang J, Li Z, Gao A, Wen Q, Sun Y. The Prognostic Landscape of Tumor-Infiltrating Immune Cells in Cervical Cancer. *BioMed Pharmacother* (2019) 120:109444. doi: 10.1016/j.biopha.2019.109444
15. Xu F, Shen J, Xu S. Integrated Bioinformatical Analysis Identifies GIMAP4 as an Immune-Related Prognostic Biomarker Associated With Remodeling in Cervical Cancer Tumor Microenvironment. *Front Cell Dev Biol* (2021) 9:637400. doi: 10.3389/fcell.2021.637400
16. Wightman SC, Uppal A, Pitroda SP, Ganai S, Burnette B, Stack M, et al. Oncogenic CXCL10 Signalling Drives Metastasis Development and Poor Clinical Outcome. *Br J Cancer* (2015) 113(2):327–35. doi: 10.1038/bjc.2015.193
17. Chen X, He H, Xiao Y, Hasim A, Yuan J, Ye M, et al. CXCL10 Produced by HPV-Positive Cervical Cancer Cells Stimulates Exosomal PDL1 Expression by Fibroblasts *via* CXCR3 and JAK-STAT Pathways. *Front Oncol* (2021) 11:629350. doi: 10.3389/fonc.2021.629350
18. Li Z, Sun G, Sun G, Cheng Y, Wu L, Wang Q, et al. Various Uses of PD1/PD-L1 Inhibitor in Oncology: Opportunities and Challenges. *Front Oncol* (2021) 11:771335. doi: 10.3389/fonc.2021.771335

19. Wu X, Gu Z, Chen Y, Chen B, Chen W, Weng L, et al. Application of PD-1 Blockade in Cancer Immunotherapy. *Comput Struct Biotechnol J* (2019) 17:661–74. doi: 10.1016/j.csbj.2019.03.006
20. Iijima M, Okonogi N, Nakajima NI, Morokoshi Y, Kanda H, Yamada T, et al. Significance of PD-L1 Expression in Carbon-Ion Radiotherapy for Uterine Cervical Adeno/Adenosquamous Carcinoma. *J Gynecol Oncol* (2020) 31(2): e19. doi: 10.3802/jgo.2020.31.e19
21. Karin N. CXCR3 Ligands in Cancer and Autoimmunity, Chemoattraction of Effector T Cells, and Beyond. *Front Immunol* (2020) 11:976. doi: 10.3389/fimmu.2020.00976
22. Callahan MK, Postow MA, Wolchok JD. CTLA-4 and PD-1 Pathway Blockade: Combinations in the Clinic. *Front Oncol* (2014) 4:385. doi: 10.3389/fonc.2014.00385
23. Chow MT, Ozga AJ, Servis RL, Frederick DT, Lo JA, Fisher DE, et al. Intratumoral Activity of the CXCR3 Chemokine System Is Required for the Efficacy of Anti-PD-1 Therapy. *Immunity* (2019) 50(6):1498–512.e5. doi: 10.1016/j.immuni.2019.04.010
24. Humblin E, Kamphorst AO. CXCR3-CXCL9: It's All in the Tumor. *Immunity* (2019) 50(6):1347–9. doi: 10.1016/j.immuni.2019.05.013
25. Liu Y, Liang X, Dong W, Fang Y, Lv J, Zhang T, et al. Tumor-Repopulating Cells Induce PD-1 Expression in CD8(+) T Cells by Transferring Kynurenine and AhR Activation. *Cancer Cell* (2018) 33(3):480–94.e7. doi: 10.1016/j.ccell.2018.02.005
26. Yi X, Du Z, Su Z. PlantGSEA: A Gene Set Enrichment Analysis Toolkit for Plant Community. *Nucleic Acids Res* (2013) 41(Web Server issue):W98–103. doi: 10.1093/nar/gkt281
27. Newman AM, Liu CL, Green MR, Gentles AJ, Feng W, Xu Y, et al. Robust Enumeration of Cell Subsets From Tissue Expression Profiles. *Nat Methods* (2015) 12(5):453–7. doi: 10.1038/nmeth.3337
28. Tokunaga R, Zhang W, Naseem M, Puccini A, Berger MD, Soni S, et al. CXCL9, CXCL10, CXCL11/CXCR3 Axis for Immune Activation - A Target for Novel Cancer Therapy. *Cancer Treat Rev* (2018) 63:40–7. doi: 10.1016/j.ctrv.2017.11.007
29. Hinshaw DC, Shevde LA. The Tumor Microenvironment Innately Modulates Cancer Progression. *Cancer Res* (2019) 79(18):4557–66. doi: 10.1158/0008-5472.CAN-18-3962
30. Griffiths JI, Wallet P, Pflieger LT, Stenehjem D, Liu X, Cosgrove PA, et al. Circulating Immune Cell Phenotype Dynamics Reflect the Strength of Tumor-Immune Cell Interactions in Patients During Immunotherapy. *Proc Natl Acad Sci U S A* (2020) 117(27):16072–82. doi: 10.1073/pnas.1918937117
31. Pandey S, Mittal RD, Srivastava M, Srivastava K, Singh S, Srivastava S, et al. Impact of Toll-Like Receptors [TLR] 2 (-196 to -174 Del) and TLR 4 (Asp299Gly, Thr399Ile) in Cervical Cancer Susceptibility in North Indian Women. *Gynecol Oncol* (2009) 114(3):501–5. doi: 10.1016/j.ygyno.2009.05.032
32. Pandey S. Toll-Like Receptor-2 and Tissue Inhibitor of Matrix Metalloproteinase-2 Genetic Variants as Predictors of Tobacco-Mediated Female Infertility Amongst Mycobacterium Tuberculi-Positive Asian Indian Cohort. *Fertil Steril* (2020) 114(3):e541. doi: 10.1016/j.fertnstert.2020.09.061
33. Pandey S, Mittal RD, Srivastava M, Srivastava K, Mittal B. Cyclooxygenase-2 Gene Polymorphisms and Risk of Cervical Cancer in a North Indian Population. *Int J Gynecol Cancer* (2010) 20(4):625–30. doi: 10.1111/IGC.0b013e3181c63f79
34. Chen L, Diao L, Yang Y, Yi X, Rodriguez BL, Li Y, et al. CD38-Mediated Immunosuppression as a Mechanism of Tumor Cell Escape From PD-1/PD-L1 Blockade. *Cancer Discov* (2018) 8(9):1156–75. doi: 10.1158/2159-8290.CD-17-1033
35. Dong P, Xiong Y, Yu J, Chen L, Tao T, Yi S, et al. Control of PD-L1 Expression by miR-140/142/340/383 and Oncogenic Activation of the OCT4-miR-18a Pathway in Cervical Cancer. *Oncogene* (2018) 37(39):5257–68. doi: 10.1038/s41388-018-0347-4
36. Bergamaschi C, Pandit H, Nagy BA, Stellas D, Jensen SM, Bear J, et al. Heterodimeric IL-15 Delays Tumor Growth and Promotes Intratumoral CTL and Dendritic Cell Accumulation by a Cytokine Network Involving XCL1, IFN-Gamma, CXCL9 and CXCL10. *J Immunother Cancer* (2020) 8(1):1–14. doi: 10.1136/jitc-2020-000599
37. Kinoshita T, Muramatsu R, Fujita T, Nagumo H, Sakurai T, Noji S, et al. Prognostic Value of Tumor-Infiltrating Lymphocytes Differs Depending on Histological Type and Smoking Habit in Completely Resected Non-Small-Cell Lung Cancer. *Ann Oncol* (2016) 27(11):2117–23. doi: 10.1093/annonc/mdw319
38. Tang Y, Zhang AXJ, Chen G, Wu Y, Gu W. Prognostic and Therapeutic TILs of Cervical Cancer-Current Advances and Future Perspectives. *Mol Ther Oncolytics* (2021) 22:410–30. doi: 10.1016/j.omto.2021.07.006
39. Gooden MJ, de Bock GH, Leffers N, Daemen T, Nijman HW. The Prognostic Influence of Tumour-Infiltrating Lymphocytes in Cancer: A Systematic Review With Meta-Analysis. *Br J Cancer* (2011) 105(1):93–103. doi: 10.1038/bjc.2011.189
40. Poh A. Aiming TILs at Melanoma, Cervical Cancer. *Cancer Discov* (2019) 9 (8):990. doi: 10.1158/2159-8290.CD-NB2019-072
41. Joyce JA, Fearon DT. T Cell Exclusion, Immune Privilege, and the Tumor Microenvironment. *Science* (2015) 348(6230):74–80. doi: 10.1126/science.aaa6204
42. Juneja VR, McGuire KA, Manguso RT, LaFleur MW, Collins N, Haining WN, et al. PD-L1 on Tumor Cells Is Sufficient for Immune Evasion in Immunogenic Tumors and Inhibits CD8 T Cell Cytotoxicity. *J Exp Med* (2017) 214(4):895–904. doi: 10.1084/jem.20160801
43. Xu H, Cong F, Hwang TH. Machine Learning and Artificial Intelligence-Driven Spatial Analysis of the Tumor Immune Microenvironment in Pathology Slides. *Eur Urol Focus* (2021) 7(4):706–9. doi: 10.1016/j.euf.2021.07.006
44. Sinjab A, Han G, Treekitkarnmongkol W, Hara K, Brennan PM, Dang M, et al. Resolving the Spatial and Cellular Architecture of Lung Adenocarcinoma by Multiregion Single-Cell Sequencing. *Cancer Discov* (2021) 11(10):2506–23. doi: 10.1158/2159-8290.CD-20-1285
45. Parra ER, Ferrufino-Schmidt MC, Tamegnon A, Zhang J, Solis L, Jiang M, et al. Immuno-Profiling and Cellular Spatial Analysis Using Five Immune Oncology Multiplex Immunofluorescence Panels for Paraffin Tumor Tissue. *Sci Rep* (2021) 11(1):8511. doi: 10.1038/s41598-021-88156-0
46. Allouch S, Malki A, Allouch A, Gupta I, Vranic S, Al Moustafa AE. High-Risk HPV Oncoproteins and PD-1/PD-L1 Interplay in Human Cervical Cancer: Recent Evidence and Future Directions. *Front Oncol* (2020) 10:914. doi: 10.3389/fonc.2020.00914
47. Ibing S, Michels BE, Mosdzien M, Meyer HR, Feuerbach L, Korner C. On the Impact of Batch Effect Correction in TCGA isomiR Expression Data. *NAR Cancer* (2021) 3(1):zcab007. doi: 10.1093/narcan/zcab007

**Conflict of Interest:** The authors declare that the research was conducted in the absence of any commercial or financial relationships that could be construed as a potential conflict of interest.

# Frontiers in
# Oncology

**Advances knowledge of carcinogenesis and tumor progression for better treatment and management**

The third most-cited oncology journal, which highlights research in carcinogenesis and tumor progression, bridging the gap between basic research and applications to imrpove diagnosis, therapeutics and management strategies.

---

## Discover the latest Research Topics

See more →

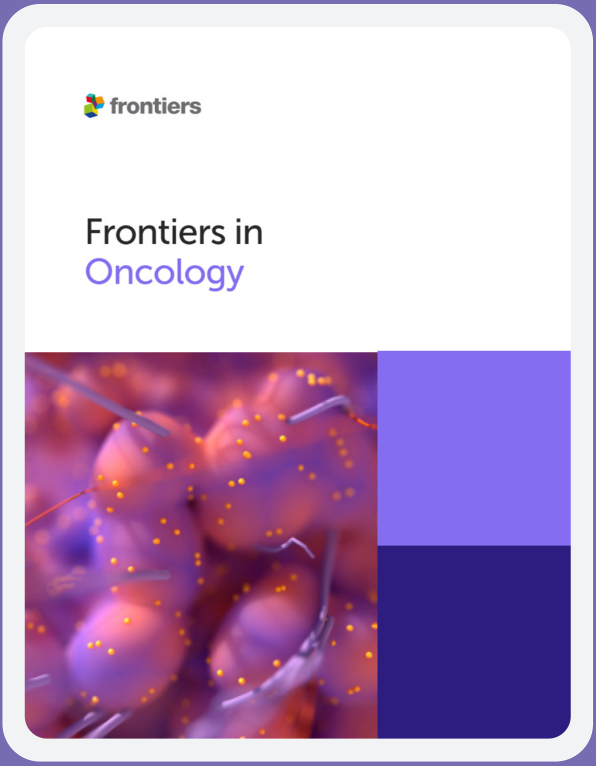

**Frontiers**

Avenue du Tribunal-Fédéral 34
1005 Lausanne, Switzerland
frontiersin.org

**Contact us**

+41 (0)21 510 17 00
frontiersin.org/about/contact